technische universität
dortmund

Deformation of ferrofluid-filled elastic capsules and swelling elastic disks as microswimmers

A thesis submitted for the degree of

Doctor rerum naturalium (Dr. rer. nat.)

by

Christian Jochen Wischnewski

TU Dortmund University
Faculty of Physics
Chair of Theoretical Physics 1b

August 2019

Contact to the author: christian.wischnewski@tu-dortmund.de

Abstract

This thesis includes two parts presenting the results on the research on the deformation of ferrofluid-filled elastic capsules in external magnetic fields as well as on the possibility of the usage of swelling elastic disks as microswimmers by triggering hysteretic shape transformations.

The first part is a primarily theoretical study of deformations and shape transitions of ferrofluid capsules induced by homogeneous and inhomogeneous magnetic fields. The thin elastic shell is modelled by a non-linear shallow shell theory resulting in a system of non-linear shape equations. The properties of the ferrofluid are represented in these equations by the magnetic surface force density that is derived from the magnetic stress tensor by Rosensweig. The elastic part and the magnetic part form a coupled self-consistent problem that is solved iteratively. With that model, two different general cases are investigated. The objective of the first investigation are linearly magnetizable ferrofluid capsules in homogeneous external fields. These capsules are elongated into spheroidal shapes at first and show a transition into shapes with conical tips for stronger magnetic fields and higher susceptibilities. This behavior is shown to be completely analogous to the behavior of simple ferrofluid drops. After that, the model is tested in a comparison with the deformation behavior of real ferrofluid-filled alginate capsules in an experiment with an inhomogeneous external field. All parameters of the capsules and the magnetic field are determined from the experiment. With the surface Poisson ratio as a fit parameter, a good agreement between the numerics and the experiment can be observed. The Poisson ratio of the given alginate capsules is found to be surprisingly close to one.

In the second part, the primary objective is to prove the concept that a flat elastic disk can be used as a microswimmer when a periodical swelling process triggers a shape transformation. Therefore, the disk is modelled by a simple spring mesh with an additional bending energy. A swelling pattern changing the springs' rest length is defined and the total energy of the disk is minimized. This leads to either elliptic dome-like shapes or hyperbolic saddle-like shapes for sufficiently strong swelling. This transition into a curved shape shows numerical pseudo-hysteretic effects that can be expanded to a real hysteresis by adding an additional potential energy. These hysteretic effects are used to break the time invariance of the deformation and bypass the scallop theorem and allow the creation of a microswimmer. Since the swimmer is assumed to operate a low Reynolds numbers, where time invariant deformations do not cause any effective propulsion, these hysteretic effects are they key component in the swimming mechanism. In order to model the hydrodynamic interaction with a surrounding fluid, a Rotne-Prager model for the interaction between small spheres, that model the disk, is used. We find that the elliptic shape is able to move into the direction of its opening, while the hyperbolic shape cannot swim due to its symmetry. In addition, a simplified five-sphere model is introduced in order to imitate the deformation behavior of the disk and finally, the fluid velocity fields of the disk and the simplified model are analyzed.

Kurzfassung

Die vorliegende Arbeit besteht aus zwei separaten Teilen. Diese handeln zum einen von der Deformation mit einem Ferrofluid gefüllter elastischer Kapseln in externen Magnetfeldern, zum anderen wird die Möglichkeit untersucht, eine anschwellende elastische Scheibe als Mikroschwimmer zu nutzen.

Der erste Teil ist eine primär numerische Untersuchung von Ferrofluidkapseln in Magnetfeldern. Die dünne elastische Schale eben jener Kapseln wird durch eine nichtlineare Theorie dünner Schalen modelliert. Zentraler Bestandteil dieses Modells ist ein System nichtlinearer Formgleichungen. Das Ferrofluid wird mit Hilfe der magnetischen Kraftdichte an der Oberfläche des Fluids an die Formgleichungen gekoppelt. Diese Kraftdichte basiert dabei auf dem magnetischen Spannungstensor von Rosensweig. Der magnetische und der elastische Teil formen dabei gemeinsam ein gekoppeltes selbstkonsistentes Problem, das iterativ gelöst wird. Mit diesem numerischen Modell werden zwei verschiedene Situationen untersucht. Zuerst werden linear magnetisierbare Kapseln in einem homogenen externen Feld betrachtet. Die Kapseln werden bei steigender Feldstärke gestreckt und nehmen die Form eines Ellipsoiden an. Bei starken Magnetfeldern und hinreichend großen Suszeptibilitäten kann ein Übergang in eine stark gestreckte Form mit konischen Spitzen beobachtet werden, wie er auch von einfachen Ferrofluidtropfen bekannt ist. Anschließend wird das Modell einem Praxistest unterzogen, indem ein experimenteller Vergleich mit der Deformation echter Alginatkapseln in einem inhomogenen Feld durchgeführt wird. Dazu werden sämtliche Parameter der Kapseln im Experiment bestimmt, die Poissonzahl wird in der Numerik jedoch als freier Fitparameter genutzt. Damit ergibt sich eine sehr gute Übereinstimmung zwischen Theorie und Experiment, sowohl bei der Kapselform als auch in der Aussage, dass die Poissonzahl dieses Alginatsystems ungewöhnlich groß, nämlich beinahe eins, ist.

Der zweite Teil dieser Arbeit ist primär eine Machbarkeitsstudie, bei der es darum geht zu zeigen, dass eine flache elastische Scheibe durch periodisches An- und Abschwellen als Mikroschwimmer eingesetzt werden kann. Dazu wird die Elastizität der Scheibe durch ein einfaches Federgitter mit einer zusätzlichen Biegeenergie modelliert. Beim Anschwellen wird die Ruhelänge der Federn verändert und durch eine Minimierung der Gesamtenergie wird die daraus resultierende Form der Scheibe berechnet. Bei hinreichend starkem Anschwellen oder Schrumpfen findet ein Übergang in eine gekrümmte Form statt. Dies ist entweder eine elliptische Kuppelform oder ein hyperbolischer Sattel. Dabei treten numerische Pseudohystereseeffekte auf, die durch eine zusätzliche potentielle Energie auch um einen echten Hysteresebereich erweitert werden können. Durch diese Hystereseffekte wird die Zeitumkehrinvarianz der Deformation gebrochen, was die Nutzung als Mikroschwimmer ermöglicht. Da der Schwimmer im Regime kleiner Reynoldszahlen angesiedelt ist, können zeitumkehrinvariante Deformationen keinen effektiven Vortrieb erzeugen und die Hysterese stellt eine Schlüsselkomponente im Antrieb des Schwimmers dar. Die hydrodynamische Wechselwirkung mit dem Fluid wird anschließend durch eine Rotne-Prager-Wechselwirkung simuliert, bei der die eigentliche Wechselwirkung zwischen kleinen Kugeln stattfindet, die die Scheibe nachbilden. Im Ergebnis gibt es eine effektive Schwimmbewegung der elliptischen Form, während die eigene Symmetrie eine Bewegung des Sattels verhindert. Anschließend wird ein vereinfachtes 5-Kugel-Modell eingeführt, um den Schwimmmechanismus der Scheibe nachzubilden. Zum Abschluss folgt eine Untersuchung des Geschwindigkeitsfeldes des Fluids in der direkten Umgebung der Scheibe und des vereinfachten Modelschwimmers.

Contents

1. Elastic instabilities and shape transitions

Elastic systems are usually solids that can be deformed in a reversible way by external forces. There is a relaxed rest state without any internal forces in the material. If external forces are applied on an elastic body, the material is deformed out of its rest state. As soon as any deformation occurs, internal forces, elastic stresses, arise and try to relax the material back to its reference shape. The larger deviations from the rest shape are, the higher the elastic stresses become. A real material under external forces always shows elastic behavior at first, but if the strains in the material, the deviations from the reference shape, become large enough, the deformation will become irreversible and cannot be called elastic anymore. Instead, there is a plastic behavior. For even stronger deformations, cracks or rupture of the material occur [83]. In practice, every solid shows elastic behavior under external forces at first, but the term *elastic system* is usually only applied to systems that can be deformed elastically on a macroscopic scale.

A very interesting feature of elastic systems under external forces is the ability to develop shape instabilities and shape transitions. The most prominent and simple example is a long straight elastic rod under compressive forces. For small forces, the rod simply becomes shorter, but if the forces exceed a certain threshold, then rod buckles into a curved shape [83]. Such a shape transition is the result of the interplay between two elastic energies that reduces the total energy: The stretching energy, which is the result of a stretching or a compression of an elastic material, is reduced, while the bending energy following from the materials resistance against bending deformations rises.

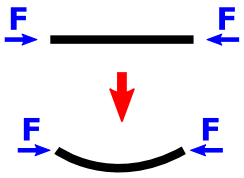

Figure 1.1.: A long rod buckles under a compressive force.

Basically, the same effect leads to the formation of wrinkles on a flat elastic sheet under compression [74]. In a similar manner, elastic capsules, thin spherical elastic shells encapsulating an inner volume, show a buckling transition under volume reduction or compressive pressures. If the volume reduction exceeds a critical value, the total energy can be reduced by the formation of a dimple. Again, the stretching energy decreases in exchange for an increased bending energy [75]. This happens particularly easy for thin elastic materials because the stretching modulus depends linearly on the thickness while the bending modulus is proportional to the third power of the thickness and, thus, much smaller for thin materials.

The main topic of this thesis is the theoretical and numerical analysis of the deformation of specific very thin elastic systems with an effectively two-dimensional elasticity. It is divided into two separated parts. In the first part, a spherical elastic capsule filled with a ferrofluid is deformed by an external magnetic field. We find a transition from a spheroidal shape into an elongated shape with conical tips in a homogeneous field. This transition is driven by an interplay between the elastic stretching energy and the magnetic field energy. In a second analysis, the numerical model is compared to the results of an experiment with a real ferrofluid-filled alginate capsule in an inhomogeneous magnetic field.

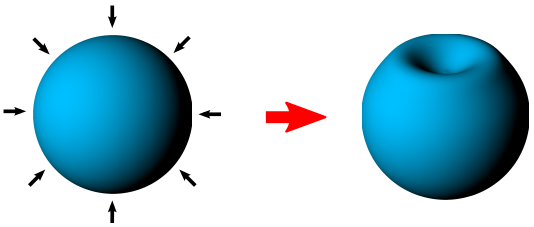

Figure 1.2.: An elastic capsule forms a dimple under volume reduction.

The second part of the thesis is about a shape transition of a swelling flat circular disk. Internal elastic stresses that result from an inhomogeneous swelling process of the material can be reduced by a transition into a curved shape for the price of an increased bending energy. The (pseudo-) hysteretic behavior of this transition is exploited in order to create a microswimmer. A periodically swelling flat elastic disk is then able to propel itself in an external fluid at low Reynolds numbers.

Part I.

Deformation of ferrofluid-filled elastic capsules in external magnetic fields

Author's publication list

Significant parts of the first part of this thesis about the deformation of ferrofluid-filled elastic capsules are based on the following previous publications and a master's thesis:

- Wischnewski, C. and Kierfeld, J. Spheroidal and conical shapes of ferrofluid-filled capsules in magnetic fields. *Phys. Rev. Fluids. 3* (2018), 043603

- Wischnewski, C. Zwar, E., Rehage, H. and Kierfeld, J. Strong Deformation of Ferrofluid-Filled Elastic Alginate Capsules in Inhomogenous Magnetic Fields. *Langmuir 34* (2018), 13534-13543

- Wischnewski, C. *Numerische Berechnung der Deformation elastischer Kapseln durch Ferrofluide.* Master's thesis, Technische Universität Dortmund, 2015

List of symbols

The following list shows an overview over frequently used or important symbols, their meaning and the page number of their first appearance or explanation. The index "0" at some elastic symbols and coordinates describes a quantity that is related to the undeformed spherical reference shape, while the symbol without that index is related to the deformed shape.

Symbol	Meaning	page
a	polar radius of the capsule	14
a	height of the capsule in an inhomogeneous field	62
α	half opening angle of the conical tip	91
b	equatorial radius of the capsule	14
b	width of the capsule in an inhomogeneous field	62
B_m	magnetic Bond number	36
$B_\mathrm{m,c1}$	lower critical magnetic Bond number	51
$B_\mathrm{m,c2}$	upper critical magnetic Bond number	51
$\boldsymbol{B}$	magnetic flux density	23
c_m	magnetite mass concentration	64
χ	magnetic susceptibility	23
χ_c	critical magnetic susceptibility	53
d	displacement in the capsule compression measurement	67
e_φ	strain in circumferential direction	14
e_s	strain in meridional direction	14
E_γ	surface energy coming from the interface tension	16
E_el	elastic energy	15
E_mag	magnetic field energy	41
ϵ	eccentricity of the spheroid	40
η	divergence exponent of the stretching factors	49
f_m	magnetic surface force density	24
F	force in the capsule compression measurement	67
g	gravitational acceleration	64
γ	interface tension	16
γ_FvK	Föppl-von Kármán number	32
Γ	one-dimensional contour line generating the surface by revolution	14
h	thickness of the elastic shell	13
$\boldsymbol{H}$	magnetic field strength of the total magnetic field	23
$\boldsymbol{H}_\mathbf{ext}$	magnetic field strength of the external magnetic field	23
I	field generating current in the coil	69
K_φ	bending strain in circumferential direction	14
K_s	bending strain in meridional direction	14
κ_B	bending modulus	15
κ_φ, $\kappa_{\varphi 0}$	curvature in circumferential direction	14
κ_s, κ_{s_0}	curvature in meridional direction	14
l_0	base factor in the calculation of L_i	30
L, L_0	arclength on the surface from the lower apex to the upper apex	13
L_i	length of the i-th boundary element	30

L_w	length of the wrinkles	21
λ_φ	stretching factor in circumferential direction	14
λ_s	stretching factor in meridional direction	14
m_φ	bending moment in circumferential direction	15
m_s	bending moment in meridional direction	15
$\boldsymbol{M}$	magnetization	23
M_s	saturation magnetization	36
μ	magnetic permeability	25
μ_0	magnetic vacuum permeability	23
μ_wall	shooting parameter for the strength of the repulsive wall	72
n	number of intervals in the multiple shooting method	18
n_B	number of boundary segments on the contour line Γ	27
$\boldsymbol{n}$	normal vector pointing outwards of the capsule	24
$\partial/\partial\boldsymbol{n}$	derivative in normal direction	25
ν	surface Poisson ratio	15
ω	rotational frequency in the spinning capsule measurement	68
Ω_FEM	two-dimensional domain representing the capsule in the (r,z)-plane	26
Ω_out	two-dimensional representation of the domain outside of the capsule	27
p_0	inner pressure, Lagrange multiplier for the volume	18
p_n	force density on the elastic shell in normal direction	16
$p_{n,\mathrm{h}}$	hydrostatic pressure	64
p_s	force density on the elastic shell in meridional direction	16
φ, φ_0	circumferential/azimuthal angle coordinate	13
ψ, ψ_0	slope angle of the capsule's contour	13
q	transversal shear stress	16
q^*_ax	normal derivative of u^*_ax	28
r, r_0	radial distance to the z-axis	13
R_0	radius of the reference sphere	13
ρ	mass density of the ferrofluid	24
$\Delta\rho$	mass density difference between the inner and the outer liquid	64
s, s_0	arclength coordinate following the capsule's contour line	13
τ_φ	elastic stress in circumferential direction	15
τ_s	elastic stress in meridional direction	15
θ	polar angle in spherical coordinates	37
θ_w	smallest polar angle where wrinkles occur	54
u	scalar magnetic potential	24
u^*_ax	axisymmetric fundamental solution of the Laplace equation	28
u_ρ	displacement of the surface in radial direction	37
u_θ	displacement of the surface in polar direction	37
V_0	constant volume of the spherical capsule	13
w_S	elastic energy density of the surface	15
Y_2D	two-dimensional Young modulus	15
z, z_0	Euclidean z-coordinate	13

2. Elastic capsules and ferrofluids

Elastic capsules are usually small objects that consist of an inner phase and a closed surrounding elastic shell. They are in general filled with a fluid or a gas. Such capsules can be found in nature, with red blood cells and virus capsids as typical examples [25, 43, 102], as well as in artificial technical applications. For example, elastic capsules are used in the food industry [57], pharmacy [153] or in the construction of self-healing materials [7]. The term elastic means that the shell of the capsule can be deformed by external forces in a reversible way. Usually there is a relaxed rest shape that is free of internal forces. An external force acting on the shell deforms the material out of its equilibrium shape, which causes internal stresses in the material. When the external force is removed again, these stresses lead to the return of the shell into its original force-free state. Therefore, elastic capsules can provide a kind of protection for their ingredients. The reference state of the elastic shell is often spherical, which is the only reference shape used in this thesis.

The elastic properties and the deformation behavior are influenced by several factors, such as material properties like the Young modulus and the Poisson ratio, the curvature of the reference shape as well as the thickness of the shell. Changing these properties can lead to different effects. For example, a lower Young modulus, which is the continuum analogon to a spring constant, leads to capsule that is easier to deform in any way. A lower shell thickness on the other hand has the effect that the shell primarily has a lower resistance against bending. Elastic capsules can be manipulated and deformed in various ways. Apart from the obvious possibility of a deformation with a direct mechanical force, which is the result of a direct contact, there are more subtle ways. An important effect, that was the topic of many studies in the past, are buckling instabilities. They can be observed by changing the inner volume or internal pressure of a capsule [37, 56, 75, 76, 77, 127]. A reduction of the volume causes the capsule to shrink, which induces compressive stresses. After exceeding a critical value, a dimple is formed, which reduces the stretching energy and increases the bending energy. There are also investigations on the deformation behavior induced by external hydrodynamic flows [9, 19, 111, 121]. The flow field of a fluid causes forces on the shell of a capsule and based on the specific properties of the capsule, different shapes are the result.

The deformation of an initially spherical elastic capsule is the main topic of this part of this thesis. Here, we want to describe a way to achieve the deformation without any mechanical contact. Some concepts on this topic can already be found in the literature. In ref. [70], elastic capsules were deformed with the help of an electric field that polarizes the fluid inside of the capsule. The polarized fluid tries to align itself in the external field and therefore stretches the capsules. This is a promising concept, but magnetic fields are much better controllable in typical environments, since they are not able to induce any unwanted currents (as long as they do not change quickly). As soon as a material is not a perfect insulator, an external electric field causes electric currents due to the potential difference. Since there are no magnetic monopoles, magnetic fields do not have this drawback. The idea to deform capsules with magnetic fields was also presented in ref. [38]. There, magnetic particles were added to the fluid inside the capsule. These particles react to the magnetic field, but a problem is that such suspensions are not stable against segregation and the formation of particle chains in the presence of a field. The particles are magnetized in the field and attract each other until they form larger clusters so that they are not evenly distributed anymore. Larger clusters are also prone to segregation due to gravity. To avoid such problems, we focus on the idea to combine

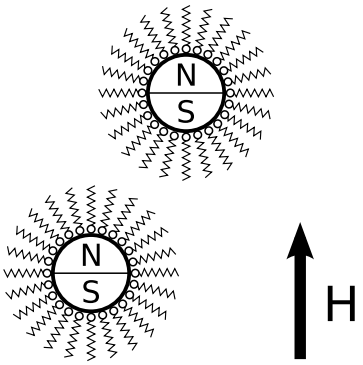

Figure 2.1.: The single magnetic domains in the magnetite (Fe_3O_4) nanoparticles in the ferrofluid build a macroscopic magnetization in an external magnetic field. The steric repulsion of the surfactants on the particles prevents the formation of clusters. The polar heads stick to the magnetite, while the nonpolar tails point towards the carrier fluid.

the elastic shell with a ferrofluid inside.

A ferrofluid is a more advanced magnetically active fluid that does not show the aforementioned disadvantages. The basic idea of a ferrofluid is to use much smaller particles in order to ensure an always constant particle density. Therefore, a ferrofluid consists of a usually non-polar carrier fluid and ferro- or ferrimagnetic nanoparticles. In most cases, magnetite (Fe_3O_4) is used for that purpose. The diameter of these particles should be smaller than about 10 nm in general. This small size ensures that the thermal energy of the particles is higher than their magnetic interaction energy. In addition, the particles are coated with an outer layer of surfactants, as it is visualized in fig. 2.1. The idea is to get an additional steric repulsion ensuring that a collision between two particles acts in an elastic way. In addition, the magnetic cores cannot make contact to each other avoiding a higher magnetic interaction. As a result, the nanoparticles are not able to form clusters or chains and stay evenly distributed in the fluid [125]. They are also very stable against segregation in external fields like a gravity field or even stronger inhomogeneous magnetic fields over long times. Another important effect of the small particle size is that the magnetite particles show a superparamagnetic behavior. They have a characteristic ferrimagnetic[1] magnetization curve, similar to a bulk of magnetite, but this curve does not show any hysteresis effects. If the external magnetic field, which caused the magnetization, vanishes, the particles completely lose their magnetization. That is a distinct contrast to the behavior of a bulk of ferromagnetic or ferrimagnetic material, where a remanent magnetization remains when the external field vanishes. Each particle consists of a single magnetic domain that stays magnetized, but thermal fluctuations can flip the magnetization inside the particle into the opposite direction so rapidly that no effective magnetization is visible on a macroscopic time scale. The thermal fluctuations have to be stronger than the energy barrier that has to be overcome in order to fulfil such a flip. Therefore, superparamagnetic effects only occur in small nanoparticles, where this barrier is sufficiently small [24, 58, 71]. Rosensweig was the first to present a complete theory that is able to describe the dynamical behavior of a ferrofluid in external magnetic fields [36, 125]. The ability to control the magnetization directly with an external field as well as the fluid properties and the long-time stability make ferrofluids interesting for different technical and also medical applications [67, 97, 107, 142]. Recently, the research on ferrofluids was even able to go one step further. A fluid with the magnetic properties of a ferromagnet, especially a permanent magnetization, was developed by exploiting the behavior of magnetic nanoparticles at interfaces [98].

If a ferrofluid is used as the inner fluid of an elastic capsule, then the convincing controllability of the ferrofluid in an external magnetic field provides the possibility to manipulate the capsule or even destroy it without a direct contact. The primary objective of this first part of this thesis is the development and investigation of a numerical model that is able to describe

[1] A ferrimagnet consists of atoms with opposing magnetic moments of unequal strengths. Thus, the magnetic behavior is analogous to a ferromagnet, but in general weaker.

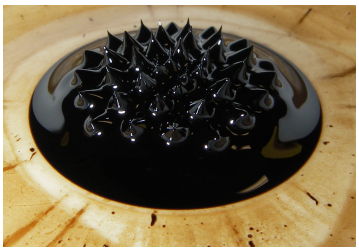

Figure 2.3.: A free ferrofluid forms a hexagonal pattern of sharp tips in an external magnetic field. This image was taken from ref. [69].

the deformation of an initially spherical elastic capsule, filled with a ferrofluid, in external magnetic fields. We focus on the steady state with an equilibrium of forces. Dynamics towards the steady state are not regarded. From a technical point of view, there are similarities to the deformation of capsules in a sedimentation process in an external flow field [19]. There, an elastic capsule is deformed by an external flow field and both the flow field and the capsule have to be calculated simultaneously. In our case, the magnetic field takes a similar role.

On the other hand, viewed from the perspective of the research on ferrofluids, this thesis can be interpreted as an expansion of a well known problem, the deformation of a simple ferrofluid drop in an external field [1, 3, 8, 11, 87, 88, 135]. Ferrofluid drops elongate in homogeneous fields into shapes that are nearly spheroidal with a homogeneous magnetization. If the susceptibility of the fluid is high enough, then these shapes can perform a transition into a highly elongated shape with conical tips for sufficiently high magnetic fields. Near these conical tips, very strong fields and high magnetizations can occur. The mechanism leading to this effect is the interplay between the surface energy, which is increased due to the increasing area, and the magnetic field energy, which is reduced in the conical shape. The transition from a spheroidal shape into a conical one is completely analogous to the formation of the normal field instabilities, a pattern of little sharp tips on a free ferrofluid surface in an external field [21, 36]. The formation of conical shapes can also be observed for water or in general dielectric drops [120, 152] and soap bubbles [145] in electric fields and is caused by the same mechanism. In our system, in addition to the interfacial tension of the fluid, the elastic shell represents an additional force acting against the magnetic force. Also, effects like the formation of wrinkles on the surface are possible for elastic capsules [6, 78, 121, 140], which a simple drop would never show. Wrinkles are a typical effect of thin elastic systems. Compressive stresses can be reduced by the formation of a wave-like pattern increasing the effective surface area. That leads to the question how the behavior of a ferrofluid capsule changes in contrast to a simple drop.

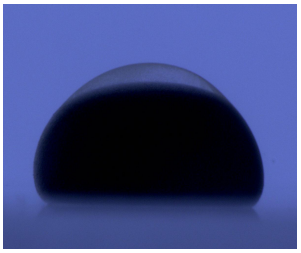

Figure 2.2.: An elastic capsule filled with a ferrofluid is deformed in an external magnetic field. This image was already published in ref. [148].

We start in chapter 3 with the presentation of the theoretical model. The elastic model describing the elastic shell based on a non-linear shell theory is introduced in section 3.1. Then the magnetic model for the ferrofluid, based on the formalism of Rosensweig that was presented in ref. [125], follows in sec. 3.2. Both models are finally combined. In chapter 4, we investigate the deformation behavior of the capsule in a homogeneous external field and also compare the shape transition to the behavior of a droplet. This chapter is motivated from a purely theoretical point of view. In contrast to that, we focus on the comparison of our model to the results of an experiment with real capsules in an inhomogeneous magnetic field in chapter 5. This experiment was performed in a collaboration with E. Zwar and H. Rehage (chair for physical chemistry II at the Technical University of Dortmund). Some final remarks in chapter 6 close this part about ferrofluid-filled elastic capsules.

The theoretical model and all results that are developed in this work about ferrofluid capsules are also applicable to capsules that are filled with a dielectric liquid in an external electric field. We show in sec. 3.2.2 that the underlying theory is the same and both formulations are equivalent. We focus on ferrofluids though, because magnetic fields often cause less unwanted side effects in a real environment than electric fields.

3. Theoretical description of ferrofluid-filled elastic capsules

In this chapter, an introduction into the models that describe the shape of elastic capsules deformed by external magnetic fields is given. We start with an axisymmetric shallow shell theory for the elastic shell, followed by a magnetic model for the ferrofluid where the central object is the magnetic stress tensor. Finally, both models are coupled.

3.1. Elastic model

In this section, we present a mathematical description of a thin elastic shell, which encapsulates an inner volume and forms an elastic capsule. The capsules are spherical in their rest state with a radius R_0. The elastic shell is assumed to be impermeable, thus the volume is fixed at $V_0 = 4\pi R_0^3/3$ and does not change for the rest of this thesis. The shell's thickness h is assumed to be small, i.e. $h \ll R_0$, so that shallow shell theory can be used. Therefore, the elastic shell can be considered to be two-dimensional. The finite thickness just comes into play in terms of the bending resistance in sec. 3.1.2. This model for the description of elastic capsules was already introduced in refs. [19, 74, 75, 78]. The following section closely follows the descriptions in the mentioned references and primarily uses the notation from Knoche [74].

3.1.1. Parametrization and strains

In the following, we only consider axisymmetric shells. The coordinate system is set such that the rotational axis is identical to the z-axis. The elastic nature of the problem requires to distinguish between the undeformed spherical reference shape free of forces and a deformed shape in general. The surface is parametrized with the help of cylindrical coordinates (r_0, φ_0, z_0) and the origin is set to the capsule's center. In order to describe a two-dimensional surface, we need two parameters. Therefore, we introduce the arc length s_0 that starts at the capsule's lower apex at $s_0 = 0$ and ranges up to the upper apex at $s_0 = L_0 = \pi R_0$ describing a one-dimensional contour line Γ_0 on the surface. This arc length $s_0 \in [0, L_0]$ and the circumferential angle $\varphi_0 \in [0, 2\pi)$ together are able to describe every point on the surface. The contour line Γ_0 generates the whole surface by a revolution around the z-axis. With the help of s_0, the slope angle ψ_0, see fig. 3.1 (a) can be defined via

$$\frac{\mathrm{d}r_0}{\mathrm{d}s_0} = \cos\psi_0, \quad \frac{\mathrm{d}z_0}{\mathrm{d}s_0} = \sin\psi_0. \tag{3.1}$$

For the spherical rest shape, we can directly see $\psi_0 = s_0/R_0$ with $\psi_0 \in [0, \pi]$. Knowing the slope angle ψ_0, we can define the principal curvatures κ_{s_0} in the meridional direction, the

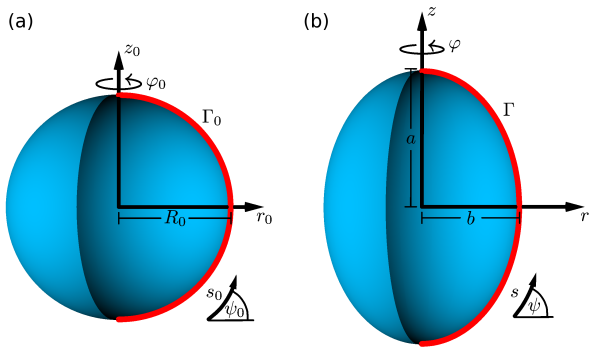

Figure 3.1.: Illustration of the parametrization in cylindrical coordinates (r_0,z_0,φ_0) for the spherical reference shape (a) and (r,z,φ) for a deformed shape (b). The two-dimensional contour lines Γ_0 and Γ with arc lengths s_0 and s are shown in red. The complete capsules are obtained by revolution of the contour lines, while the angles ψ_0 and ψ describe the slopes. The contour line of the deformed shape is calculated numerically. The polar radius is called a, while b denotes the equatorial radius.

s_0-direction, and κ_{φ_0} in circumferential direction. These curvatures are calculated via

$$\kappa_{s_0} = \frac{\mathrm{d}\psi_0}{\mathrm{d}s_0}, \quad \kappa_{\varphi_0} = \frac{\sin\psi_0}{r_0} \tag{3.2}$$

with $\kappa_{s_0} = \kappa_{\varphi_0} = 1/R_0$ for the spherical reference shape.

When the elastic surface is deformed, then points on that surface are moved to new positions. The deformed surface is described in a similar way as the reference shape but without the index "0". This index always refers to the spherical reference shape. The two-dimensional contour line Γ of the deformed shape is given by the two functions $r(s)$ and $z(s)$. The slope angle and curvatures are written in the form

$$\frac{\mathrm{d}r}{\mathrm{d}s} = \cos\psi, \quad \frac{\mathrm{d}z}{\mathrm{d}s} = \sin\psi \quad \text{and} \quad \kappa_s = \frac{\mathrm{d}\psi}{\mathrm{d}s}, \quad \kappa_\varphi = \frac{\sin\psi}{r}. \tag{3.3}$$

Since the deformed shape is no longer spherical, we also define a polar radius a and an equatorial radius b. Then the aspect ratio a/b gives information about the elongation of the capsule. For an illustration of the parametrization of the deformed shape, see also fig. 3.1 (b). Since the arc length s ranges now from 0 to $L \neq L_0$ in general, s is unknown a priori at a given point on the surface. In order to be able to have well defined parameters, we still use the arc length s_0 and the angle φ_0 of the reference shape as coordinates. Therefore, we need to define a relation between s_0 and s. We define the stretching factor λ_s in meridional direction via

$$\lambda_s(s_0) = \frac{\mathrm{d}s}{\mathrm{d}s_0}. \tag{3.4}$$

The arc length then follows via

$$s = \int_0^{s_0} \lambda_s(s_0')\mathrm{d}s_0'. \tag{3.5}$$

Similarly, the stretch factor in circumferential direction is given by

$$\lambda_\varphi(s_0) = \frac{r(s_0)}{r_0}. \tag{3.6}$$

Finally, we need to define the strains e_s and e_φ, the deviations to the reference shape and analogously bending strains K_s and K_φ via

$$e_s = \lambda_s - 1, \quad e_\varphi = \lambda_\varphi - 1 \quad \text{and} \quad K_s = \lambda_s\kappa_s - \kappa_{s_0}, \quad K_\varphi = \lambda_\varphi\kappa_\varphi - \kappa_{\varphi_0}. \tag{3.7}$$

3.1.2. Energies and stresses

The elastic behavior of the capsule's shell is modelled by a non-linear theory of thin shells [75, 78, 94, 113]. The shell features a Hookean energy density w_S, which is given by

$$w_S = \frac{1}{2}\frac{Y_{2D}}{1-\nu^2}(e_s^2 + 2\nu e_s e_\varphi + e_\varphi^2) + \frac{1}{2}\kappa_B(K_s^2 + 2\nu K_s K_\varphi + K_\varphi^2). \tag{3.8}$$

The constant Y_{2D} is the two-dimensional Young modulus. It describes the material's resistance against stretching and is related to the three-dimensional Young modulus via $hY_{3D} = Y_{2D}$. The parameter ν is the surface Poisson ratio, which quantifies the ratio between the transversal strain and axial strain in a stretching process. In can take values in a range of $\nu \in [-1, 1]$. In the theoretical investigations of ferrofluid-filled capsules in homogeneous magnetic fields in chapter 4 we use a value of $\nu = 1/2$ in general, which is a typical value for an incompressible polymeric material. After that, in chapter 5, where a real experiment with alginate capsules is investigated, ν is found to be close to one for these specific capsules. The last constant in front of the bending term, κ_B, represents the bending modulus. Analogously to the Young modulus, κ_B describes the materials resistance against bending. For thin shells, it can be calculated from the Young modulus and the Poisson ratio via

$$\kappa_B = \frac{Y_{2D}h^2}{12(1-\nu^2)} = \frac{Y_{3D}h^3}{12(1-\nu^2)}. \tag{3.9}$$

Since we have $\kappa_B \sim h^3$ and $Y_{2D} \sim h$, it is easy to understand why the contribution of the bending to the total energy is usually small compared to the stretching part for thin shells. The energy density (3.8) is defined as an elastic energy per unit area of the undeformed reference shape. Therefore, the total elastic energy can be calculated via

$$E_{el} = \int w_S \mathrm{d}A_0 = 2\pi \int_0^{L_0} w_S r_0 \mathrm{d}s_0. \tag{3.10}$$

Starting from the elastic energy density, we can derive the stresses τ_s, τ_φ and the bending moments m_s, m_φ in the material as derivatives of w_S with respect to the strains and bending strains [74, 94]:

$$\tau_s = \frac{1}{\lambda_\varphi}\frac{\partial w_S}{\partial e_s} = \frac{Y_{2D}}{(1-\nu^2)\lambda_\varphi}\left[(\lambda_s - 1) + \nu(\lambda_\varphi - 1)\right], \tag{3.11}$$

$$\tau_\varphi = \frac{1}{\lambda_s}\frac{\partial w_S}{\partial e_\varphi} = \frac{Y_{2D}}{(1-\nu^2)\lambda_s}\left[(\lambda_\varphi - 1) + \nu(\lambda_s - 1)\right], \tag{3.12}$$

$$m_s = \frac{1}{\lambda_\varphi}\frac{\partial w_S}{\partial K_s} = \frac{\kappa_B}{\lambda_\varphi}(K_s + \nu K_\varphi), \tag{3.13}$$

$$m_\varphi = \frac{1}{\lambda_s}\frac{\partial w_S}{\partial K_\varphi} = \frac{\kappa_B}{\lambda_s}(K_\varphi + \nu K_s). \tag{3.14}$$

These relations, that link stresses, strains and bending moments together, are also called constitutive relations. Despite using a Hookean energy density, these constitutive relations are non-linear due to the $1/\lambda_s$ and $1/\lambda_\varphi$ prefactors. These prefactors appear for geometrical reasons. In order to have quantities of more practical relevance, the stresses and bending moments are defined per unit length of the deformed shape. The energy density w_S on the other hand is defined per unit area of the undeformed shell. The $1/\lambda$-prefactors then compensate this discrepancy.

3.1.3. Equilibrium of forces and shape equations

Since we do not want to consider empty capsules in a vacuum, but capsules filled with a fluid that are also surrounded by another fluid in general, we need to add a constant isotropic interfacial tension γ. The energy related to that interfacial tension is proportional to the total area A:

$$E_\gamma = \int \gamma \mathrm{d}A = \int \gamma \lambda_s \lambda_\varphi \mathrm{d}A_0 = \gamma A. \tag{3.15}$$

In this thesis, we are only interested in stationary configurations of the capsule. Therefore, there must always be an equilibrium of forces in every direction inside the elastic shell. The equations describing the equilibrium of forces can be derived in an elegant way by a variation of the elastic energy density w_S. For details of this calculation the reader may be referred to the reference [74]. This results in three equilibrium equations:

$$0 = (\tau_s + \gamma)\kappa_s + (\tau_\varphi + \gamma)\kappa_\varphi + \frac{1}{r}\frac{\mathrm{d}(rq)}{\mathrm{d}s} - p_n, \tag{3.16}$$

$$0 = \frac{\cos\psi}{r}\tau_\varphi + \kappa_s q - \frac{1}{r}\frac{\mathrm{d}(r\tau_s)}{\mathrm{d}s} - p_s, \tag{3.17}$$

$$0 = q + \frac{1}{r}\frac{\mathrm{d}(rm_s)}{\mathrm{d}s} - \frac{\cos\psi}{r} m_\varphi. \tag{3.18}$$

The first equation (3.16) describes the equilibrium of forces in normal direction. The surface tension γ only appears in that single equation, because a surface tension is only able to cause forces that are normal to the surface. The term p_n describes other force densities acting on the surface in normal direction that are not of an elastic origin. A constant inner pressure p_0, a hydrostatic pressure p_h and the magnetic force density f_m, which is caused by the ferrofluid, enter the model at that position, later. Analogously, the second equation (3.17) represents the force equilibrium in the tangential direction, i.e. in s-direction (due to the rotational symmetry, there is always an equilibrium of forces in the circumferential φ-direction). In the same way as before, p_s describes possible external forces acting in s-direction. The last equation (3.18) does not describe a force equilibrium, but gives the definition of the quantity q, the *transverse shear stress*. It describes a normal force caused by a shear process. Figure 3.2 illustrates the directions of stresses and bending moments inside of the elastic shell.

The equilibrium equations can now be rearranged in order to derive a system of differential equations. Therefore, the derivatives of any function g with respect to s are replaced by derivatives with respect to s_0 via

$$\lambda_s \frac{\mathrm{d}g}{\mathrm{d}s} = \frac{\mathrm{d}g}{\mathrm{d}s_0} \equiv g'(s_0). \tag{3.19}$$

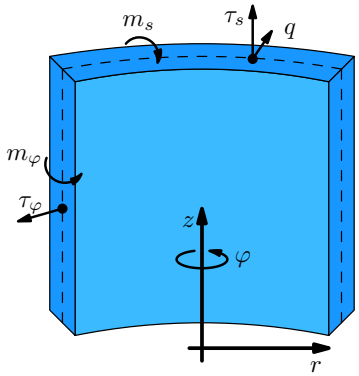

Figure 3.2.: Illustration of stresses and bending moments in a cross-section of the elastic shell. The dashed line implies the midsurface. While τ_s and τ_φ act tangential to that midsurface, q points in normal direction. The bending moments m_s and m_φ try to rotate the surface.

Finally, we find

$$\begin{aligned} q'(s_0) &= \lambda_s \left(-\kappa_s(\tau_s + \gamma) - \kappa_\varphi(\tau_\varphi + \gamma) - \frac{q}{r}\cos\psi + p_n \right), & r'(s_0) &= \lambda_s \cos\psi, \\ \tau_s'(s_0) &= \lambda_s \left(\frac{\tau_\varphi - \tau_s}{r}\cos\psi + \kappa_s q - p_s \right), & z'(s_0) &= \lambda_s \sin\psi, \\ m_s'(s_0) &= \lambda_s \left(\frac{m_\varphi - m_s}{r}\cos\psi - q \right), & \psi'(s_0) &= \lambda_s \kappa_s. \end{aligned} \tag{3.20}$$

These equations are called *shape equations*. They form a system of six coupled first-order nonlinear differential equations that cannot be solved analytically except for trivial cases. This system has to be solved numerically in order to calculate the contour line of elastic capsule (the red line in fig. 3.1) for given external forces. The three equations in the left column are the rearranged equilibrium equations, while the right column represents geometrical relations. The functions ($q(s_0)$, $\tau_s(s_0)$, $m_s(s_0)$, $r(s_0)$, $z(s_0)$, $\psi(s_0)$) form our basic quantities that have to be calculated, but we need additional relations to close the system (3.20). For that purpose, we use the constitutive relations (3.11)-(3.14) and the definitions of λ_φ, K_s, K_φ, κ_s and κ_φ. Summarized, we have

$$\begin{aligned} \lambda_s &= (1-\nu^2)\lambda_\varphi \frac{\tau_s}{E_{2\mathrm{D}}} - \nu(\lambda_\varphi - 1) + 1, & \lambda_\varphi &= \frac{r}{r_0}, \\ K_s &= \frac{1}{E_B}\lambda_\varphi m_s - \nu K_\varphi, & K_\varphi &= \frac{\sin\psi - \sin\psi_0}{r_0}, \\ \kappa_s &= \frac{K_s + \kappa_{s_0}}{\lambda_s}, & \kappa_\varphi &= \frac{\sin\psi}{r}, \\ \tau_\varphi &= \frac{E_{2\mathrm{D}}}{1-\nu^2}\frac{1}{\lambda_s}((\lambda_\varphi - 1) + \nu(\lambda_s - 1)), & m_\varphi &= E_B \frac{1}{\lambda_s}(K_\varphi + \nu K_s). \end{aligned} \tag{3.21}$$

Behavior at the capsule's poles

The integration of the shape equations starts and ends at the capsule's poles on the symmetry axis, at $s_0 = 0$ and $s_0 = L_0 = \pi R_0$ respectively. These two points require a special treatment, because the shape equations have removable singularities there. The problem is that $r = r_0 = 0$ at the poles and r and r_0 appear in several denominators. These singularities can be removed analytically by using the rule of L'Hôspital, which is shown in detail in reference [74]. As a result, we get at $s_0 = 0$ and $s_0 = L_0$:

$$\begin{aligned} q' &= \lambda_s(p_n/2 - \kappa_s(\tau_s + \gamma)), & \tau_s' &= m_s' = 0, \\ \lambda_s &= \lambda_\varphi = \frac{Y_{2\mathrm{D}}}{Y_{2\mathrm{D}} - \tau_s(1-\nu)}, & \kappa_s &= \kappa_\varphi = \frac{m_s}{Y_{2\mathrm{D}}(1+\nu)} + \frac{\kappa_{s_0}}{\lambda_s}. \end{aligned} \tag{3.22}$$

Finally, we need boundary conditions to solve the six first-order differential equations. Therefore, we consider the values of ($q(s_0)$, $\tau_s(s_0)$, $m_s(s_0)$, $r(s_0)$, $z(s_0)$, $\psi(s_0)$) at the poles. First of all, the transverse shear stress vanishes at the poles, $q(0) = q(L_0) = 0$. A finite q at the poles would otherwise require an external point force in order to be balanced [74]. The stresses $\tau_s(0)$ and $\tau_s(L_0)$ and also the bending moments $m_s(0)$ and $m_s(L_0)$ are a priori unknown and have to be estimated as a part of the solution of the shape equations. The radial coordinate r vanishes at the poles, $r(0) = r(L_0) = 0$, otherwise the capsule would have a hole. The shape equations show a translational invariance in z-direction (except for a possible z-dependency of p_n). Therefore, we can choose $z(0)$ arbitrarily and have to estimate $z(L_0)$ as a part of the solution. Finally, the slope angles are set to $\psi(0) = 0$ and $\psi(L_0) = \pi$ in order to avoid kinks in the shell.

3.1.4. Numerical solution of the shape equations

The shape equations are solved by a shooting method that tries to arrange the unknown boundary values $\tau_s(0)$, $\tau_s(L_0)$, $m_s(0)$, $m_s(L_0)$, $z(L_0)$. These values are treated as shooting parameters. The shape equations themselves are solved by a Runge-Kutta method of fourth order with a step size Δs_0 and N total steps. The solution method that is presented in the following is basically the same as in refs. [19, 74, 75].

It is numerically difficult to integrate a differential equation into (removable) singularities that we find at the poles. Therefore, we use a parallel shooting method [114]. We start to integrate the shape equations in both poles and get two trajectories. The first trajectory runs from $s_0 = 0$ to $s_0 = L_0/2$ and the second one runs from $s_0 = \pi R_0$ to $s_0 = L_0/2$. Then the shooting parameters are adjusted that way that both trajectories meet at the fitting point at $s_0 = L_0/2$. So, we can define residuals that must vanish:

$$\begin{aligned} q_1(L_0/2) - q_2(L_0/2) &\stackrel{!}{=} 0, & \tau_{s,1}(L_0/2) - \tau_{s,2}(L_0/2) &\stackrel{!}{=} 0, \\ m_{s,1}(L_0/2) - m_{s,2}(L_0/2) &\stackrel{!}{=} 0, & r_1(L_0/2) - r_2(L_0/2) &\stackrel{!}{=} 0, \\ z_1(L_0/2) - z_2(L_0/2) &\stackrel{!}{=} 0, & \psi_1(L_0/2) - \psi_2(L_0/2) &\stackrel{!}{=} 0. \end{aligned} \tag{3.23}$$

These residuals are numerical functions of the shooting parameters. Effectively, we have the problem of a six-dimensional root finding, which is solved by a Newton method with a numerically calculated Jacobi matrix. Now it is conspicuous that we try to find the root of six functions with only five shooting parameters, which should not work in general. But as long as no total force is acting on the capsule, which is the case for a ferrofluid capsule in a homogeneous magnetic field, we have effectively only five residuals. This can be quickly seen in the definition of q, eq. (3.18): q is a continuous function of the other five functions. So, if the other five residuals force τ_s, m_s, r, z and ψ to be continuous, then q is also continuous and its residual vanishes automatically. That does not work anymore with inhomogeneous fields, when a total force acts on the capsule. Then, another shooting parameter is needed, which is discussed in section 5.4.

The strongly non-linear shape equations show in general a very unstable behavior in a way that the Newton method has great problems to find the correct shooting parameters. The stability of the integration of the shape equations can be increased by a multiple shooting method. The idea is to divide the two integration intervals from the parallel shooting method further into smaller intervals. Each interval (except for the first and the last at the poles) then provides six additional shooting parameters at its starting point and six additional residuals at its end. Thus, the dimension of the Newton method to find the shooting parameters is increased by six for each additional interval. On one hand, additional intervals allow a parallel computation, but on the other hand, the Newton method becomes very laborious for higher numbers of intervals. For the calculation of the shape of a ferrofluid filled capsule a number n of intervals between $n = 100$ and $n = 250$ was found to be a good compromise between computation speed and numerical stability.

Constant volume

Since we only want to consider capsules with an impermeable shell and thus a constant inner volume $V = V_0$, we need to ensure that the volume is preserved when the capsule is deformed. Therefore, we can use an inner pressure p_0 as a Lagrange multiplier to adjust the volume. This pressure is added at the position of p_n in the shape equations, because it can only cause normal forces. So, we have $p_n = p_0 + \tilde{p}_n$. In order to adjust the pressure, several different ways are possible. The simplest possible way is a one-dimensional root finding with the pressure

as a variable and the volume as a residual, $V - V_0 \stackrel{!}{=} 0$. The shape equations are solved and the resulting volume is calculated via

$$V = \pi \int r^2 \mathrm{d}z = \pi \int_0^{L_0} r^2 \lambda_s \sin\psi \mathrm{d}s_0. \tag{3.24}$$

Now p can be adjusted, and the procedure has to be repeated until the volume residual vanishes. This algorithm is very slow, because p can only be changed in small steps. Otherwise, the Newton method in the multiple shooting procedure quickly does not find a solution for the correct shooting parameters of the shape equations anymore.

Another modified method was used in ref. [63]: There, p_0 was treated as another shooting parameter and added to the Newton method. The volume was calculated during the integration of the shape equations and, therefore, p_0 was adjusted simultaneously to the other shooting parameters. This method is much faster since it increases the dimension of the Newton method by one, but the non-linear equation system of the residuals only has to be solved once and not multiple times. The disadvantage of that method is that it can also quickly become unstable. The Newton method does not find a solution when the solution trajectories of the single intervals during the integration of the shape equations are located too far away from the fitting points. Adding the pressure and the volume to the shooting method visibly aggravates that problem. Therefore, we improve that method here.

During the multiple shooting method, the volume needs to be calculated for the volume residual. However, the integral in eq. (3.24) over the actual trajectories of r and z can give very inaccurate values for the volume, especially in the beginning of the shooting method. The reason are the misleading trajectories of r and z when the shooting parameters are not correctly adjusted yet and the residuals do not vanish, see the red trajectories in the (r, z)-plane in fig. 3.3. This effect is enhanced by the high non-linearity of the shape equations, when slightly wrong shooting parameters lead to drastically changing trajectories and thus also changing volumes. This results in a wrong adjustment of p_0 because the volume is expected to be different from the value that it would be, based on the starting points of the intervals (blue area in fig. 3.3). So, the idea is now to use only the starting points of the integration intervals for the volume calculation and not the trajectories themselves. We calculate an approximation of the volume that only uses the r- and z-values at the beginning of the intervals. In order to do that, the capsule's shape is interpolated by two cubic splines: $r_{\mathrm{spline}}(s_0)$ and $z_{\mathrm{spline}}(s_0)$. Consequently, these splines use n sampling points for n intervals. With these splines, the volume can be precisely approximated during the shooting method, even with few intervals in use, because elastic shells try to reduce their bending energy, which is also the basic idea of the spline interpolations [53]. This leads to a considerably increased stability of the whole shooting method, especially because the volume is now only related to r and z and is independent of the other four variables.

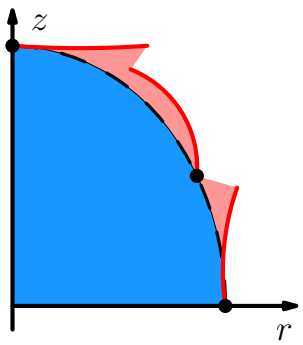

Figure 3.3.: Illustration of the volume estimation during the shooting method in the upper half of a capsule. The red lines show the rz-trajectories, when the shooting parameters are not correctly adjusted yet and the read area indicates the volume that is calculated when these trajectories are used. The blue area shows the volume that is estimated by a cubic interpolation (dashed line) between the starting points of the intervals (black circles).

3.1.5. Shape equations without bending energy

There are few effects in the topic of elastic capsules, like the buckling transition into a shape with a polygonal dimple [76], where the bending energy plays an important role. But in most cases, the bending energy is very small compared to the stretching energy and the resulting shape is completely dominated by the stresses τ_i and not by the bending moments m_i. In these cases, the bending energy and thus the bending moments can be neglected. That is the limit of an infinitely thin shell ($h \to 0$), also called *membrane regime* [63]. The elastic energy density w_S simplifies to

$$w_S = \frac{1}{2}\frac{Y_{2D}}{1-\nu^2}(e_s^2 + 2\nu e_s e_\varphi + e_\varphi^2). \tag{3.25}$$

Since we have no bending moments and also q vanishes in eq. (3.18), the equilibrium equations simplify to

$$0 = (\tau_s + \gamma)\kappa_s + (\tau_\varphi + \gamma)\kappa_\varphi - p_n, \tag{3.26}$$

$$0 = \frac{\cos\psi}{r}\tau_\varphi - \frac{1}{r}\frac{\mathrm{d}(r\tau_s)}{\mathrm{d}s} - p_s. \tag{3.27}$$

Consequently, we now get a system of four shape equations:

$$\begin{aligned} \tau_s'(s_0) &= \lambda_s\left(\frac{\tau_\varphi - \tau_s}{r}\cos\psi - p_s\right), & r'(s_0) &= \lambda_s\cos\psi, \\ \psi'(s_0) &= \frac{\lambda_s}{\tau_s+\gamma}(-\kappa_\varphi(\tau_\varphi+\gamma) + p_n), & z'(s_0) &= \lambda_s\sin\psi. \end{aligned} \tag{3.28}$$

Note that the equation for ψ' shows a removable singularity when τ_s equals $-\gamma$ and needs a special treatment then, which can be very difficult as it depends on the outer forces p_n. The system is closed by the relations that are already known from (3.21):

$$\begin{aligned} \lambda_s &= (1-\nu^2)\lambda_\varphi\frac{\tau_s}{E_{2D}} - \nu(\lambda_\varphi - 1) + 1, & \lambda_\varphi &= \frac{r}{r_0}, \\ \tau_\varphi &= \frac{E_{2D}}{1-\nu^2}\frac{1}{\lambda_s}((\lambda_\varphi - 1) + \nu(\lambda_s - 1)), & \kappa_\varphi &= \frac{\sin\psi}{r}. \end{aligned} \tag{3.29}$$

The starting values at the poles stay the same as before. These shape equation without bending energy also allow sharp kinks. But since we use this model only as an approximation for a shell that has a finite (but very small) bending energy, we have to keep the conditions $\psi(0) = 0$ and $\psi(L_0) = \pi$ in order to prevent kinks that would lead to a diverging bending energy. We have basically (without additional intervals) three shooting parameters here, $\tau_s(0)$, $\tau_s(L_0)$ and $z(L_0)$. These shooting parameters have to match four residuals at the fitting point. Again, this is not a problem for a capsule free of total forces due to the same explanation as before. Every additional interval then provides four additional shooting parameters and also four residuals.

3.1.6. Wrinkling

An elastic shell is able to provide the development of wrinkles under certain circumstances. In the following, we include this effect into the shape equations. In this thesis, we restrict the wrinkling effect to the circumferential direction. The method of the inclusion of wrinkling effects into modified shape equations was primarily developed by S. Knoche in refs. [74] and [78]. In general, wrinkles can only be formed when negative stresses occur. This is mostly the case when a capsule is stretched. Then the volume preservation forces the capsule

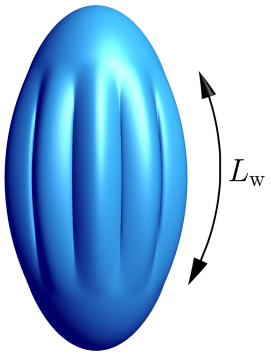

Figure 3.4.: Three-dimensional illustration of a capsule with wrinkles in circumferential direction. The length L_w of the wrinkles is measured as the length of the region, where $\tau_\varphi+\gamma<0$. The wrinkling wavelength is not determined explicitly here.

to lower its radius in its equatorial regions. This results in negative circumferential stresses τ_φ there. In the moment when the negative stress exceeds the interfacial tension, $\tau_\varphi+\gamma<0$, wrinkles occur. Then, the elastic shell can reduce its stress in circumferential direction and thus its total energy by developing wrinkles, as it is illustrated in fig. 3.4. The wrinkles stretch the surface slightly in s-direction thus increasing the stretch energy in that direction and the additional surface area increases the interface energy. But that is compensated as the shell can relax in φ-direction, which reduces the total energy after all. It has to be kept in mind that the condition $\tau_\varphi+\gamma<0$ is only an approximation for a vanishing bending energy. In fact, the total negative stress $\tau_\varphi+\gamma$ has to exceed a small Euler-like threshold [74].

In the following, the wrinkling effect is added to the shape equations in the same way it was done for pendant capsules in reference [78]. Since the wrinkles break the axial symmetry and thus a basic requirement of the shape equations, they can only be indirectly included. Therefore, we modify the shape equations to calculate an approximated axial symmetric pseudo-midsurface $(\overline{r}(s_0),\,\overline{z}(s_0))$ in the wrinkled region. In this region, we set $\tau_\varphi+\gamma=0$ and assume the real surface to oscillate around that pseudo-surface. Implementing the condition $\tau_\varphi+\gamma=0$ leads to some changes in the shape equations. The shape equations without bending energy now become

$$\begin{aligned}
\overline{\tau}_s'(s_0) &= -\lambda_s\frac{\cos\overline{\psi}}{\overline{r}}(\overline{\tau_s}+\overline{\gamma}), & \overline{r}'(s_0) &= \lambda_s\cos\overline{\psi},\\
\overline{\psi}'(s_0) &= \frac{\lambda_s}{\overline{\tau}_s+\overline{\gamma}}p_n, & z'(s_0) &= \lambda_s\sin\overline{\psi}.
\end{aligned} \tag{3.30}$$

The overlined quantities refer explicitly to the pseudo surface. That system is closed by the relations

$$\lambda_s=\frac{\overline{\tau}_s\overline{\lambda}_\varphi+Y_\mathrm{2D}}{Y_\mathrm{2D}-\nu\gamma}, \qquad \overline{\lambda}_\varphi=\frac{\overline{r}}{r_0}. \tag{3.31}$$

In this modified shape equations we also have to introduce a modified interfacial tension $\overline{\gamma}=\gamma\lambda_\varphi/\overline{\lambda_\varphi}$. That is due to the fact that the surface area of the real, wrinkled surface is higher than the pseudo-surface's area. Thus, the interface energy is increased, which we respect by increasing $\overline{\gamma}$ instead.

To calculate wrinkled capsule shapes, the following procedure is used practically: We start to integrate the shape equations (3.28) at the capsule's poles as described before. Then, when the condition $\tau_\varphi+\gamma=0$ is valid (at $s_0=s_{0,a}$), we continue the integration by solving the modified shape equations (3.30). Finally, when the stress condition is no longer valid at $s_0=s_{0,b}$, we switch back to the original shape equations. In praxis, it is much more efficient and numerically stable to determine $s_{0,a}$ and $s_{0,b}$ in a first integration of the shape equations and to keep them constant during the multiple shooting method. This procedure has to be repeated a few times in order to iteratively find the correct values for $s_{0,a}$ and $s_{0,b}$.

By following the solution of the modified shape equations, the length of the wrinkles in meridional direction, L_W can be calculated via

$$L_\mathrm{w} = \int\limits_{\tau_\varphi+\gamma<0} \mathrm{d}s. \tag{3.32}$$

It is also possible to calculate the wavelength of the wrinkles from the bending modulus. But in this thesis, we are not interested in that information and, therefore, refer to the references [74] and [78] as well as for further details of the derivation of the modified shape equations.

3.1.7. Vanishing elasticity

After all, we are now able to calculate the deformed shapes of elastic capsules that are filled with a fluid and experience external forces. But we also need be able to compare the behavior and effects that are caused by the elasticity with a simple fluid drop that is only determined by its interfacial tension. Therefore, we need similar shape equations for vanishing elasticity ($Y_\mathrm{2D}/\gamma = 0$). The interfacial tension on the surface of a fluid drop can only cause forces in normal direction. As soon as tangential forces arise, the fluid starts to move, and we do not have a static case anymore, which is not the topic here. Therefore, we only have a single equilibrium equation describing the force equilibrium in normal direction:

$$\gamma(\kappa_s + \kappa_\varphi) - p_n = 0. \tag{3.33}$$

This equation is known as the Laplace-Young equation. In case of a constant isotropic inner pressure p_0, the resulting shape is a sphere. There are several ways to find a shape that satisfies this equation with a volume constraint, for example with finite elements [23] but we try to stay as close as possible to the formalism that we have introduced for the elastic capsules. Compared to the elastic capsules, things are a bit different now: A fluid drop has no reference shape. Therefore, our parametrization with the arc length of the reference shape s_0 cannot be used without further advances. In order to be able to stay in our formalism, we introduce a stretch factor λ_s for the fluid drop. This stretch factor is always constant over the whole surface, because any change of the surface area of a fluid can be interpreted as a homogeneous stretching of the surface of a reference shape. We define the sphere with the radius R_0 as our reference shape.

Similar to the elastic case, the Laplace-Young equation can now be rearranged as a function of the reference arc length s_0 and combined with the geometric relations for r and z, we get a system of three differential equations:

$$\psi'(s_0) = \lambda_s \left(\frac{p_n}{\gamma} - \frac{\sin\psi}{\gamma} \right), \qquad r'(s_0) = \lambda_s \cos\psi, \qquad z'(s_0) = \lambda_s \sin\psi. \tag{3.34}$$

Here, we do not need additional relations like the constitutive relations for the elastic shape equations. We have two shooting parameters ($z(L_0)$ and λ_s) and three matching conditions at the fitting point (and of course the pressure as a shooting parameter for the volume constraint). Due to the lack of removable singularities in the system (3.34), a single integration interval from pole to pole is also possible.

In contrast to an elastic shell, a simple fluid surface can support sharp kinks and corners. In that case, the sum of the curvatures $\kappa_s + \kappa_\varphi$ diverges, so the external force density p_n also has to diverge. A further discussion on that point follows in section 4.3.2.

3.2. Magnetic model

Now we have all that we need to calculate the shape of an elastic capsule or a drop exposed to external forces. So, we have to specify these external forces now. The main goal of this thesis

is to investigate the deformation behavior of elastic capsules that are filled with a ferrofluid and placed in an external magnetic field. Therefore, we need to model the forces on the capsule's shell that are caused by the ferrofluid.

3.2.1. Properties of the ferrofluid

As it was already implied in the elastic section, we assume the elastic shell to be impermeable for the ferrofluid. In addition we assume the ferrofluid to be incompressible, which is a very good approximation in most cases [125]. As a direct consequence, we have a constant amount of ferrofluid with the volume V_0.

Magnetization of the fluid

The primary difference between a ferrofluid and an ordinary fluid is the ferrofluid's ability to achieve a remarkable magnetization in external magnetic fields due to its magnetic nanoparticles inside. The ferrofluid is located in an external magnetic field $\boldsymbol{H}_{\mathbf{ext}}(r,z)$, which is inhomogeneous in general. The nanoparticles react to that field by setting up an own magnetization $\boldsymbol{M}$. Here and in the following, the term *magnetization* describes the volume magnetization, which is related to the magnetic field $\boldsymbol{H}$ and the magnetic flux density $\boldsymbol{B}$ via

$$\boldsymbol{B} = \mu_0(\boldsymbol{H} + \boldsymbol{M}), \tag{3.35}$$

with the magnetic vacuum permeability μ_0. The magnetization of the ferrofluid causes an additional magnetic field, the stray field, which adds up with the external field resulting in a total magnetic field $\boldsymbol{H}$, which is a priori unknown and has to be calculated, see sec. 3.2.2.

The magnetization curve $M(H)$ (with M, H being the absolutes of the respective vectors) of a ferrofluid shows typical characteristics of a ferromagnet: The magnetization increases linearly for small fields and then runs into a saturation with a saturation magnetization M_s for higher fields. But when the field is lowered again, the fundamental difference to a ferromagnet becomes visible: The magnetization of the nanoparticles does not show any hysteretic behavior and completely vanishes again for a vanishing field. This effect is called *super paramagnetism* and is primarily caused by the small size of the particles: Each magnetic nanoparticle consists of a single magnetic domain that is completely magnetized and thus always features a magnetic moment. The domains are small enough so that the direction of their magnetization can be easily changed by thermal fluctuations. These fluctuations change the magnetic moments of the nanoparticles so quickly that they average to zero on macroscopic time scales without external fields [24]. For an example of a magnetization curve of a ferrofluid, see fig. 5.8 for the ferrofluid used in the experiment in chapter 5. Another effect of the small particle size is that the magnetization and the external field always point into the same direction, $\boldsymbol{M} \parallel \boldsymbol{H} \parallel \boldsymbol{H}_{\mathbf{ext}}$. For small fields, a linear magnetization law

$$M(H) = \chi H \tag{3.36}$$

with the magnetic susceptibility χ is a good approximation and is used in chapter 4.

Magnetic stress

When the ferrofluid is magnetized by an external magnetic field, it tries to minimize its magnetic energy by aligning itself to the direction of the field. Consequently, each volume element of the ferrofluid causes direct forces on its neighbor volume elements. The magnetic force per volume element, $\boldsymbol{f}_{\mathbf{m}}^{\mathbf{V}}$, can be written as the divergence of the magnetic stress tensor $\underline{\underline{\boldsymbol{T}}}$:

$$\boldsymbol{f}_{\mathbf{m}}^{\mathbf{V}} = \nabla \cdot \underline{\underline{\boldsymbol{T}}}. \tag{3.37}$$

In this thesis, the description of the ferrofluid uses the formalism and the model of R. E. Rosensweig [36, 125]. There, the representation of the magnetic stress tensor turns out to be

$$\underline{\underline{\boldsymbol{T}}} = -\left[\mu_0 \int_0^H \frac{\partial(\rho^{-1}M)}{\partial(\rho^{-1})}\mathrm{d}H' + \frac{\mu_0}{2}\right]\underline{\underline{\boldsymbol{I}}} + \boldsymbol{B}\otimes\boldsymbol{H}. \tag{3.38}$$

The operator $\otimes$ describes a dyadic product, $\underline{\underline{\boldsymbol{I}}}$ represents the identity matrix and ρ^{-1} is the specific volume, the inverse of the ferrofluid's mass density ρ.

Each volume element interacts with its neighbors that counter the forces, so in total we only get an effective force on the surface of the ferrofluid. This surface force density, $\boldsymbol{f_m}$ (also called magnetic pressure), can be calculated with the magnetic stress tensor as the difference between the stresses on the inner side and the outer side of the surface. Here, we assume that the outer phase does not feature any magnetization, such as a vacuum, or any non-ferromagnetic material in a very good approximation. This is the case for the ferrofluid filled elastic capsules, because neither the polymeric shell itself nor the surrounding liquid are ferro- or ferrimagnetic substances. In addition, another assumption simplifies things drastically: In most cases, it is a very good approximation to assume that a ferrofluid is incompressible. Then the term with the derivative with respect to the specific volume simplifies to a simple magnetization and we find for the absolute of the magnetic surface force density:

$$f_\mathrm{m}(r,z) = |\boldsymbol{f_m}| = \mu_0 \int_0^{H(r,z)} M(r,z)\mathrm{d}H'(r,z) + \frac{\mu_0}{2}M_n^2(r,z). \tag{3.39}$$

The expression M_n means that the normal component of the magnetization on the surface has to be taken into account. The surface force density $\boldsymbol{f_m}$ is the force that the ferrofluid causes on its surface in *normal direction*. It is important to note that a fluid in rest can only cause normal forces. Any tangential forces in the fluid would result in a floating motion until a steady state is reached. Therefore, we only use the absolute f_m in the following.

Finally, we know how to couple the ferrofluid to the elastic shape equations (3.20) or (3.28): The external force density in normal direction, p_n, is modified by the magnetic surface force density. So we have

$$p_n = p_0 + f_\mathrm{m} + p_n', \tag{3.40}$$

where p_n' can describe additional forces, such as the hydrostatic pressure in section 5.1.2.

Scalar magnetic potential

The magnetic field $\boldsymbol{H}$ and the magnetization $\boldsymbol{M}$ inside of the ferrofluid are unknown a priori. Therefore, the magnetic force density f_m cannot be determined without the calculation of the magnetic field. This calculation is the topic of the following section 3.2.2. But before, another special property of ferrofluids should be mentioned here, especially since it simplifies the following task drastically.

Most ferrofluids are non-conducting [125] (especially the ferrofluid in chapter 5 is based on a mixture of hexanol and chloroform), so there is no electric current inside the fluid. Since we do not consider additional external electric fields, it follows from Maxwell's equations that

$$\nabla \times \boldsymbol{H} = 0. \tag{3.41}$$

That means, we can introduce a *scalar* magnetic potential u, which generates the magnetic field $\boldsymbol{H}$ as its gradient:

$$\nabla u(r,z) = \boldsymbol{H}(r,z). \tag{3.42}$$

The existence of a scalar potential allows a much easier computation of the magnetic field, because the usage of the magnetic vector potential can be avoided.

3.2.2. Calculation of the magnetic field

The task to calculate the magnetic field as a superposition of the external field and the field from the ferrofluid's magnetization can be expressed in terms of solving a partial differential equation. We start with Maxwell's equation

$$\nabla \cdot \boldsymbol{B} = \nabla \cdot \mu_0(\boldsymbol{H} + \boldsymbol{M}) = 0. \tag{3.43}$$

Replacing $\boldsymbol{H}$ with (3.42) leads to Poisson's equation in magnetostatics:

$$\nabla^2 u(r,z) = -\nabla \cdot \boldsymbol{M}(r,z). \tag{3.44}$$

The magnetization on the right side of the equation is also linked to u via the magnetization curve of the ferrofluid $M(H) = M(|\nabla u|)$. In case of the linear magnetization law (3.36), Poisson's equation can be simplified to the Laplace equation $\nabla^2 u(r,z) = 0$. The partial differential equation (3.44) has to be solved numerically in order to calculate the magnetic potential u and thus the magnetic field $\boldsymbol{H}$. Therefore, boundary conditions are needed. First of all, the stray field of the ferrofluid should vanish at infinity and only the external field remains:

$$\lim_{|r|,|z|\to\infty} u = u_{\text{ext}}. \tag{3.45}$$

Secondly, we have two different magnetic domains: Inside the capsule, there is the ferrofluid and outside of the capsule we have a non-magnetic domain. The magnetic continuity conditions [68]

$$\boldsymbol{n} \cdot (\boldsymbol{B}_{\mathbf{in}} - \boldsymbol{B}_{\mathbf{out}}) = 0, \quad \boldsymbol{t} \cdot (\boldsymbol{H}_{\mathbf{in}} - \boldsymbol{H}_{\mathbf{out}}) = 0 \tag{3.46}$$

with a surface tangential vector $\boldsymbol{t}$ have to be satisfied on the surface. In order to express these conditions with the magnetic potential u, we introduce the magnetic permeability μ at this point. Based on the context, there are several different definitions for the permeability. Here, for ferrofluids without hysteresis and with a magnetization parallel to the magnetic field, we define

$$\boldsymbol{B} \equiv \mu \boldsymbol{H} \quad \Leftrightarrow \quad \mu = \frac{B}{H} = \mu_0 \left(1 + \frac{M}{H}\right). \tag{3.47}$$

With that magnetic permeability, we can simply express the magnetic continuity conditions on the ferrofluid's surface, represented by the two-dimensional contour line Γ of the capsule, as

$$u_{\text{in}}(r,z) = u_{\text{out}}(r,z), \qquad \mu \frac{\partial u_{\text{in}}(r,z)}{\partial n} = \mu_0 \frac{\partial u_{\text{out}}(r,z)}{\partial n} \quad \text{for} \quad (r,z) \in \Gamma. \tag{3.48}$$

The derivative $\partial/\partial n$ means the derivative in normal direction, while the normal vector points outwards of the capsule. With the equations (3.44), (3.45) and (3.48), the magnetostatic problem of the ferrofluid is well defined and can be solved. Due to the axial symmetry of the problem, here and in the following, all operations are set in the (r, z)-plane.

The next step is to discretize the (r, z)-plane and to solve the Poisson equation numerically. Therefore, we use a combination of two different methods. The problem is divided into two coupled sub problems. First, we use the finite element method (FEM) [52, 80] to calculate the

magnetic field inside of the capsule. In order to be able to simply refer to that magnetizable domain, we call that domain (and its two-dimensional representation in the (r, z)-plane) Ω_{FEM} . On the other hand, we use the boundary element method (BEM) [52, 80] for the field calculation in the non-magnetic domain outside of the capsule. Both methods are not independent but coupled to each other via the continuity conditions (3.48) [4, 5, 35, 144]. Such a coupling of the FEM and BEM was also used by Lavrova et al. for free ferrofluid drops [85, 87, 88], of which the notation here is inspired. Earlier, this method was already used to calculate the field in electric drops, e.g. by Harris and Basaran [62].

The reason for the combination of these two methods is quite convincing: The finite element method became the standard method in the discipline of electro-magnetic field calculation [52, 80]. It is easy to use and has no problems to deal with non-linear materials. The downside lies in the infinity condition (3.45). Such a condition cannot be exactly modelled by the finite element method. Theoretically, an infinitely large region has to be discretized. Therefore, a cutoff distance has to be chosen, that is defined as infinity. The BEM on the other side excels at such conditions: They are natively included. However, the BEM is not able to handle non-linear materials and is numerically quite challenging due to the appearance of integrals with singularities in the integrand. So, the strengths of both methods can be effectively combined: We use the FEM's ability to calculate non-linear materials for the magnetizable inner domain, while we use the BEM's strength with infinity conditions in the outer region.

In the following, the basic ideas of both methods as well as special properties shall be briefly presented. For further details, the interested reader may be referred to the literature [4, 5, 35, 80, 85, 144].

The finite element method (FEM)

In order to present an advantageous formulation of our problem and to apply the FEM, we start with the Poisson equation (3.44) and rearrange it to

$$\nabla \cdot (\mu \nabla u) = 0. \tag{3.49}$$

It is important to remember at this point, that μ is not a constant in the general case. The first idea of the FEM is now not to ask for an exact solution of this rearranged Poisson equation, but for a solution of a weak formulation of the problem. Therefore, we do not demand the term $\nabla \cdot (\mu \nabla u)$ to disappear, but the integral over that term and an additional weight function w over the whole region of the problem:

$$\int\limits_{\Omega_{\mathrm{FEM}}} \nabla \cdot (\mu \nabla u) w \mathrm{d}\Omega = 0. \tag{3.50}$$

The weight function w is a priori arbitrary. Now we use Green's first identity to get rid of the second derivatives of u and obtain

$$-\int\limits_{\Omega_{\mathrm{FEM}}} \mu \nabla w \nabla u \mathrm{d}\Omega + \oint\limits_{\Gamma} w \mu \frac{\partial u}{\partial n} \mathrm{d}\Gamma = 0. \tag{3.51}$$

This equation is called the *weak formulation* of the problem. There, we only have first derivatives of u left for the trade of an additional boundary integral over the edge of the solution region, in our case the capsule's contour line Γ. In the following, the weak problem must be discretized. Therefore, we start with the region Ω_{FEM}, which is a two-dimensional area in the (r, z)-plane due to the axial symmetry. We divide that area into a mesh of triangular *elements*. The objective is to calculate the magnetic potential u at the knots of the

mesh (the corners of the triangles, the *vertices*). Inside the triangles, between the vertices, u is approximated via

$$u(r,z) = \sum_{k=1}^{N_\mathrm{v}} \alpha_k(r,z) u_k \tag{3.52}$$

with the potential u_k at the vertex k, while we have N_v vertices in total. The function $\alpha_k(r,z)$ is the basis function of the vertex k, telling how much this vertex contributes to $u(r,z)$. In this thesis, we use linear basis functions inside of each element. That means that $u(r,z)$ is the superposition of the potential at the three vertices of the specific element, where (r,z) is located inside and these vertices are weighted linearly. In addition, the linear basis functions α_k are also used as the weight functions w in eq. (3.51). This method is also known as a local Galerkin method [80].

The boundary integral, which is a line integral in our case, is discretized in exactly the same way: $u(r,z)$ on Γ is a superposition of the potential on the two neighbor vertices with linear weighting. Consequently, the derivative $\partial u/\partial n$ is constant on each boundary element. In the following, we substitute the normal derivative of the potential on the surface with $q = \partial u/\partial n$.

Finally, the discrete version of the weak problem can be written as

$$\sum_{i=1}^{N_\mathrm{e}} \sum_{k=1}^{N_\mathrm{v}} \left(u_k \int\limits_{\Omega_i} \mu_i \nabla\alpha_l \nabla\alpha_k \mathrm{d}\Omega \right) - \sum_{j=1}^{n_\mathrm{B}} \mu_j q_j \int\limits_{\Gamma_j} \alpha_l \mathrm{d}\Gamma = 0, \qquad l \in [1,N_\mathrm{v}]. \tag{3.53}$$

The integral in the first term is an integral over the whole element i (the area of a triangle in our case) and can be solved analytically. The inner sum with index k runs over all vertices, while the i-sum runs over all N_e triangular elements. The j-sum in the last term runs over all n_B boundary segments. This equation can be written down for each vertex basis function $l \in [1,N_\mathrm{v}]$. So we get N_v equations for N_v unknown vertex potentials u_k, a $N_\mathrm{v} \times N_\mathrm{v}$ equation system that has to be solved. It is important to note that this equation system is in general a non-linear system, since the permeabilities μ_i in each element are non-linear functions of the vertex potentials. At this point, we are still not able to calculate the magnetic field, because the normal derivatives of the potential on the boundary are still unknown. That is the point, where the BEM has to be coupled.

The boundary element method (BEM)

The boundary element method uses a completely different approach. It transforms the partial differential equation in the domain Ω_out into an integral equation over the domain's boundary Γ. Analogous to the FEM section, a brief motivation of the BEM's basic ideas follow, for a fully detailed derivation, we refer again to the specialized literature, since it is a common technique next to the FEM, especially in multiple disciplines of engineering [52, 80].

In the domain Ω_out outside of the capsule, we have a non-magnetic liquid, so the magnetization is vanishing there. Consequently, we have to solve the Laplace equation

$$\Delta u = 0. \tag{3.54}$$

Similar to before in eq. (3.50), we only demand the integral with a weight function w to disappear,

$$\int\limits_{\Omega_\mathrm{out}} w \Delta u \mathrm{d}\Omega = 0. \tag{3.55}$$

This time, we use Green's second identity and can state the following identity:

$$\int_{\Omega_{\text{out}}} (w\Delta u - u\Delta w)\mathrm{d}\Omega = \oint_{\partial\Omega} \left(u\frac{\partial w}{\partial n} - w\frac{\partial u}{\partial n} \right) \mathrm{d}S. \tag{3.56}$$

The integral on the right side is a surface integral over the surface $\partial\Omega$ of the domain Ω. It is very important to note here, that the normal vector points outside of the domain Ω_{out}, so it points inside of the capsule, the opposite direction of the normal vector in eq. (3.51). Using (3.55), we get

$$\int_{\Omega_{\text{out}}} u\Delta w\mathrm{d}\Omega = \oint_{\partial\Omega} \left(w\frac{\partial u}{\partial n} - u\frac{\partial w}{\partial n} \right) \mathrm{d}S. \tag{3.57}$$

The idea is now to get rid of the integral over the whole domain Ω_{out}. Therefore, we chose the weight function w to be a Green's function, or fundamental solution of the Laplace equation:

$$w \equiv u^*(\boldsymbol{r},\boldsymbol{r'}), \qquad \Delta u^* = -\delta(\boldsymbol{r} - \boldsymbol{r'}). \tag{3.58}$$

In the general three-dimensional case, the fundamental solution of the Laplace equation is known as $u^*(\boldsymbol{r},\boldsymbol{r'}) = 1/(4\pi|\boldsymbol{r} - \boldsymbol{r'}|)$, but later we need a version that has already incorporated the rotational symmetry. In this context, the prime does not denote a derivative, but a different coordinate vector. With that weight function, we get a relation between the potential u located at $\boldsymbol{r}$ and an integral over the potential and its normal derivative on the boundary,

$$u(\boldsymbol{r}) = \oint_{\partial\Omega_{\text{out}}} \left(u(\boldsymbol{r'})q^*(\boldsymbol{r},\boldsymbol{r'}) - u^*(\boldsymbol{r},\boldsymbol{r'})\frac{\partial u(\boldsymbol{r'})}{\partial n} \right) \mathrm{d}S', \tag{3.59}$$

with $\boldsymbol{r} \in \Omega_{\text{out}}$. Analogous to the potential itself, q^* denotes the derivative of the fundamental solution u^* in normal direction (with the normal vector pointing into the capsule). The boundary integral is meant to run over the coordinates with a prime. This equation represents the basic relation between the potential at an arbitrary point inside of the domain Ω_{out} and the potential and its normal derivative on the domain's surface. In the following, this equation has to be rearranged in order to respect the axial symmetry and the external field. This leads in the space outside of our capsule to

$$cu_{\text{out}}(\boldsymbol{r}) - \int_0^L \left[u_{\text{out}}(\boldsymbol{r'})q^*_{\text{ax}}(\boldsymbol{r},\boldsymbol{r'}) - q_{\text{out}}(\boldsymbol{r'})u^*_{\text{ax}}(\boldsymbol{r},\boldsymbol{r'}) \right] r'\mathrm{d}s' = u_{\text{ext}}(\boldsymbol{r}) \tag{3.60}$$

in the case of a homogeneous external field [85, 87] with $q_{\text{out}} = \partial u_{\text{out}}(\boldsymbol{r'})/\partial n$ and the normal vector $\boldsymbol{n}$ pointing outside of the capsule. Here, we only have an integral over the capsule's boundary Γ, which is expressed as an integral over the whole arc length s. The prefactor c is a geometric constant that gives $c = 1$ for $\boldsymbol{r} \in \Omega_{\text{out}}$ and $c = 1/2$ for $\boldsymbol{r} \in \Gamma$. The quantity u^*_{ax} is the axial symmetric fundamental solution of the Laplace equation,

$$u^*_{\text{ax}}(\boldsymbol{r},\boldsymbol{r'}) = \int_0^{2\pi} u^*(\boldsymbol{r},\boldsymbol{r'})\mathrm{d}\varphi = \frac{K(\eta)}{\pi\sqrt{(r+r')^2 + (z-z')^2}}, \qquad \eta = \frac{4rr'}{(r+r')^2 + (z-z')^2}, \tag{3.61}$$

and q^*_{ax} its derivative in normal direction. The function in the numerator, $K(\eta)$, is the complete elliptic integral of the first kind.

The idea is now to use the integral equation (3.60) in order to replace the normal derivative of the potential on the boundary Γ in the FEM equation (3.53) by an integral over the potential

itself. The boundary Γ is discretized into one-dimensional elements that are compatible to the edge of the triangular mesh inside of the capsule's inner domain. Therefore, u is piecewise linear on the boundary, while q_{out} is piecewise constant. That means, we have in total n_{B} unknown values $q_{\mathrm{out},j}$. The points $\boldsymbol{r}$, where potential in the integral equation (3.60) is evaluated, the collocation points, are placed in the middle of each boundary element. In that way, we get n_{B} boundary integral equations, one for each boundary element. With these equations, the values $q_{\mathrm{out},j}$ could be calculated, if the potential on the boundary was known. Each $q_{\mathrm{out},j}$ can be written as a function of the potentials $u_{\Gamma,i}$ at the $n_{\mathrm{B}}+1$ starting and ending points of the boundary elements:

$$q_{\mathrm{out},j} = q_{\mathrm{out},j}(u_{\Gamma,0},\ \dots\ ,\ u_{\Gamma,n_{\mathrm{B}}}), \qquad j = 1,\dots,n_{\mathrm{B}}. \tag{3.62}$$

At this point we combine the BEM system with the system (3.53) from the FEM. Therefore, we use the continuity conditions (3.48) and replace $\mu_j q_j$ by an integral equation (3.62):

$$\sum_{i=1}^{N_{\mathrm{e}}}\sum_{k=1}^{N_{\mathrm{v}}}\left(u_k \int\limits_{\Omega_i} \mu_i \nabla\alpha_l \nabla\alpha_k \mathrm{d}\Omega\right) - \sum_{j=1}^{n_{\mathrm{B}}} q_{\mathrm{out},j}(u_{\Gamma,0},\ \dots\ ,\ u_{\Gamma,n_{\mathrm{B}}}) \int\limits_{\Gamma_j} \alpha_l \mathrm{d}\Gamma = 0 \qquad l \in [1,N_{\mathrm{v}}]. \tag{3.63}$$

In that notation, $u_{\Gamma,0},\ \dots\ ,\ u_{\Gamma,n_{\mathrm{B}}}$ describe the potentials at all boundary vertices. After all, we have a system of N_{v} equations for N_{v} unknown potentials that can now be solved in principle.

The numerical solution of the system (3.63) is everything but trivial. Some of the integrals in $q_{\mathrm{out},j}(u_{\Gamma,0},\ \dots\ ,\ u_{\Gamma,n_{\mathrm{B}}})$ or (3.60) become weakly singular. That means that the integrands (in detail u^*_{ax} and q^*_{ax}) diverge for $\boldsymbol{r} = \boldsymbol{r'}$ but the integrals themselves still exist. Especially challenging are collocation points that are located close to the z-axis. The weak singularities become strong singularities and the integrals cease to exist for $\boldsymbol{r} = \boldsymbol{r'}$ and $r \to 0$. These integrals are a source of potentially high numerical errors. Therefore, we do not just use the polygon that forms the edge of the mesh as a discrete version of the boundary Γ, but additional cubic splines similar to the splines used for the volume calculation of the capsule. With such a much more precise, smooth representation of Γ, the precision of the boundary integrals can be increased significantly. A detailed discussion of the behavior of the singular integrals can be found in ref. [85]. The ordinary integrals are solved with Gaussian quadrature formulas, while we use a midpoint rule to integrate over the weak singularities. Finally, the complete equation system (3.63) is solved by a multidimensional Newton method.

Calculation of the field from the magnetic potential

After the calculation of the potentials u_k at each mesh vertex k, the magnetic field inside the capsule could easily be calculated as the gradient of the potential inside of each element. Thus, the magnetic field would be constant within a single element. The downside of that method is that a piecewise constant magnetic field causes nearly piecewise constant magnetic forces f_{m} in the shape equations, which lead to significant problems in the shooting method. Jumping forces on the solution trajectory massively decrease the convergence quality of the method. In order to improve the numerical quality of the magnetic field data and to overcome the problems in the solution algorithm of the shape equations, we use a more advanced method for the field calculation from the potential data here. Therefore, the magnetic field is not associated with a triangular element but with the vertices of the mesh. That means that we assign field values $\boldsymbol{H_k}$ to each vertex, similar to the potential u_k. For the calculation of $\boldsymbol{H_k} = (H_{r,k}, H_{z,k})$, we use the potential of all direct neighbor vertices of the vertex k. Then, $H_{r,k} = \partial u_k/\partial r$ and $H_{z,k} = \partial u_k/\partial z$ are calculated as discrete derivatives that are governed from a two-dimensional Taylor expansion of the potential around the vertex k and the solution

of the resulting equation system in a least square sense [96, 146]. With these magnetic field values at each vertex, the field can be linearly interpolated between the vertices ensuring a continuous $\boldsymbol{H}(r,z)$.

Outside of the capsule, the magnetic field can be calculated as a numerical derivative of the potential, which is gained by directly solving the integral equation (3.60). That has to be repeated on every single position where the field shall be known. Thus, the calculation of the field outside of the capsule is a very laborious task, which is fortunately only of academical interest, since it is not needed for the calculation of the capsule's shape.

Inhomogeneous Delauney triangulation

The triangular mesh that forms the finite elements inside of the capsule and whose edge represents the boundary elements on the capsule's edge is created as a Delauney triangulation. The algorithm of a Delauney triangulation tries to maximize the smallest inner angular of the triangles in order to create a mesh that is as uniform as possible and tries to avoid sharp angles [72]. For the creation of the mesh in our numerical calculation, the Fade2D software package [79] is used.

The boundary of the domain that has to be triangulated is prescribed to the algorithm, which gives a good control over the resulting mesh. In most cases, $n_\mathrm{B} = 250$ boundary elements form the capsule's boundary Γ in this thesis.

It is known from ferrofluid drops in homogeneous fields (at least from a theoretical point of view [1, 87, 88]) that very sharp conical tips can occur with very high magnetic field strengths in the tip. In chapter 4 we also see these effects for elastic capsules. Therefore, we need a discretization mechanism that can provide a very high density of triangular and boundary elements near the capsule's pole. The naive way would be a massive increase of the total element number. This is not practical, because every additional vertex increases the dimension of the equation system (3.63) by one, which increases the computation time drastically. The solution of that problem is to place the elements in an inhomogeneous way: More smaller elements are set near the capsule's pole when a strongly elongated shape occurs, while a few bigger elements form the central regions. This increased density of elements near the pole is only relevant for the homogeneous external magnetic fields in chapter 4 and is not used with the inhomogeneous field in chapter 5. In the presence of homogeneous external fields, only one half of the capsule has to be discretized due to symmetry reasons. Then, we place the i-th boundary element with a length of

$$L_i = c \cdot l_0^{\frac{i-1}{n_\mathrm{B}}}. \tag{3.64}$$

The prefactor c has to be chosen that way, that the sum over all elements fits the total arc length:

$$\sum_{i=1}^{n_\mathrm{B}} L_i = L/2 = \int_0^{L_0/2} \lambda_s ds_0. \tag{3.65}$$

In general, $l_0 = 0.1$ seems to be a good choice and is used for every numerical calculation in chapter 4 unless something different is stated, see also the discussion about oscillating shape solutions in sec. 4.3.1. An illustration of the discretization near the capsule's pole for a conical capsule shape is shown in figure 3.5.

Equivalence to the electrostatic problem

The approach that was presented to calculate the magnetic pressure of a ferrofluid in an external magnetic field was based on the introduction of the scalar magnetic potential due

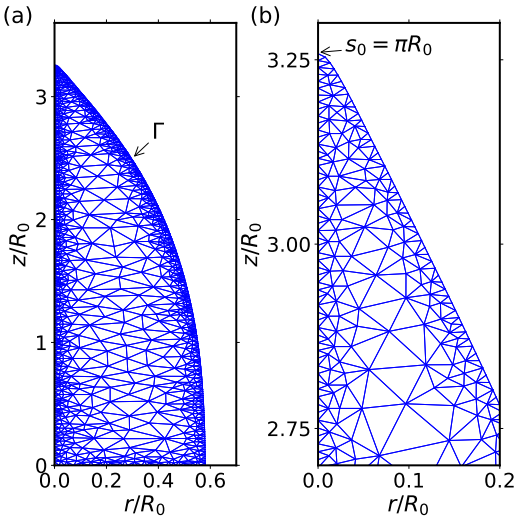

Figure 3.5.: Example triangulation of the upper half of a strongly elongated conically shaped capsule in a homogeneous magnetic field. (a): Complete upper hemisphere. (b): Zoom into the pole region.

to the absence of a conductivity in the ferrofluid. A side effect is that our magnetic model is mathematically completely equivalent to the description of a dielectric fluid in an external electric field. If we want to describe a dielectric fluid in an electric field instead of the ferrofluid, then we simply have to replace the magnetic field $\boldsymbol{H}$ by the electric field $\boldsymbol{E}$, the magnetic permeabilities μ_0 and μ become the electric vacuum permittivity ϵ_0 and the electric permittivity ϵ. The magnetization $\boldsymbol{M}$ is replaced by the polarization $\boldsymbol{P}$ and finally the scalar electric potential ϕ takes the role of the scalar magnetic potential u. Then, the Poisson equation (3.44) becomes

$$\nabla^2\phi(r,z) = -\frac{1}{\epsilon_0}\nabla\cdot\boldsymbol{P}(r,z), \tag{3.66}$$

which simplifies to the Laplace equation $\nabla^2\phi(r,z) = 0$ for a linear polarization law. Finally, the force density at the surface of the fluid is analogously to (3.39) given by

$$f_\mathrm{e}(r,z) = \int_0^{E(r,z)} P(r,z)\mathrm{d}E'(r,z) + \frac{1}{2\epsilon_0}P_n^2(r,z). \tag{3.67}$$

Consequently, all results for ferrofluid-filled capsules are also valid for capsules filled with a dielectric fluid in external electric fields, but for the sake of simplicity, we always use the magnetic formulation.

3.3. Coupled system

Finally, we have enough information to describe the whole problem. We are able to calculate the capsule's shape for given forces, we know the forces from the ferrofluid and we are able to calculate the magnetic field for a given shape. But in order to calculate the resulting shape of the capsule for a given external magnetic field, there is one problem left: The calculation of the elastic shell by solving the shape equations and the calculation of the magnetic field are coupled in a self-consistent way. The solution of the shape equations depends on the magnetic field, but the magnetic field itself depends on the actual shape, the solution of the shape equations. So, both problems, the magnetic and the elastic one, have to be solved simultaneously in a self-consistent way. Therefore, we apply an iterative solution scheme, similar to the iterative scheme in reference [19] for the shape calculation of sedimenting elastic capsules in external flow fields and for ferrofluid drops in the references [85, 86, 87, 88]. We start with the spherical

reference shape (r_0, z_0) and calculate the resulting magnetic field $\boldsymbol{H}(r,z)$ for a given external field $\boldsymbol{H}_{\mathrm{ext}}$. With that field, we can solve the shape equations giving us a new capsule shape. Then a recalculation of the magnetic field follows and so on, until the iteration converges. At this fixed point, we have a joint solution of the coupled elastic and magnetic problem.

The described iterative solution scheme can quickly cause massive numerical problems in the shooting method for the shape equations, especially when rapid changes of the shape and the field occur. Then, the shooting method often does not find a solution. This problem can be addressed by artificially slowing down the iteration. For the solution of the shape equations in the n-th step of the iteration, we do not simply use the n-th updated magnetic field $\boldsymbol{H_n'}$, but a convex linear combination of $\boldsymbol{H_n'}$ and the previous field $\boldsymbol{H_{n-1}}$ [19, 85]:

$$\boldsymbol{H_n} = \boldsymbol{H_{n-1}} + \beta(\boldsymbol{H_n'} - \boldsymbol{H_{n-1}}). \tag{3.68}$$

The parameter β is chosen from the interval $\beta \in]0, 1]$ and has to be lowered when the capsule shapes change rapidly during the simulation. Finally, β has to be set back to $\beta = 1$ in order to ensure real convergence.

Another improvement of the numerical stability can be achieved when the external magnetic field $\boldsymbol{H_{ext}}$ is increased in small steps $\Delta\boldsymbol{H_{ext}}$ and when the capsule's shape can converge after each step. The computation speed is slowed down drastically, but on the other hand this method also helps to track a specific branch of stable solutions, which is necessary in section 4.3.1. A final problem with that iterative solution scheme can still occur when the capsule's shape becomes nearly conical with a very sharp tip. In that case, the iterative scheme does not converge to a fixed point but seems to oscillate around that point. This phenomenon is discussed in more detail in section 4.3.1.

While we only try to simulate a static equilibrium of forces, there are dynamic alternatives to our iterative solution scheme. That means that the dynamic motion of the fluid as a result of the elastic, magnetic and hydrodynamic forces could be simulated directly over the time until it reaches its rest state. That kind of solution strategy was for example used by Karyappa et al. for elastic capsules in electric fields [70]. In addition, it was applied to comparable problems with sharp tips and numerical singularities for liquid drops, such as the emission of fluid jets at the tip of drops in electric fields [33], pinch-off dynamics [139] and coalescence phenomena [2]. The downside of that approach is that a third sophisticated problem, the hydrodynamics (next to the elasticity and the magnetic field), comes into play, which also increases the computing time significantly, because the fluid also has to be discretized.

3.4. Dimensionless quantities

At the end of this chapter, we finally introduce dimensionless quantities in order to be able to apply our results to arbitrary real systems. Therefore, we need to define some basic units of the system that define our natural scales. The basic length scale is defined by the radius R_0 of the undeformed spherical reference capsule. That means that all distances are measured as multiples of R_0. The next basic unit, that ensures our ability to describe forces, is the two-dimensional Young modulus $Y_{2\mathrm{D}}$. Finally, in order to be able to have dimensionless magnetic quantities, we also use the magnetic vacuum permeability μ_0 as the last basic unit. Table 3.1 gives an overview over the dimensionless versions of all important physical quantities that are used in the context of the capsules in magnetic fields. If nothing contrary is stated, all physical quantities are always meant to be measured as multiples of these reduced units. The definition of the dimensionless bending modulus κ_{B} is also known as the definition of the Föppl-von Kármán number γ_{FvK}:

$$\tilde{\kappa}_{\mathrm{B}} = \frac{\kappa_{\mathrm{B}}}{R_0^2 Y_{2\mathrm{D}}} = \frac{h^2}{12(1-\nu^2)R_0^2} = \frac{1}{\gamma_{\mathrm{FvK}}}. \tag{3.69}$$

Length and distances:	$\tilde{r} = r/R_0$	$\tilde{s} = s/R_0$
	$\tilde{z} = z/R_0$	$\tilde{L}_0 = L_0/R_0 = \pi$
Curvatures and volumes:	$\tilde{\kappa}_i = R_0\kappa_i$	
	$\tilde{V} = V/R_0^3$	$\tilde{V}_0 = V_0/R_0^3 = 4/3\pi$
Stresses, tensions and pressures:	$\tilde{\tau}_i = \tau_i/Y_{2\mathrm{D}}$	$\tilde{q} = q/Y_{2\mathrm{D}}$
	$\tilde{\gamma} = \gamma/Y_{2\mathrm{D}}$	$\tilde{p} = R_0 p/Y_{2\mathrm{D}}$
Bending moments and strains:	$\tilde{m}_i = m_i/(R_0 Y_{2\mathrm{D}})$	$\tilde{K}_i = R_0 K_i$
Energies:	$\tilde{E} = E/(Y_{2\mathrm{D}} R_0^2)$	
Magnetic field and magnetization:	$\tilde{\boldsymbol{H}} = \sqrt{\mu_0 R_0/Y_{2\mathrm{D}}}\boldsymbol{H}$	$\tilde{\boldsymbol{M}} = \sqrt{\mu_0 R_0/Y_{2\mathrm{D}}}\boldsymbol{M}$

Table 3.1.: Summary of the reduced dimensionless quantities. The same dimensionless system was already used in the author's master's thesis [146].

The Föppl-von Kármán number can be interpreted as a quantification of the relevance of the bending energy in relation to the stretching energy. Low values of γ_{FvK} correspond to a significant influence of the bending energy, while bending effects become less important for for increasing γ_{FvK}. Therefore, the limit case of a vanishing bending modulus, or an infinitely thin elastic shell, which is represented by the four shape equations (3.28), leads to $\gamma_{\mathrm{FvK}} = \infty$.

4. Elongation in a homogeneous field

The deformation behavior of ferrofluid or dielectric drops in uniform external magnetic or electric fields is well known [1, 3, 8, 11, 87, 88, 120, 135, 145, 152]. Analogously, the topic of the following chapter is a theoretical and numerical discussion of a ferrofluid-filled capsule in a homogeneous magnetic field. First, special properties like a linear magnetization law and the additional symmetry are presented in section 4.1. Then, an investigation of the behavior at small fields follows, including analytical approaches for a linear response and an energy minimization. In the last section, higher field strengths are used and the transition to shapes with nearly conical tips is discussed.

4.1. Properties and assumptions in a homogeneous field

When a magnetizable object is placed in a homogeneous external magnetic field, a magnetization is enforced and a total magnetic moment is created. A magnetic moment, or in general a magnetic dipole, tries to align itself to the external field. Therefore, there is torque acting on the magnetized object, until it is aligned in the field direction. But there is no total force on the dipole and, therefore, no translational movement. That would only occur with an existing field gradient. The same happens with our ferrofluid-filled capsule in a homogeneous field. Due to the symmetric structure of the magnetic stress (3.39), no total force is acting on the capsule. Therefore, the capsule does not move in the external field and is only stretched symmetrically in order to minimize its magnetic energy. We set our coordinate system in a way that the external magnetic field is pointing in z-direction: $\boldsymbol{H}_{\mathbf{ext}} = H_{\mathrm{ext}}\boldsymbol{e}_{\boldsymbol{z}}$. Thus, the capsule is stretched in z-direction and since the center of mass must not move, the $(z = 0)$-plane is a mirror plane, adding an additional symmetry to the axial symmetry. It is strictly advisable to exploit that symmetry in the numerical calculations: Only the upper half of the capsule needs to be discretized, as it is also illustrated in fig. 3.5 (a). Then, a finer discretization is possible with the same resulting computation time.

In this chapter, we only use the four shape equations without bending energy, equations (3.28), for the numerical solutions. On the one hand, it is justified, because we observe strongly elongated capsules that feature high elastic stresses in contrast to minor curvature changes. Especially for the stronger external fields in section 4.3, the capsule is completely dominated by stretching effects. Therefore, the errors by omitting the bending effects are neglectable. On the other hand, the numerical stability of the shooting method for the solution of the shape equations can be significantly improved when the system is reduced to the four equations.

In order to quantify the elongation of the capsule, we use the ratio a/b of the polar radius a and the equatorial radius b. These radii can be easily calculated as $a = |z(s_0 = 0)| = z(s_0 = \pi R_0)$ and $b = r(s_0 = \pi/2R_0)$.

4.1.1. Linear magnetization law

In this chapter, we assume that the ferrofluid follows the linear magnetization law

$$\boldsymbol{M}(\boldsymbol{H}) = \chi \boldsymbol{H}. \tag{4.1}$$

The constant χ describes the magnetic susceptibility that is connected via $\chi = \mu - 1$ to the permeability. This is a good approximation when the fields are small compared to the ratio of the saturation magnetization and the susceptibility: $H \ll M_\mathrm{s}/\chi$. When a capsule or a drop deforms to a nearly conical shape, higher fields can easily occur. The deformation behavior of a drop with a non-linear Langevin magnetization (polarization) law was studied in the references [10, 20]. The saturation effects forbid sharp tips there and lead to more rounded drops. In this thesis, we are explicitly interested in conical shapes. Therefore, we use the linear law, which is only realistic for a fluid with a very high susceptibility and saturation magnetization.

With the linear magnetization law, the integral in the magnetic stress (3.39) can be easily evaluated and we get

$$f_\mathrm{m}(r,z) = \frac{\mu_0 \chi}{2}(H^2(r,z) + \chi H_n^2(r,z)) \tag{4.2}$$

with H_n being the normal component of the magnetic field on the inner side of the surface. With that knowledge, we can finally write the normal pressure p_n in the shape equations (3.28) as

$$p_n = p_0 + f_\mathrm{m} = p_0 + \frac{\mu_0 \chi}{2}(H^2(r,z) + \chi H_n^2(r,z)). \tag{4.3}$$

4.1.2. Magnetic Bond number and control parameters

In order to reduce the parameter space, another dimensionless control parameter, the magnetic Bond number B_m, is introduced in a similar way as it was done in ref. [85]:

$$B_\mathrm{m} \equiv \frac{\mu_0 R_0 \chi H_\mathrm{ext}^2}{2\gamma}. \tag{4.4}$$

The introduction of the Bond number is motivated by the description of ferrofluid drops in a homogeneous field. With the help of the Bond number B_m, the Laplace Young equation (3.33) can be easily written in a dimensionless way:

$$\tilde{\kappa}_s + \tilde{\kappa}_\varphi = \tilde{p}_0 + B_m(\tilde{H}^2 + \chi \tilde{H}_n^2), \tag{4.5}$$

with $\tilde{H} = H/H_\mathrm{ext}$, $\tilde{\kappa}_i = R_0 \kappa_i$ and $\tilde{p}_0 = R_0 p_0/\gamma$. With that description, the shape of a droplet depends only on the parameters B_m and χ.

Obviously, B_m and χ are not enough parameters to describe the deformation of a capsule universally, since they do not state anything about the elasticity. Therefore, we need to introduce another parameter, which gives information about the relation between the elasticity in terms of the Young modulus and the surface tension. The dimensionless surface tension γ/Y_2D would be suitable, but since we also want to be able describe simple drops without elasticity, we use the inverse, Y_2D/γ, as our third control parameter. The limit case $Y_\mathrm{2D}/\gamma = 0$ represents a simple drop without elasticity, while $Y_\mathrm{2D}/\gamma \gg 1$ describes a system that is in general completely dominated by the elasticity.

The Poisson ratio ν also influences the elastic behavior. In this chapter, we set ν to the fixed value of $\nu = 1/2$, which represents an average Poisson ratio.

Finally, we have a three-dimensional parameter space (B_m, Y_2D/γ, χ). In order to simplify the parameter space, we also restrict the susceptibility χ to a fixed value of $\chi = 21$. This

value is chosen as an intermediate value for two reasons. First, it is high enough, that it is located over the critical susceptibility, which is at least needed for the occurrence of a shape transitions, see the discussion in section 4.3.4. Secondly, it is low enough that our numerical system is still able to find the resulting conical solution of the shape equations, which is not possible when the capsule is elongated too much. For the same reasons $\chi = 21$ was also used in refs. [85, 87].

In the following sections, we consider Bond numbers between 0 and 1000, which correspond to magnetic field strengths between 0 and about 500 kA/m for a typical capsule with $R_0 = 1\,\mathrm{mm}$ (like the capsules in refs. [70, 156] or in chapter 5), $\chi = 21$ and $\gamma = 0.01\,\mathrm{N/m}$. Additionally, we consider the full axis of possible ratios $Y_{2\mathrm{D}}/\gamma$, from $Y_{2\mathrm{D}}/\gamma = 0$ (drop) to $Y_{2\mathrm{D}}/\gamma = \infty$ (purely elastic system).

4.2. Spheroidal shapes at small and moderate fields

4.2.1. Linear shape response at small fields

The topic of the following section is the derivation of the linear response theory for spherical elastic capsules of the radius R_0 in a uniform magnetic field. That means that we try to find a linear relation between the capsule's elongation a/b and the magnetic forces which results in a simple quadratic relation, $a/b \sim H_{\mathrm{ext}}^2$.

The basic idea is that for small fields (and thus for small forces) the displacements of the capsule's shell change in a linear way with the magnetic surface force density f_{m}. Since we only want to consider small displacements from the spherical reference shape here, the usage of spherical coordinates (ρ,θ, φ) is advised. The spherical radial coordinate is called ρ, while θ is the polar angle and φ still describes the azimuthal angle. The capsule's upper apex is found at $\theta = 0$, while $\theta = \pi/2$ describes the equator. Now we introduce the radial and tangential displacements of the surface, $\boldsymbol{u_\rho} = u_\rho(\theta)\boldsymbol{e_\rho}$ and $\boldsymbol{u_\theta} = u_\theta \boldsymbol{e_\theta}$ (u_φ is always zero due to the axial symmetry). With these displacements, the deformed shape of the capsule can be parametrized as[1]

$$\boldsymbol{r}(\theta,\varphi) = (R_0 + u_\rho(\theta))\boldsymbol{e_\rho}(\theta) + u_\theta \boldsymbol{e_\theta}. \tag{4.6}$$

In the linear response regime, f_{m} contributes in linear order to the displacements, $u_i = O(f_{\mathrm{m}})$ and due to eq. (4.2), the magnetic field does it in a quadratic way, $u_i = O(H^2)$. Since we only want to consider small displacements, we use the completely linear elastic theory from ref. [83]. In this formalism, the stretch factors are given by

$$\lambda_s = \frac{\mathrm{d}s}{\mathrm{d}s_0} = \frac{1}{R_0}\left|\frac{\partial \boldsymbol{r}}{\partial \theta}\right| = 1 + \frac{1}{R_0}\left(u_\rho + \frac{\partial u_\theta}{\partial \theta}\right), \tag{4.7}$$

$$\lambda_\varphi = \frac{r}{r_0} = \frac{1}{R_0 \sin\theta}\left|\frac{\partial \boldsymbol{r}}{\partial \varphi}\right| = 1 + \frac{1}{R_0}(u_\rho + u_\theta \cot\theta). \tag{4.8}$$

The constitutive relations, the link between strains and stresses, follow as

$$\tau_\varphi - \nu\tau_s = Y_{2\mathrm{D}}(\lambda_\varphi - 1) = \frac{Y_{2\mathrm{D}}}{R_0}(u_\theta \cot\theta + u_\rho), \tag{4.9}$$

$$\tau_s - \nu\tau_\varphi = Y_{2\mathrm{D}}(\lambda_s - 1) = \frac{Y_{2\mathrm{D}}}{R_0}\left(\frac{\partial u_\theta}{\partial \theta} + u_\rho\right). \tag{4.10}$$

Now we have all the tools we need, and we can start to consider the force equilibria. The force equilibrium in normal direction is given by the Laplace-Young equation

$$\kappa_s(\tau_s + \gamma) + \kappa_\varphi(\tau_\varphi + \gamma) = p_0 + f_{\mathrm{m}}. \tag{4.11}$$

[1] There is a mistake in ref. [147]: $\boldsymbol{r}(\theta,\varphi)$ is given incompletely there.

Since the surface tension γ cannot be considered as a small term, we need to respect corrections to the curvature up to the linear order $O(u_\rho,u_\theta)$,

$$\kappa_s + \kappa_\varphi \approx \frac{2}{R_0} - \frac{1}{R_0^2}\left(2u_\rho - \frac{\partial^2 u_\rho}{\partial\theta^2} + \frac{\partial(u_\rho\cot\theta)}{\partial\theta}\right). \tag{4.12}$$

Then, the normal equilibrium becomes

$$\begin{aligned} &-\gamma\left(2u_\rho - \frac{\partial^2 u_\rho}{\partial\theta^2} + \frac{\partial(u_\rho\cot\theta)}{\partial\theta}\right) + R_0(\tau_s+\tau_\varphi) \\ &\quad = (p_0R_0^2 - 2R_0\gamma) + \frac{\mu_0}{2}\chi H^2R_0^2(1+\chi\cos^2\theta), \end{aligned} \tag{4.13}$$

where every contribution higher than $O(u_\rho,u_\theta)$ was omitted.

The tangential equilibrium states

$$0 = \frac{\cos\psi}{r}\tau_\varphi - \frac{1}{r}\frac{\mathrm{d}(r\tau_s)}{\mathrm{d}s} \tag{4.14}$$

$$\Leftrightarrow \tau\varphi = \frac{\partial(r\tau_s)}{\partial r} = \tau_s + r\frac{\partial\tau_s}{\partial r}. \tag{4.15}$$

With the aid of

$$r = \left|\frac{\partial \boldsymbol{r}}{\partial\varphi}\right| = \sin\theta\,(R_0 + u_\rho + u_\theta\cot\theta) \tag{4.16}$$

and the constitutive relation (4.10), we can rewrite the tangential force equilibrium as

$$\begin{aligned} \tau_\varphi - \tau_s &= \frac{Y_{2\mathrm{D}}}{(1+\nu)R_0}\left(u_\theta\cot\theta - \frac{\partial u_\theta}{\partial\theta}\right) \\ = \frac{\partial\tau_s}{\partial r} &= \frac{Y_{2\mathrm{D}}}{(1-\nu^2)R_0}\left(\tan\theta\frac{\partial^2 u_\theta}{\partial\theta^2} + \nu\frac{\partial u_\theta}{\partial\theta} - \frac{\nu u_\theta}{\cos\theta\sin\theta} + (1-\nu)\tan\theta\frac{\partial u_\rho}{\partial\theta}\right). \end{aligned} \tag{4.17}$$

Both force equilibria, (4.13) and (4.17) can be formulated as a system of two equations with two unknown functions (u_ρ and u_θ), when τ_s and τ_φ are completely eliminated through the constitutive relations. This system can be solved with an ansatz

$$u_\rho = A + B\cos^2\theta, \quad u_\theta = C\sin\theta\cos\theta. \tag{4.18}$$

This ansatz describes a spheroid to leading order in the displacements. From the tangential equilibrium follows

$$C = -\frac{2(1+\nu)}{5+\nu}B \tag{4.19}$$

and the normal equilibrium leads to

$$B = \frac{\mu_0(5+\nu)}{8(Y_{2\mathrm{D}} + (5+\nu)\gamma)}\chi^2R_0^2H^2. \tag{4.20}$$

The last missing constant A is determined by the constraint of a fixed volume. This constraint, $V = V_0 = 4\pi R_0^3/3$, requires

$$A = -\frac{B}{3}. \tag{4.21}$$

Finally, we only need to calculate the elongation a/b up to the first order in the displacements and get

$$\begin{aligned}\frac{a}{b} &= \frac{R_0 + u_\rho(0)}{R_0 + u_\rho(\pi/2)} \approx 1 + \frac{B}{R_0} \\ &= 1 + \frac{9\mu_0 R_0 \chi^2 (5+\nu)}{8(Y_{2\mathrm{D}} + \gamma(5+\nu))(3+\chi)^2} H_{\mathrm{ext}}^2 = 1 + \frac{9}{4}\frac{\chi}{(3+\chi)^2}\frac{B_m}{Y_{2\mathrm{D}}/\gamma(5+\nu)+1},\end{aligned} \tag{4.22}$$

the central result of this section. In the second to last step, the magnetic field H was replaced by the external field H_{ext}. Therefore, the magnetic field for a linearly magnetizable sphere in a uniform field [68],

$$H = \frac{3}{3+\chi} H_{\mathrm{ext}}, \tag{4.23}$$

was used. A similar approach in ref. [70] for capsules that are filled with a dielectric fluid and placed in an electric field showed comparable results.

The comparison between this linear response result and the numerical results from the shape equations (and the Laplace-Young equation for the simple drop) is shown in fig. 4.1. The elongation a/b is shown as a function of a rescaled Bond number. There is an excellent agreement for small Bond numbers. With increasing B_{m}, the elongations of the numerically calculated capsules become larger than it is predicted by the linear response. The linear response is a good approximation, as long as $a/b - 1 \ll 1$ is satisfied. As soon as wrinkling effects occur (pink squares), the deviations become significantly larger. Especially for ferrofluids, the linear regime is very important, because small magnetic fields are easily accessible experimentally and the susceptibilities are quite small for many ferrofluids (for example, $\chi \simeq 0.36$ in ref. [154] and $\chi = 0.25$ in the experiment in chapter 5). If the magnetic properties are known, the relation (4.22) can be used in order to determine the elastic properties of the capsule in an experiment, especially the Young modulus.

4.2.2. Spheroidal shapes

The ferrofluid-filled capsule is spherical at $B_{\mathrm{m}} = 0$ at first. Similar to a ferrofluid drop, it is more and more elongated for increasing B_{m}. Thus a/b rises, as it was already indicated in the linear response section. At small and even at medium field strengths, the capsule's shape can be described as a prolate spheroid, which also was the solution for the displacements in the linear response regime. It can be quickly shown that the spheroid is not an exact solution of the shape equations or the Laplace-Young equation. But the spheroid is a very good

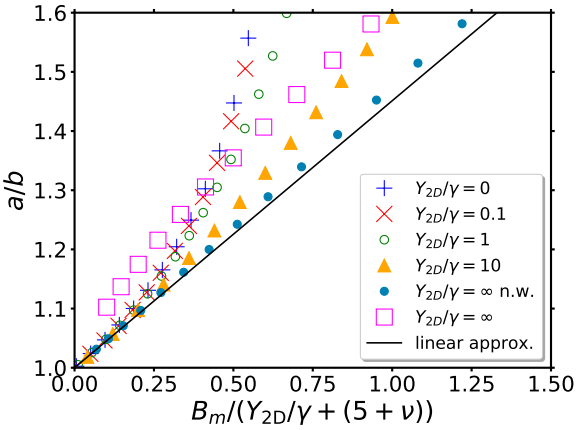

Figure 4.1.: Elongation a/b of a capsule filled with a ferrofluid with $\chi = 21$ as a function of $B_m/[Y_{2\mathrm{D}}/\gamma + (5+\nu)]$ for different values of $Y_{2\mathrm{D}}/\gamma$ in the region of small deformations. The solid line describes the linear approximation from eq. (4.22). The best agreement between the numerical data and the linear approximation is given for a purely elastic system without wrinkling effects (closed blue circles). Wrinkling effects lead to considerable deviations (squares). The data of this diagram have already been published in [147].

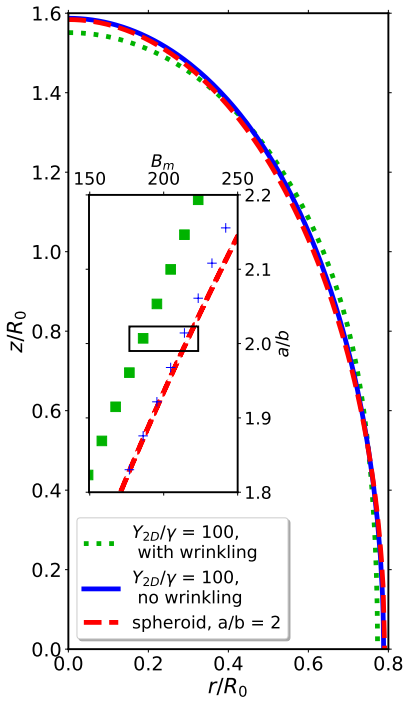

Figure 4.2.: Comparison of the numerically calculated $r(z)$ contour of a capsule with $Y_{2D}/\gamma = 100$, and $\chi = 21$, for a value B_m chosen such that the elongation is $a/b \approx 2$. The shape calculated without wrinkling (blue solid line) shows a very good agreement with a spheroid of the same volume and elongation (red dashed line). Including wrinkling effects leads to visible deviations (green dotted line). The inset shows the Bond number B_m as a function of the elongation a/b in the neighborhood of the compared shapes next to an approximative red dashed curve for a spheroid (see section 4.2.3). The data of this diagram have already been published in [147].

approximation for the numerically and experimentally found shapes [1, 3, 8, 70]. Also, the solution of our shape equations is very difficult to differ from a spheroid as fig. 4.2 impressively shows. There, the blue solid line describes the contour $z(r)$ as a solution of the shape equations for a capsule that is dominated by its elasticity with $Y_{2D}/\gamma = 100$. The elongation of that capsule is $a/b \approx 2$ at $B_m \approx 214$ and wrinkling effects are not included. The red dashed line shows a prolate spheroid with the same volume and elongation. Both objects are very hard to differ, so the spheroid is a very good approximation despite $a/b = 2$ being not a small deformation anymore. When wrinkling effects are included, a deviation from the spheroidal shape is visible. The inset diagram shows the location of the shapes in the corresponding $(a/b, B_m)$-plane. There, the red dashed line is still related to a spheroid and is gained from the approximation with the energy minimization that is presented in the following section 4.2.3.

In the following, due to the good agreement to a prolate spheroid, we call every capsule shape in a uniform magnetic field a spheroidal shape, if it did not proceed a shape transition to a conical shape (see sec. 4.3). This nomenclature also includes wrinkled shapes with deviations from a real spheroid.

4.2.3. Approximative energy minimization

In the following, we use the knowledge about spheroidal shapes in order to derive an analytical approximation for the capsule's elongation $a/b(B_m)$. Therefore, we assume a spheroidal shape and minimize an approximative total energy, the sum of the elastic energy E_{el}, the surface tension energy E_γ and the magnetic energy E_{mag}. Bacri and Salin [8] successfully used this approach and were able to predict the elongation of a ferrofluid drop in a uniform magnetic field with very high precision. So, the idea is now to do exactly the same but with an additional elastic energy. Similar to Bacri and Salin, we start with the simple ferrofluid drop. The surface energy is the product of the surface tension γ and the total surface area A of the spheroid,

$$E_\gamma = \gamma A = 2\pi ab \left(\frac{b}{a} + \frac{1}{\epsilon} \arcsin \epsilon \right) \gamma, \tag{4.24}$$

with $\epsilon \equiv \sqrt{1 - b^2/a^2}$ being the eccentricity of the spheroid.

The next step is the magnetic energy. First, it is important to recognize that the spheroid is uniformly magnetized in a homogeneous external field and thus, also the field inside the spheroid is homogeneous. Spheroids are the only class of objects with this feature [136]. The field and also the magnetic energy can be calculated analytically. The energy is then given as

$$E_{\mathrm{mag}} = -\frac{V\mu_0}{2}\frac{\chi}{1 + n_{\mathrm{d}}\chi}H_{\mathrm{ext}}^2 \tag{4.25}$$

for a non-magnetizable external medium. The factor n_{d} describes the demagnetization factor [136],

$$n_{\mathrm{d}} = \frac{b^2}{2a^2\epsilon^3}\left(-2\epsilon + \ln\frac{1+\epsilon}{1-\epsilon}\right). \tag{4.26}$$

The volume V of the spheroid can be expressed as $V = (4\pi/3)ab^2 \stackrel{!}{=} V_0 = (4\pi/3)R_0^3$ and has to be kept constant.

Now we have to add the elastic energy and come to the point, where we have to leave the known terrain. The total elastic energy is the reference surface integral over the elastic energy density w_s (without bending energy, eq. (3.25)):

$$E_{\mathrm{el}} = \int w_s \mathrm{d}A_0 = \int \frac{1}{2}\frac{Y_{2\mathrm{D}}}{1-\nu^2}((\lambda_s - 1)^2 + 2\nu(\lambda_s - 1)(\lambda_\varphi - 1) + (\lambda_\varphi - 1)^2)\mathrm{d}A_0. \tag{4.27}$$

To calculate this integral exactly, we would need the solution of the shape equations, which is not accessible analytically. Therefore, we need some rather harsh approximations for the stretch factors λ_s and λ_φ. Indeed, both stretch factors are approximated by constant values phenomenologically chosen. The spheroid is elongated in the magnetic field and due to the preservation of the volume, it becomes thinner, which means the elastic shell has to be compressed in circumferential direction. Therefore, we approximate λ_φ by the stretch factor of a circumferential fiber at the equator and set

$$\lambda_\varphi = \frac{b}{R_0}. \tag{4.28}$$

Analogously, we do nearly the same in meridional direction: We assume a constant stretching of a fiber from the lower pole to the upper pole. The numerical results in section 4.3 and in fig. 4.4 show that this is an astonishingly good approximation for medium elongations of the spheroidal shape. Similar to before, the stretch factor is the ratio of the actual fiber length and the reference length. The reference length is simply given by πR_0, but the actual fiber length is the half of the perimeter of an ellipse, P_{ellipse}, with the major half axis a and the minor half axis b. This perimeter cannot be calculated analytically (it is the original definition of an elliptic integral), but it can be approximated in a very precise way by the approximation of Ramanujan [119]. This results in

$$\lambda_s = \frac{P_{\mathrm{ellipse}}}{P_{\mathrm{circle}}} \approx \frac{a+b}{2R_0}\left(1 + \frac{3\eta^2}{10 + \sqrt{4 - 3\eta^2}}\right), \tag{4.29}$$

with $\eta \equiv (b-a)/(b+a)$. Due to the now constant stretch factors, the integral in eq. (4.27) can be written as a simple product with the reference surface area $A_0 = 4\pi R_0^2$:

$$E_{\mathrm{el}} = \frac{1}{2}\frac{Y_{2\mathrm{D}}}{1-\nu^2}(e_s^2 + 2\nu e_s e_\varphi + e_\varphi^2)A_0. \tag{4.30}$$

At this point, we have everything we need: We know all three energies as functions of the polar and equatorial radii a and b and these two radii can be coupled together by the volume constraint. Therefore, we can now minimize the total energy as a function of the elongation a/b or, as it simplifies things a bit, as a function the inverse elongation ratio $k \equiv b/a < 1$. That means we demand

$$0 = \frac{\mathrm{d}E_\gamma|_V}{\mathrm{d}k} + \frac{\mathrm{d}E_\mathrm{mag}|_V}{\mathrm{d}k} + \frac{\mathrm{d}E_\mathrm{el}|_V}{\mathrm{d}k}, \tag{4.31}$$

where $...|_V$ indicates the constant volume constraint. The volume constraint helps to express all relevant quantities in terms of k:

$$a|_V = R_0 k^{-2/3}, \quad b|_V = R_0 k^{1/3}, \tag{4.32}$$

$$E_\gamma|_V = \gamma A_0 \frac{1}{2} k^{-1/3} \left(k + \frac{1}{\epsilon(k)} \arcsin \epsilon(k) \right), \tag{4.33}$$

$$\epsilon(k) = \sqrt{1-k^2}, \tag{4.34}$$

$$E_\mathrm{mag}|_V = -\frac{V_0 \mu_0}{2} \frac{\chi}{1+n\chi} H_0^2 = -\gamma A_0 B_m \frac{1}{3(1+n(k)\chi)}, \tag{4.35}$$

$$n(k) = \frac{k^2}{2\epsilon^3(k)} \left(-2\epsilon(k) + \ln \frac{1+\epsilon(k)}{1-\epsilon(k)} \right), \tag{4.36}$$

$$E_\mathrm{el}|_V = A_0 \frac{Y_\mathrm{2D}}{2(1-\nu^2)} \left((\lambda_s|_V - 1)^2 + 2\nu(\lambda_s|_V - 1)(\lambda_\varphi|_V - 1) + (\lambda_\varphi|_V - 1)^2 \right), \tag{4.37}$$

$$\lambda_s|_V = \frac{k^{-2/3}(1+k)}{2} \left(1 + \frac{3\eta^2(k)}{10 + \sqrt{4 - 3\eta^2(k)}} \right), \tag{4.38}$$

$$\eta(k) = (b-a)/(b+a) = (k-1)/(k+1), \tag{4.39}$$

$$\lambda_\varphi|_V = k^{1/3}. \tag{4.40}$$

Finally, from eq. (4.31) we find

$$B_\mathrm{m}(k = b/a) = -3 \left(\frac{1}{\chi} + n(k) \right)^2 \chi \frac{c_1(k) + \frac{Y_\mathrm{2D}}{2\gamma(1-\nu^2)} c_2(k,\nu)}{c_3(k)}, \tag{4.41}$$

with

$$c_1(k) \equiv \frac{1}{A_0} \frac{\mathrm{d}A|_V}{\mathrm{d}k}, \tag{4.42}$$

$$c_2(k,\nu) \equiv \left(2e_s|_V \frac{\mathrm{d}e_s|_V}{\mathrm{d}k} + 2\nu \left(e_\varphi|_V \frac{\mathrm{d}e_s|_V}{\mathrm{d}k} + e_s|_V \frac{\mathrm{d}e_\varphi|_V}{\mathrm{d}k} \right) + 2e_\varphi|_V \frac{\mathrm{d}e_\varphi|_V}{\mathrm{d}k} \right), \tag{4.43}$$

$$c_3(k) \equiv \frac{\mathrm{d}n}{\mathrm{d}k} = \frac{-3k}{\epsilon^4(k)} + \left(\frac{k}{\epsilon^3(k)} + \frac{3k^3}{2\epsilon^5(k)} \right) \ln \frac{1+\epsilon(k)}{1-\epsilon(k)}. \tag{4.44}$$

The functions $c_1(k)$ and $c_3(k)$ are generated by the surface energy and the magnetic energy, while $c_2(k,\nu)$ represents the elastic part. In the limit case of a ferrofluid drop with $Y_\mathrm{2D} \to 0$, c_2 vanishes and the original result of Bacri and Salin is restored.

The result relation (4.41) cannot be inverted analytically to our preferred representation $a/b(B_\mathrm{m})$, because it is not injective. A detailed discussion of the behavior and the properties of the result of this energy approximation follows in the next section in a comparison to the behavior of the numerical solution of the shape equations for medium and stronger fields.

4.3. Stronger fields and shape transitions

In the following section, the deformation behavior of capsules in stronger external fields shall be investigated. A special focus is set to the transition to nearly conical shapes. These capsule shapes are strongly elongated and feature a sharp tip near the poles, where very high magnetic fields and magnetizations occur.

4.3.1. Deformation in strong fields

It was already stated in section 4.2 that the ferrofluid-filled capsule elongates in the homogeneous field and takes the shape of a prolate spheroid, even after leaving the linear regime. That is the case for ferrofluid droplets as well as for purely elastic systems. Figure 4.3 shows the general elongation behavior of different systems with $\chi = 21$ from $Y_{2D}/\gamma = 0$ to $Y_{2D}/\gamma = \infty$. The elongation a/b is shown as a function of the rescaled Bond number, so it is directly comparable to fig. 4.1.

The first interesting result, that became already apparent during the investigation of the linear region in fig. 4.1, is that the linear region is much more extended for a purely elastic system than for a droplet. A ferrofluid drop (blue lines and markers in fig. 4.3) or a weak capsule that is dominated by the surface tension (green) quickly leaves the linear region. Then, the elongation drastically rises with the increasing Bond number. So, if a drop is elongated enough, it becomes easier to elongate it further. With stronger elasticity (increasing Y_{2D}/γ), the elongation curve becomes flatter. In a purely elastic system, there is still a nearly linear relation between a/b and the Bond number, even for remarkable elongations of about $a/b \approx 3$. After that, the slope of the curve only slightly increases. The solid lines represent the elongation that was calculated via the approximative energy minimization with the assumption of a spheroid, eq. (4.41). This approximation features a good agreement with the numerical data points. The best agreement is shown by the ferrofluid drop, which is already known from the literature. That is easy to explain since the only approximation is the assumption of a spheroidal shape in that case and that assumption is very well justified. With increasing elasticity, the approximative character of our spheroidal energy minimization comes more into play. Nevertheless, we still see a very good agreement between the solution of the shape equations and the approximation (4.41), if wrinkling effects are not respected. Especially elongations up to about $a/b \approx 3$ can be described quite precisely by the energy minimization. For higher elongations or Bond numbers, the approximation predicts too low elongations. The reason why the approximative curve with that harsh assumptions (especially constant stretch factors) works surprisingly well is that there is a range of elongations where the assumption $\lambda_s = \text{const}$ is astonishingly precise. Figure 4.4 shows the meridional stretching factor λ_s for different elongations from $a/b = 1.5$ to $a/b = 3.5$. Here it becomes clearly visible that even at $a/b = 2.5$ a constant stretching factor is a good approximation. Also, at $a/b = 3$ it is still acceptable. Near the poles ($s_0 = 0$) λ_s may increase significantly, but that is till not that important, because the surface area near the poles is much smaller than the area near the equator. The elastic energy (4.27) is related to the integral over the surface, thus the equator has much more influence. This approximation begins to fail for $a/b > 3$, when λ_s strongly increases near the poles. At $a/b = 3.5$, the strain $e_s = \lambda_s - 1$ is already twice as high as it is near the equator.

The shape transition

Increasing the Bond number further leads to a point, where the elongation suddenly jumps to a much higher value and where the spheroidal shape ceases to exist. At this point we see a transition to a highly elongated shape with nearly conical tips at the poles. This transition is

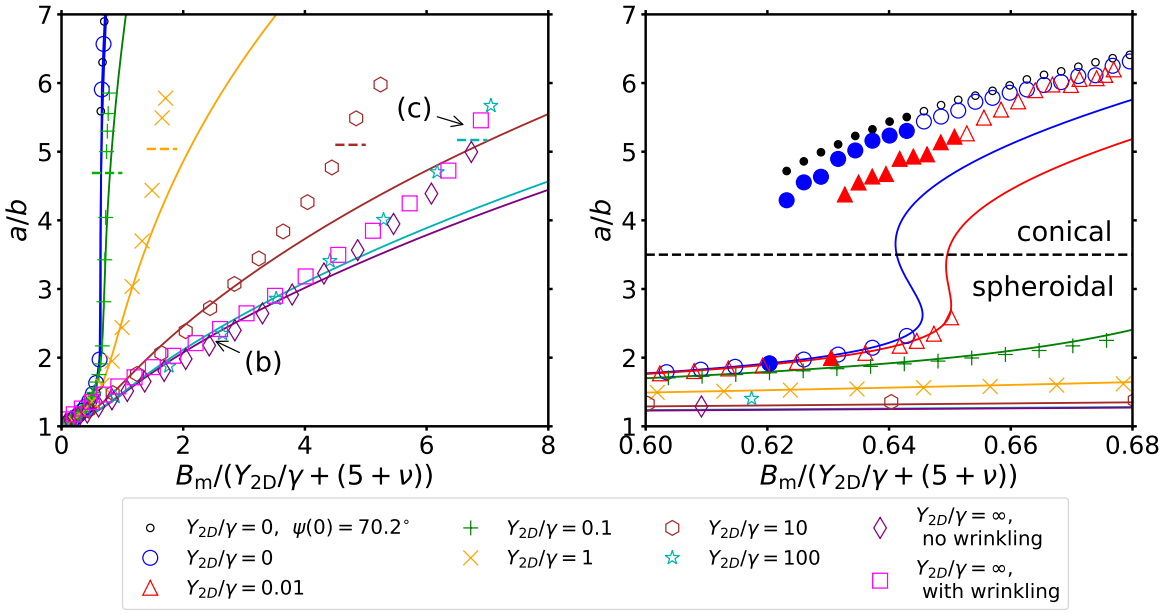

Figure 4.3.: Elongation a/b of a capsule filled with a ferrofluid with $\chi = 21$ as a function of the magnetic Bond number B_m for different values of the dimensionless elastic parameter Y_2D/γ. The magnetic Bond number is rescaled by $Y_\mathrm{2D}/\gamma + (5+\nu)$, which is motivated by the small field behavior in equation (4.22). The solid lines describe the theoretical results from the approximative energy minimization (see section 4.2.3). Open (closed) symbols denote numerical data for increasing (decreasing) B_m. The agreement is good for small to medium elongations, but the approximation fails for higher elongations, especially at the shape transition (close-up in the right diagram), where a/b jumps for small changes of B_m. Hysteresis effects are clearly visible in that area. There are two sets of numerical data for $Y_\mathrm{2D}/\gamma = \infty$: Square data points are based on the modified shape equations that take wrinkling into account, while diamonds are calculated without wrinkling. There are also two sets of data without elasticity: The upper data points (black) describe a droplet with a real conical tip with a cone angle of $\psi(0) = 70.2°$, as it was given in reference [135]. For the lower points (blue) the boundary condition $\psi(0) = 0$ was used. Dashed lines indicate the position of shape transitions. Above these lines, shapes are conical, while they are spheroidal below. The markers (b) and (c) correspond to the shapes in figure 4.5. The data of these diagrams have already been published in ref. [147].

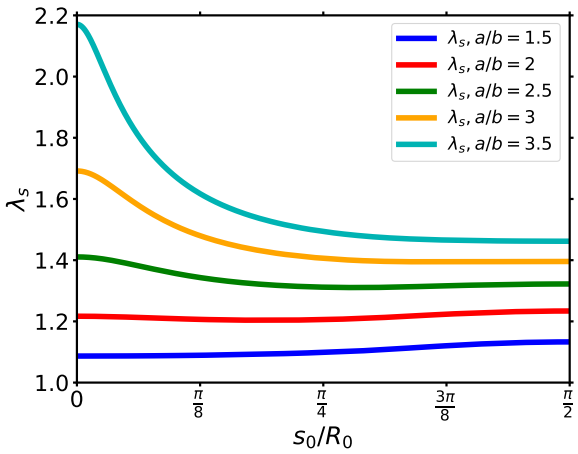

Figure 4.4.: Meridional stretching factor λ_s as a function of the undeformed arc length s_0 shown from the pole ($s_0 = 0$) to the equator ($s_0 = \pi/2$) of a capsule with $\chi = 21$ and $Y_\mathrm{2D}/\gamma = 100$ for different elongations.

well known for ferrofluid and dielectric drops [1, 8, 87, 93, 135]. The diagram on the right side in fig. 4.3 shows a zoom to the critical region. The pure drop (blue markers) elongates from about $a/b \approx 2.6$ to $a/b \approx 5.4$ when B_m reaches the critical value $B_\mathrm{m,c2}$. If the Bond number is further increased after that transition, the shape is simply more elongated (represented by the open circles). But when B_m is lowered below $B_\mathrm{m,c2}$ (filled circles), the drop stays conical at first, so there is a hysteretic behavior. Only after lowering B_m below a lower critical value, $B_\mathrm{m,c1}$, we see a transition back to the spheroidal shape.

This transition is the result of a competition between the magnetic energy and the surface energy. The magnetic energy is lowered for long elongated shapes, while the increasing surface leads to a higher surface energy. The effect is basically the same as in the case of the formation of a needle-like pattern on a free ferrofluid surface for sufficiently large magnetic fields, the *normal field instabilities* or Rosensweig instabilities [18, 54, 125]. At $B_\mathrm{m} > B_\mathrm{m,c2}$, the spheroidal shape becomes unstable, while on the other hand the conical shape cannot exist for $B_\mathrm{m} < B_\mathrm{m,c1}$. Between these values, in the region of hysteresis, both conformations are possible.

The approximative curve (4.41) from the spheroidal energy minimization also features a transition effect. This is clearly recognizable from the s-shape of the curve (blue and red curve in the right-hand diagram of fig. 4.3). Since the approximative curve is very precise for the spheroidal shape, also the critical Bond number $B_\mathrm{m,c2}$, where the transition to a more elongated shape occurs, is precisely predicted for systems with small and vanishing elasticity. But after the transition, there are very high deviations to the numerical solutions of the Laplace-Young equation and the elastic shape equations. That is not surprising, because the approximative curve is still based on the assumption of a spheroidal shape, but after the transition, the real shape shows great differences to a spheroid, especially near the poles. Thus, the size of the hysteresis region, that is predicted by the approximative curve, is far too small. For a more detailed discussion on the hysteresis area, see also sec. 4.3.3. With increasing elasticity, the approximative energy minimization does not predict a transition anymore. For the green curve ($Y_\mathrm{2D}/\gamma = 0.1$), the transition already seems to be suppressed by the elasticity.

Nevertheless, the numerical results show the opposite: Every capsule in fig. 4.3, even the purely elastic system without any surface tension, shows a transition to a conical shape. With higher contributions of the elasticity, it is just harder to recognize by considering the elongation a/b. With higher values of Y_2D/γ, the spheroidal shape of the capsule is far more elongated than the shape of a ferrofluid drop before the transition occurs at $B_\mathrm{m} = B_\mathrm{m,c2}$. Thus, there is a much smaller jump of a/b. A visual evaluation of the capsule's contour line $z(r)$ clearly shows nearly conical shapes. But the stretching factor at the poles, $\lambda_s(s_0)$, is a control parameter that is much easier to use for the detection of the transitions at $B_\mathrm{m,c2}$ and $B_\mathrm{m,c1}$, see also the discussion in section 4.3.3.

The magnetic field

After all, our numerical results indicate, that even purely elastic ferrofluid-filled capsules show a transition to a conical shape (of course only for a sufficiently high susceptibility). The mechanism is exactly the same as it is for the ferrofluid drop. At the critical point $B_\mathrm{m,c2}$, the transition to the conical shape is energetically favorable.

Before the transition occurs, we have a homogeneous magnetization and thus also a homogeneous magnetic field in the spheroidal capsule. The magnetic forces are balanced by the product of the elastic tensions and moderate curvatures near the poles. At this point, the balance of forces is very easy to understand. Due to the uniform field and magnetization, only the M_n term in the magnetic force (4.2) is position-dependent. At the equator, we have $M_n = 0$ (the homogeneous field is always parallel to the capsule's symmetry axis), thus there

is only a small curvature that balances the internal pressure p_0. Near the poles, M_n increases, because the normal vector becomes more and more parallel to the field, so a higher curvature is needed there.

After the transition to the conical shape, things are different. While the field stays nearly uniform in the equator region and thus the argumentation remains the same there, a uniform field near the poles is impossible now. A nearly conical surface features very high curvatures, so the product with the surface tension and the elastic tensions results in high force densities that have to be balanced by the field and the magnetization. Therefore, the magnetic field must become drastically stronger near the tip. Indeed, electric and magnetic fields even diverge in the vicinity of a real sharp tip. In order to be able to resolve the force balance for such high magnetic fields, the increased resolution of the boundary elements near to pole, which was presented in sec. 3.2.2, is needed. Figure 4.5 shows the numerically calculated magnetic field $\boldsymbol{H}$ in a spherical (a), a spheroidal (b) and a nearly conical capsule (c). The homogeneous fields of the spherical and the spheroidal shape are clearly visible as well as the drastically increasing field near the conical tip. The markers (b) and (c) in fig. 4.3 point to the positions where these capsules are located in the $(a/b, B_\mathrm{m})$-plane.

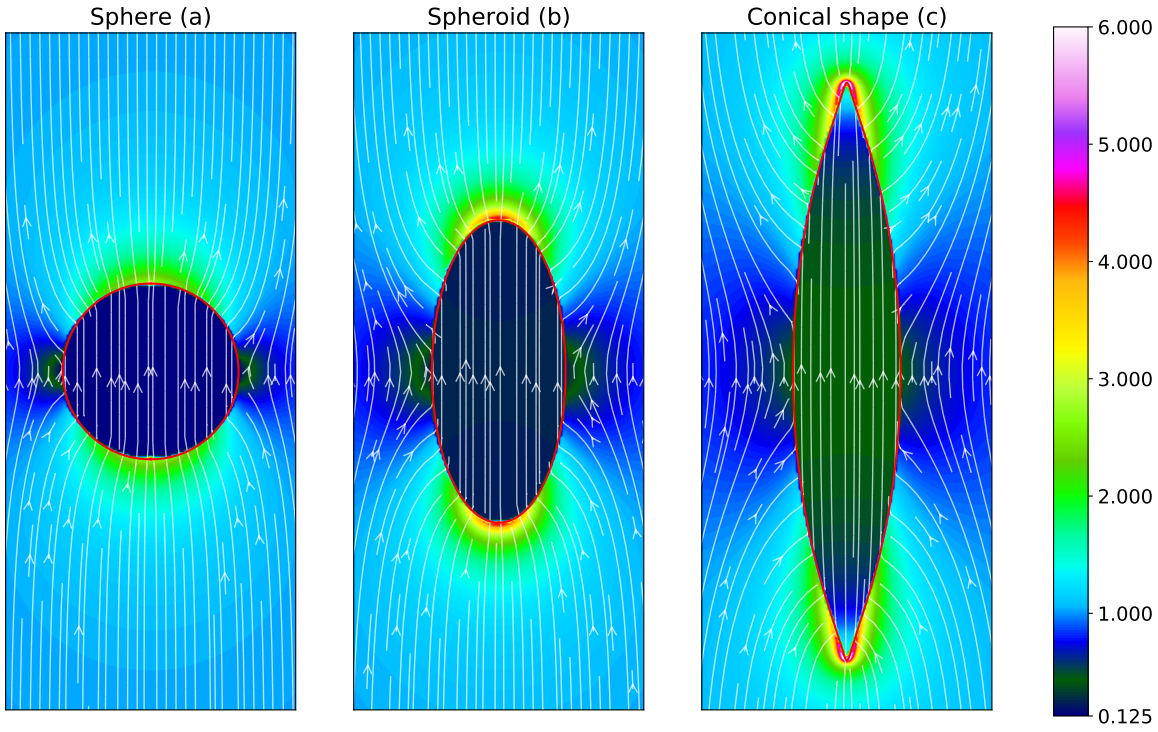

Figure 4.5.: Numerical results for the magnetic field distribution for a capsule filled with a ferrofluid with a susceptibility of $\chi = 21$. The red solid lines show the capsule's contour line $z(r)$. The ratio of the Young modulus and surface tension is $Y_{2\mathrm{D}}/\gamma = 100$. The external magnetic field H_0 is uniform and points in the upward direction. Arrows indicate the local direction of H and colors denote the absolute value of H in units of H_0. The spherical capsule (a) and the spheroidal capsule (b) have uniform fields inside while the field in the conical shaped capsule (c) increases strongly near the tips, but still remains nearly uniform near the equator. The elongations a/b are (a): $a/b = 1$, (b): $a/b = 2.26$, and (c): $a/b = 5.38$. The magnetic Bond numbers B_m read (a): $B_m = 0$, (b): $B_m = 262.4$, and (c): $B_m = 702.2$. This is a modified version of a figure that has already been published in ref. [147].

Numerical oscillations

A special kind of numerical problems occurs after the shape transition. The iterative coupling of the elastic and the magnetic subproblems (which was described in sec. 3.3) has no problem to converge to the fixed point for a spheroidal shape, even for high elongations in the purely elastic system. That changes directly after the transition to a nearly conical shape. There, the iteration has serious problems to converge. Instead, a kind of oscillation can be observed. That means that the resulting elongation oscillates in a relatively small interval and no fixed point can be found, even with very high numbers of iterations. Even a drastic slowing down of the iteration by choosing very small values of β in the combination of the old and the new magnetic field, eq. (3.68), does not solve the problem. Therefore, we estimate the capsule's elongation a/b as a mean value after averaging it over a sufficiently high number of iterations.

The source of that problem is probably found in the boundary condition for the slope angle at the pole, $\psi(s_0 = 0) = 0$. At this point, we forbid a real sharp cone, which would feature a real diverging magnetic field. So, a pseudo cone with a slightly rounded tip is the result, which is probably not the real solution of the joint problem. Therefore, a fixed point cannot be found. In addition, the quickly changing magnetic field near the tip, where relevant errors can occur, worsens the problem. The question whether an elastic capsule (without bending energy) should be able to form a real conical tip is discussed in the following section 4.3.2.

On the other hand, a simple drop without elasticity is definitely able to support a sharp tip. With a drop, the condition $\psi(s_0 = 0) = 0$ is only valid for the spheroidal shape. After the transition to the conical shape, the opening angle of the cone can freely adjust to the value that minimizes the total energy. Therefore, we have two sets of numerical data for the simple ferrofluid drop in figure 4.3. The blue circles correspond to a drop that was calculated with the (physically wrong) condition $\psi(s_0 = 0) = 0$, where the mentioned oscillation problems occur. The black circles represent data that were recorded with the condition $\psi(s_0 = 0) = 70.2°$ (opening angle of 39.6°). This value was taken from the analysis for ferrofluid and dielectric drops in homogeneous fields in ref. [135] with a susceptibility of $\chi = 21$. In that case, we get a slightly more elongated shape with an even higher magnetic field near the now real tip. The oscillations do not disappear completely, but they are drastically reduced. They are still present probably due to errors in the field calculation and slight deviations of the opening angle to the angle of the real solution.

4.3.2. (Im-)Possibility of sharp cones

In the following, we want to show, that the same kind of sharp conical tips, that appear for ferrofluid drops, are also possible for elastic capsules with a spherical rest shape without bending energy. A sharp tip requires a non-zero slope angle $\psi(s_0 = 0) > 0$, which also defines the half opening angle $\alpha = \pi/2 - \psi(0)$ of the cone. Another requirement are asymptotically isotropic and diverging stretch factors with an exponent determined by the opening angle of the cone. On the other hand, the elastic tensions have to remain finite. Therefore, the non-linear constitutive relations (3.11) and (3.12) take a key role.

First, we start to consider conical phenomenons in the topic of elasticity that are known from the literature. In ref. [149], sharp cones in deformed elastic plates, that feature a planar rest shape, are discussed. If external forces act in such a way that a stretching of the plate can be avoided, the plate always responds by pure bending, because the bending energy scales with the third power of the thickness, while the stretching energy scales linearly with the thickness. Any deformation that does not include stretching has to preserve the metric and the Gaussian curvature of the plate, which is vanishing. A possible result is the formation of developable cones, typically under compression as it can be observed in the crumpling of paper. Cones also have zero Gaussian curvature except for the tip (a deeper discussion of the metric

and curvature of plates can be found in the second part of this thesis, in chapter 8). Then, elastic plates develop folds and wrinkles in the area around the developable cones, which is the response to store the unnecessary area as a result of the compression [14, 28, 149]. Finally, cones can be interpreted as a typical response of elastic plates to external forces that avoid any stretching.

For our ferrofluid-filled capsule, things are quite different. First, we have a spherical rest shape. There is no deformation of a spherical shape without stretching possible, since any deformation of a sphere changes its metric. In addition, the magnetic forces always act in normal direction. Therefore, a stretching cannot be avoided in order to keep the tangential force equilibrium satisfied. Similar conditions are also given when a point force acts on a spherical elastic shell. In such systems, conical solutions have also been observed [141].

An elastic cone under magnetic forces establishes a kind of positive feedback between the shape of the shell and the magnetic field that is needed to stabilize that shape. A sharp tip leads to a higher field in the tip, which creates even stronger forces and further stretching. After all, we need to find the shape of equilibrium.

In order to do so, we start with the tangential force equilibrium (3.27), rewritten as

$$\tau_\varphi = \frac{\partial(r\tau_s)}{\partial r} = \tau_s + r\frac{\partial \tau_s}{\partial r}. \tag{4.45}$$

This equilibrium has to be satisfied everywhere in the shell, even in the direct vicinity of the tip, and it is independent of the normal magnetic forces in the first place. Combined with the non-linear constitutive relations (3.11) and (3.12), it follows that the tensions remain finite in the tip (at $s_0 = 0$), even if the field diverges, and also remain isotropic:

$$0 < \tau_s(s_0 = 0) = \tau_\varphi(s_0 = 0) < \infty. \tag{4.46}$$

This can be understood by the following consideration: A diverging tension can only be caused by a divergence of one or both stretch factors. Now we reach the point where the non-linearity of the constitutive relations becomes essential. They state that both λ_s and λ_φ cannot diverge simultaneously, because the ratios $\lambda_s/\lambda_\varphi$ and $\lambda_\varphi/\lambda_s$ cannot show a divergence at the same time. So only a single stretch factor could diverge, but on the other hand, that would violate the tangential equilibrium (4.45). In conclusion, both tensions have to remain finite at $s_0 = 0$. From the finiteness of the tensions, the isotropy follows immediately from the tangential equilibrium. If $\tau_s(0) \neq \tau_\varphi(0)$, we get

$$\frac{\partial \tau_s}{\partial r} \approx (\tau_\varphi(0) - \tau_s(0))/r \tag{4.47}$$

for small r. The non-vanishing difference of the tensions causes an $1/r$-divergence of the derivative of τ_s, and thus a logarithmically divergence $\tau_s \propto -\ln r$. That is a contradiction to the finiteness of the tensions. With the isotropy of the tensions, the constitutive relations also directly give

$$\lambda_s(s_0 = 0) = \lambda_\varphi(s_0 = 0), \tag{4.48}$$

but these stretch factors do not necessarily have to be finite. If the stretches at the capsule's pole are isotropic and finite, i.e. $\lambda_s(0) = \lambda_\varphi(0) < \infty$, then l'Hôspital's rule can be applied on λ_φ at the pole:

$$\lambda_\varphi(0) = \lim_{s_0 \to 0} \frac{r}{r_0} = \lim_{s_0 \to 0} \frac{r'}{r_0'} = \frac{\lambda_s \cos(\psi(0))}{\cos(\psi_0(0))} = \lambda_s(0)\cos(\psi(0)). \tag{4.49}$$

In the last step, $\psi_0(0) = 0$ in the spherical rest shape has to be used. The isotropy of the stretches then requires $\psi(0) = 0$, which forbids a sharp cone. So, the only way out are

diverging stretch factors. Then l'Hôspital's rule must not be applied and in the vicinity of the tip, we can write

$$\lambda_s(s_0) \approx \lambda_\varphi(s_0) \approx \text{const}\, s_0^{-\eta}, \quad \text{for} \quad s_0 \approx 0 \tag{4.50}$$

with an exponent $\eta > 0$. From $\lambda_s = r'/\cos\psi$ it follows

$$r(s_0) \approx \text{const} \cdot \frac{s_0^{1-\eta}\cos(\psi(0))}{(1-\eta)} \quad \text{for} \quad s_0 \approx 0. \tag{4.51}$$

In the spherical rest shape, we have $r_0(s_0) = R_0 \sin(s_0/R_0) \approx s_0$. With these two radial coordinates, we can express λ_φ as

$$\lambda_\varphi(s_0) = \lim_{s_0\to 0} \frac{r}{r_0} = \text{const} \cdot \frac{s_0^{-\eta}\cos(\psi(0))}{(1-\eta)} = \lim_{s_0\to 0} \frac{1}{1-\eta}\frac{r'}{r_0'} = \lambda_s(s_0)\frac{\cos(\psi(0))}{1-\eta} \tag{4.52}$$

which now replaces eq. (4.49). In the second to last step, $r_0' \approx 1$ was used to artificially introduce r_0'. From the required isotropy $\lambda_s(s_0) \approx \lambda_\varphi(s_0)$, we get the condition

$$\eta = \cos(\psi(0)) - 1 = \sin\alpha - 1, \tag{4.53}$$

a relation between the divergence exponent η and the half opening angle α of the cone.

In conclusion, we can state that the deformation of an elastic shell with a spherical rest shape is possible in principle, if the stretch factors are isotropic and diverging via

$$\lambda_s(s_0) \approx \lambda_\varphi(s_0) \sim s_0^{-\eta} \tag{4.54}$$

with an exponent η that is linked to the half opening angle of the cone via eq. (4.53). The elastic tensions in the tip then follow from the constitutive relations:

$$\tau_s(0) = \tau_\varphi(0) = \frac{Y_{2D}}{1-\nu}. \tag{4.55}$$

Although the stretch factors are diverging, the stretch energy as the area-integral over the strains remains finite, because (4.53) states $\eta > -1$.

In the numerical simulation, where the arc length s_0 has to be discretized, the stretches have to remain finite. But then we are forced to use the boundary condition $\psi(0) = 0$, which only allows a rounded pseudo cone. With a rounded tip, also the magnetic field and, therefore, the magnetic forces remain finite and can only support finite curvatures. These numerical drawbacks then possibly result in the previously mentioned oscillation of the fixed-point iteration. Such a boundary condition for a rounded cone was also used in the literature for the solution of the Laplace-Young equation for a ferrofluid drop [85, 87, 88].

The (nearly) divergent behavior of the stretch factor $\lambda_s(s_0)$ in the numerical simulation is shown in fig. 4.6. The left diagram (a) shows λ_s from the pole to the equator for the spheroid with $a/b = 2$ (red curve, nearly constant and already known from fig. 4.4) and for a pseudo conical shape with $a/b = 5.34$ (note that the scale for the conical curve is logarithmic). It is clearly visible that (although it ends in a finite value) λ_s shows a kind of nearly divergent behavior near the tip. Figure 4.6 (b) then presents a zoom to the vicinity of the tip near $s_0 = 0$ with a logarithmic scale for s_0. There, the assumed power law (4.54) becomes clearly visible for the conical shape. A fit of the numerical data states $\lambda_s \approx 0.651 s_0^{-0.562}$, so we have a numerically estimated exponent of $\eta_{\text{num}} = 0.562$. The contour line $z(r)$ of the conical tip of the corresponding shape is shown in fig. 4.6 (c). There, we can estimate an opening angle of about $\alpha \approx 25°$. Over the relation (4.53), this angle is related to an exponent of $\eta = 0.577$.

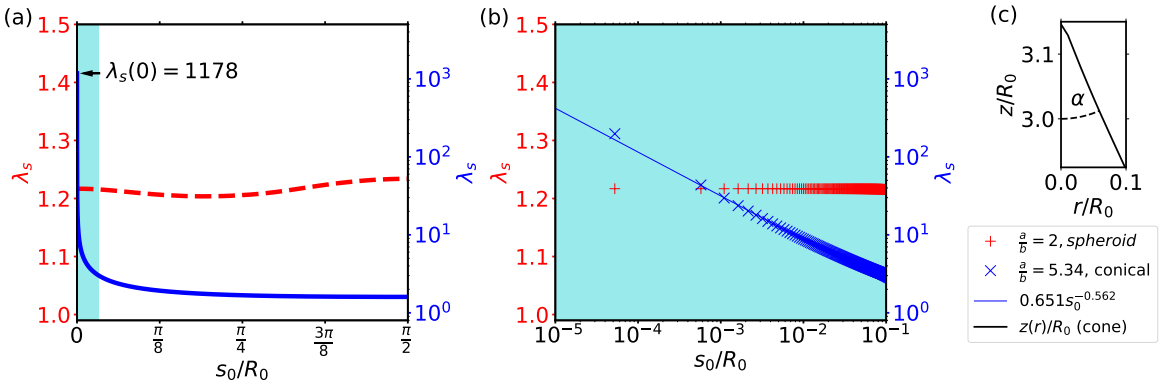

Figure 4.6.: (a): Stretch factors in the meridional direction $\lambda_s(s_0)$ following the whole contour line from the south pole ($s_0 = 0$) to the equator ($s_0/R_0 = \pi/2$) for a capsule with $Y_{2D}/\gamma = 100$ and $\chi = 21$. The left scale (red dashed line) gives almost constant stretch factors for a spheroidal shape with $a/b = 2$ (same curve as shown in fig. 4.4). The right scale (blue solid line) gives a nearly diverging stretch factor for a conical shape with $a/b = 5.34$. (b): Logarithmic plot of $\lambda_s(s_0)$ near the tip for $s_0/R_0 < 10^{-1}$. The colored area in the diagram (a) represents the region shown in (b). The function $\lambda_s(s_0) = \text{const} \cdot s_0^{-\eta}$ (see eq. (4.50)) was fitted to the data of the conical shape, which gave $\eta = 0.562$, corresponding to an angle of $\alpha = 25.98°$ in eq. (4.53). (c): Zoom into the tip of the contour line $z(r)$ for the conical shape. The half opening angle is $\alpha \approx 25°$. This is a modified version of a figure that has already been published in ref. [147].

That underlines impressively the agreement between the theoretical thoughts about a real sharp cone and the numerical results for a rounded pseudo cone.

After all, these results also show that a conical shape of an elastic capsule is only possible in theory. A real capsule would quickly suffer from a rupture at the tip, because no material can resist such high stretch factors. Typical alginate materials can only support stretch factors of about $\lambda \approx 1.2$ before they take irreversible damage. And even materials that are developed in order to resist very high stretching, like highly stretchable hydrogels, cannot go beyond $\lambda \approx 20$ [137]. Our elastic model here uses a non-linear Hookean law that becomes invalid for higher stretch factors and the usage of a more suited material law is advised. Nevertheless, very high stretch factors at the tip are a robust feature that should always appear, independently of the actual material law. This is underlined by the fact that such rupture events at the capsule's tip were already observed in experiments with dielectric capsules in electric fields in ref. [70].

In conclusion, that means that conical shapes of elastic capsules are only of theoretical interest and the transition to the conical shape provides an interesting tool for the controlled destruction of the capsule's shell as long as the fluid can be magnetized or polarized enough.

4.3.3. Critical Bond numbers

In the following, the meridional stretch factor λ_s shall be introduced as an order parameter giving us the possibility to clearly detect the transitions between a spheroidal and a conical shape and vice versa. This allows a precise investigation of the region of hysteresis, especially for a comparison between drops and purely elastic systems.

Stretch factors as a distinct order parameter

In the previous section, it was shown that the stretch factors diverge in a real conical tip. In the numerical simulation, we cannot have a real cone due to finite stretches as a result of the

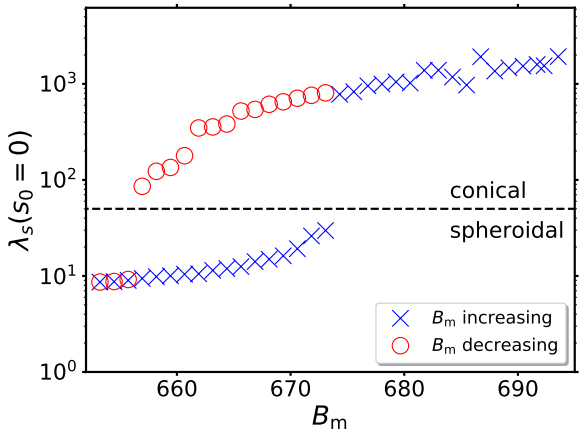

Figure 4.7.: Meridional stretch factor λ_s at the capsule's pole ($s_0 = 0$) as a function of the Bond number B_m for $Y_\mathrm{2D}/\gamma = 100$ and $\chi = 21$. The stretch factor clearly exhibits a jump at the locations of the discontinuous shape transition and shows a hysteretic behavior. Crosses denote increasing Bond numbers while circles represent decreasing B_m. The data of this diagram have already been published in ref. [147].

discretization. Nevertheless, although being finite, the stretch factors feature a very strong increase in the capsule's (rounded) tip. Since the transition into a conical shape is easy to detect with the elongation a/b for a ferrofluid drop and weak elastic systems, but difficult to see in purely elastic systems, it is a better idea to consider one of the stretch factors at the capsule's pole in order to distinguish between a spheroidal and a conical shape. For example, a capsule with $Y_\mathrm{2D}/\gamma = 100$ and $\chi = 21$ proceeds a rather small jump from $a/b = 5.2$ to $a/b = 5.35$ at the spheroidal to conical transition for increasing Bond numbers. On the other hand, fig. 4.7 shows the behavior of the stretch factors at the poles as a function of B_m near the region of hysteresis. After a moderate increase of the stretch factor in the spheroidal shape (which was already visible in fig. 4.4 at $s_0 = 0$), there is suddenly a jump of almost two orders of magnitude at the transition point. When the Bond number is decreased again (red circles), $\lambda_s(s_0 = 0)$ is quickly reduced, but still jumps down by a factor of about 10 at the transition point back to the spheroidal shape. In conclusion, we are able to clearly distinguish the position of both discontinuous transitions by considering the stretch factors directly at the capsule's pole. With that knowledge, we can define a clear transition criterion. A shape transition occurs if

$$\lim_{\Delta B_\mathrm{m} \to 0} |\lambda_s(s_0 = 0, B_\mathrm{m}) - \lambda_s(s_0 = 0, B_\mathrm{m} + \Delta B_\mathrm{m})| > 0. \tag{4.56}$$

For ferrofluid drops, this criterion is not applicable. There we have to use the elongation a/b in a similar way, which is not a problem since the elongation of a drop proceeds clearly visible jumps at the transitions, as it can be seen in fig. 4.3.

Extent of the hysteresis region

In order to investigate the size of the hysteresis region and the positions $B_\mathrm{m,c1}$ and $B_\mathrm{m,c2}$ of the shape transitions, we have to change B_m systematically in small steps ΔB_m. In practice, values from $\Delta B_\mathrm{m} = 0.005$ for $Y_\mathrm{2D}/\gamma < 1$ up to $\Delta B_\mathrm{m} = 0.5$ for $Y_\mathrm{2D}/\gamma = 100$ are feasible. For higher values of Y_2D/γ, bigger steps ΔB_m can be chosen, because $B_\mathrm{m,c1}$ and $B_\mathrm{m,c2}$ grow approximately linearly with Y_2D/γ. Positive values of ΔB_m (increasing Bm) are needed for the detection of $B_\mathrm{m,c2}$, while negative steps are a requirement to detect the transition from the conical shape back to the spheroidal one at $B_\mathrm{m,c1}$. The results of the search for the critical Bond numbers are shown in figure 4.8 for the susceptibility of $\chi = 21$. The left diagram (a) shows $B_\mathrm{m,c1}$ and $B_\mathrm{m,c2}$ for a ferrofluid drop and for weak elastic systems with $Y_\mathrm{2D}/\gamma < 0.05$. There is a nearly linear increase in both critical Bond numbers. That is not surprising as the increasing elasticity represents an additional resistance, which requires a stronger magnetic field to counter. More interesting is the prediction of the transition points

by the spheroidal energy minimization. They can be found as the extrema of the curve $\mathrm{V_m}(k)$, eq. (4.41). The predicted values for $B_{\mathrm{m,c2}}$ in the case of a drop and very weak shells are very precise, confirming again that the spheroidal approximation is a very good approximation for a droplet. On the other hand, as it was already indicated in the $(a/b, B_{\mathrm{m}})$-plane in fig. 4.3, the prediction of $B_{\mathrm{m,c1}}$ completely fails for reasons that were already mentioned above. The consequence is, that the approximative energy minimization for spheroidal shells does not predict a transition for $Y_{\mathrm{2D}}/\gamma \gtrsim 0.15$, which is in a massive contrast to the numerical data. The numerical solutions clearly show conical shapes for all values of Y_{2D}/γ.

In order to consider the interplay between $B_{\mathrm{m,c1}}$ and $B_{\mathrm{m,c2}}$ for an increasing shell strength, we can define the relative size of the hysteresis loop:

$$\Delta B_{\mathrm{m,c}} \equiv 2(B_{\mathrm{m,c2}} - B_{\mathrm{m,c1}})/(B_{\mathrm{m,c2}} + B_{\mathrm{m,c1}}). \tag{4.57}$$

Figure 4.8 (b) shows this relative size as a function of the ratio Y_{2D}/γ on a logarithmic scale. While the spheroidal approximation predicts a quick decrease to zero, the numerical data show an initially much larger relative hysteresis size, which decreases slightly for stronger shells. It never vanishes but converges to a plateau value. While the numerical results for $B_{\mathrm{m,c2}}$ can be treated as quite precise, caution is needed with the values for $B_{\mathrm{m,c1}}$ and $\Delta B_{\mathrm{m,c}}$ as they clearly seem to depend on the discretization. In both diagrams, the blue data points represent calculations with the standard discretization, that is also used for every other calculation in the context of homogeneous external fields, $l_0 = 0.1$ in eq. (3.64). The red points correspond to $l_0 = 0.2$ and show noticeable deviations, especially for higher Y_{2D}/γ.

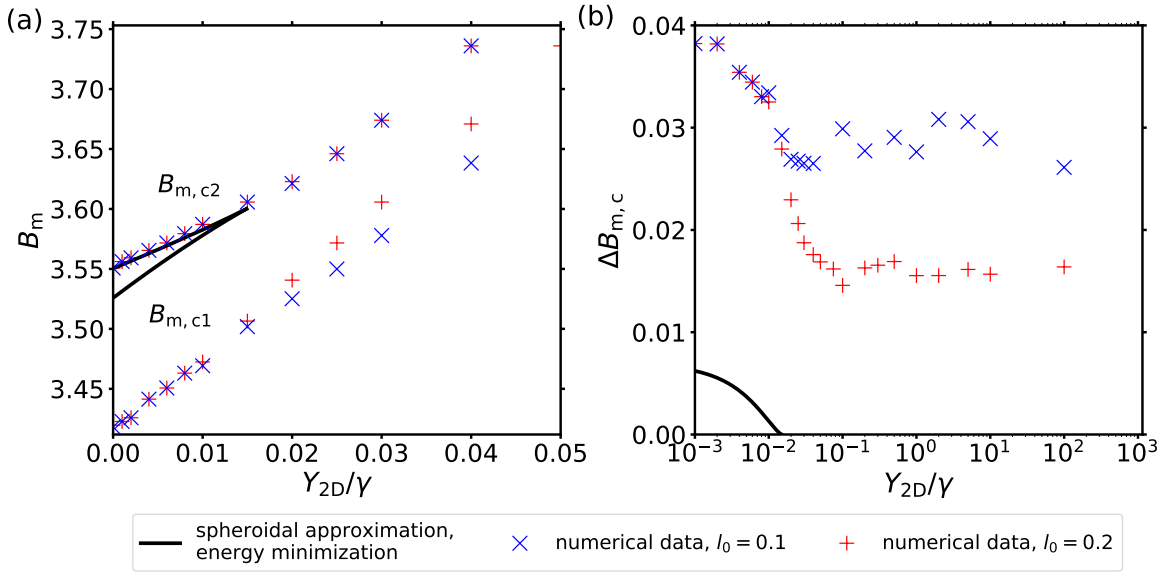

Figure 4.8.: (a): Critical Bond numbers $B_{\mathrm{m,c1}}$ (lower data points) and $B_{\mathrm{m,c2}}$ (upper data points) for varying Y_{2D}/γ with $\chi = 21$. The solid lines describe the prediction by the approximative energy minimization for spheroidal shapes. Both critical Bond numbers increase nearly linearly for increasing Y_{2D}/γ. In the region $B_{\mathrm{m,c1}} < B_{\mathrm{m}} < B_{\mathrm{m,c2}}$, there are hysteresis effects in the spheroidal-conical shape transition. (b): Relative size $\Delta B_{\mathrm{m,c}}$ of the hysteresis area for a wider range of Y_{2D}/γ. This is a modified version of a figure that has already been published in ref. [147].

Discretization errors

The discretization of the magnetic field calculation is a critical topic for the observation of a transition into a conical shape. In principle, a high resolution near the capsule's pole is needed in order to be able to resolve the high field strength in the tip. For a fixed number of $n_\mathrm{B} = 250$ boundary elements, the density of elements near the tip can be varied by changing the parameter l_0 in the relation (3.64). Different values of l_0 lead to a quite different numerical behavior. The difference between $l_0 = 0.1$ and $l_0 = 0.2$ was already shown above. If l_0 is lowered to significantly smaller values below 0.1, in order to improve the precision of the field calculation, then the resulting conical shapes cannot be calculated. There is an obvious transition at $B_\mathrm{m} = B_\mathrm{m,c2}$, but the shooting method that solves the system of the shape equations does not find a solution anymore. The problem are rapidly changing and extremely high stretch factors ($\lambda_s(s_0 = 0) > 10^4$). On the other hand, if l_0 is increased for example to $l_0 = 1$, which represents a constant element density on the boundary, there is no shape transition anymore and the capsule's shape stays nearly spheroidal. The resolution of the magnetic field calculation is then too low to resolve the high field strength in the small vicinity of the pole that is needed for the nearly conical tip. After all, the discretization of the magnetic field calculation is a key subject for the observation of the conical shape transition and strongly influences the resulting numerical values. In contrast, the spheroidal shape is very robust towards changes of the discretization and results related to that shape can be considered as being very precise.

4.3.4. Critical susceptibility

The question whether a transition from a spheroidal to a conical shape can occur for a given susceptibility χ was intensively discussed in the literature for ferrofluid and dielectric drops. Only with χ being above a critical susceptibility, $\chi > \chi_\mathrm{c}$, a discontinuous transition may be observed [1, 8, 87]. A theoretical approach in ref. [93] found a critical susceptibility $\chi_\mathrm{c} = \mu_\mathrm{c}/\mu_\mathrm{out} - 1 \approx 16.59$. Below that value, no conical shape can exist. In ref. [135], a slender-body approximation led to $\chi_\mathrm{c} = 16e/3 \approx 14.5$. The approximative energy minimization for a spheroidal shape, which was introduced by Bacri and Salin in ref. [8], gives $\chi_\mathrm{c} \approx 19.8$ for a simple ferrofluid drop. In numerical studies, a range from $\chi_\mathrm{c} \approx 19$ to $\chi_\mathrm{c} \approx 19.5$ was observed [150]. The question now is whether these results for simple drops can be transferred to elastic systems or not.

The elastic expansion of the approximative energy minimization, which was presented in sec. 4.2.3, completely fails in the prediction of χ_c except for the limit case of a drop. It predicts a strongly increasing χ_c, which already exceeds $\chi_\mathrm{c} = 21$ for $Y_\mathrm{2D}/\gamma = 0.015$, and that drastically contradicts the numerical results of the shape equations. The reason is found in the false assumptions about the elastic behavior that weight more, the higher the ratio Y_2D/γ is.

Therefore, we use another approach here. In a conical tip, the magnetic field diverges. The exact type of the divergence is set by the electromagnetic boundary conditions and determined by the equation [93, 120]

$$P_\zeta(\cos\alpha)P'_\zeta(-\cos\alpha) + (\chi+1)P_\zeta(-\cos\alpha)P'_\zeta(\cos\alpha) = 0. \tag{4.58}$$

P_ζ represents the Legendre function of the first kind. The magnetic field in the tip can then diverge with $H \propto r^{\zeta-1}$. The crucial point is now to recognize that the elastic tensions $\tau_s(0)$ and $\tau_\varphi(0)$ are finite in the tip due to the non-linear constitutive relations, as it was already discussed in sec. 4.3.2. Therefore, the magnetic field has to diverge with the same $\zeta = 1/2$ as it does in the case of a simple drop. The curvature κ_φ diverges with $\kappa_\varphi \propto r^{-1}$ and in relation with a finite surface tension and a finite elastic tension, this has to be balanced by

the magnetic stress via $f_\mathrm{m} \propto H^2 \propto r^{-1}$. That means eq. (4.58) is exactly the same as it is for a ferrofluid drop and, therefore, leads to the same $\chi_\mathrm{c} \approx 16.59$.

In conclusion, we can state that the finite tension in the tip is the reason for the critical electromagnetic behavior of the capsule being identical to that of a drop. Therefore, all results that were gained about the critical behavior of a drop also apply for an elastic capsule filled with a ferrofluid or dielectric liquid. To underline that, for $\chi = 21$ (this value was chosen to be slightly but certainly above χ_c) we find numerically a transition to a conical shape for every ratio $Y_\mathrm{2D}/\gamma \in [0, \infty]$.

On the other hand, the critical behavior of the capsule is very prone to the constitutive relation of the underlying elastic model. If the elastic tensions in the tip also diverge, then their divergence behavior modifies the divergence of the magnetic field and thus determines another χ_c.

4.4. Wrinkling

It was already visible in fig. 4.1 and in fig. 4.3 that wrinkling effects have a noticeable effect on the elongation of a ferrofluid-filled capsule in a uniform magnetic field. This effect is easy to understand. Wrinkles occur when the total hoop stress becomes negative, $\tau_\varphi + \gamma < 0$, see also the presentation of the modified shape equations in sec. 3.1.6. Then the formation of wrinkles reduces the compressive stretching energy. This energy is then available for an additional elongation of the elastic shell at the same magnetic field strength. This additional stretching leads to noticeable deviations from a spheroidal shape and is also visible in the comparison of the contour lines in fig. 4.2. Now the question arises in which systems wrinkles appear and how far they are extended.

4.4.1. Linear response predictions

In order to analyze the existence and the extent of wrinkled regions on the capsule's surface, we start again with the linear response regime, because the linear theory that we developed in sec. 4.2.1 also allows some predictions about wrinkling effects. In the linear response regime, we operate close to a spherical shape and, therefore, spherical coordinates are advised. The size of the wrinkled region can be characterized in terms of the polar angle θ. The angle θ_w denotes the smallest polar angle where the wrinkling condition $\tau_\varphi(\theta_\mathrm{w}) + \gamma = 0$ is satisfied. That means $\theta_\mathrm{w} = \pi/2$ corresponds to wrinkles starting only at the equator, which is equivalent to the complete absence of wrinkles in the system. On the other side, $\theta_\mathrm{w} = 0$ describes a system with a maximum extent of wrinkles, from pole to pole. This wrinkle angle is directly related to the length of the wrinkles L_w via $L_\mathrm{w} = (\pi - 2\theta_\mathrm{w})R_0$ (see also the illustration in fig. 3.4). To calculate θ_w, we need a closed expression for τ_φ first. Therefore, we use the normal and the tangential force equilibrium, eqs. (4.13) and (4.17) and get

$$\tau_\varphi = \frac{Y_\mathrm{2D}}{(1-\nu^2)R_0}\left(u_\theta \cot\theta + (1+\nu)u_\rho + \nu\frac{\partial u_\theta}{\partial\theta}\right). \tag{4.59}$$

Using the obtained solution for u_ρ and u_θ, we find

$$\tau_\varphi \approx B\frac{1-\nu^2}{5+\nu}\left(-\frac{5}{3} + 3\cos^2\theta\right) \tag{4.60}$$

with the constant B, that we already know from eq. (4.20). Substituting the result for τ_φ into the wrinkling condition then finally leads to

$$\cos^2\theta_\mathrm{w} = \frac{5}{9} - \frac{\gamma R_0}{Y_\mathrm{2D}B}\frac{5+\nu}{3} = \frac{5}{9} - \frac{4(3+\chi)^2}{27\chi}\frac{1+(5+\nu)\gamma/Y_\mathrm{2D}}{B_m}. \tag{4.61}$$

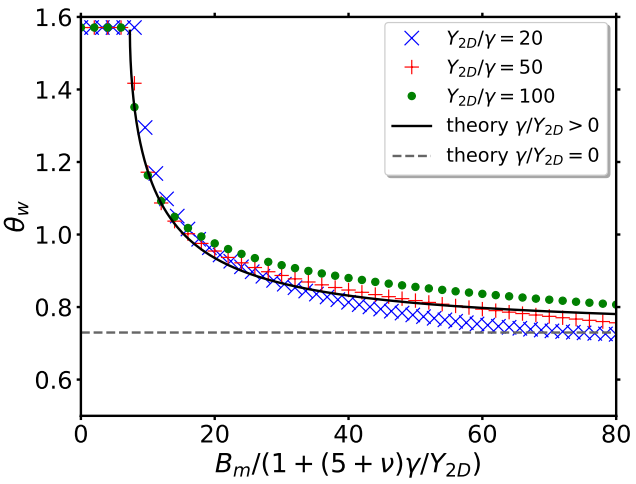

Figure 4.9.: Extent of the wrinkled region expressed by the polar angle θ_w as a function of $B_m/(1+(5+\nu)\gamma/Y_{2\mathrm{D}})$. The general linear response result (4.61) is given by the black solid line and the dashed line shows the asymptotic result $\cos^2\theta_\mathrm{w} = 5/9$ for large values of $B_m/(1+(5+\nu)\gamma/Y_{2\mathrm{D}})$ or purely elastic systems with $\gamma = 0$. The crosses and circles denote numerical data points for different values of $Y_{2\mathrm{D}}/\gamma$. Note that numerical data for a purely elastic system cannot be displayed here due to the definition of B_m in equation (4.4). The data of this diagram have already been published in ref. [147].

Analyzing this result quickly leads to a very interesting phenomenon. We find a universal extent of the wrinkled region with $\cos^2\theta_\mathrm{w} = 5/9$ in a purely elastic system, with $\gamma = 0$. Neither the elongation nor the magnetic field have an influence on the wrinkles then. In addition, $\cos^2\theta_\mathrm{w} = 5/9$ is also the limit value for large values of $B_\mathrm{m}/(1+(5+\nu)\gamma/Y_{2\mathrm{D}})$. But on the other hand it should be kept in mind that the linear response theory is only valid for small elongations with $B_\mathrm{m}/(1+(5+\nu)\gamma/Y_{2\mathrm{D}}) \ll \chi Y_{2\mathrm{D}}/\gamma$. Figure 4.9 shows a comparison between the linear response results and numerical data from the shape equations (3.28) and (3.30). For small Bond numbers, there is no wrinkling ($\theta_\mathrm{w} = \pi/2$). Then, the point where wrinkling occurs for the first time is very precisely predicted by the linear response theory and also beyond that point, the deviations are quite small at first. Only for higher values of the reduced Bond number, more deviations become visible, which is not surprising due to the limited range of validity of the linear response theory.

The very good agreement between the theory and the numerical data for the first occurrence of the wrinkles offers the possibility to determine unknown parameters of the capsule-ferrofluid system. In the following, a proposal for an experiment that is able to measure the Young modulus $Y_{2\mathrm{D}}$ and the surface tension γ simultaneously shall be given.

Experimental measurement of $Y_{2\mathrm{D}}$ and γ via wrinkling

The basic idea to determine $Y_{2\mathrm{D}}$ and γ is to use the information provided by the formation of the wrinkles. The capsule is elongated into a spheroidal shape and the elongation $(a/b)_{\theta_\mathrm{w}=\pi/2}$ where wrinkles are formed for the first time provides information about the relation between $Y_{2\mathrm{D}}$ and γ. Together with the knowledge of the external forces that led to that elongation, both parameters can be calculated using the linear response theory. In sec. 4.2.1, the elongation of the capsule in the linear regime was found to be

$$\frac{a}{b} = 1 + \frac{9(5+\nu)\mu_0 R_0 \chi H_\mathrm{ext}^2}{8(3+\chi)^2(Y_{2\mathrm{D}} + (5+\nu)\gamma)}. \tag{4.62}$$

This equation can be rearranged to

$$Y_{2\mathrm{D}} = g\left(\frac{a}{b}\right) - (5+\nu)\gamma \tag{4.63}$$

with

$$g\left(\frac{a}{b}\right) = \left(1 + \frac{9(5+\nu)\mu_0 R_0 \chi^2 H_\mathrm{ext}^2}{8(3+\chi)^2}\right)\left(\frac{a}{b}\right)^{-1}. \tag{4.64}$$

In the moment, when wrinkles appear for the first time, we have $\theta_\mathrm{w} = \pi/2$. Consequently, eq. (4.61) states

$$0 = \frac{5}{9} - \frac{4(3+\chi)^2}{27\chi^2\mu_0 R_0 H_\mathrm{ext}^2}\gamma\left(1 + (5+\nu)\frac{\gamma}{Y_\mathrm{2D}}\right). \tag{4.65}$$

So, we have a system of two equations and two unknown parameters Y_2D and γ. This system has the solution

$$\gamma = g\left(\frac{a}{b}\right)_{\theta_\mathrm{w}=\pi/2}\left[(5+\nu) + \frac{4(3+\chi)^2}{15\chi^2\mu_0 R_0 H_\mathrm{ext}^2} g\left(\frac{a}{b}\right)_{\theta_\mathrm{w}=\pi/2}\right]^{-1}, \tag{4.66}$$

$$Y_\mathrm{2D} = g\left(\frac{a}{b}\right)_{\theta_\mathrm{w}=\pi/2} - (5+\nu)\gamma. \tag{4.67}$$

This method can also be applied to non-magnetic systems, as long as the external forces are of the same form as the magnetic forces that are exerted by the ferrofluid. An important example is a spinning capsule experiment, where a capsule is deformed by its own rotation in an external fluid of higher density [111, 115, 143]. This type of experiment provides the same pattern of forces as the magnetic deformation (see the more detailed discussion in section 5.3.5). If the existence of the wrinkles can be determined (for example with the help of light scattering methods), we have an additional tool to measure the interfacial tension between the fluid and the elastic shell as well as the Young modulus itself. When the Poisson ratio ν is also unknown, only a second experiment, like a capsule compression experiment, which is explained in section 5.3.4, is needed. Then a system of three unknown parameters (Y_2D, γ and ν) with three equations has to be solved.

After all, this method is only applicable for small elongations, as it is based on the linear response theory. Another consequence is, that the surface tension must not be too strong, as a high surface tension prevents the formation of wrinkles, especially in the linear regime, which is presented in the next section.

4.4.2. Extent of the wrinkled region

In the following, an investigation on the numerically determined wrinkle length L_w that goes beyond the linear response shall follow. In order to do that, we calculate the shape of capsules for different ratios Y_2D/γ. The magnetic field is increased in small steps so that we effectively increase the elongation a/b that way. After calculating the equilibrium shape in each step, we evaluate the elongation and the wrinkle length. This allows the calculation of the diagram that is shown in fig. 4.10. There, the relative wrinkle length L_w/L is shown as a numerical function of the elongation a/b, still for a fixed susceptibility of $\chi = 21$. The first obvious result that can be extracted from the diagram is that there are no wrinkles ($L_\mathrm{w} = 0$) for $Y_\mathrm{2D}/\gamma \lesssim 8.93$. It is completely indifferent, how strong the capsule is elongated, the negative hoop stress in the equator region never succeeds the surface tension causing the appearance of wrinkles to be impossible. On the other hand, if we consider a purely elastic system with $\gamma = 0$ (blue curve), we see the quick formation of long wrinkles, even for very small elongations close to the spherical reference shape. Indeed, that is not surprising since we have no barrier for the wrinkling in that case and even an infinitesimal small elongation leads to negative stresses in the equator region and thus to wrinkling effects. Of course, a real system would show a small barrier due to the small but finite bending energy. With increasing surface tension γ, higher elongations are needed to achieve wrinkles. Wrinkling effects only appear beyond the linear response regime for about $Y_\mathrm{2D}/\gamma \lesssim 15$. With that knowledge, we can state that the linear response relation (4.61) is only useful for sufficiently high ratios Y_2D/γ, which limits the applicability of the experiment presented in the previous section.

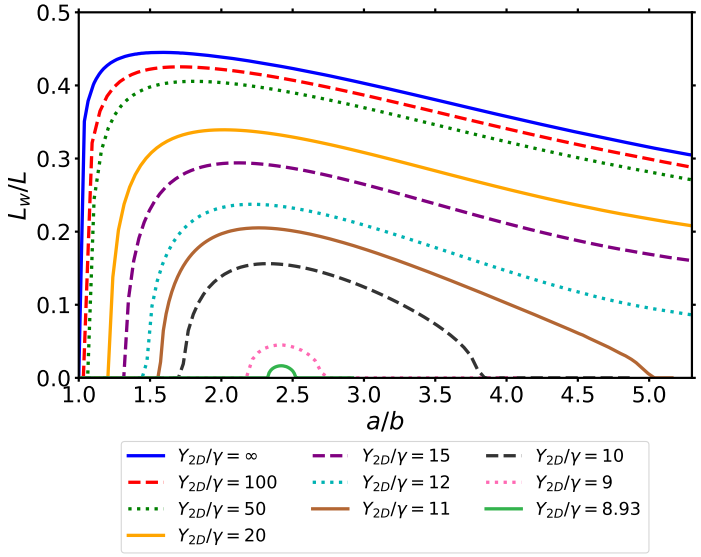

Figure 4.10.: Relative wrinkle length L_w/L as a function of the elongation a/b for spheroidal capsules with a fixed susceptibility $\chi = 21$ and different ratios of Y_{2D}/γ. There are no wrinkles ($L_w/L = 0$) for $Y_{2D}/\gamma \lesssim 8.93$. The range of $L_w/L > 0$ and the extent of wrinkles increase with Y_{2D}/γ until they converge to an asymptotic curve for purely elastic shells without an interfacial tension. The data of this diagram have already been published in ref. [147].

As soon as wrinkles appear, they nearly immediately develop a remarkable length and the maximum of the relative length L_w/L is achieved for only slightly higher elongations. When the capsule is stretched even more, then the wrinkles start to become shorter again. With lower ratios Y_{2D}/γ, they even disappear completely. The reason for this effect can be found in the transverse strain, which is related to the Poisson number ν. The more the capsule is elongated and stretched in meridional direction, the more it tends to shrink in circumferential direction. Then, at a distinct point, the negative hoop stress at the equator, $\tau_\varphi(\pi/2)$, becomes that small, that the wrinkling condition is not fulfilled anymore and there is no energy gain in the formation of wrinkles. Figure 4.10 was calculated with a fixed susceptibility of $\chi = 21$. It can be expected, that the diagram looks very similar for other values of χ. The reason is simple: In theory, the susceptibility does not affect the actual shape of the capsule, since the force pattern stays the same. The elongated capsules are always nearly spheroidal. Only the field strength that is needed to achieve the specific elongation changes. Therefore, no influence of χ on the wrinkles is to be expected, as long as no shape transition occurs. In order to underline that statement, fig. 4.11 shows the critical ratio Y_{2D}/γ, where wrinkles occur for the first time, as a function of the susceptibility χ. With our standard value $\chi = 21$, we found wrinkles for the first time at the ratio $Y_{2D}/\gamma \approx 8.93$. Even if χ is varied over a wide range, that ratio only changes slightly and thus it can be assumed to be nearly constant, as it was expected.

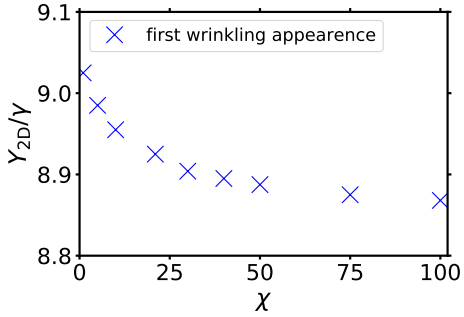

Figure 4.11.: Critical ratio Y_{2D}/γ where wrinkles occur for the first time (at an arbitrary elongation a/b) as a function of the susceptibility of the ferrofluid. The nearly constant behavior underlines the statement about the independence of wrinkles from the susceptibility for spheroidal shapes.

4.5. Conclusion

In this chapter, we investigated the deformation behavior of an elastic capsule that is filled with a ferrofluid with a linear magnetization law and is placed in a homogeneous external magnetic field. Starting from a spherical reference shape, the capsule was deformed into a prolate spheroid in the same way as it is known from simple ferrofluid or dielectric drops. To reach the same elongation, just stronger external fields are needed, because the additional elastic forces have to be compensated.

An analytic approximation in the linear regime in sec. 4.2.1 yielded very precise predictions for the deformation, as long as the elongations did not become too big. This approximative model should be suited for many practical applications where only small elongations occur. In order to model medium elongations beyond the linear regime, the approximative energy minimization from sec. 4.2.3 should be used as it shows surprisingly precise results for elongations between about $a/b = 1.5$ and $a/b = 2.5$, which can be explained with the stretching factor λ_s in meridional direction being nearly constant in that range. For higher elongations, it is advised to use the numerical solution of the shape equations.

If the elasticity of the capsule's shell is dominating over the surface tension, we see the formation of wrinkles near the equatorial region of the capsule. The reduction of the elastic energy by the wrinkling allows the capsule to elongate even more in the same external field leading to noticeable deviations from the analytical predictions. Wrinkles only occur for elastically dominated capsules with $Y_{2D}/\gamma \gtrsim 8.9$ and were found to be nearly independent of the ferrofluid's susceptibility χ. If the wrinkles are already formed for smaller elongations, which is the case for about $Y_{2D}/\gamma \gtrsim 15$, then the linear response approximation is also able to predict the length of the wrinkles precisely. A measurement of the elongation where wrinkles appear for the first time provides a very interesting tool for an experimentalist to determine an additional capsule parameter, especially because it provides the possibility to measure two different parameters (like Y_{2D} and γ) within a single measurement. This procedure goes even beyond the magnetic or dielectric deformation and is applicable for every external force that is proportional to the square of the surface normal vector (leading to a nearly spheroidal shape), like the centrifugal forces in a spinning capsule experiment [111], for example.

For higher elongations, the numerical results of the shape equations with $\chi = 21$ show a discontinuous transition to a nearly conical shape. This transition occurs for every ratio Y_{2D}/γ, from a simple drop to a purely elastic system. The transition is difficult to recognize with the help of the elongation a/b, because the jump in a/b from the spheroidal shape to the nearly conical shape becomes quite small in purely elastic systems. The stretching factor $\lambda_s(s_0 = 0)$ at the capsule's pole is a much better suited control parameter, because the stretching factors at the pole show a divergence behavior in a conical shape. These very high stretching factors are a good justification to neglect the bending energy and to use only the reduced system of four shape equations. On the other hand, a conical shape should be impossible for a real capsule, because the elastic shell would rupture at the tip since no real material could support that high stretching factors. This effect could be an interesting tool for the distinct destruction of an elastic capsule in order to release an ingredient that was previously encapsulated. The description and prediction of such a rupture process would be a promising topic for future works. Such a rupture process shows some interesting analogies to the disintegration of dielectric drops in electric fields by the emission of fluid jets from the tip. Such jets are formed in high fields, because real fluids are neither perfect insulators nor perfect conductors, which causes tangential forces near the tip. Such effects were observed in experiments [145] as well as they are known in theory [33, 34]. An additional elastic shell around the fluid would prevent the formation of such jets at first, but the additional forces could support the destruction of the capsule.

Our numerical calculations use a rounded tip with $\psi(0) = 0$ as a boundary condition due

to numerical reasons. This is probably the primary source of the shape oscillations that were observed in the iterative solution scheme of the shape and the field calculation. Together with relevant discretization errors in the region of very high magnetic fields near the tip, the calculation of the exact shape of the capsule becomes quite inaccurate. This problem could be addressed to a certain degree by the usage of a more advanced mesh algorithm, such as an elliptic mesh generation, as it was presented in ref. [31]. An analytical investigation on the elastic model in sec. 4.3.2 showed that a real conical tip is in theory also possible with our non-linear Hookean elastic model, as it was observed for simple drops in uniform fields. The key property for the comparable behavior to a drop is the finite tension in the non-linear constitutive relations (3.11) and (3.12) when the stretches diverge. Consequently, the critical susceptibility χ_c, above which a transition to a conical shape can occur, stays the same as it is for a simple drop system. Future works could investigate the influence of more advanced elastic models for large strains [64] on the critical behavior.

A questionable point in the precision of the results for large deformations and especially conical shapes is the usage of a linear magnetization law. A larger range of validity is ensured if the fluid is highly magnetizable or polarizable with a large susceptibility.

5. Deformation of a real capsule in an inhomogeneous field

In the following chapter, we discuss and analyze an experimental realization of a ferrofluid-filled capsule in an external magnetic field. This experiment was developed and performed by E. Zwar from the chair for physical chemistry II (Professor H. Rehage) at the Technical University of Dortmund. The author of this thesis supported the experiment with theoretical advice and direct support during the measurements.

This experiment was also described in detail with a focus on the experimental and chemical properties (especially the new encapsulation system) in the PhD-thesis of E. Zwar [155] and was published in addition in ref. [148]. Here, we set the focus on the theoretical aspects of the experiment and the analysis of the results.

5.1. General concept

The main objective of the experiment was the development of a new system for the direct encapsulation of ferrofluids by sodium alginate, which allows strong deformations. Secondly, it provides a perfect opportunity to verify the presented model for a ferrofluid-filled capsule in a real system. In order to accomplish these tasks, some modifications to the theoretical system from the previous chapter are needed. In chapter 4, we discussed the deformation of linearly magnetizable capsules in a homogeneous external field. The main difference is, that we now use inhomogeneous fields. There are two simple reasons: First, much higher deformations can be achieved with inhomogeneous fields compared to homogeneous ones. This statement can be understood from the structure of the magnetic force density. In a homogeneous field, the capsule elongates into a spheroidal shape and the magnetization is also homogeneous. The deformation is driven by the M_n^2-term in eq. (3.38), while the first term, the field integral over the magnetization, is only an isotropic pressure. So, the deformation is limited by the saturation magnetization M_s. In an inhomogeneous field, on the other hand, the integral term provides the possibility to achieve forces that are only limited by the field gradient. The second argument for an inhomogeneous field is just a practical one. It is very difficult to prepare a ferrofluid capsule or also a simple drop in a completely force free state, otherwise the assumptions from the previous chapter are not valid anymore. The external magnetic field has to be perfectly homogeneous and also the gravity has to be countered exactly by the adjustment of the fluid's density. Therefore, an experiment with an inhomogeneous field is much easier controllable.

5.1.1. Experimental set-up

In an inhomogeneous field, a total force acts on a dipole in the direction of the field's gradient. The same effects occur for magnetizable or polarizable capsules. The normal forces on the

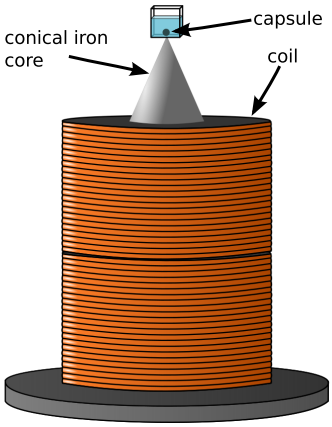

Figure 5.1.: Visualization of the experimental set-up. The ferrofluid-filled capsule (black dot) sits at the bottom of a glass cuvette and is surrounded by a non-magnetic liquid. The cuvette is placed directly above the tip of the conical iron core of a copper coil. This is a modified version of a graphic originally created by E. Zwar that was already published in refs. [148] and [155].

surface are stronger in regions of higher fields than in regions of a lower field strength, which results in a total force. Since we do not want to consider a dynamical experiment here, where friction effects come into play, we need a static counterforce. Therefore, we use a solid wall where the capsule is pushed against. In praxis, this is realized in the way that the capsule is placed in a non-magnetic glass cuvette, surrounded by a non-magnetic fluid with a lower density. The magnetic field is generated by a copper coil. In order to get as strong fields as possible and also very high field gradients over a short distance (the capsule with a size of about 1 mm is small compared to the coil), the field of the coil is amplified by a conical iron core. The cuvette is placed directly above the tip of the conical core, where the field strength and the field's gradient are maximal. Therefore, the gravity and the magnetic field gradient pull the capsule against the bottom of the cuvette. This set-up is visualized in fig. 5.1. It respects the axial symmetry that is a necessary condition in our elastic model.

5.1.2. Differences to the homogeneous set-up

Some significant differences to the discussion in the previous chapter follow from the usage of the inhomogeneous field as well as from the direct experimental conditions. First, there is no symmetry plane anymore that could be exploited in the numerics due to the inhomogeneous field of the coil. The only symmetry left is the rotational symmetry around the z-axis. Since the shape equations themselves are invariant in the z-direction, it is now much more intuitive to set the origin of the coordinate system to the lower pole of the capsule, where it contacts the cuvette. The coordinate system and the parametrization are visualized in fig. 5.2. The elongation a/b of the capsule also has to be redefined. The upper and the lower part of the capsule deform in a different way, so we define a as the total height of the capsule, which has its maximum at the symmetry axis. The equatorial radius also does not necessarily represent the width of the capsule. Therefore, we define b as the double of the maximum radial coordinate of the capsule, so the elongation a/b keeps its interpretation as the ratio between the height and the width.

In order to achieve a precise description of the ferrofluid, we now have to use a more general non-linear magnetization curve. The exact magnetization curve $M(H)$ of the ferrofluid that was used in the experiment is calculated in section 5.3.7. A direct mathematical consequence is that the equation system (3.53) in the finite element method is not linear anymore and its solution becomes more sophisticated. The magnetic Bond number B_m was motivated for homogeneous fields and is not a useful parameter anymore. In the following, we use SI units to describe the magnetic field.

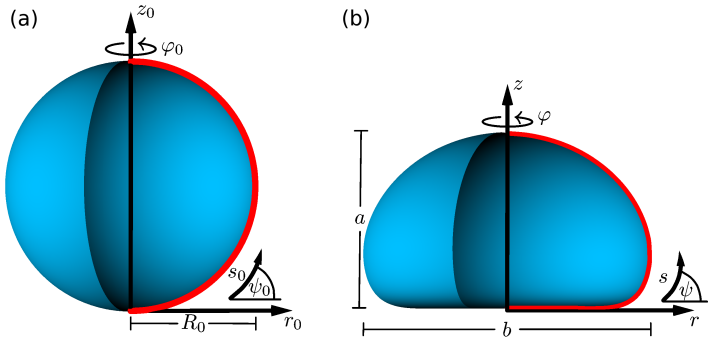

Figure 5.2.: Illustration of the parametrization in cylindrical coordinates (r_0, z_0, φ_0) for the spherical reference shape (a) and (r, z, φ) for a shape deformed in an inhomogeneous field (b). The two-dimensional contour lines with arc lengths s_0 and s are shown in red. The complete capsules are obtained by revolution of the contour lines, while the angles ψ_0 and ψ describe the slopes. The height of the capsule is called a, while b now denotes the width.

Calculation of the inhomogeneous field

If we want to calculate the total magnetic field that results from an inhomogeneous external field, we can basically use the method that was described in section 3.2. Besides the already mentioned effect that the FEM system becomes non-linear, we have to take a look at the BEM, especially at the integral equation (3.60):

$$cu_{\text{out}}(\boldsymbol{r}) - \int_0^L \left(u_{\text{out}}(\boldsymbol{r'})q^*_{\text{ax}}(\boldsymbol{r},\boldsymbol{r'}) - q_{\text{out}}(\boldsymbol{r'})u^*_{\text{ax}}(\boldsymbol{r},\boldsymbol{r'})\right) r'\mathrm{d}s' = u_{\text{ext}}(\boldsymbol{r}). \tag{5.1}$$

This equation is only exactly valid in the case of a uniform external field. In the more general case, we have [85]

$$\begin{aligned} cu_{\text{out}}(\boldsymbol{r}) - \int_0^L &\left(u_{\text{out}}(\boldsymbol{r'})q^*_{\text{ax}}(\boldsymbol{r},\boldsymbol{r'}) - q_{\text{out}}(\boldsymbol{r'})u^*_{\text{ax}}(\boldsymbol{r},\boldsymbol{r'})\right) r'\mathrm{d}s' \\ &= \int_{S_r} u^*_{\text{ax}}(\boldsymbol{r},\boldsymbol{r'})q_{\text{ext}}(\boldsymbol{r})\mathrm{d}S' - \int_{S_r} q^*_{\text{ax}}(\boldsymbol{r},\boldsymbol{r'})u_{\text{ext}}(\boldsymbol{r})\mathrm{d}S'. \end{aligned} \tag{5.2}$$

The integrals on the right side are taken over the surface S_r of a sphere with its center in $\boldsymbol{r}$ and with an infinitely large radius. In order to calculate our total magnetic field exactly, we cannot treat the external magnetic field as a property of the infinite space. In the inhomogeneous case, the source of the magnetic field lies inside of the outer domain, not infinitely far away. Therefore, a simulation of the complete system, the capsule, the coil and the iron core, would be necessary. That would be extremely work intensive in the numerical calculation and also create another source of errors, because the electromagnetic properties of the coil and its core have to be known exactly. In order to avoid these problems, we chose a much simpler, approximative way here. We use the fact that we are only interested in the field in a very small region, namely at the position of the capsule. We measure the real external magnetic field without the presence of a capsule in the region of the capsule and the cuvette. Then we search for a fitting function and interpret it to be infinitely expanded. With that function as a global external field, we use the homogeneous integral equation (5.1) for the field calculation. That is of course not exact, but sufficiently precise compared to other sources of errors in this experiment and the asymptotic behavior is even exact for high distances and low magnetizations.

Gravity

The density of the ferrofluid inside of the capsule and the density of the non-magnetic surrounding fluid are different in general. Therefore, the gravity causes a hydrostatic pressure $p_{n,\mathrm{h}}$ in the capsule, which has to be taken into account in the shape equations. It is another modification of the normal pressure [78]:

$$p_{n,\mathrm{h}}(s_0) = \Delta\rho g(z_{\max} - z(s_0)) = \Delta\rho g(z(s_0 = L_0) - z(s_0)). \tag{5.3}$$

The density difference between the ferrofluid and the outer fluid is given by $\Delta\rho$, while g represents the gravitational acceleration. Consequently, the capsule will be pushed against the bottom of the cuvette, even without a magnetic field, if the density of the ferrofluid is higher than that of the non-magnetic fluid.

5.2. Synthesis of the system

The heart of the ferrofluid are magnetite (Fe_3O_4) nanoparticles that were synthesized in a procedure described by Sun *et al.* [138]. A possible agglomeration of the particles is suppressed by an additional stabilization with surfactants that cause a steric repulsion. In our case, the surfactants are oleic acid and oleylamine. The coated magnetic particles are dispersed in a mixture of chloroform and 1-hexanol (7:3 by volume). The resulting mass concentration of the magnetite is $c_{\mathrm{m}} = 516\,\mathrm{g/mol}$.

The elastic capsule shell is created by an alginate gelation process. Calcium chloride is dissolved in the ferrofluid which causes the gelation of the alginate when it gets into contact with a sodium alginate solution. The addition of $1\,\%_V$ of each oleylamine and oleic acid can improve the gelation process. This process is started and controlled in the following way: A cylinder is filled up to 7/8 with a $1\,\%_m$ sodium alginate solution (green in fig. 5.3). This solution is overlaid with distilled water (light blue in fig. 5.3). A ferrofluid drop is then set into the water and sinks downwards. As soon as it reaches the alginate solution, the gelation process is started by the calcium chloride. This procedure prevents the ferrofluid drop from spreading due to the high portion of chloroform, which occurs on an interface between air and the sodium alginate solution. The developing capsule is prevented from getting into contact with a glass surface by rotating the cylinder. After 30 s, the gelation is stopped by washing the capsules with water. Finally, the capsules are stored in a saturated sodium chloride solution. This has the effect, that the elastic moduli are lowered to ensure an easier deformation [156]. The sodium chloride solution represents the non-magnetic outer fluid.

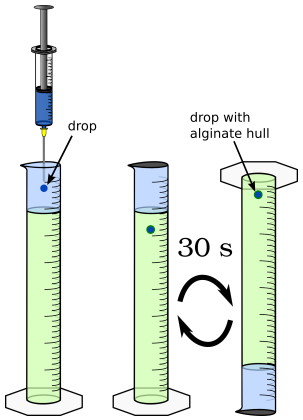

Figure 5.3.: Visualization of the gelation process for the production of an elastic shell around a ferrofluid drop. Green: $1\,\%_m$ sodium alginate solution, light blue: distilled water, dark blue: ferrofluid with calcium chloride. This is a modified version of a graphic that was originally created by E. Zwar and that was already published in refs. [148] and [155].

5.3. Estimation of the experimental parameters

If we want to compare the numerically simulated system with the real experiment, all parameters of the real system have to be known and must be measured in the real system. In detail, these are the elastic parameters, the Young modulus Y_{2D} and Poisson ratio ν and the geometrical parameters, the reference radius R_0 and the shell's thickness h. Necessary properties of the fluid are the density difference $\Delta\rho$ and the interfacial tension γ. Finally, the external magnetic field $\boldsymbol{H}_{\mathbf{ext}}$ as well as the magnetization curve have to be measured.

The capsule's size, especially the radius R_0 of the undeformed reference shape, can be measured from photographic images, the procedure is discussed in section 5.3.1. After that, the thickness h of the elastic shell is investigated in sec. 5.3.2. The density difference of the fluids was found to be $\Delta\rho = 0.24\,\mathrm{g/cm^3}$. The surface tension γ is discussed and estimated in section 5.3.3.

The elastic properties are calculated from the results of measurements with two different methods, because they cannot be determined independently. The first method, the *capsule compression* is presented and generalized for the usage together with an additional surface tension in the section 5.3.4. Then, the second method, the *spinning capsule* experiment, is shown and also generalized in section 5.3.5. If the Poisson ratio ν is known for a specific system, then both methods give Y_{2D}. Since ν is very difficult to determine, a generic value is often assumed in the literature [15, 90]. The combination of both methods offers the possibility to calculate both parameters simultaneously [89]. The measurement and fitting procedure of the magnetic field follow in section 5.3.6, while the magnetization curve is finally determined in section 5.3.7.

5.3.1. Volume and initial radius R_0 of the capsule

The measurement of the radius of the undeformed spherical capsule, R_0, is not a trivial task. After the polymerization process, the capsule is already deformed due to the gravity, even without a magnetic field. A simple, but relatively inaccurate method is to measure the height and the width of the capsule from a photographic image and to calculate the average of both quantities. This method is theoretically exact for an undeformed sphere and loses accuracy the more the capsule is deformed by the gravity. Since we already see noticeable deformations in the experiment without an external magnetic field, a more precise way is chosen here: We calculate the volume V_0 of the capsule from the photographic image with the help of a numerical integration. Then the initial radius of the sphere follows directly from

$$R_0 = \left(\frac{3}{4\pi}V_0\right)^{\frac{1}{3}}. \tag{5.4}$$

The determination of the volume works in the following way: We assume the capsules to be axisymmetric, which seems to be a very good approximation for the best capsules that could be produced. Then, the axial radius r_i is measured at different heights z_i. The total volume follows from the numerical integration over small cylindrical volumes:

$$V_0 = \pi \int r^2 \mathrm{d}z \approx \pi \sum_i r_i^2 (z_{i+1} - z_i). \tag{5.5}$$

Using that method, the volumes of the capsules can also be verified to be constant during the whole experiment.

5.3.2. The shell's thickness

Since the thickness h of the elastic shell was too small to be measured from photographic images or even by optical microscopy, scanning electron microscopy (SEM) measurements

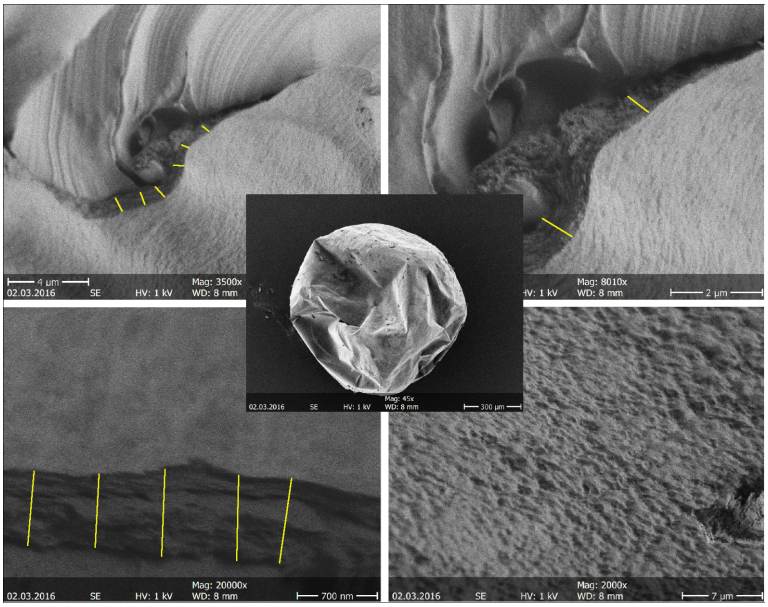

Figure 5.4.: SEM images of the elastic shell of broken capsules. The image in the center shows a complete capsule, while the bottom right image shows a zoom to the outer surface of the shell. The other images show cross sections of ruptured parts of the shell. The thickness was measured with the help of the yellow lines. This is a modified version of a graphic that was originally created by E. Zwar and that has already been published in ref. [148] and in parts in ref. [155].

had to be used. In order to avoid a bursting in the vacuum, the capsules had to be broken before the measurement. Figure 5.4 shows the resulting images from the measurement. Of course, a precise measurement of the thickness is not possible by an evaluation of the images. In addition to optical errors like parallax effects, there is another systematic source of errors. The SEM has to be performed in vacuum, that means that the elastic shell has to be brought into a dried unhydrated state. In this dried state the shell thickness was found to be around 600 nm. From measurements with thicker alginate capsules that could be resolved with optical microscopy, the swelling factor between the dried state and the hydrated state was found to be about five. That implies that our shell has a thickness of about 3 µm. Since the shell could not be resolved with optical microscopy, we can conclude that the thickness has to be below 5 µm, which is compatible with the SEM result. So, we use the value $h = (3 \pm 1)\,\mu\text{m}$, where the high relative error represents the uncertainties of this method.

5.3.3. Estimation of the surface tension

The interfacial tension γ is in fact an effective tension, because it is the sum of the interfacial tension between the ferrofluid and the elastic shell and the interfacial tension between the shell and the external fluid. This tension is very difficult to measure. A determination with the help of the formation of wrinkles was not possible due to the lack of the necessary equipment. In general, the interfacial tension between a solid and a liquid surface can be expected to be smaller than the tension at the interface between two liquids [104]. That implies that the effective surface tension should be smaller than the tension between the ferrofluid and the outer liquid, but on the other hand, the elastic shell probably has pores that lead to a partial liquid-liquid contact. Consequently, we expect the effective tension to be lower, but still comparable to the tension between the ferrofluid and the external liquid. The liquid-liquid interfacial tension of a similar system without magnetic nanoparticles was measured by a pendant drop tensiometry and yielded a value of 14.6 mN/m. The presence of the elastic shell of the capsule as well as the appearance of surfactants from the stabilized nanoparticles lower this value. In addition, Afkhami et al. have found an increasing interfacial tension of a ferrofluid for increasing external fields [1]. Therefore, we estimate an average value and expect $\gamma = (10 \pm 4)\,\text{mN/m}$ to be a valid average. The relative high error shall again represent the high uncertainty.

5.3.4. The capsule compression method

In the following, we discuss the first of the two methods used to find the two elastic parameters Y_{2D} and ν, the capsule compression method. In this method, a capsule is compressed between two parallel plates, as it is visualized in fig. 5.5. This is a well-known and often used method for the mechanical characterization of elastic capsules [26, 51]. The force F that is needed to compress the capsule is then recorded as a function of the displacement d. There are different ways to analyze this function. Here, we only use a fit of the linear regime in order to keep forces small. The reason is that it was shown previously in reference [39], that water leaks out of alginate capsules under compression and this effect shall be kept as small as possible. A theoretical model is needed now in order to describe the relation between the force F and the displacement d. Therefore, we use the model of Reissner, which describes the effect of a point force acting on the apex of a capsule [51, 122, 123]. The force as a function of the displacement in this model is given as

$$F = \frac{4Y_{2D}h}{R_0\sqrt{3(1-\nu^2)}}\, d. \tag{5.6}$$

Since a point force is a very rough approximation for a plate, this model is only valid for very small displacements. In addition, it assumes an unpressurized shell that has a rest radius R_0 and features only purely elastic tensions. That means that it cannot be applied to a system which includes an additional interfacial tension. Therefore, we have to generalize the model now.

Generalization of the Reissner model

An additional tension γ is equivalent to an internal pressure of $p_0 = 2\gamma/R_0$, which represents the Laplace-Young equation. Pressurized capsules have been studied by Vella et al. in ref. [141], so we can directly adapt their results. In the mentioned reference, an internal pressure leads to an isotropic stress. In our case it is exactly the other way round: An isotropic stress, the surface tension leads to an internal pressure. Using that knowledge, we find a linearized shallow shell equation

$$\kappa_B \nabla^4 w - \gamma \nabla^2 w + \frac{Y_{2D}}{R_0^2} w = -\frac{F}{2\pi}\frac{\delta(r)}{r}, \tag{5.7}$$

which describes the normal displacement $w(r)$ in polar coordinates, where r is the radial distance from the origin, where the point force F acts. The bending modulus is still given by κ_B. In this equation, the pressure-induced isotropic stress σ_∞ from ref. [141] is replaced by $p_0 R_0/2$ due to the equivalence of both problems. Eq. (5.7) is solved in the same way as shown in ref. [141]. To obtain the force F that results from a given indentation $d = -w(0)$, the solution $w(r)$ has to be integrated over the whole reference plane:

$$F = -2\pi \left(\frac{Y_{2D}}{R_0^2}\right) \int_0^\infty w(r) r \mathrm{d}r'. \tag{5.8}$$

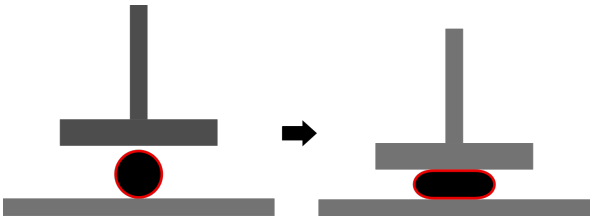

Figure 5.5.: Visualization of the capsule compression measurement. This graphic has been created by E. Zwar and has already been published in ref. [148].

That leads us to a modification of the force-displacement relation

$$F(d) = \frac{4Y_{2D}h}{R_0\sqrt{3(1-\nu^2)}}\, G(\tau)\, d \tag{5.9}$$

with

$$G(\tau) = \frac{\pi}{2}\frac{(\tau^2-1)^{1/2}}{\operatorname{artanh}\,(1-\tau^{-2})^{1/2}} \tag{5.10}$$

and

$$\tau = 3(1-\nu^2)\,(\gamma/Y_{2D})^2\,(R_0/h)^2\,. \tag{5.11}$$

If the interfacial tension vanishes, $\gamma = 0$ leads to $\tau = 0$ and then the original result from Reissner is restored because of $G(0) = 1$. Note that in this case, both the numerator and the denominator in (5.10) become imaginary. For Poisson ratios close to unity ($\nu \approx 1$) and small interfacial tensions compared to the Young modulus, which is the case for our alginate capsules, the corrections due to the interfacial tension in $F(d)$ remain quite small. A problem of this relation is in our case the dependency on the thickness h that we only know with a relative high uncertainty.

The force-displacement curve was measured for 15 individual capsules. Then the ratio FR_0/d was calculated for each capsule separately and averaged over all capsules. The first half of the equation system that determines Y_{2D} and ν is then given as

$$\frac{FR_0}{d} = \frac{4Y_{2D}h}{\sqrt{3(1-\nu^2)}}\, G(\tau). \tag{5.12}$$

5.3.5. The spinning capsule method

The second equation for the mechanical characterization of elastic capsules comes from the spinning capsule experiment. This is an adaptation of the original spinning drop experiment, which was developed to determine interfacial tensions [115, 143]. For that method, a drop is placed in a capillary. This capillary is filled with another fluid that features a higher mass density. Then, the capillary is rotated, and the drop is deformed as a result of the centrifugal forces. This method was transferred to the deformation of elastic capsules in order to determine the elastic properties [111]. The basic principle is visualized in fig. 5.6. In the beginning, the initial state is given by an undeformed capsule in a slow rotating capillary. The slow rotation is needed to avoid a sinking caused by the gravity. The rotation frequency is increased then and the deformation of the capsule is measured as a function of that frequency. The deformation is quantified by the Taylor deformation parameter

$$D = \frac{a-b}{a+b} \tag{5.13}$$

with the length (height) a and the width b of the capsule. The deformation is related to the rotation frequency ω via [111]

$$\frac{D}{R_0^3} = -\Delta\rho\omega^2\frac{(5+\nu)}{16Y_{2D}}. \tag{5.14}$$

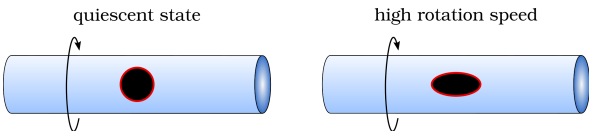

Figure 5.6.: Visualization of the spinning capsule measurement. This graphic was originally created by E. Zwar and has already been published in ref. [148].

The density difference between the inner liquid and the outer liquid is described by $\Delta\rho$. Now we have the same problem as before with the capsule compression, because (5.14) is also only valid for purely elastic systems and does not take the interfacial tension into account. Therefore, we also have to generalize this model. Again, we are only interested in the linear response regime. It quickly becomes clear, that the deformation of a capsule through a rotation is completely equivalent to the deformation of a ferrofluid-filled capsule in a homogeneous field, which we have discussed in section 4.2.1. We only have to set the susceptibility to $\chi = -1$ and the field strength to $\mu_0 H^2 = \Delta\rho R_0^2\omega^2$. This equivalence can be easily understood due to the fact that both forces, the centrifugal force in the spinning capsule experiment as well as the magnetic forces in the ferrofluid, are forces that are transmitted by a fluid in a rest state and, therefore, they are normal forces. So, we just need to take the result from the magnetic problem, eq. (4.22), and translate it to the quantities required here. That leads us to

$$\frac{D}{R_0^3} = -\Delta\rho\omega^2 \frac{(5+\nu)}{16(Y_{2\mathrm{D}} + (5+\nu)\gamma)}. \tag{5.15}$$

Comparing this relation to the original purely elastic relation (5.14), we see that $Y_{2\mathrm{D}}$ only has to be replaced by $Y_{2\mathrm{D}} + (5+\nu)\gamma$. Similar to the capsule compression experiment, several different capsules are deformed in the spinning drop apparatus and the slopes resulting from linear regressions with eq. (5.15) are finally averaged.

Combining the results from the capsule compression and the spinning drop experiment, we get an equation system for the two unknown parameters $Y_{2\mathrm{D}}$ and ν. As a result, we find a value for the Poisson ratio ν that is extremely close to one ($1 - \nu \ll 10^{-6}$). We can use this knowledge now for a more precise calculation of the Young modulus $Y_{2\mathrm{D}}$: We set $\nu = 1$ in the spinning drop equation (5.15) and can calculate $Y_{2\mathrm{D}}$ without being influenced by the high uncertainty from the thickness h in the capsule compression relation (5.12). This is an effective decoupling of the equation system. We finally find

$$Y_{2\mathrm{D}} = 0.186 \pm 0.040\,\mathrm{N/m}. \tag{5.16}$$

Using this value, ν follows from (5.12), resulting in

$$\nu = 1 - (1.9 \pm 2.8) \cdot 10^{-7}. \tag{5.17}$$

Such a high Poisson ratio is a remarkable result as it implies a nearly incompressible area [111]. The high relative error of of $1 - \nu$ directly leads to extremely high errors in the calculation of elastic stresses due to the existence of prefactors like $1/(1-\nu^2)$ in the constitutive relations. Therefore, we keep ν as a free fit parameter in the numerical calculations and compare that parameter to the experimental results afterwards.

The Young modulus is quite low compared to other alginate systems [15, 156], which is a result of the very small thickness and probably also an effect of the nanoparticles in the ferrofluid [39]. Since the main objective is to achieve strong deformations here, a low Young modulus is a helpful precondition.

5.3.6. Characterization of the external magnetic field

The external magnetic field $\boldsymbol{H}_{\mathbf{ext}}$ created by the coil with the conical iron core is characterized by a measurement with a Hall probe. The field is characterized by three main measurements. The first measurement captures the location dependence of the field in z-direction at $r = 0$ and with a fixed field generating current of $I = 2\,\mathrm{A}$ in the coil, see fig. 5.7 (a). The coordinate system is set that way, that the tip of the core is located at $z = 0$ (only for the characterization of the field - later it must be translated to be compatible to the system of the shape equations). The second measurement then investigates the radial dependency of

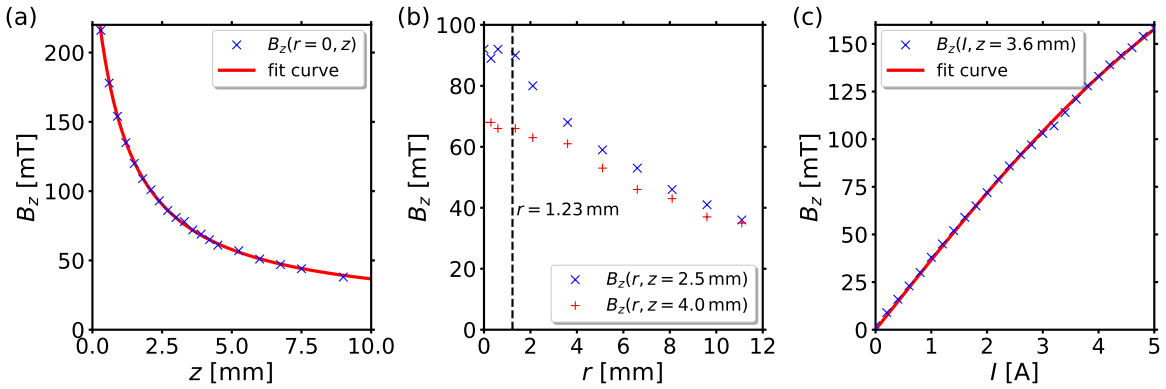

Figure 5.7.: (a): z-component of the magnetic flux density B_z as a function of the distance to the conical iron core in z-direction for $I = 2\,\text{A}$ and $r = 0$. (b): B_z as a function of the radial coordinate r at $z = 2.5\,\text{mm}$ and $z = 4.0\,\text{mm}$ for $I = 2\,\text{A}$. The dashed line marks the highest appearing radial coordinate of a capsule in the experiment. (c): B_z as a function of the current I in the coil at $z = 3.6\,\text{mm}$ and $r = 0$. The data in these diagrams have already been published in ref. [148].

the field. Two submeasurements (at $z = 2.5\,\text{mm}$ and $z = 4.0\,\text{mm}$) with $I = 2\,\text{A}$ (fig. 5.7 (b)) show that the field can be considered to be constant in the radial direction over the size of the capsule (the highest radial coordinate of a capsule in the experiment was found to be at $r = 1.23\,\text{mm}$). This is not a surprise, because the capsules are very small compared to the size of the coil and the iron core. Consequently, we only need to consider the z-component of the field and state $B_r = 0$ (which is also verified with the Hall probe). In the final measurement, we record the non-linearity of the magnetization of the iron core. Therefore, we measure the magnetic field at the position $r = 0$, $z = 3.6\,\text{mm}$ for varying currents $I \in [0, 5\,\text{A}]$, fig. 5.7 (c). In order to transfer the measured field values into our simulation of the capsule, we have to look for a fitting function that is able to describe the field correctly. The location dependency can be described very well by a hyperbola and the current dependency by a Langevin function $L(x) = \coth x - 1/x$. We find

$$B_z(z, I) = a \left(\coth(b_I I) - \frac{1}{b_I I} \right) \left(\frac{a_z}{z - b_z} + c_z \right) \tag{5.18}$$

with parameters

$$a = 4.647, \tag{5.19}$$

$$b_I = 0.332\,\frac{1}{\text{A}}, \tag{5.20}$$

$$a_z = 286.7 \cdot 10^{-6}\,\text{Tm}, \tag{5.21}$$

$$b_z = -1.104 \cdot 10^{-3}\,\text{m}, \tag{5.22}$$

$$c_z = 10.86 \cdot 10^{-3}\,\text{T}. \tag{5.23}$$

The comparison with the real data in fig. 5.7 shows that this curve is able to describe the field with an overall error that is far below 1 %.

5.3.7. Magnetization curve of the ferrofluid

An essential influence on the overall deformation of the capsule is found in the magnetization curve of the ferrofluid. This curve has to be known as precisely as possible. In the following,

d_i [nm]	5	6	7	8	9	10	11	12	13	14
n_i [%]	2.0	14.1	23.9	23.9	16.1	8.6	7.6	5.5	3.8	2.4

Table 5.1.: Particle size distribution of the nanoparticles with the relative frequencies n_i of the particle diameters d_i. These data have already been published in refs. [148] and [155].

we calculate this curve from the microscopic size distribution of the magnetic nanoparticles. This distribution was measured by a dynamic light scattering technique and verified by an analytical ultracentrifugation and an X-ray powder diffraction measurement, see ref. [155] for further details. The resulting data are shown in table 5.1. The specific diameters of the magnetite particles are denoted by d_i and their relative frequencies by n_i. For the calculation of the magnetization curve we use the following relation by Rosensweig [125],

$$M(H) = M_\mathrm{s} \sum_i \left[n_i (d_i - d_s)^3 \cdot L\left(\frac{\mu_0 M_\mathrm{d} H}{k_b T} \frac{\pi}{6} (d_i - d_s)^3 \right) \right] \Big/ \sum_i n_i d_i^3, \tag{5.24}$$

which is basically the sum over the magnetization of every single particle type. In this relation $L(x) = \coth x - 1/x$ describes the Langevin function again. The saturation magnetization of our ferrofluid, M_s can be calculated from the magnetite concentration ($c_\mathrm{m} = 516\,\mathrm{g/mol}$) in the fluid. We find $M_\mathrm{s} = 34650\,\mathrm{A/m}$. In addition, the quantity M_d describes the bulk magnetization of pure magnetite, which is $M_\mathrm{d} = 446000\,\mathrm{A/m}$. The diameters d_i of the particles in the numerator are replaced by a corrected value $d_i - d_\mathrm{s}$. This correction is reasoned in the structure of the nanoparticles. The magnetite particles are stabilized by a layer of a dispersing agent. The chemical connection of this dispersing agent disturbs the crystal order of the magnetite near the surface, which lowers the magnetization and also the effective saturation magnetization. We take this effect into account by using an effective diameter with a correction of $d_\mathrm{s} = 1.66\,\mathrm{nm}$, as it was suggested by Rosensweig [125]. The resulting magnetization curve is shown in fig. 5.8. The initial susceptibility χ_0, the slope in the linear regime, was found to be about $\chi_0 \approx 0.25$.

5.4. Numerical realization

Finally, we know everything that is needed from the experiment and can start to implement a numerical calculation in order to perform a comparison to the real behavior. A major difference to the calculation of the elongation of a capsule in a homogeneous field is that we now have a total force acting on the capsule in negative z-direction (magnetic field gradient and gravity). In the experiment, the counter force is provided by the bottom wall of the cuvette. Such a wall has to be implemented in the simulation. In the force free initial

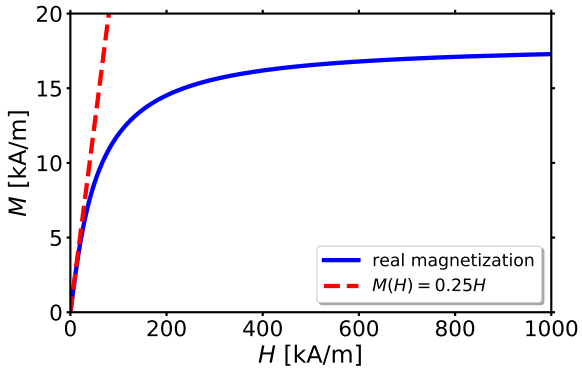

Figure 5.8.: Magnetization curve of the ferrofluid compared to a linear law $M = 0.25\,H$ with the same initial slope. The data in this diagram have already been published in refs. [148] and [155].

reference state, the spherical capsule touches the bottom wall only with a single point, its lower apex at $s_0 = 0$. If an effective force acts on the capsule, then the wall provides the counter force and thus it deforms the capsule, which results in a larger area of contact (as it is indicated in the sketch 5.2). Now, there are different possibilities how that behavior can be simulated. One way is to define an arc length $s_{0,\mathrm{c}}$ which bounds the region of contact between the capsule and the wall. That means we have $z = 0$ for $s_0 \leq s_{0,\mathrm{c}}$ and $z > 0$ for $s_0 > s_{0,\mathrm{c}}$. The disadvantages of this method are quite difficult to find continuity conditions at $s_0 = s_{0,\mathrm{c}}$ and a tendency to numerical instability. Therefore, we use a simpler and faster way to simulate the wall: We model the wall with the help of a repulsive force density $p_{n,\mathrm{wall}}$ and $p_{s,\mathrm{wall}}$ on the elastic shell, that is a continuous function of the z-coordinate, in normal direction to the wall, in z-direction. We define

$$p_{n,\mathrm{wall}}(s_0) = -\mu_{\mathrm{wall}} \cos(\psi(s_0)) \exp(-c_{\mathrm{wall}} z(s_0)), \tag{5.25}$$

$$p_{s,\mathrm{wall}}(s_0) = \mu_{\mathrm{wall}} \sin(\psi(s_0)) \exp(-c_{\mathrm{wall}} z(s_0)). \tag{5.26}$$

These are the normal and the tangential component of an exponentially decreasing force density, that only acts in z-direction, normal to the wall, to avoid non-physical shear forces. In order to imitate a hard wall, the force must decrease very quickly for $z > 0$ and increase strongly for $z < 0$. That can be achieved by choosing the constant c_{wall} as high as possible ($c_{\mathrm{wall}} \to \infty$ represents a perfect, completely impenetrable wall). A value of $c_{\mathrm{wall}} = 100/R_0$ was found to be a very useful compromise with the numerical stability. The prefactor μ_{wall} is the control parameter that allows us to control the total force F_{wall} on the capsule, which is exerted by the wall. This force can directly be calculated via

$$F_{\mathrm{wall}} = \int -\cos(\psi) p_{n,\mathrm{wall}} + \sin(\psi) p_{s,\mathrm{wall}} \mathrm{d}A_0. \tag{5.27}$$

Note that the minus sign comes from the direction of the force density p_n. This force has to counter the total force by the gravity F_g and the magnetic forces F_{m} exactly,

$$F_{\mathrm{wall}} = F_g + F_{\mathrm{m}}. \tag{5.28}$$

Consequently, there is no total force acting on the capsule anymore. In order to choose μ_{wall} in the correct way, we do not need to calculate the total forces. Instead, we use μ_{wall} as an additional shooting parameter. In section 3.1.4, we stated that the shape equations can be solved with more continuity conditions than shooting parameters as long as the capsule is free of total forces. Now we use the same continuity conditions with the additional shooting parameter that controls the total force. The shooting method then chooses μ_{wall} that way that all conditions are satisfied, which directly ensures the total force balance.

With that knowledge, the shape equations can be solved and the deformed shape of the capsule can be calculated. The small thickness of the shell (see the discussion in section 5.3.2) implies a usage of the reduced shape equations without bending energy, (3.28). But instead it is advised to use the full system (3.20), because it shows a better numerical stability in the presence of the wall and thus it allows quicker changes in the magnetic field and the shape.

5.5. Results

In this section, the experimental results as well as the numerical calculations are presented. A very limiting problem in the experiment was the fact, that many capsules that were manufactured, were not perfectly spherical. In the following, we discuss the results for the three best capsules, that showed a nearly spherical shape[1]. These capsules are labelled with the

[1] A higher number of capsules were produced, but most of them showed some asymmetries in the shape of the elastic shell that would violate the rotational symmetry of the theoretical model. Therefore, they were not used for the comparison between the model and the experiment.

Y_{2D}	ν (fit)	h	R_0	$\Delta\rho$	γ	$\boldsymbol{H}_{\mathbf{ext}}$	$M(H)$
$0.186\,\frac{\mathrm{N}}{\mathrm{m}}$	0.946	$3\,\mu\mathrm{m}$	$0.903 - 1.044\,\mathrm{mm}$	$0.24\,\frac{\mathrm{g}}{\mathrm{cm}^3}$	$10\,\frac{\mathrm{mN}}{\mathrm{m}}$	eq. (5.18)	eq. (5.24)

Table 5.2.: Numerical parameters

numbers 1, 2 and 3. The initial radii of these capsules were calculated as $R_{0,1} = 0.903\,\mathrm{mm}$ for capsule 1, $R_{0,2} = 1.044\,\mathrm{mm}$ for capsule 2 and $R_{0,3} = 0.965\,\mathrm{mm}$ for capsule 3. The current I in the coil was increased from 0 to 5 A, which leads to a variation of the magnetic field of about 50 mT over the size of the capsules. Photographic images were taken after steps of 0.5 A. From these images, the height-to-width ratio a/b can be determined. The resulting data $a/b(I)$ are shown in fig. 5.9 (a). On the other side, the numerical calculations with the capsule parameters from the previous sections (summarized in table 5.2) show a very good agreement to the experimental data for all three capsules, if the Poisson ratio is set to $\nu = 0.946$ (solid lines in fig. 5.9 (a)). The overall deformation that was possible to reach is quite remarkable as a/b could be decreased to about $a/b = 0.6$ for the highest possible current on the coil. Especially for medium and higher deformations with a current greater than 1 A in the coil, the numerical data describe the relation between a/b and I very well. Only without a magnetic field or very small currents, we see significant deviations. These deviations are probably caused by small asymmetries of the shell, which have a high impact due to the small overall deformation. Figure 5.9 (b) again shows the data of capsule 1 but now in comparison to numerical data for different Poisson ratios ν. We find that the best fitting Poisson ratio ($\nu = 0.946$) is not as extremely close to one as it was implied by the capsule compression and the spinning capsule measurements, but it is still very high. That causes the effect, that even small variations of ν lead to significant deviations in the deformation of the shell. Therefore, we can state for sure that the Poisson ratio of this specific alginate system is very close to one.

5.5.1. Evaluation of photographic images

In order not to compare only the height-to-width ratio, but the whole shape of the capsules, fig. 5.10 shows photographic images of all three capsules. The first state without a magnetic field can be found on the left side. The deformation by the gravity and some small asymmetries

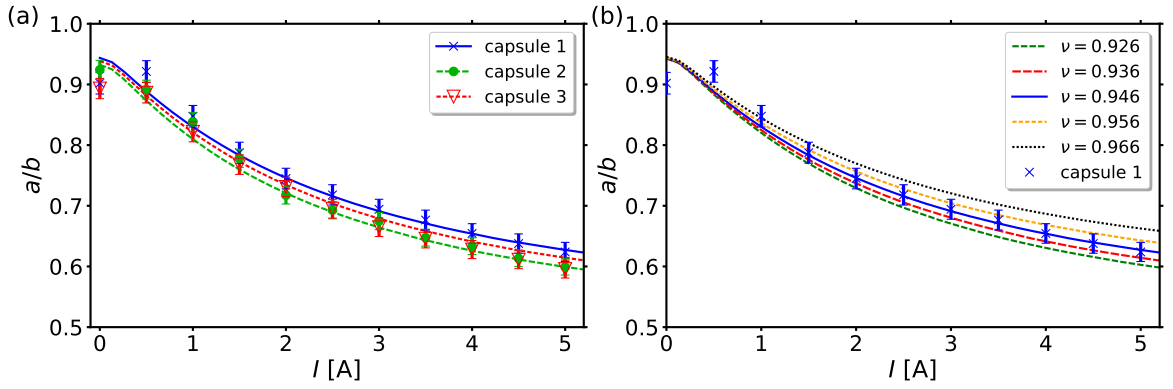

Figure 5.9.: (a): Comparison of the experimental data of a/b as a function of the current I with numerical calculations with a Poisson ratio of $\nu = 0.946$. (b): Comparison of the experimental data from capsule 1 with numerical data for slightly different Poisson ratios ν. The data of these diagrams have already been published in ref. [148] and partly published in ref. [155].

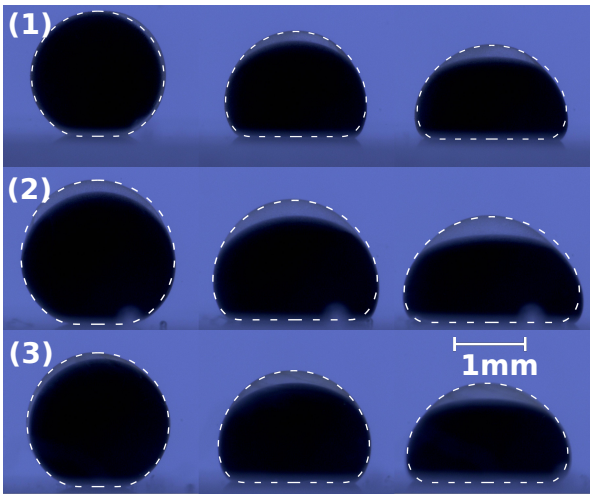

Figure 5.10.: Photographic images of three different capsules with radii (1) $R_0 = 0.903\,\mathrm{mm}$, (2) $R_0 = 1.044\,\mathrm{mm}$, and (3) $R_0 = 0.965\,\mathrm{mm}$, each for increasing magnetic fields with $I = 0\,\mathrm{A}$ (left), $I = 2\,\mathrm{A}$ (central) and $I = 5\,\mathrm{A}$ (right). The dashed lines describe numerically calculated capsule contours. This image was already published in ref. [148] and with small variations in ref. [155].

in the shapes are clearly visible. The states in the central column are related to $I = 2\,\mathrm{A}$. Here, the magnetic forces lead to a much larger contact with the bottom of the cuvette. Finally, the images on the right side show the maximum possible deformation at $I = 5\,\mathrm{A}$ with an even more compressed shape. The white dashed lines represent the numerical solutions $z(r)$ of the shape equations. Despite some small asymmetries of the real capsules, we find a very good agreement in the contour lines. In the photographic images of the capsules in fig. 5.10, we find a cap of a transparent liquid in the upper part of the capsules, see also fig. 5.11 for a magnified image of capsule 1 at $I = 5\,\mathrm{A}$. These caps were formed in every capsule when the magnetic field was increased. There is a clear phase separation between this unknown liquid and the ferrofluid. Therefore, we can conclude that it is a polar liquid. Probably it contains water that diffused through the shell before the measurement started. From the behavior of the liquid - it is pushed upwards by the ferrofluid - and from its transparency, we can conclude that the liquid is non-magnetic and does not contain magnetic particles. Since the total amount of this non-magnetic liquid is relatively small compared to the amount of ferrofluid, we assume this fluid to have the same properties as the ferrofluid in the numerics. The errors of this assumption should be quite small, because the ferrofluid causes a magnetic pressure at the interface to the other liquid. This pressure is transmitted to the elastic shell by the liquid, so that the error of this concept only comes from the inhomogeneity of the magnetic field over the size of the non-magnetic cap. Therefore, the behavior of the capsules in the experiment should be comparable to the behavior of a perfect ferrofluid capsule. If this liquid was also magnetically active, the deformation would be higher, which would lead to an even higher Poisson ratio from the fit.

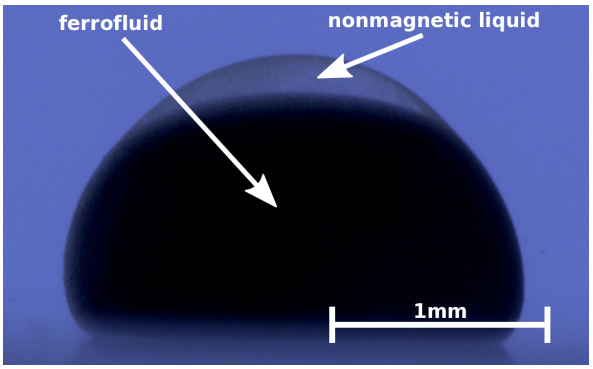

Figure 5.11.: Magnified photographic image of capsule 1 at $I = 5\,\mathrm{A}$. This image was already published in ref. [148].

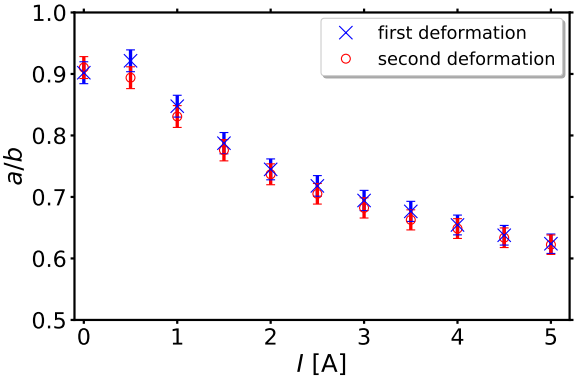

Figure 5.12.: Ratio a/b of capsule 1 for an increasing current I in a first deformation process (blue crosses) and in a second deformation process (red circles). The data from this diagram were already published in ref. [148].

Reversibility of the deformation

For possible technical applications the reversibility of the deformation is very important. It could be possible, that the elastic shell is weakened by the deformation. If that is the case, then the capsule should be deformed even more in a second deformation process, after the capsule was deformed and relaxed again. Figure 5.12 shows the deformation of capsule 1 in the first and in a second deformation process. There are small deviations in the beginning at low currents, but a very good agreement for high currents. The deviation can be explained with small asymmetries in the shape of the shell. These asymmetries have the effect that the capsule changes its alignment during the first deformation, leading to deviations in a/b. The high agreement for higher deformations indicates a very good reversibility of the deformation, which is also underlined by the constant volume in the experiment.

5.5.2. Calculation of inaccessible quantities

With the knowledge about a good agreement between the numerics and the real capsules, the solution of the shape equations coupled to the magnetic field allows us to get access to physical quantities, that are very difficult to measure directly. While we were able to measure the external magnetic field in absence of the capsule, our theoretical model gives access to the complete field, even inside of the capsule. Figure 5.13 (a) shows the absolute of the magnetic field strength $|\boldsymbol{H}|$. The magnetization of the capsule leads to an increased field at the bottom wall, which can be observed very clearly in the stray field of the capsule, $\boldsymbol{H}_{\text{stray}} = \boldsymbol{H} - \boldsymbol{H}_{\mathbf{ext}}$, in fig. 5.13 (b). The magnetization itself varies only slightly over the size of the capsule, fig. 5.13 (c).

Even more interesting for technical applications than the magnetic data are the internal strains and stresses of the elastic shell. Too high stresses could lead to a possible damage of the shell. The examination of the strains e_s, e_φ, the elastic stresses τ_s, τ_φ and the magnetic force density f_{m} is shown in fig. 5.14 for capsule 1 at $I = 0\,\text{A}$, $I = 2\,\text{A}$ and $I = 5\,\text{A}$. The position of the highest strains and stresses is located slightly above the bottom wall, where the highest curvatures occur. This region is also identical to the region of the highest magnetic field inside of the capsule (see fig. 5.13) and the magnetic forces have their maximum there. The highest strain is found at about 17 %. Depending on the material, stronger magnetic fields or higher field gradients could lead to irreversible damages of the shell at the position right above the bottom wall.

An interesting fact following from the elastic stresses is that the shape of the capsule is dominated by the interfacial tension γ for small deformations. In the absence of the magnetic field, the elastic stresses τ_i do not exceed the value about $0.02\,Y_{2\text{D}}$. The interfacial tension in contrast measures the constant value of $\gamma = 0.054\,Y_{2\text{D}}$, which is nearly three times as high. On the other hand, in the presence of stronger fields with higher deformations, the stresses

are that high, that the interfacial tension becomes nearly irrelevant.

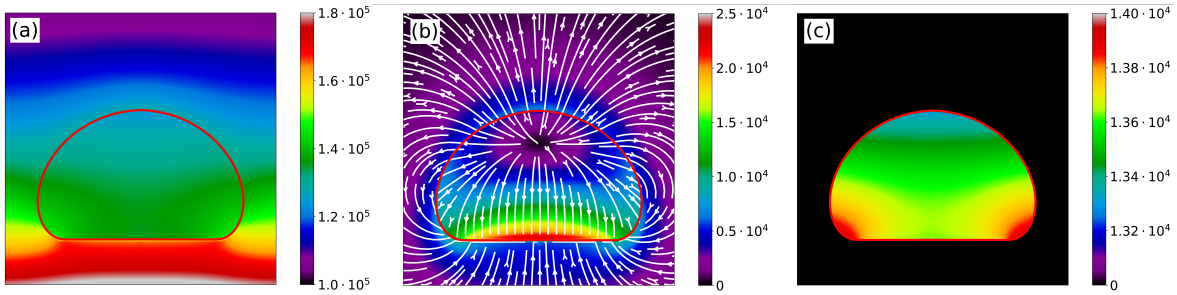

Figure 5.13.: (a): Numerically calculated distribution of the absolute of the magnetic field strength $|\boldsymbol{H}|$ (in A/m). (b): Stray field $\boldsymbol{H}_{\text{stray}} = \boldsymbol{H} - \boldsymbol{H}_{\text{ext}}$ (in A/m). (c): Absolute of the magnetization $|\boldsymbol{M}|$ in (A/m). All three diagrams represent a cut through the capsule 1 (see figure 5.10) at $I = 5\,\text{A}$. The solid line describes the capsule's elastic shell. The data of these graphics have already been published in ref. [148].

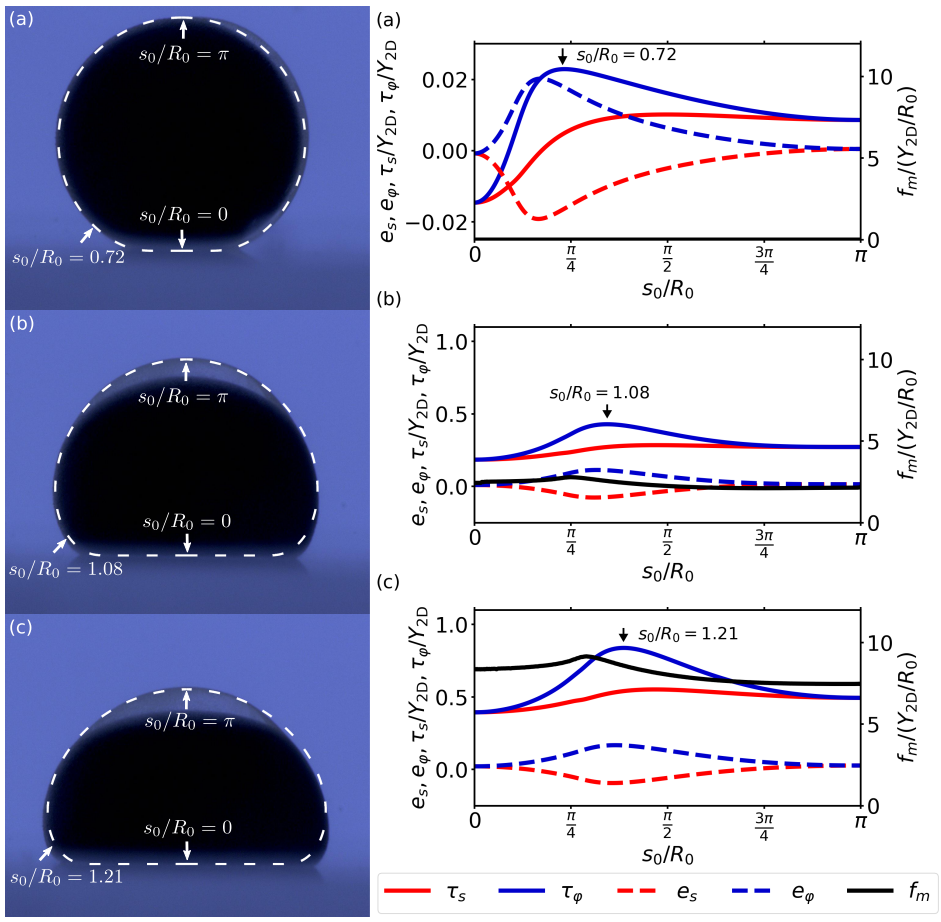

Figure 5.14.: Stresses and strain distributions for different deformation states of capsule 1 without magnetic field (a), with $I = 2\,\text{A}$ (b) and $I = 5\,\text{A}$ (c). The left scales show the strain in meridional (e_s) and circumferential (e_φ) direction and the corresponding elastic stresses (τ_s, τ_φ in units of Y_{2D}) inside the shell. The right scale shows the magnetic pressure f_m (in units of Y_{2D}/R_0). For comparison, the interfacial tension has a value of $\gamma = 0.054\,Y_{2D}$. This shows that the interfacial tension γ is the dominating stress for small deformations ($e_{s,\varphi} < 0.05$) by gravity and at small magnetic fields, while the strongly deformed shell is completely dominated by the elasticity. The data of these graphics have already been published in ref. [148].

5.5.3. Interpretation of very high Poisson ratios

Our numerical results as well as the results from the mechanical characterization coincide in a way that both methods predict very high surface Poisson ratios ν that are located close to one ($\nu_{\text{num}} = 0.946$, $\nu_{\text{exp}} = 1 - (1.9 \pm 2.8) \cdot 10^{-7}$). In the literature, there are only values for barely comparable systems available, that usually rely purely on the mechanical characterization [89, 156], often generic values like $\nu = 1/3$ or $\nu = 1/2$ are assumed [15, 90].

In order to interpret the effects of a Poisson ratio close to one, we can define the area compression modulus $K_{2\text{D}}$, which is a proportionality constant between an isotropic elastic stress τ and the relative change of the surface area $\Delta A/A_0$ [74]:

$$\tau = K_{2\text{D}} \frac{\Delta A}{A_0}, \tag{5.29}$$

$$K_{2\text{D}} = \frac{Y_{2\text{D}}}{2(1-\nu)}. \tag{5.30}$$

This area compression modulus diverges for $\nu \to 1$, which means that the area stays constant during an infinitely small deformation. In conclusion, our polymerized alginate shell nearly preserves its area during a (small) deformation process.

A common view on alginate gels is to assume them as volume-incompressible, which can also be confirmed by measurements [50, 129]. The three-dimensional Poisson ratio is set to $\nu_{3\text{D}} = 1/2$ in that case. If such a volume conserving material preserves its surface area during a small deformation ($\nu = 1$), then the thickness of the shell is required to stay constant. The microscopic cause of the high Poisson ratio that can be observed in our system can possibly be found in the anisotropic structure of the alginate gel, which is formed in an ionotropic gelation process [99], but needs to be clarified in future works.

5.6. Conclusion

In this chapter, we were able to show that our coupled elastic and magnetic model is able to describe a real system, even for remarkable high deformations. Strong deformations of ferrofluid-filled capsules are easily achievable through the usage of inhomogeneous magnetic fields generated by an iron tip. The aspect ratio a/b of the capsule could be decreased to about $a/b = 0.6$ with a magnetic field variation of about 50 mT over the size of the capsule. With higher field gradients, even stronger deformations should be possible. A good agreement between the experiment and the numerical model provides access to physical quantities that are difficult to measure like stresses and strains. We saw a maximum strain of about 17 % in this experiment. Depending on the elastic shell's material, irreversible damages in the shell could be possible at the position right above the bottom wall, where the highest curvatures occur. With that point in mind, our theoretical model provides an interesting tool to ensure a save deformation of a capsule or on the other hand to predict the necessary magnetic field strength for a desired destruction of the elastic shell.

There are several sources of errors, which can cause the deviations between theory and experiment. These errors resulted especially in the deviation of the Poisson ratio between the numerical fit and the mechanical characterization. On the other hand, improvements in the experimental characterization of the capsule should lead to an even better agreement to the theoretical model. A better controllable production method, especially in the polymerization process, could ensure more homogeneous and symmetric elastic shells. A great source of errors is probably, that different capsules had different shell properties, because the production process was not perfectly repeatable, leading to deviations between different capsules. The mechanical characterization assumed the same elastic properties for different capsules, so an

improvement of the exact repeatability of the capsule production should drastically increase the precision of the elastic parameters. In addition, a direct measurement of the magnetization curve could also contribute to an increase in the overall precision. The interfacial tension γ was estimated to have a value of about 10 mN/m. A direct measurement of this value should improve the precision significantly in the regime of small deformations. While the interfacial tension was found to be nearly irrelevant for stronger deformations, it is the dominating quantity when the capsule is only weakly deformed, especially in the absence of the magnetic field, where only gravity works. Of special interest for such a measurement could be the spinning capsule experiment with a focus on the formation and detection of wrinkles of the shell, as it was described in section 4.4.1.

Despite the differences between theory and experiment, both the mechanical characterization and the numerical calculations coincide in the fact that the Poisson ratio of the alginate gel, that was used for the encapsulation, is located very close to one. Since both methods share this result, it is a very robust statement that this alginate system is nearly area conserving for small deformations. The microscopic causes of this effect are an interesting topic for future investigations.

6. Final remarks

The manipulation and the deformation of axisymmetric initially spherical elastic capsules, that are filled with a ferrofluid, through an external magnetic field was the central point of this first part of this thesis. We developed a numerical model for the calculation of the coupled elastic and magnetic problem. The elastic part consists of a non-linear Hookean model that was primarily taken from Knoche [74, 75, 78]. The central part of the elastic model is the non-linear differential equation system, the shape equations (3.20). This system is coupled to the magnetic part of the problem through the magnetic force density f_{m}, which is directly related to the magnetization of the ferrofluid and the total magnetic field. The magnetic field is calculated by a coupled finite element method (FEM) and boundary element method (BEM). Because this coupling between the magnetic and the elastic part of the model results in a self-consistent problem, an iterative solution scheme was introduced.

We applied this model to two different situations. In the first case, we investigated the behavior of a linearly magnetizable ferrofluid capsule in a homogeneous external magnetic field from a theoretical point of view. This set-up shows many parallels to the situation of a simple ferrofluid droplet in a homogeneous magnetic field, that was extensively investigated in the literature [1, 3, 8, 11, 87, 88]. This well-known problem is also the limit case of our system for vanishing elasticity, $Y_{2\mathrm{D}}/\gamma \to 0$. Overall, we found the behavior of the capsules being very similar to the behavior of the ferrofluid drops, which especially results in the same critical susceptibility for the transition into a conical shape. At this point, future works should point their interest on the investigation of that transition with a more advanced material law, that is more suitable to describe high strains.

The second set-up, shown in chapter 5, described a more realistic situation, a real experiment with a ferrofluid encapsulated by an alginate gel. An inhomogeneous magnetic field generated by a coil with a conical iron core pushed the capsule against the bottom wall of a cuvette. We found our model to be well suited for the description of the shape of the deformed capsule. This provides the possibility to gain access to physical quantities that are difficult to measure, like stresses, strains or the magnetic field inside of the capsule. An interesting result coming from both the mechanical characterization of the capsule as well as the numerical investigation is that the Poisson ratio of the presented alginate system is very close to one, so the surface is nearly area preserving under small deformations.

For future works, some improvements should be added to the model. First, a more advanced material law, like the Mooney-Rivlin law [94], should be adapted. This allows a more accurate description of higher strains and stretching factors for the price of more sophisticated calculations. In addition, more advanced methods for the calculation of the magnetic field, like adaptive mesh-generations, could also increase the accuracy, especially near the conical tip in a homogeneous field.

In general, all theoretical results about ferrofluid-filled capsules in this part of this thesis are also applicable for capsules that are filled with a dielectric liquid in an electric field, because the underlying theory is the same due to the absence of any currents in the ferrofluid (see the discussion in sec. 3.2.2). We focussed here on the magnetic description with a ferrofluid, because in many real systems a magnetic field shows nearly no interaction with the environment in contrast to strong electric fields that can easily induce unwanted electric currents. The encapsulation of the ferrofluid is then a promising tool to prevent the ferrofluids, that are often chemically aggressive, from reacting with their surroundings in a technical application.

Part II.

Swelling flat elastic disks as microswimmers

List of symbols

The following list shows an overview over frequently used or important symbols, their meaning and the page number of their first appearance or explanation.

Symbol	Meaning	page
a	radius of a spherical particle in the fluid	119
A	surface area	91
A_i	area around the vertex i	100
A_n, B_n	coefficients in the series expansion of the velocity field	135
α	swelling factor	91,93
$\alpha_{\mathrm{c,e}}$, $\alpha_{\mathrm{c,h}}$	swelling factor at the flat end of the pseudo-hysteresis region	110
$\alpha_{\mathrm{c2,e}}$, $\alpha_{\mathrm{c2,h}}$	swelling factor at the curved end of the pseudo-hysteresis region	110
$\alpha_{\mathrm{c3,e}}$, $\alpha_{\mathrm{c3,h}}$	swelling factor at the flat end of the real hysteresis region	111
$\Delta\alpha$	swelling factor step size	109
β	swelling factor in the first deformation phase of the five-sphere model	129
c	real constant in the solution for a constant K	116
γ	swimmer characterization ratio	136
γ_{FvK}	Föppl-von Kármán number	102
δ_i	movement distance of the vertex i during shaking	102
$\delta_{\max}$	maximum movement distance of the vertices during shaking	102
E_{B}	bending energy	96
E_{S}	stretching energy	95
$\boldsymbol{f}$	force acting on the fluid	121
$\boldsymbol{f}_{\mathbf{ext}}$	external force density in the fluid	119
$\boldsymbol{F}$	force vector	95
$\underline{\underline{\boldsymbol{g}}}$	metric tensor of the first fundamental form	89
h	thickness of the disk	94
H	mean curvature	97
η	fluid viscosity	119
$\underline{\underline{\boldsymbol{I}}}$	identity matrix	121
j_S	fluid stream through the swimmer surface	141
j_{P}	fluid stream through a hypothetically permeable surface	142
k_i	spring constant of a specific spring i	95
k_{out}	spring constant in the outer annulus, basic unit	102
K	Gaussian curvature	90
$\overline{K}$	averaged Gaussian curvature	108
κ_{B}	bending modulus	96
κ_ρ, κ_φ	principal curvatures	97
l_{B}	spring length on the disk's outer boundary	99
l_i	rest length of a spring	95
$\underline{\underline{\boldsymbol{L}}}$	matrix of the second fundamental form	90
$\lambda_{\min}$	lowest eigenvalue of the Hessian matrix of the energy	109
$\underline{\underline{\underline{\underline{\boldsymbol{M}}}}}$	mobility matrix	122
n	number of swelling steps in a whole deformation cycle	123
$\boldsymbol{n}$	surface normal vector	89

n_B	number of vertices on the disk's edge	99
n_in	number of vertices on the edge of the inner disk	99
ν	surface Poisson ratio	96
p	fluid pressure	119
P	perimeter of the disk	105
P_n	n-th Legendre polynomial	135
φ	azimuthal angle in polar coordinates	89
r	radial coordinate	89
$\boldsymbol{r}$	position vector	95
r_0	radial coordinate related to the unswollen disk	91
R	radius of a (nearly) spherical swimmer	135
R_0	radius of the unswollen circular disk, basic length unit	89
R_in	radius of the inner disk region	93
Re	Reynolds number	120
ρ	radial Gaussian normal coordinate	91
ρ_h	fluid mass density	119
s	distance or curve length on a surface	90
Δs_CoM	swimming distance of the center of mass	124
t	time	119
$t_\mathrm{h,end}$	time when a hydrodynamic step reaches equilibrium	124
$\underline{\underline{\boldsymbol{T}}}$	Oseen matrix	121
T_el	time corresponding to a single swelling step	123
θ	polar angle in spherical coordinates	102,135
θ_j	inner angle of the triangle j at a specific vertex	101
u_1, u_2	general two-dimensional surface coordinates	89
$\boldsymbol{u}$	fluid velocity field	119
$\boldsymbol{v}$	velocity	119
$\boldsymbol{v_S}$	local velocity of the swimmer surface	141
V_n	function related to the derivative of the n-th Legendre polynomial	135
x, y, z	coordinates in the three-dimensional Euclidean space	89
$\boldsymbol{x}$	coordinate vector in the $\mathbb{R}^3$ given by a regular local parametrization	89
Y_2D	two-dimensional Young's modulus	96
Δz	height of the deformed disk	105
Δz	height of the five-sphere swimmer	130

7. Microswimmers and elastic disks

The central idea of the following second part of this thesis is the development of a shape-changing microswimmer by using an elastic circular flat disk which undergoes a periodic swelling process. This non-uniform swelling process causes a shape transition into a curved conformation. If this transition shows hysteretic effects, these effects may be used as a propulsion mechanism in an external fluid. The focus of this work is set to a general proof of concept of this basic idea by developing and implementing the simplest possible model.

As their name already indicates, microswimmers can be found on a micrometer length scale. They are no artificial invention, as nature itself created an enormous amount of microswimmers: Many types of bacteria such as E. coli, some algae like Chlamydomonas, spermatozoa of many higher organism [84] and also many other unicellular organism are microswimmers. They live surrounded by fluids and they are able to propel themselves. In this context, the process of a self-propulsion in an external fluid is called *swimming*, which is a contrast to swimming in everyday life, where it usually refers to floating on a fluid surface. The laws of physics of swimming on a micro scale are different from swimming in a macroscopic regime. Macroscopic swimmers, such as fish in the water, primarily use inertial effects to move. For example, the fluid is pushed away by a quick motion of a fin generating thrust and accelerating the fish. If the fish now suddenly stops its swimming motions, its inertia will still keep it in motion over a distance of up to several body lengths before it completely stops. A human in water can also experience the same effects. But these effects are very ineffective on the microscopic scale.

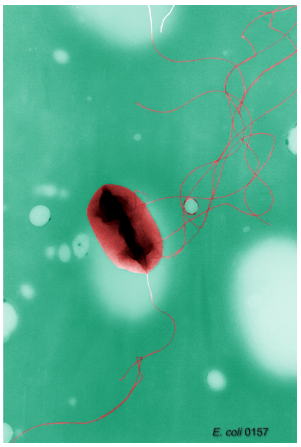

Figure 7.1.: TEM image of an E. coli bacterium, a typical natural microswimmer. The organism has a size of about $2\,\mu m$ and uses its flagella for propulsion. This image was taken from ref. [27].

Due to their small size, microswimmers usually operate at low Reynolds numbers $Re \ll 1$, for example a typical Reynolds number of moving E. coli bacteria is about $Re \approx 10^{-5}$ [82]. The Reynolds number is a dimensionless control parameter that is proportional to the velocity and the size of a particle in a fluid. If the Reynolds number is sufficiently small, then the Navier-Stokes equation, which models the motion of a fluid in general, can be simplified resulting in the Stokes equation. The Stokes equation is a linear partial differential equation, where nonlinear convective terms of the Navier-Stokes equation are neglected. It describes a laminar fluid flow without any turbulences. Therefore, there is a linear relation between force and velocity of a particle in the fluid. This causes microswimmers to effectively move in an overdamped environment: When the propulsive forces vanish, the swimmer immediately stops. A common analogy on this point is a human trying to swim in honey. Without propulsive forces, every motion immediately stops. This linearity between forces and velocities has the consequence that time-invariant motion patterns with just different velocities on single parts of the motion do not work anymore. An effective movement can only be achieved if the time invariance of the motion is broken by the usage of more than a single degree of freedom. This is also known as the scallop theorem [117]. A scallop is moving on a macroscopic scale with a slow opening motion followed by a quick thrust generating closing motion. On a microscopic

scale with low Reynolds numbers, the velocity of the opening and closing motions become irrelevant. The slow opening leads to a propulsion over a distinct distance, while the quick closing causes a propulsion in the opposite direction over the same distance. There is no net movement after a complete opening and closing cycle, because the swimming motion of the scallop has only a single degree of freedom (its opening angle) and is time-invariant.

Therefore, microswimmers that rely on mechanical deformation had to develop more efficient propulsion mechanisms in order to be able to swim efficiently under such circumstances. These propulsion mechanisms and the general swimming behavior became a very wide topic in the modern research. Often with biological swimmers as a prototype, also many completely different types of artificial swimmers have been constructed. Microswimmers can use completely different propulsion mechanisms, even when they have a simple spherical shape. There are shape-changing swimmers, that use small deformations on their surface to create a propulsive fluid flow [30, 46, 92]. These cyclic deformations always have to be time-invariant due to the scallop theorem.

Microswimmers that do not rely on mechanical deformation are not affected by the scallop theorem. An example for this category are phoretic swimmers. This type of swimmer uses a gradient in the fluid for propulsion, for example a chemical concentration gradient or a temperature gradient. A prominent example of this swimmer type is the Janus particle: Two half spheres of different materials are put together and different chemical reactions [91] causing a concentration gradient or thermophoretic effects [16, 151] on both sides lead to a net movement due to a fluid flow on the surface. Phoretic swimmers are often not directly affected by Also, the Marangoni effect can be exploited in order to generate propulsion. Different interfacial tensions on opposite sides of a Marangoni swimmer also create a propulsive fluid flow on the surface of the swimmer [65].

The theoretical understanding of microswimmers in general, their collective behavior, interaction with surfaces and also external flow fields has massively increased in the last years [81, 100, 133]. The swimming mechanisms were even transferred into elastic media instead of fluids [116]. Another direction of research tries to find microswimmer models that are as simple as possible and ideally also constructible in experiments. The probably most prominent and simplest example for a mechanical swimmer is the linear three-sphere swimmer that consists of three linked spheres and swims by periodically changing the distance between the spheres [60, 105]. Since two spheres can be moved independently in relation to the third one, a deformation cycle that is not time-invariant and bypasses the scallop theorem can be defined. With some modifications, a three-sphere swimmer is even able to steer and can be interpreted as a minimal model for the flagella of Chlamydomonas [124]. A downside is that these theoretically simple swimmers are often very difficult to construct in experiments, because control over two independent deformation parameters is necessary [59]. Nevertheless, the concept of a swimmer being propelled by self-deformation has much potential. A good microswimmer in general should provide some basic properties: It should be easily constructible, the swimming motion should be externally controllable and finally it should be sufficiently

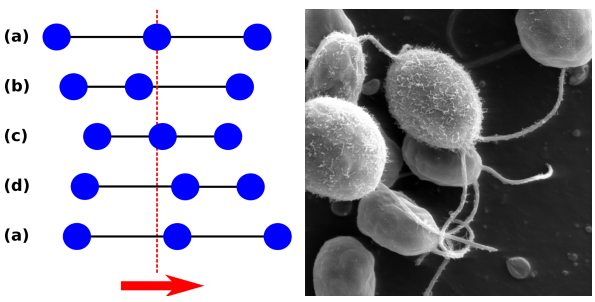

Figure 7.2.: Artificial and natural microswimmers. Left: Visualization of the deformation cycle of the three-sphere swimmer model from ref. [105]. Right: SEM image of multiple chlamydomonas reinhardtii algae. A synchronized motion of the two flagella at the front of each organism propels this microswimmer. This image was taken from ref. [132].

fast. The term *fast* primarily refers to a sufficiently large net swimming distance in relation to the swimmer's size after one complete deformation cycle. Simple model swimmers that rely on mechanical deformation usually move over a net distance in the order of 0.1-1 % of their own size in a single deformation cycle.

In the following, we focus on elastic systems. These systems feature the advantage that a well-defined type of deformation can be easily triggered from outside the swimmer using the intrinsic properties of the material. There are already some attempts in the literature to implement elastic deformation swimmers: Elastic capsules, as they were presented in the first part of this thesis, perform a buckling transition and create a dimple when the external pressure is increased. This buckling transition shows hysteresis effects breaking the time invariance and, therefore, such capsules can be used as swimmers as well [44]. In another way, the elastic behavior was exploited to create a soft microrobot in ref. [109]. A swimmer can be realized by using photoactive liquid-crystal elastomers. These elastomers deform in a structured external light pattern which results in a swimming motion.

In this part of the thesis, we want to go on and simplify things further. An elastic deformation swimmer shall be discussed that is even easier to build and to control from the outside. We build upon the theoretical and experimental framework about elastic circular flat disks that perform a transition to a non-flat conformation due to swelling processes [48, 73, 110]. If distinct regions of a flat disk start to swell or to shrink a transition into dome-like or saddle-like curved shapes can be observed.

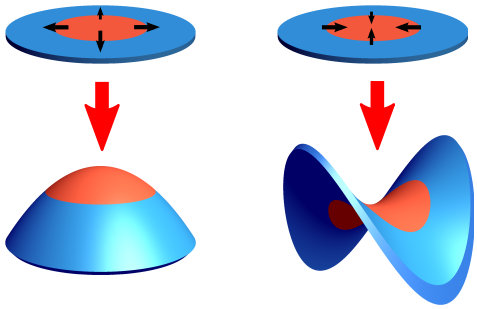

Figure 7.3.: Swelling or shrinking of the central region of an elastic disk triggers a transition into a curved shape.

A simple isotropic elastic disk is very easy to fabricate, a swelling process can be induced by external fields and this should be possible quickly enough to achieve sufficient movement speeds. In the following the general possibility of this swimmer concept is proven and some basic properties are determined.

The chapters 8 to 10 only regard the dry deformation behavior of the disk. We start in chapter 8 with the theoretical background of the dry elastic disk without any fluid. Principles and methods from differential geometry, especially the famous *Theorema Egregium* is used to describe the reaction of a flat circular disk to a radial symmetric swelling process. After that, the model of a mechanical spring mesh with an additional curvature sensitive bending energy is introduced in order to add elastic properties to the up to that point purely geometrical problem. Subsequently, numerical solution strategies to calculate the disk's preferred conformation after the swelling process by energy minimization are discussed in chapter 9. The results of the energy minimization are shown in chapter 10. After a general presentation of possible resulting conformations, the first main part of this chapter is a comparison of the Gaussian curvature to experimental results from the literature. A wide discussion of pseudo-hysteresis effects in a deformation cycle for both hyperbolic and elliptic shapes as a result of a periodical swelling process follows as a second focus. The term pseudo-hysteresis is chosen, because these effects have a numerical origin and probably do not reliably occur in a real system. After that, the introduction of an additional energy barrier ensures the existence of real hysteretic effects.

Finally, in chapter 11 a surrounding fluid and the hydrodynamic interaction are added. At first, the basic principles of the hydrodynamic interaction are introduced and the finally used model, the Rotne-Prager model for hydrodynamic interaction, is presented. A brief introduction into the properties of a very simple numerical simulation with a fluid follows. The core

of that simulation is to model the continuous disk with a mesh of sparse small spheres. After that, the swimming behavior of the elastic disk undergoing a periodical swelling process is analyzed. For a better understanding of the basic swimming principles of that type of swimmer, a minimal model, a swimmer consisting of only five small spheres is presented in chapter 12. This minimal swimmer imitates the swimming behavior of the swelling disk with the help of a prescribed deformation pattern. The topic of the final investigation chapter, chapter 13, is the fluid velocity field of both the swelling disk as well as the five-sphere swimmer. The velocity fields in each phase of the deformation cycle are compared and characterized. Also, the quality of the sphere mesh model is discussed by examining the fluid stream through the disk's surface. The ending of this thesis is then given by a short conclusion and a brief outlook to future work in chapter 14.

8. Theory of the deformation of a thin elastic disk

The objective of this second part of the thesis is to realize swimming motions by deforming an initially flat disk into a non-flat shape and back. Therefore, in the following section, we investigate the question how a flat object can be deformed into a non-flat shape without any external forces by introducing some basic concepts of differential geometry.

8.1. Changing a disk's metric

We start with a circular flat disk with a radius R_0 that we assume to be infinitely thin - a two-dimensional flat plane embedded in the three-dimensional Euclidean space. The disk is located in the $(z = 0)$-plane and because of its rotational symmetry it is parametrized in polar coordinates by a regular local parametrization

$$\boldsymbol{x}(r,\varphi) = (r\cos\varphi, r\sin\varphi, 0)^T \tag{8.1}$$

with the radial coordinate $r \in [0, R_0]$, the azimuthal angle $\varphi \in [0, 2\pi)$ and the origin of the coordinate system being located in the disk's center.

8.1.1. First fundamental form and Theorema Egregium

We now introduce the basic concepts of the first and the second fundamental form. For a more detailed and general overview the reader may be referred to the references [45, 49].

We start in a bit more generalized way and come back to our disk in polar coordinates later. Let the covariant vector $\boldsymbol{u} = (u_1, u_2)^T$ describe points in $\mathbb{R}^2$ and $\langle\cdot,\cdot\rangle$ be the Euclidean scalar product in $\mathbb{R}^3$. $\boldsymbol{x}(u_1, u_2)$ describes points in the Euclidean space $\mathbb{R}^3$ given by a regular local parametrization of a surface. We define derivatives to the coordinates u_1, u_2 via

$$\boldsymbol{x_1} \coloneqq \frac{\partial \boldsymbol{x}}{\partial u_1} \quad \boldsymbol{x_2} \coloneqq \frac{\partial \boldsymbol{x}}{\partial u_2} \tag{8.2}$$

$$\boldsymbol{x_{11}} \coloneqq \frac{\partial^2 \boldsymbol{x}}{\partial u_1^2} \quad \boldsymbol{x_{22}} \coloneqq \frac{\partial^2 \boldsymbol{x}}{\partial u_2^2} \quad \boldsymbol{x_{12}} \coloneqq \frac{\partial^2 \boldsymbol{x}}{\partial u_1 \partial u_2}. \tag{8.3}$$

If $\boldsymbol{x}$ and its derivatives are continuous, $\boldsymbol{x_{ij}} = \boldsymbol{x_{ji}}$ directly follows. We now restrict the derivatives (8.2) to linearly independent derivatives in every point. A surface with this feature is called an *immersion*. The unit normal vector $\boldsymbol{n}$ of the surface in $\mathbb{R}^3$ is given by

$$\boldsymbol{n}(\boldsymbol{u}) = \frac{\boldsymbol{x_1} \times \boldsymbol{x_2}}{|\boldsymbol{x_1} \times \boldsymbol{x_2}|}. \tag{8.4}$$

Now we can define the first fundamental form in the form of the covariant metric tensor $\underline{\underline{\boldsymbol{g}}}$:

$$\underline{\underline{\boldsymbol{g}}} \coloneqq \begin{pmatrix} g_{11} & g_{12} \\ g_{12} & g_{22} \end{pmatrix}, \quad g_{ij} : \mathbb{R}^2 \to \mathbb{R}, \quad \boldsymbol{u} \mapsto \langle \boldsymbol{x_i}(\boldsymbol{u}), \boldsymbol{x_j}(\boldsymbol{u}) \rangle. \tag{8.5}$$

The first fundamental form contains only intrinsic information about the surface, like distances, areas and angles between curves on the surface, which is called the *inner geometry*.

That means $\underline{\underline{\boldsymbol{g}}}$ is independent of actual immersions of the surface in the $\mathbb{R}^3$. The term *first fundamental form* is often related to the equivalent formulation as a differential for an infinitesimal short distance $\mathrm{d}s$ on the surface:

$$\mathrm{d}s^2 = g_{11}\mathrm{d}{u_1}^2 + 2g_{12}\mathrm{d}u_1\mathrm{d}u_2 + g_{22}\mathrm{d}{u_2}^2. \tag{8.6}$$

This differential directly relates the metric tensor to distances between points on the surface and is often called the *metric* of the surface. With this information, we can calculate the length l of a curve $\boldsymbol{x}(u_1(t), u_2(t))$ on the surface that is given by two functions $u_1(t)$ and $u_2(t)$ with a parameter $t \in [t_0, t_1]$:

$$l = \int_{t_0}^{t_1} \sqrt{g_{11}\left(\frac{\mathrm{d}u_1}{\mathrm{d}t}\right)^2 + 2g_{12}\frac{\mathrm{d}u_1}{\mathrm{d}t}\frac{\mathrm{d}u_2}{\mathrm{d}t} + g_{22}\left(\frac{\mathrm{d}u_2}{\mathrm{d}t}\right)^2}\,\mathrm{d}t. \tag{8.7}$$

Depending on the actual metric, in some cases different realizations (different immersions) of surfaces with the same metric in the $\mathbb{R}^3$ are possible. Different immersions that feature the same metric are called *isometric* immersions. A simple example is a flat plane $\boldsymbol{x}(u,v) = (u, v, 0)^T$ with $g_{11} = g_{22} = 1$ and $g_{12} = 0$. It can be easily recognized, that the mantle of a cylinder $\boldsymbol{x}(u,v) = (\cos u, \sin u, v)^T$ has the same metric tensor. In conclusion the flat plane and the cylinder mantle are isometric immersions of the same metric. Actually, it can be shown, that even the mantle of a cone is isometric to the plane and the cylinder [49]. On the other hand, there are metrics that have only a single immersion (for example the only immersion of a metric with a constant positive Gaussian curvature is a sphere) and also metrics without any immersion in the $\mathbb{R}^3$ exist. The question whether an immersion exists or not plays an important role in the topic of the hyperbolic differential geometry [29, 47, 66, 103, 112], see also sections 8.1.3 and 10.4.

While the first fundamental form does not contain any information about an actual immersion, the *second fundamental form* $\underline{\underline{\boldsymbol{L}}}$ does. Similar to $\underline{\underline{\boldsymbol{g}}}$, we define $\underline{\underline{\boldsymbol{L}}}$ via a scalar product, but this time we use the second derivatives and the normal vector:

$$\underline{\underline{\boldsymbol{L}}} \coloneqq \begin{pmatrix} L_{11} & L_{12} \\ L_{12} & L_{22} \end{pmatrix}, \quad L_{ij} : \mathbb{R}^2 \to \mathbb{R}, \quad \boldsymbol{u} \mapsto \langle \boldsymbol{n}(\boldsymbol{u}), \boldsymbol{x}_{\boldsymbol{ij}}(\boldsymbol{u}) \rangle. \tag{8.8}$$

The second fundamental form contains information about the outer geometry, like curvatures and the orientation in the surrounding space. With the help of the first and the second fundamental form, the Gaussian curvature K, the product of the two principal curvatures, can be easily expressed as

$$K = \frac{\det\left(\underline{\underline{\boldsymbol{L}}}\right)}{\det\left(\underline{\underline{\boldsymbol{g}}}\right)}. \tag{8.9}$$

This equation describes a very easy way to calculate the Gaussian curvature K of a given immersion, but it gives a false impression of the nature of the Gaussian curvature. The appearance of $\underline{\underline{\boldsymbol{L}}}$ in eq. (8.9) implies that K is a property of the outer geometry, the actual immersion. In fact, the opposite is the case: The Gaussian curvature only depends on the inner geometry and is independent of any immersion in the $\mathbb{R}^3$. This is a fundamental result in the differential geometry and known as *Theorema Egregium* which was found by C. F. Gauss [61]. Thus, K can be expressed using only the first fundamental form, which is known

as the Brioschi formula [134]

$$K = \frac{1}{(g_{11}g_{22} - {g_{12}}^2)^2} \left(\begin{vmatrix} -\frac{1}{2}\partial v^2 g_{11} + \partial u_1 \partial u_2 g_{12} - \frac{1}{2}\partial {u_1}^2 g_{22} & \frac{1}{2}\partial u_1 g_{11} & \partial u_1 g_{12} - \frac{1}{2}\partial u_2 g_{11} \\ \partial u_2 g_{12} - \frac{1}{2}\partial u_1 g_{22} & g_{11} & g_{12} \\ \frac{1}{2}\partial u_2 g_{22} & g_{12} & g_{22} \end{vmatrix} - \begin{vmatrix} 0 & \frac{1}{2}\partial u_2 g_{11} & \frac{1}{2}\partial u_1 g_{22} \\ \frac{1}{2}\partial u_2 g_{11} & g_{11} & g_{12} \\ \frac{1}{2}\partial u_1 g_{22} & g_{12} & g_{22} \end{vmatrix} \right). \tag{8.10}$$

Consequently, in the little example the flat plane, the cylinder and the cone have the same Gaussian curvature $K = 0$. The main message in this section here is that we now have a direct link between the (Gaussian) curvature of a surface and the metric, i.e. local distances between points on the surface.

8.1.2. Changing the metric via swelling

Now we know a mathematical mechanism to deform the disk without external forces. The flat disk has a vanishing Gaussian curvature. By changing the metric, the Gaussian curvature increases or decreases, which must result in a curved shape. Consequently, the question arises: How can the metric of a flat disk be manipulated in a real experiment? The metric describes distances between points on the surface, so the distances on the surface have to be changed. One possible and easily feasible way is to induce a swelling process in the material of the disk. Swelling can be achieved by chemical or physical effects and was already used to deform flat disks in experiments [73, 110]. By swelling we mean a change of the rest lengths of fibers in the material, which starts and results in a force free, relaxed state (we discuss some special cases with remaining stresses later). To quantify the term swelling, we introduce a swelling factor α in a way that a fiber of the disk's material has the length s_0 in the force free rest state before the swelling. After the swelling process the fiber's rest length changes to $s = \alpha s_0$ and is still free of any forces. The value of α is reasonably found in the interval $\alpha \in (0, \infty)$. A value $\alpha > 1$ describes a swelling process, $\alpha < 1$ is related to shrinking (in the following we call both processes with $\alpha < 1$ and $\alpha > 1$ *swelling* due to simplicity) and $\alpha = 1$ is a neutral process without any changes. The case $\alpha = 0$ has to be excluded, because this would mean that all the material of the disk collapses to a single point, which is not a physically reasonable behavior. In this thesis, we define the swelling to be isotropic, i.e. fibers in all directions are swollen in the same manner. That means if the whole disk swells with a constant swelling factor α, then the radius changes to $R = \alpha R_0$ and the area to $A = \alpha^2 A_0$. A global constant swelling is equivalent to a rescaling of the coordinates and does not change the metric. Therefore, we do not use a constant swelling factor but a function $\alpha(r_0)$ depending on the radial coordinate r_0, which still satisfies the rotational symmetry. The index 0 at the radial coordinate indicates that this coordinate is related to the unswollen flat disk, because a point located at r_0 on the unswollen disk is not necessarily located at the same coordinate $r = r_0$ in the deformed state.

Now we have to investigate how swelling with $\alpha(r_0)$ changes the metric and the Gaussian curvature. We do not know the resulting immersion a priori. Therefore, we do not use the definition of the metric tensor to find the first fundamental form, but distances on the swollen surface together with the differential (8.6), see also [48, 110] for this argumentation. First of all, we switch to Gaussian normal coordinates (ρ, φ) to parametrize the surface. The polar angle φ remains the same as in the standard polar coordinates, but the radial coordinate ρ now describes the distance of a point to the origin of the coordinate system following the surface and not its projection to the $(z = 0)$-plane, as the standard radial coordinate r does. Despite being applied to different systems, the coordinate ρ is mathematically identical to the

arc length s of the contour line of an elastic capsule in the first part of this thesis. So only in case of a flat plane we have $\rho = r$, but in general ρ is greater than r and without knowing the actual immersion, r is not a useful coordinate anymore. Therefore, we primarily use r_0 and ρ in the following. The coordinate r_0 is related to the flat, unswollen disk, while ρ acts on the swollen disk.

In order to link r_0 and ρ, we consider a fiber in the disk in radial direction, starting in the disk's center. The length of this fiber, up to a point corresponding to r_0 is given by $\rho(r_0)$ with

$$\rho(r_0) = \int_0^{r_0} \alpha(r_0')\mathrm{d}r_0'. \tag{8.11}$$

Again, note the analogy to the capsule part, especially to eq. (3.5). Because of $\alpha > 0$ it follows that $\rho(r_0)$ is a bijective function and can be inverted to $r_0(\rho)$. After that, we consider the length of a fiber in circumferential direction. A fiber in shape of a circle with radius r_0 on the flat disk has the perimeter $P = 2\pi r_0$. The assumed isotropic nature of the swelling increases this fiber's length in the same way as it extends the radial fiber. The mentioned fiber is found at constant r_0 and together with the swelling factor $\alpha(r_0)$, which is independent of φ, we can calculate the fiber's length l_φ via

$$l_\varphi = \int_0^{2\pi} r_0\alpha(r_0)\mathrm{d}\varphi = 2\pi r_0\alpha(r_0). \tag{8.12}$$

As a consequence of that, the infinitesimal length element of an arbitrarily oriented fiber can be calculated with the differential

$$\mathrm{d}l^2 = \mathrm{d}\rho^2 + (r_0(\rho)\alpha(r_0(\rho)))^2\mathrm{d}\varphi^2. \tag{8.13}$$

In comparison to eq. (8.6), we find the metric of the swollen disk,

$$\underline{\underline{\boldsymbol{g}}} = \begin{pmatrix} 1 & 0 \\ 0 & r_0(\rho)^2\alpha(\rho)^2 \end{pmatrix}. \tag{8.14}$$

Using (8.10), the Guassian curvature is given by

$$K(\rho) = \frac{-\frac{\partial^2}{\partial\rho^2}[r_0(\rho)\alpha(r_0(\rho))]}{r_0(\rho)\alpha(r_0(\rho))} \tag{8.15}$$

in Gaussian normal coordinates. Using our knowledge about $\alpha(r_0)$, we can make some statements about the resulting shape of the swollen disk, especially by considering the sign of K. We demanded α to be always positive. Therefore, the denominator $r_0\alpha$ is also always positive and we only need to investigate the numerator now. There we find the second derivative of the term $r_0\alpha$, so the functional behavior of $r_0\alpha$ determines the sign of K. If the second derivative of $r_0\alpha(r_0)$ is positive, that means that the slope of $r_0\alpha(r_0)$ is a monotonically increasing function, then the resulting surface has a globally negative Gaussian curvature, a hyperbolic shape. A descriptive way to interpret this case is to make the simplified assumption, that $\alpha(r_0)$ is monotonically increasing. That means, that the disk has to be swollen more in the outer regions than near the center. The length of a fiber that forms a circle at the edge of the unswollen flat disk is increased during this kind of swelling. So, the fiber forms a kind of a wave instead of a planar circle to handle that additional length, which results in the hyperbolic shape illustrated in fig. 8.1. We implement this case later by swelling the outer region and shrinking the center of the disk. One example for a hyperbolic shape (that does

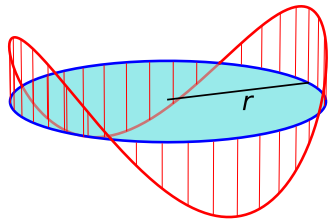

Figure 8.1.: Illustration of a fiber forming a hyperbolic 'wave'. In the initial state, a fiber forms the edge of a planar circle (blue). If the length of that fiber increases, while the radial coordinate r is not allowed to adjust freely, the fiber evades into the third dimension to store the additional length.

not satisfy our metric anyways) is a hyperbolic paraboloid, a saddle-like shape, where the 'wavelength' of the fiber at the edge is the half of the perimeter.

On the other hand, if the second derivative of $r_0\alpha$ is negative, we find a globally positive Gaussian curvature. That is, in a simplified consideration, the case when the disk swells stronger in the central region and less in the outer region. We implement that case by swelling the center and shrinking in greater distances. Examples for shapes with positive K are elliptic paraboloids and also a half sphere, which has a constant Gaussian curvature and also satisfies our metric. Thus, the sphere can be realized by our swelling program, see also section 10.4. In this thesis, we focus on these two general cases: Elliptic shapes with $K > 0$ and hyperbolic shapes with $K < 0$.

8.1.3. Non-Euclidean geometry

For a given swelling function $\alpha(r_0)$, we know the metric of the swollen disk, the target metric. But we also know, that not every metric has an immersion in the Euclidean space $\mathbb{R}^3$. So the question arises, which shape a swollen disk adopts, when no immersion exists. This leads to the topic of non-Euclidean geometry. If no immersion of the metric exists, not every fiber in the disk can take its new rest length and stresses in the material remain. Until now, we argued from a purely geometric point of view, but now the elasticity of the disk's material comes into play. If we ignore bending energies for the moment, a swollen disk with an existing immersion of the target metric will have a vanishing elastic energy, without any stresses. If the target metric cannot be reached because of the lack of an immersion, the actually taken shape will be the conformation which minimizes the elastic energy. Usually this is the shape that comes as close as possible to the target metric.

In order to simulate a system that could be easily reproduced in an experiment, we use a very simple swelling function $\alpha(r_0)$. We already know that $\alpha(r_0) = \text{const}$ does not change the metric, so we choose a piecewise constant α. We divide our disk in two parts: An inner disk with the radius R_{in} and a directly following outer annulus with inner radius R_{in} and outer radius R_0. We want α to be constant on the inner disk and the outer annulus, so we define

$$\alpha(r_0) = \begin{cases} \frac{1}{\alpha}, & r_0 \in [0, R_{\text{in}}] \\ \alpha, & r_0 \in (R_{\text{in}}, R_0] \end{cases} \tag{8.16}$$

with a constant swelling factor α. So, the rest length of a fiber in the outer annulus increases for $\alpha > 1$ and decreases for $\alpha < 1$. The inner disk acts exactly contrary. It is obvious that the inner disk and the outer annulus are not compatible at $r_0 = R_{\text{in}}$ for $\alpha \neq 1$, so even without a bending energy, there is no possible immersion. A swelling factor $\alpha > 1$ corresponds to the previously discussed case of a monotonically increasing swelling function and thus leads to a hyperbolic, saddle-like, shape. On the other hand, we expect an elliptic shape for $\alpha < 1$.

The same swelling function (8.16) was also used in ref. [110], which allows a comparison of the results in section 10.1.1. For an experimentalist it would be even easier to prepare a disk, where only a single part is swelling, while the other part is unchanged. But this experiment would be equivalent to the case that we have just discussed. As it was already mentioned, a

globally constant swelling does not change the metric and is equivalent to a rescaling of the coordinates. Consequently, we can perform another swelling process with a globally constant factor α after applying the swelling function (8.16). The resulting total swelling factor is $\alpha \cdot 1/\alpha = 1$ on the inner disk and $\alpha \cdot \alpha = \alpha^2$ on the outer annulus. In conclusion, applying our swelling function (8.16) is equivalent to swell only the outer annulus with a factor of α^2 and rescale the coordinate system by α.

8.2. Elastic model

In reality, there is also a bending energy in an elastic system. The rest state of our system is the flat plane, so every kind of bending out of this plane is punished by the bending energy. The consequences are quite extensive: A swollen disk in a completely relaxed state is impossible, there is always a finite elastic energy and the disk never takes a conformation that exactly satisfies the target metric, even if an immersion exists. But for thin disks with a thickness h that is small compared to the disk's radius R_0, $h \ll R_0$, the bending energy is actually quite small compared to the appearing stretching energy, so the deformed shape is very similar to the conformation predicted by the target metric. For all disks considered in this thesis, we always assume that the condition $h \ll R_0$ is satisfied. Completely analogously to the first part of this thesis about thin elastic capsules, we use the elastic theory of thin plates here, which means we focus on a two-dimensional model.

Even if it is small compared to the stretching energy, the additional bending energy provides effects that are impossible without. The bending energy and the stretching energy work against each other: In the case of swelling, the stretching energy is lowered by deforming the disk into an (elliptic or hyperbolic) curved shape, while the bending energy is minimal in the flat state. Consequently, the bending energy stabilizes the flat disk during the swelling and only when the swelling factor $\alpha(r_0)$ differs enough from the neutral constant $\alpha = 1$, a transition into a curved shape occurs. This is quite analogous to the competition between the elastic energy and the magnetic energy in the first part of this thesis about ferrofluid-filled capsules in uniform magnetic fields. In a similar way, this energetic competition is the base of pseudo-hysteresis effects that we investigate in section 10.2 and together with an additional energy barrier we see real hysteresis effects in sec. 10.3. That allows us to bypass the scallop theorem and create a microswimmer in section 11.1.

In the same way as in the part about the elastic capsules, we neglect the thickness h of our elastic system, so we have a two-dimensional system. The thickness only comes indirectly into play in terms of the bending energy.

8.2.1. Stretching energy

Elastic strains, that are the consequence of a deformation out of the reference shape, give rise to the elastic stretching energy. If the conformation of the disk exactly satisfies the target metric, the material is completely relaxed and the stretching energy vanishes. Any deformation into a shape apart from the target metric causes the disk to have a different metric. In the following, we denote the actual metric of the stretched disk with $\underline{\underline{\boldsymbol{g}}}$ and the relaxed target metric $\underline{\underline{\overline{\boldsymbol{g}}}}$. The elastic strain tensor can be expressed as the difference between the actual metric and the target metric [32, 48],

$$\epsilon_{ij} = \frac{1}{2}(g_{ij} - \overline{g}_{ij}). \tag{8.17}$$

Consequently, the whole stretching energy E_s can be expressed in terms of the metrics $\underline{\underline{\boldsymbol{g}}}$ and $\underline{\underline{\overline{\boldsymbol{g}}}}$. Analogously to ref. [48], we use a more general notation in covariant coordinates u_1, u_2

and contravariant coordinates u^1, u^2 in the following. The stretching energy E_s is quadratic in the strains and can be written as

$$E_\mathrm{s} = \int \frac{1}{8} A^{ijkl}(g_{ij} - \overline{g}_{ij})(g_{kl} - \overline{g}_{kl}) \sqrt{|\underline{\underline{\overline{g}}}|} \mathrm{d}u_1 \mathrm{d}u_2 \tag{8.18}$$

with

$$A^{ijkl} = \frac{Y_\mathrm{2D}}{(1-\nu^2)} \left(\nu \overline{g}^{ij} \overline{g}^{kl} + \frac{(1-\nu)}{2} (\overline{g}^{ik} \overline{g}^{jl} + \overline{g}^{il} \overline{g}^{jk}) \right). \tag{8.19}$$

Here, we use the Einstein notation, where a sum is taken over identical upper and lower indices. The contravariant reference metric tensor is defined via

$$\overline{g}^{ij} = \langle \boldsymbol{x}^{\boldsymbol{i}}(\boldsymbol{u}), \boldsymbol{x}^{\boldsymbol{j}}(\boldsymbol{u}) \rangle. \tag{8.20}$$

The integral in eq.(8.18) has to be taken over the whole surface. For deeper details of the derivation of this energy, as well as the bending energy in sec. 8.2.3, the reader may be referred to the refs. [32] and [48].

The surface energy

If an elastic disk is used as a microswimmer, the disk is surrounded by an external fluid. Therefore, an additional interfacial tension γ_S between the disk and the fluid exists. The energy related to the interfacial tension is proportional to the total area A:

$$E_\gamma = \gamma_\mathrm{S} A. \tag{8.21}$$

Due to the fact that the greatest part of the area change is caused by the swelling process, which is driven by a chemical or physical process that we do not want to regard in detail, we neglect the interfacial tension and set $\gamma_\mathrm{S} = 0$.

8.2.2. Spring-mesh model

To simulate a microswimmer moving in a surrounding fluid, we need to calculate elastic forces all over the disk in a dynamical simulation. Therefore, we need to discretize the elastic energies. The whole disk is modeled by a network of mechanical springs. The springs are connected to each other at the knots of the mesh. These knots are called *vertices*. The springs provide a linear force law. A spring i between two vertices at positions $\boldsymbol{r_1}$ and $\boldsymbol{r_2}$ exerts a force on the vertex at $\boldsymbol{r_2}$ which is given by

$$\boldsymbol{F_2} = -k_i(|\boldsymbol{r_2} - \boldsymbol{r_1}| - l_i) \frac{\boldsymbol{r_2} - \boldsymbol{r_1}}{|\boldsymbol{r_2} - \boldsymbol{r_1}|}, \tag{8.22}$$

and accordingly, the force on the other vertex is $\boldsymbol{F_1} = -\boldsymbol{F_2}$. The spring constant is k_i, while l_i describes the rest length of the spring. So the stretching energy of the spring can be calculated via

$$E_{\mathrm{s},i} = \frac{1}{2} k_i (|\boldsymbol{r_2} - \boldsymbol{r_1}| - l_i)^2. \tag{8.23}$$

The stretching energy of the whole disk then follows as a simple sum over all springs

$$E_\mathrm{s} = \sum_i E_{\mathrm{s},i}, \tag{8.24}$$

which is a discrete version of the continuous stretching energy (8.18). The difference between the actual length of a spring and its rest length is directly related to the difference between $\underline{\underline{\boldsymbol{g}}}$ and $\overline{\underline{\underline{\boldsymbol{g}}}}$. The vertex positions and rest lengths of the springs are given by the actual geometry of the mesh, so we only have the spring constant k as a free parameter to adjust our spring mesh to model the correct elastic behavior. It can be shown that the springs' constant is directly related to the two-dimensional Young's modulus of the modelled system [108, 131]. In a hexagonal mesh the relation between k and the elastic moduli is found to be

$$Y_{\mathrm{2D}} = \frac{2}{\sqrt{3}}k, \tag{8.25}$$

$$\nu = \frac{1}{3}. \tag{8.26}$$

To model a homogeneous material, we can simply adjust the spring constant k to get the desired Y_{2D}, but the surface Poisson ratio ν is fixed to the value of 1/3, which is a major disadvantage of spring mesh models. With other mesh geometries, different values for ν are possible, but they share the same drawback of being fixed and not freely adjustable. An extension of the simple spring mesh model would be necessary to model arbitrary systems [12, 130]. In our case here, we can accept to be limited to a fixed value of ν, because we are only interested in a general proof of concept. With the two-dimensional surface, the stretching energy is effectively independent of the discretization of the surface and in contrast to a one-dimensional or three-dimensional system, the elastic constants do not have to be adjusted if the discretization is refined. Due to the quadratic dependency on the metric differences in eq. (8.18), the length scale of the discretization is cancelled together with the two-dimensional surface element.

8.2.3. Bending energy

In contrast to the stretching energy, the bending energy depends not only on the first fundamental form, but also on the second fundamental form. Analogously to eq. (8.18), the bending energy E_{B} is quadratic in the deviations of the second fundamental form $\underline{\underline{\boldsymbol{L}}}$ from the second fundamental form of the reference shape $\overline{\underline{\underline{\boldsymbol{L}}}}$:

$$E_{\mathrm{B}} = \int \frac{h^2}{24} A^{ijkl}(L_{ij} - \overline{L}_{ij})(L_{kl} - \overline{L}_{kl})\sqrt{|\overline{\underline{\underline{\boldsymbol{g}}}}|}\mathrm{d}u_1\mathrm{d}u_2. \tag{8.27}$$

That means that differences in the curvature of the surface give rise to the bending energy. In our case of the initially flat disk, we have no spontaneous curvature and thus we have $\overline{\underline{\underline{\boldsymbol{L}}}} = \underline{\underline{\mathbf{0}}}$. In contrast to the stretching energy, the bending energy depends on the actual immersion in the Euclidean space. But on the other hand, the stretching energy is indirectly influenced by the actual immersion, because the disk always minimizes the sum of E_{S} and E_{B}.

In the previous section, we introduced a very simple spring mesh to model metric differences and to calculate stretching forces in the disk. Up to this point, the springs that come together at a mesh vertex can take arbitrary angles to each other. We need to define the bending energy (8.27) in our spring mesh. In order to do so, we can readjust the bending energy and replace the first and the second fundamental form with the mean curvature H and the Gaussian curvature K, because these quantities are much easier to implement in a spring mesh. Without the spontaneous curvature, $\overline{\underline{\underline{\boldsymbol{L}}}} = \underline{\underline{\mathbf{0}}}$, we find [48]:

$$\begin{aligned} E_{\mathrm{B}} &= \int \frac{h^2}{24} A^{ijkl} L_{ij} L_{kl} \sqrt{|\overline{\underline{\underline{\boldsymbol{g}}}}|}\mathrm{d}u_1\mathrm{d}u_2. \\ &= \int \frac{Y_{\mathrm{2D}} h^2}{24(1-\nu^2)}(4H^2 - 2(1-\nu)K)d\overline{A}. \end{aligned} \tag{8.28}$$

The integral is meant to run over whole surface of the disk, actually the surface of the target metric. The mean curvature H is defined as the mean value of both principal curvatures κ_ρ and κ_φ (at this point, there is no need to specify the exact directions of the principal curvatures):

$$H = \frac{1}{2}(\kappa_\rho + \kappa_\varphi). \tag{8.29}$$

The Gaussian curvature is also given as the product of the principal curvatures, $K = \kappa_\rho \kappa_\varphi$. By introducing the bending modulus κ_B in the same way as is the first part,

$$\kappa_\mathrm{B} = \frac{Y_\mathrm{2D} h^2}{12(1-\nu^2)}, \tag{8.30}$$

we can write

$$E_\mathrm{B} = \int \frac{1}{2}\kappa_\mathrm{B}(4H^2 + 2(\nu-1)K)\mathrm{d}\overline{A}. \tag{8.31}$$

Implementing this bending energy is not trivial, the mean curvature and the Gaussian curvature inside the mesh are needed. We relate these curvatures to the vertices in the mesh. From the relative positions of the neighbor vertices, the curvatures can be calculated. The discrete versions of the mean curvature and the Gaussian curvature is defined in section 9.2.

9. Numerical simulation

In the following sections we will give a brief overview about some properties of the numerical calculation of the disk's deformed shape by minimizing the total energy. We start with the creation of a spring mesh, a Delauney triangulation, followed by the definition of the discrete energies in this mesh, especially the definition of the curvatures. After that, we discuss the minimization process of the total energy and close the chapter with a presentation of dimensionless quantities and the natural units of the system.

9.1. Mesh creation

The goal of this section is to create a spring mesh with some special properties. On the one hand, the mesh has to cover the whole disk and represent its geometry, i.e. it has to cover the area of a circle. On the other hand, the mesh shall be as uniform and isotropic as possible to represent a uniform elastic material. Therefore, we choose a Delauney triangulation. The basic properties of Delauney triangulations were already introduced in sec. 3.2.2 in the first part of this thesis. Similarly, we use the Fade2D library [79] to create the mesh. As a control parameter for the discretization and the average spring size, we use the number of vertices n_B on the disk's boundary at $r_0 = R_0$, as a boundary condition. So, the vertices on the edge are placed at the positions

$$r_{0,\mathrm{B},i} = R_0, \quad \varphi_{\mathrm{B},i} = \frac{2\pi i}{n_\mathrm{B}}, \quad i \in [1, n_\mathrm{B}]. \tag{9.1}$$

In addition, we have another boundary condition to satisfy. The mesh has to represent the structure of the disk that is divided into an inner disk with radius R_in and an outer annulus in order to be able to implement the structure of the swelling function $\alpha(r_0)$ in eq. (8.16). We must be able to decide whether a spring belongs to the inner disk or the outer annulus. The consequence is that no spring, the connection between two vertices, is allowed to cross the edge of the inner disk at R_in, so *both* vertices of every spring fulfill either the condition $r_1, r_2 \leq R_\mathrm{in}$ or $r_1, r_2 > R_\mathrm{in}$. Therefore, we place a set of vertices at $r_0 = R_\mathrm{in}$ that form the edge of the inner disk. The number of vertices on this edge depends on the ratio R_in/R_0 so that the length of the springs on this edge is roughly the same than on the outer edge. We place $n_\mathrm{in} = n_\mathrm{B} R_\mathrm{in}/R_0$ (n_in is rounded up) points on the inner edge at positions

$$r_{0,\mathrm{in},i} = R_\mathrm{in}, \quad \varphi_{\mathrm{in},i} = \frac{2\pi i}{n_\mathrm{in}}, \quad i \in [1, n_\mathrm{in}]. \tag{9.2}$$

The algorithm which creates the triangulation also needs a minimum and a maximum value for the spring length in the mesh. We set the minimal spring length in the mesh l_min to 70 % of the spring length on the boundary, $l_\mathrm{min} = 0.7\, l_\mathrm{B}$ and the maximum length to 120 %, $l_\mathrm{max} = 1.2\, l_\mathrm{B}$. These values were estimated empirically as a good compromise between the mesh quality and a relative homogeneous spring length.

Results of the mesh creation are shown in fig. 9.1. The left side (a) shows the triangulation with $n_\mathrm{B} = 40$ vertices on the boundary and an inner radius of $R_\mathrm{in} = 0.5\, R_0$. The right side (b) features $n_\mathrm{B} = 120$ vertices and the same radius ratio. The black lines represent the springs in the mesh. The inner disk is highlighted in red and the outer annulus in blue. Note that the springs that form the edge of the inner disk are marked with thicker red lines.

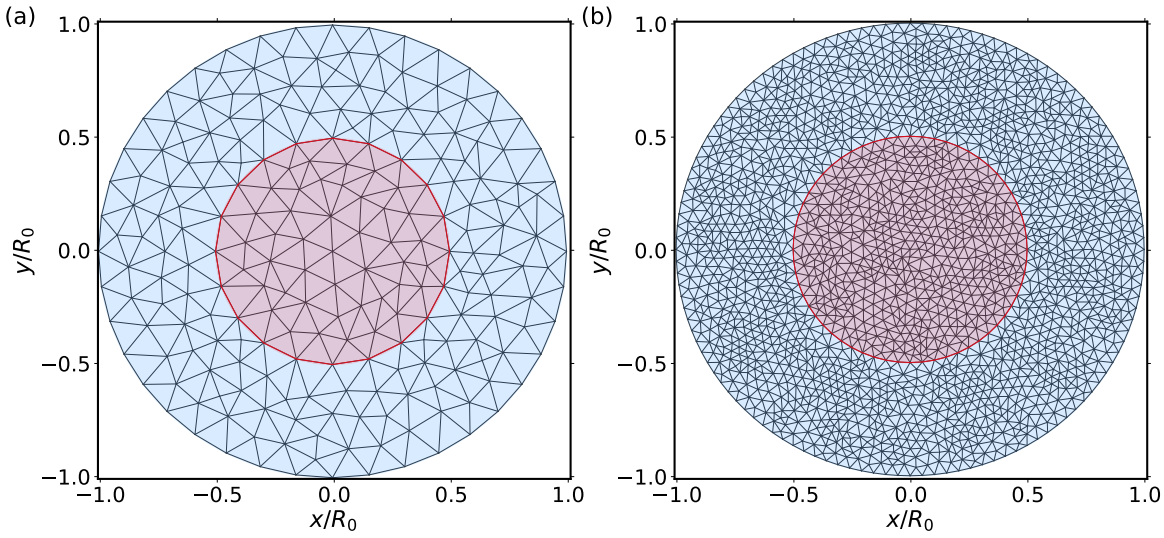

Figure 9.1.: Delauney triangulation of the flat disk for $R_{\text{in}} = 0.5\,R_0$ with (a): $n_{\text{B}} = 40$ and (b): $n_{\text{B}} = 120$.

Triangulating a flat plane results on average in a hexagonal mesh, because the hexagonal mesh is the perfect uniform triangulation for an infinite plane without any boundaries. In our Delauney triangulation, every vertex has about six neighbor vertices on average, for example triangulation (a) in fig. 9.1 features 5.62 neighbors per vertex and triangulation (b) 5.88 neighbors per vertex. In general, this value converges to six for higher n_{B} because the influence of the boundary decreases relative to the total number of vertices. Therefore, we can assume that we have a hexagonal mesh on average and set the Poisson ratio to the fixed value of $\nu = 1/3$, as mentioned in eq. (8.26).

9.2. Discrete energies

To calculate the total energy of the mesh, three different contributions have to be evaluated: The spring energy, the mean curvature part of the bending energy and the Gaussian curvature part of the bending energy. The spring energy is a simple sum over all springs as it was already introduced in eq. (8.24). Every spring i features the same spring constant $k_i = \sqrt{3}/2Y_{\text{2D}}$ and a rest length $l_i = \alpha(r_0)l_{i,0}$, which depends on the position and the original rest length $l_{i,0}$ that is determined by the Delauney triangulation of the flat disk.

The bending energy is transformed into a discrete version by replacing the integral in (8.31) with a sum over every vertex and the associated area around these vertices. Therefore, the curvatures have to be evaluated at each vertex:

$$E_{\text{B}} = \sum_i \kappa_{\text{B}} \left(2{H_i}^2 - \frac{2}{3} K_i \right) \frac{A_i}{3}. \tag{9.3}$$

The term $A_i/3$ describes the area that is associated with the vertex at $\boldsymbol{r_i}$ (blue area in fig. 9.2). This is one third of the area A_i of all triangles around the vertex. The reason behind that is that each triangle distributes its area among all of its three corner vertices.

There are different approaches to calculate discrete curvatures. One possibility is to calculate the mean curvature at the vertex $\boldsymbol{r_i}$ with the help of the inner angles of the triangles surrounding the vertex [40, 101]. In order to avoid excessively many evaluations of trigonometric functions, we use a different way here. The curvature of a surface is closely related to the variation of the surface area [49]. Thus, in a discrete system the equivalent is an area gradient.

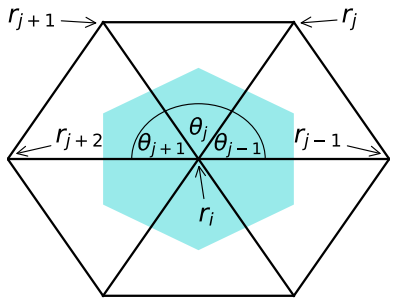

Figure 9.2.: Illustration of the neighborhood of a vertex i at $\boldsymbol{r_i}$ in the spring mesh. The highlighted area in blue is the surrounding area that is associated with the vertex. That is exactly one third of the area of all surrounding triangles. The angles θ_j are the angles between the vectors from the central vertex to two direct neighbor vertices j and $j+1$ at $\boldsymbol{r_j}$ and $\boldsymbol{r_{j+1}}$. If the central vertex and all of its neighbors are located in the same plane, then $\sum \theta_j = 2\pi$. Otherwise, this is in general not the case.

The area gradient $\nabla_i A_i$ is the gradient of the area A_i around the vertex with respect to its own coordinates $\boldsymbol{r_i}$. Such an area gradient can be calculated using only basic mathematical operations on the vertex coordinates. We implement H in form of [22]

$$H_i = \frac{3}{2}\frac{|\nabla_i A_i|}{A_i}. \tag{9.4}$$

Such implementations of the mean curvature are known to cause instabilities and non-physical behavior when the vertex forms a very sharp corner, which simply means that the discretization is not sufficiently fine in that case. But this property is no problem for the simulation of the deformation of the elastic disk, because such high curvatures do not occur.

Finally knowing the mean curvature in the spring mesh, we still need an expression for the Gaussian curvature. The Gaussian curvature can be calculated using the inner angles θ_j at the vertex $\boldsymbol{r_i}$ in its neighbor triangle j with the corner vertices $\boldsymbol{r_i}$, $\boldsymbol{r_j}$ and $\boldsymbol{r_{j+1}}$, see fig. 9.2. This is a direct consequence of the Gauss-Bonnet-theorem where the boundary integral over the geodesic curvature can be transformed into a sum over the angles between the edges [22, 101]:

$$\begin{aligned} \iint_{A_i/3} K_i \mathrm{d}A &= 2\pi - \sum_j \theta_j \\ \Rightarrow K_i &= (2\pi - \sum_j \theta_j)/(A_i/3). \end{aligned} \tag{9.5}$$

This version of the Gaussian curvature is valid for every vertex inside the mesh surrounded by other vertices. Therefore, we cannot calculate the Gaussian curvature with this method on the boundary of the mesh. A modification would be needed, but because of the very limited influence of the boundary, we ignore the bending energy on the boundary and set

$$H_i = 0, \quad K_i = 0 \quad \text{for} \quad r_{0,i} = R_0. \tag{9.6}$$

Now we are able to calculate the total energy of the mesh, the sum of the stretching energy in all springs and the bending energy in the vertices.

9.3. Energy minimization

As a physical system tries to minimize its energy, the preferred shape of the disk is the shape which belongs to the global energy minimum. In case of the unswollen initial disk, $\alpha(r_0) = 1 = \text{const}$, this global minimum is the flat disk with $E = E_\mathrm{s} + E_\mathrm{B} = 0$. For every change of α, the vertices of the mesh have to be moved until the new minimum of the energy is found. This minimization is realized in a systematic way by a minimization algorithm. For the calculation of the dry deformation, without any hydrodynamics, which is added later, a Broyden-Fletcher-Goldfarb-Shanno (BFGS) algorithm [106] was used in this thesis with an

implementation from the GNU scientific library [55]. The BFGS algorithm is a quasi-Newton method. The basic idea of the algorithm is to find the root of the energy gradient with respect to the vertex coordinates. The Hessian matrix of the energy is not calculated explicitly but approximated by several gradient evaluations. Therefore, the BFSG algorithm is not a real Newton method but a quasi-Newton method. The gradient itself is given in an analytical form to the algorithm.

As it is the case for every derivative of a Newton method, the BFGS algorithm cannot guarantee the convergence of the energy minimization. Therefore, we try to ensure that we start the algorithm in a local area around the desired minimum in the energy hyperplane. We start with the well-known state of the relaxed flat disk and change α in small steps until the desired swelling is reached. After each step the energy is minimized, and the system is translated into its new ground state. In order to have the ability to leave small local energy minima or metastable states, we add a function to 'shake' the vertices. Shaking means that each vertex is moved over a random distance δ_i (up to a prescribed maximum value $\delta_{\max}$) in a random direction:

$$\boldsymbol{r_{i,\mathrm{new}}} = \boldsymbol{r_{i,\mathrm{old}}} + \delta_i \begin{pmatrix} \cos\phi_i \sin\theta_i \\ \sin\phi_i \sin\theta_i \\ \cos\theta_i \end{pmatrix}. \tag{9.7}$$

Three random numbers are needed per vertex: $\delta_i/R_0 \in [0, \delta_{\max}/R_0]$, $\phi_i \in [0, 2\pi)$ and $\theta_i \in [0, \pi]$. It should always be ensured that the maximum distance of the shaking is small compared to the rest length of the springs in the mesh $\delta_{\max} \ll l_j$. Thus, we can interpret the artificial shaking as a kind of thermal fluctuations. The most important example, where the shaking is needed, is directly in the beginning when the simulation starts with the flat disk. Even if α is changed drastically, the minimizing algorithm will always find a local minimum where the disk is still flat and only stretched but not curved. The reason is simple: All components of the energy gradient, that belong to directions normal to the surface, are zero. Thus, the minimizing algorithm does not move any vertex out of the plane. The shaking, however, allows to leave this local minimum, even with quite small moving distances.

9.4. Dimensionless quantities

In order to extract the actual control parameters of the system and being able to avoid unit conversions, we rescale all physical quantities with natural units of the system and get dimensionless reduced quantities. Therefore, we have to define a set of basic units of the system. We choose the radius of the initial relaxed disk, R_0, as the length unit and the spring constant in the outer annulus, k_{out}, as the unit related to forces. Table 9.1 summarizes the most important quantities in natural units. This list of dimensionless quantities is expanded in sec. 11.2.3 with hydrodynamic quantities. If it is not explicitly stated in another way, all physical quantities are always meant to be measured in these units. As for the elastic capsules, we can also define the dimensionless ratio between the Young modulus and the bending modulus, the Föppl-von Kármán number γ_{FvK} [74, 118]:

$$\gamma_{\mathrm{FvK}} = \frac{Y_{\mathrm{2D}} R_0^2}{\kappa_{\mathrm{B}}} = 12(1-\nu^2)\frac{R_0^2}{h^2}. \tag{9.8}$$

Higher Föppl-von Kármán numbers describe elastic systems that are easier to bend, while lower γ_{FvK} correspond to thicker plates with a higher bending resistance.

Finally, we have four dimensionless control parameters defining the system. These are the Föppl-von Kármán number controlling the relation between the stretching and the bending energy, the ratio $R_{\mathrm{in}}/R_{\mathrm{out}}$ defining the geometric relation between the inner disk and the

lengths	spring constants
$\tilde{x} = x/R_0, \quad \tilde{y} = y/R_0, \quad \tilde{z} = z/R_0, \quad \tilde{r} = r/R_0$	$\tilde{k} = k/k_{\text{out}}$
areas	energies
$\tilde{A} = A/R_0^2$	$\tilde{E} = E/(k_{\text{out}}R_0^2)$
curvatures	forces
$\tilde{H} = HR_0, \quad \tilde{K} = KR_0^2$	$\tilde{F} = F/(k_{\text{out}}R_0)$
Young moduli	bending moduli
$\tilde{Y}_{\text{2D}} = Y_{\text{2D}}/k_{\text{out}}$	$\tilde{\kappa}_{\text{B}} = \kappa_{\text{B}}/(k_{\text{out}}R_0^2)$

Table 9.1.: Summary of dimensionless quantities.

outer annulus and similarly the ratio $k_{\text{in}}/k_{\text{out}}$ controlling the relation between the elastic properties of the inner disk and the annulus. The final control parameter, which is changed most frequently, is the swelling factor α controlling the target metric.

10. Dry deformation results

In this chapter, the numerical results of the energy minimization are presented. We start with a general analysis of the two possible types of deformed shapes: elliptic and hyperbolic shapes. The Gaussian curvature is analyzed in more detail and compared to experiments from the literature. After that, a complete *deformation cycle* is defined. We analyze the energy, the shape and the stability of the disk for a whole deformation cycle in order to discuss numerical pseudo-hysteresis effects. Based on this discussion, a critical swelling factor α_c can be defined, followed by a short discussion about consequences for microswimmers. After that, we introduce an additional potential energy for the disk, a modified Lennard-Jones potential imitating a van der Waals interaction, that leads to a real hysteresis. The topic of the last section of this chapter is the question how a shape with constant Gaussian curvature is realizable.

10.1. Elliptic and hyperbolic shapes

We implement the piecewise constant swelling function (8.16) in the spring mesh and minimize the energies from the previous chapter with a value of α deviating sufficiently enough from 1 (the question what 'enough' means is a topic of sec. 10.2). This leads to an elliptic or hyperbolic shape, as it was already implied in sec. 8.1.2. In this section, an example calculation is presented that tries to reproduce experiments performed by Pezulla et al. [110]. In these experiments, the disk was constructed from two different materials, one material for the inner disk and another one for the outer annulus. The three-dimensional Young modulus, Y_{2D}/h was given by $Y_{2D,in}/h = 2.3 \cdot 10^5\, N/m^2$ for the material of the inner disk and $Y_{2D,out}/h = 9.6 \cdot 10^5\, N/m^2$ in the outer annulus. So, in natural units we have now $k_{out} = 1$ and $k_{in} = 2.3/9.6\, k_{out} \approx 0.24\, k_{out}$. The disk's thickness was $h = 1.6\,\text{mm}$ with a total radius of $R_0 = 12\,\text{mm}$, so we have $h = 1.6/12\, R_0 \approx 0.13\, R_0$ in our simulation, which results in $\gamma_{FvK} = 600$. The elliptic shape is adopted for $\alpha < 1$. Figure 10.1 (a) and (b) show the elliptic shape with $\alpha = 0.96$ for two different discretizations with $n_B = 40$ and $n_B = 120$ vertices on the boundary. The inner disk was chosen to have a radius of $R_{in} = 0.5\, R_0$. The springs which belong to this inner disk are stretched by the factor of $1/0.96 \approx 1.042$ and are drawn in red in the figure, while the springs of the outer annulus shrink by 4 % and are marked in blue. A dome-like shape occurs, which shows a very good rotational symmetry, as far as the discretization allows. Even though the springs' rest lengths were only changed by about 4 %, the resulting dome shape has a total height of about $\Delta z \approx 0.23\, R_0$. That shows directly that even with small amounts of swelling, high deformations of a disk are possible, which feeds the hope that applications of swollen disks as microswimmers are possible. The resulting dome-like shape can be easily descriptively understood: The ring of springs that form the boundary of the disk has a perimeter of $P_0 = 2\pi R_0$ and tries to reduce its perimeter due to the shrinking to $P = 2\pi\alpha R_0 = 0.96 \cdot 2\pi R_0$ (the perimeter in fig. 10.1 (b) is found to be $\approx 0.959 \cdot 2\pi R_0$). The swelling of the inner regions of the disk has the consequence that the swollen material does not find enough area inside the inner circle. So, the inner material bends into the third dimension and forms a dome in order to store its increased area.

On the other hand, the hyperbolic shape is the result of $\alpha > 1$, shown in fig. 10.1 (c) and (d) with $\alpha = 1.04$ and the same settings as before. In this case, it is exactly the other

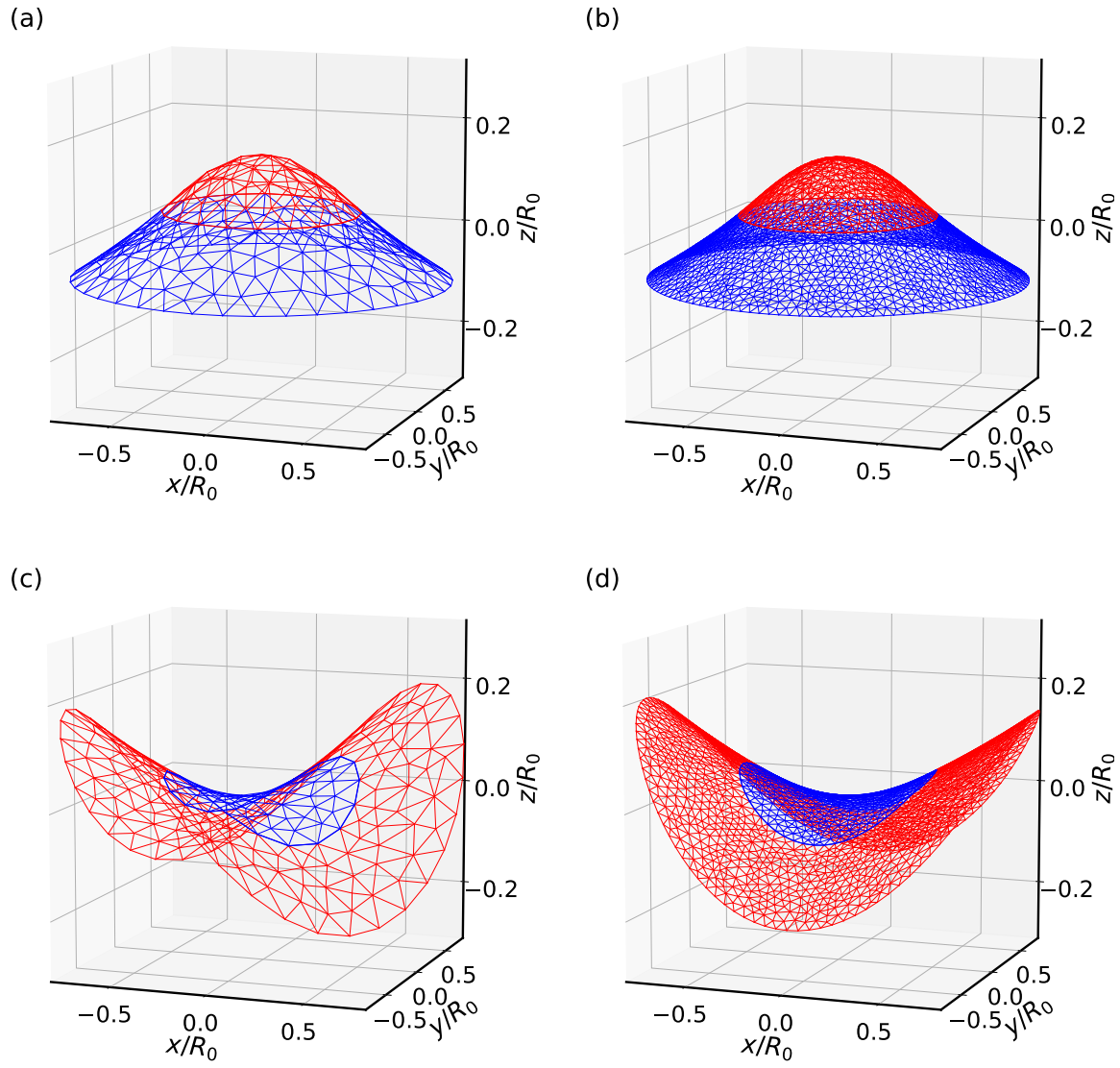

Figure 10.1.: Deformed meshes for a disk with $R_{\text{in}}/R_0 = 0.5$, $\gamma_{\text{FvK}} = 600$ and $k_{\text{in}}/k_{\text{out}} = 0.24$. The number of boundary vertices is $n_{\text{B}} = 40$ for (a) and (c) and $n_{\text{B}} = 120$ for (b) and (d). The upper plots (a) and (b) show the shapes of minimal energy for $\alpha = 0.96$ while (c) and (d) feature $\alpha = 1.04$. Swollen springs are plotted in red while shrunk springs are represented in blue.

way round: The inner disk shrinks by the factor $1/1.04 \approx 0.962$ and the outer annulus is stretched by additional $4\,\%$ to the rest lengths. This results in a saddle-like shape which has similarities with a hyperbolic paraboloid. This hyperbolic shape has obviously lost the rotational symmetry but features other symmetries. The deformation is very symmetrical in a way that the shape is invariant to a rotation by an angle of π around the z-axis. In addition, the center of mass still lies in the central point of the mesh, in contrast to the elliptic dome, where the mesh's central point sits on top. Furthermore, the shape is invariant to a rotation by $\pi/2$ around the z-axis with an addition mirroring at the $(z = 0)$-plane $(z \to -z)$. That means that the 'top' and the 'bottom' of this saddle shape cannot be distinguished. The fatal consequence of this symmetry is that a disk, which is deformed into this shape, is not able to swim, see also sec. 11.3 for a more detailed discussion.

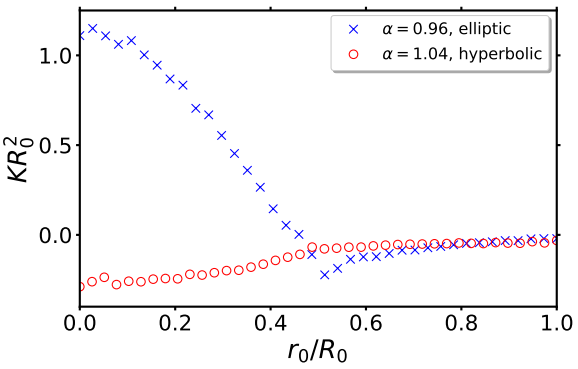

Figure 10.2.: Gaussian curvature K as a function of the flat disk's radial coordinate r_0 for the elliptic shape in fig. 10.1 (b) and the hyperbolic shape in fig. 10.1 (d). The Gaussian curvature was calculated as an average value over circular rings with a thickness of $\Delta r = 0.025\, R_0$.

The descriptive explanation for this kind of shape is also easy to understand. In contrast to the elliptic shape, the perimeter of the boundary circle now increases but the material in the inner region shrinks. There is not enough material in the central region to cover the whole area of the boundary circle. Instead, the outer regions form a kind of wave to store their additional material. The wavelength of this wave is found by a consideration of the energies: A wavelength of half the perimeter with two wave peaks is the highest possible non-trivial wavelength that does not result in a flat disk. A smaller wavelength with more wave peaks would be possible in principle, but leads to a higher curvature and thus a higher bending energy.

The Gaussian curvature as a function of the radial coordinate corresponding to the elliptic shape in fig. 10.1 (b) and the hyperbolic shape in fig. 10.1 (d) is shown in fig. 10.2. In the elliptic case, the curvature has its maximum in the middle, at the highest point of the dome and then drops rapidly to even slightly negative values in the outer annulus with the minimum at $r_0 = R_{\text{in}}$. The hyperbolic shape shows a more monotonous behavior. The minimum is located in the middle of the saddle and then tends towards zero at the edge.

10.1.1. Comparison with experiments

In the following, we try to compare our numerical results with experimental and numerical results from Pezulla et al. [110]. Therefore, the focus is set to the Gaussian curvature as it is a quantity which is easy to compare. In the following, a brief presentation of the work by Pezulla et al. is given first.

The experimental part consisted of a set of disks with a total radius of $R_0 = 12\,\text{mm}$, as it was already mentioned in the previous section. Several disks were constructed with different inner radii R_{in} between 5 mm and 11 mm. The materials used in the experiment are two different types of polyvinylsiloxane, a soft type for the inner disk and a harder one for the outer annulus. The swelling process itself was driven by a diffusion process of free polymer chains. These free chains move from the inner disk, which is the region of higher density, to the outer annulus, the region of lower density. As a result, the inner disk shrinks and the annulus swells until a steady state is reached, which is the case after about 40 hours, so a hyperbolic saddle-like shape is the result. This system is in general not suitable as a microswimmer, as it is too big (see the discussion about low Reynolds numbers in sec. 11.1.1) and the deformation process is too slow. However, it is an excellent test case for our dry deformation model. Due to its diffusive nature, the swelling factor α in the steady state depends on the ratio R_{in}/R_0 and can be approximated by

$$\alpha = \left[1 + 0.54 \left(\frac{R_{\text{in}}}{R_0}\right)^2 \left(1 - \left(\frac{R_{\text{in}}}{R_0}\right)^2\right)\right]^{\frac{1}{3}}. \tag{10.1}$$

Figure 10.3 shows the Gaussian curvature for different ratios R_{in}/R_0 with the corresponding swelling factor from eq. (10.1). In order to investigate the Gaussian curvature as a function of the radial coordinate, we calculate $K(r)$ as mean values over the whole polar angle φ in small circular rings. The radius of the inner disk was varied from 4 mm (a) to 11 mm (h) while the outer radius stayed constant at $R_0 = 12$ mm. The red markers show experimental data from Pezulla et al., while the black lines show the results from our spring mesh model. In fig. 10.3 (a) and (b) is no curvature visible, because α was too close to 1 (1.025 and 1.033) so that the disk remained flat in the simulation. When a transition to a saddle shape occurs, the behavior of the Gaussian curvature is qualitatively the same for each radius ratio as it was already seen in fig. 10.2. The lowest curvature (the most strongly curved region, since the curvature is negative) is found in the center of the saddle, stays nearly constant in the inner region of the inner disk and then starts to increase strongly. The region of highest slope is found close to the edge of the inner disk, where the different materials and spring with different rest lengths meet each other. Finally, the curvature increases only slightly in the outer region.

The available experimental data show a quite different behavior. While the accordance in the central region of the inner disk is not that bad, the strong increase of the Gaussian curvature is missing. In the experiment, the Gaussian curvature stays nearly constant over a quite large distance and changes slightly near the edge. On the other hand, a high agreement between the simple spring model and the experiment would be very surprising for different reasons. First, the Poisson ratio in our model is fixed to $\nu = 1/3$, while the material used in the experiment features $\nu = 1/2$. And second, the piecewise constant swelling function $\alpha(r_0)$ is a very rough assumption and the swelling factor (10.1) is also based on approximations and simplifications. The real swelling function $\alpha(r_0)$ is probably not piecewise constant. The swelling function calculated in sec. 10.4 in order to achieve a constant negative Gaussian curvature could be a better approximation.

Due to the fact that nearly constant Gaussian curvatures were observed in the experiment, a constant mean value $\overline{K}$ is now calculated. While Pezulla et al. used the whole disk to calculate this value, we restrict the mean value to the inner regions of nearly constant K in the spring mesh model, namely $r < 1/2\, R_{in}$. Figure 10.4 compares numerical results from the spring mesh model with experimental and numerical results from Pezulla et al., which were

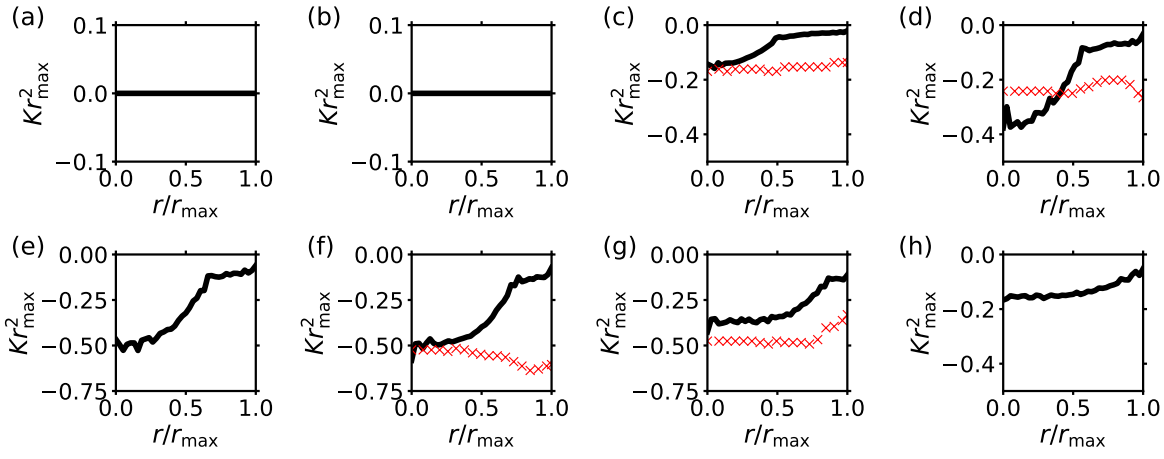

Figure 10.3.: Gaussian curvature as a function of the radial coordinate r for different radius ratios R_{in}/R_0 and swelling factors α. Red crosses denote experimental data by Pezulla et al. [110]. (a): $R_{in}/R_0 = 4/12$, $\alpha = 1.017$; (b): $R_{in}/R_0 = 5/12$, $\alpha = 1.025$; (c): $R_{in}/R_0 = 6/12$, $\alpha = 1.033$; (d): $R_{in}/R_0 = 7/12$, $\alpha = 1.039$; (e): $R_{in}/R_0 = 8/12$, $\alpha = 1.043$; (f): $R_{in}/R_0 = 9/12$, $\alpha = 1.042$; (g): $R_{in}/R_0 = 10/12$, $\alpha = 1.037$; (h): $R_{in}/R_0 = 11/12$, $\alpha = 1.024$.

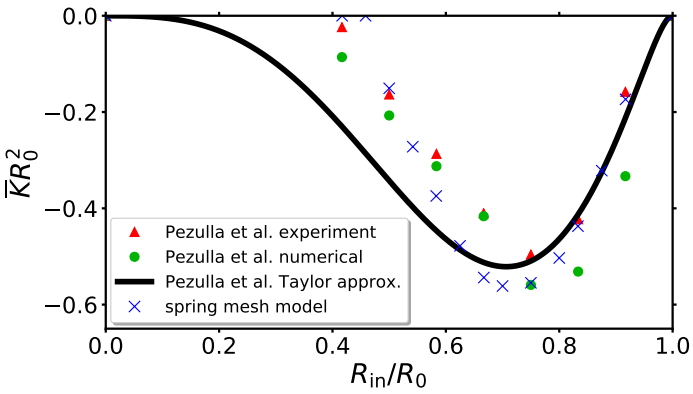

Figure 10.4.: Mean values of the Gaussian curvature for different radius ratios R_{in}/R_0. Blue crosses denote numerical data from the spring mesh model. Green circles are numerical data calculated with the COMSOL software and red triangles show the corresponding experimental data by Pezulla et al. [110]. The black line shows the approximation given by eq. (10.2).

generated by the COMSOL Multiphysics software with a Neo-Hookean material model. A Taylor approximation of an analytical solution of the elastic model used by Pezulla et al. is denoted by the black solid line. This approximation is given by

$$\overline{K}R_0^2 \approx -0.043\tilde{Y}(R_{in}/R_0)^3 \frac{(1-(R_{in}/R_0)^2)(1-(R_{in}/R_0)^3)}{(R_{in}/R_0)^6(1-\tilde{Y})+\tilde{Y}}, \tag{10.2}$$

with $\tilde{Y} = Y_{2D,out}/Y_{2D,in} = k_{out}/k_{in} \approx 4.17$. Again, α is given by eq. (10.1). The swelling factor was too close to one for $R_{in}/R_0 \lesssim 0.5$ to deform the flat disk into a saddle shape. Considering the simplicity of the spring mesh model, there is a quite good agreement to the experimental data. The minimum of the Gaussian curvature is found at $R_{in}/R_0 \approx 0.75$ in the experiment, which is also captured quite well by the spring mesh model. After all, our simple model shows here the same qualitative behavior as the experiment and also does not deviate that much quantitatively.

10.2. The deformation cycle

In this section we are not only interested in a specific deformed shape, but in a whole cycle of deformation. That means we start at $\alpha = 1$ with the piecewise constant swelling function and increase α to a maximum α_{max} (or decrease to α_{min} analogously) in small steps $\Delta\alpha$. After each small step, the energy is minimized. Once α_{max} or α_{min} is reached, the direction is changed and we go back to the original configuration of $\alpha = 1$ with the same step size. As an example, we use the same system as in the previous section, with $R_{in}/R_0 = 0.5$ and $n_B = 120$ boundary vertices. At each step, the vertices are slightly shaken, so it is possible to observe the first occurrence of a curved shape. Together with the point when the curved shape becomes flat on the way back to $\alpha = 1$, we can determine an area of numerical pseudo-hysteresis. In addition, we calculate the Hessian matrix of the disk's total energy and its eigenvalues with respect to the vertex coordinates after each step. Negative eigenvalues indicate an unstable shape and that there is a possible deformation mode that lowers the energy. So if the flat disk with $\alpha \neq 1$ has a lowest eigenvalue $\lambda_{min} < 0$, then a spontaneous deformation to a curved conformation should happen for this α. Figure 10.5 shows a full deformation cycle of an elliptic shape ($\alpha_{min} = 0.96$) and a hyperbolic shape ($\alpha_{max} = 1.04$). The first plot (a) features the total energy and its parts: The spring energy, the mean curvature part of the bending energy and the Gaussian curvature part. The second plot (b) shows the height Δz and the lowest eigenvalue of the Hessian matrix, λ_{min}. Note that $-\lambda_{min}$ is plotted in order to reach positive values due to clarity. Starting at $\alpha = 1$, the disk first remains flat (white area), while the total energy increases due to the spring energy in a parabolic way. The height of the shape is zero accordingly and λ_{min} is also zero, which means that the flat disk is still

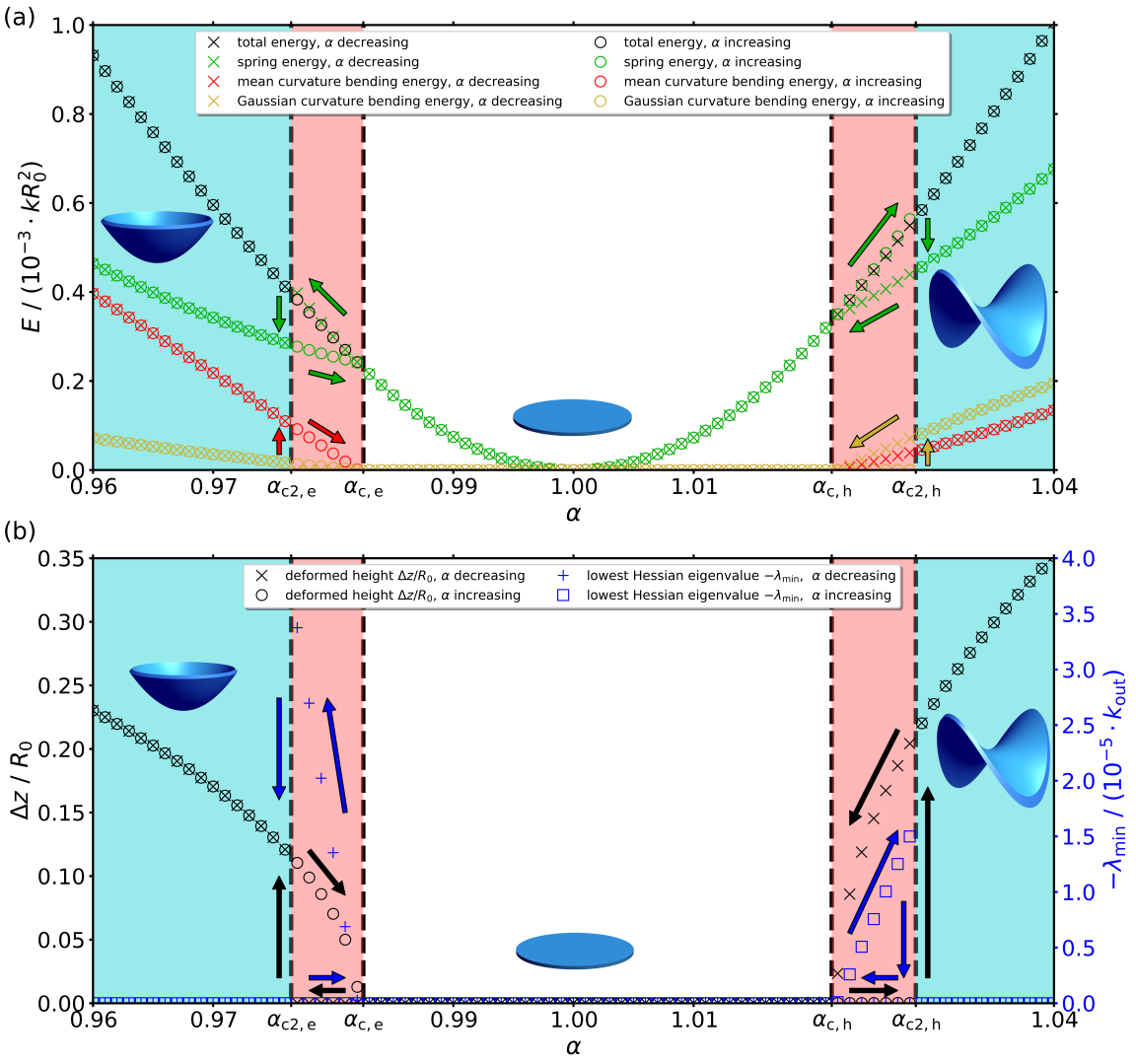

Figure 10.5.: Energies (a), shape's height Δz and negative of the lowest Hessian eigenvalue $-\lambda_{\min}$ (b) in the spring mesh model as functions of the stretch factor α. Circles denote numerical values calculated with increasing α, while crosses are related to decreasing α. The disk is always flat if it is located in the white area and always curved in the blue regions. The blue shapes illustrate the corresponding conformations of the disk. The region of pseudo-hysteretic effects is marked in red. The arrows illustrate the directions inside the hysteresis loops. The simulated disk featured a mesh with 120 boundary vertices, $R_{\text{in}}/R_0 = 0.5$, $\gamma_{\text{FvK}} = 600$, $k_{\text{in}}/k_{\text{out}} = 0.24$ and a maximum shaking movement distance of $\delta_{\max} = 5 \cdot 10^{-4} R_0$. Note that the total energy and the spring energy are identical in the flat state.

stable. Then we reach a critical point, $\alpha_{\text{c,e}}$, for decreasing and $\alpha_{\text{c,h}}$ for increasing α, the black dashed lines at the edge of the white area. At these points, $\lambda_{\min}$ becomes negative, which indicates that a deformation mode exists that lowers the energy. The disk still stays flat in the red region until it finally reaches the points $\alpha_{2,\text{e}}$ and $\alpha_{2,\text{h}}$, where the transitions to the elliptic and hyperbolic shapes occur. At this point, the spring energy is drastically reduced, while the bending energies jump from zero to a significant percentage of the total energy. In addition, the lowest Hessian eigenvalue, whose absolute has grown rapidly in the red region, jumps back to zero. So, the curved shapes are stable. Going on to $\alpha_{\min}$ and $\alpha_{\max}$, nothing of special interest happens anymore, only the energies further increase.

Changing now the direction, increasing α in the elliptic case and reducing it in the hyperbolic case, we go exactly the same way back in a completely reversible manner until the red areas are reached ($\alpha_{c2,e}$ and $\alpha_{c2,h}$). Entering these areas now, the shapes stay curved. In addition, λ_{min} stays zero, indicating that the curved shapes are still stable in the red areas. To underline this, the total energy is now slightly lower than it was before at exactly the same α in the flat state. At the other end of these areas, the curved shapes smoothly translate to a flat disk. The height Δz as well as the bending energies move to zero in a steady way without a jump. As a consequence, the total energies of the first direction and of the way back converge and meet at this point, where the curved shapes cease to exist. The point where that happens, we call it $\alpha_{c3,e}$ and $\alpha_{c3,h}$, seems to be the same point, where the flat disk first became unstable. So it seems that $\alpha_{c3,e} \approx \alpha_{c,e}$ and $\alpha_{c3,h} \approx \alpha_{c,h}$. This question is also further investigated in fig. 10.6. Finally, the ways back to $\alpha = 1$ are again completely the same as in the forward direction of the deformation cycle.

After all, we can conclude, that the red areas are the regions of a pseudo-hysteresis, where the flat disk is unstable and has a higher energy than the curved shapes, but external distortions are needed to induce the transition in the numerics. This pseudo-hysteretic behavior could in principle be the engine of the disk used as a microswimmer. The critical points $\alpha_{c,e}$ and $\alpha_{c,h}$ can be exactly determined with the Hessian eigenvalues. But this is impossible for the points of the transition from the flat disk to the curved conformation at $\alpha_{c2,e}$ and $\alpha_{c2,h}$. These positions depend on the distortions, the shaking of the vertices. If the fluctuations are high enough, or if the vertices are moved into the correct direction (given by the corresponding eigenvector of the Hessian matrix), then the transition occurs instantly at $\alpha_{c,e}$ and $\alpha_{c,h}$. So the actual size of the pseudo-hysteresis area is related to the fluctuations in the system. In a real system, it may be possible that the region of pseudo-hysteresis is nearly non-existent. We address this problem in the next section 10.3 by introducing an additional energy barrier, which ensures the existence of a real hysteretic behavior.

Having understood the general behavior of the pseudo-hysteresis in this system, we now focus on the question how the position of the pseudo-hysteresis loop and the shape transition can be manipulated natively, independently from an additional energy barrier. This is of tremendous interest for experiments, as some materials may only support stretch factors very close to one, so we want to have the possibility to trigger shape transitions at best for arbitrary values of α. As the transition to the curved shape at a distinct distance to $\alpha = 1$ is the result of the interplay between the spring energy and the bending energy, it is obvious to use the bending energy as a control mechanism for the pseudo-hysteresis. The bending energy is proportional to the bending modulus κ_B, which depends in turn on the Young modulus Y_{2D} and the thickness h of the disk, see the definition (8.30). Since the spring energy is independent of h, the thickness provides a valid tool to control the position as well as the size of the pseudo-hysteresis region, $|\alpha_c - \alpha_{c2}|$. An analytic investigation on the buckling threshold, the thickness that is needed to get a bended shape in a related system, can be found in ref. [48]. Figure 10.6 shows the critical $\alpha_{c,e}$ and in addition the stretch factor where the curved shape becomes flat again, $\alpha_{c3,e}$, as functions of the thickness h for two different discretizations of otherwise the same system as in fig. 10.5. We focus on $\alpha_{c,e}$ and $\alpha_{c3,e}$ here, since $\alpha_{2,e}$ in contrast depends primarily on fluctuations, which would render a systematic investigation quite arbitrary. At first, fig. 10.6 confirms the observation $\alpha_{c,e} = \alpha_{c3,e}$. So the critical swelling factor $\alpha_{c,e}$, where the curved shape can exist for the first time, indicated by $\lambda_{min} < 0$, is identical to the point where the curved shape becomes flat again in the other direction. If the system had a real hysteresis, $\alpha_{c,e} \neq \alpha_{c3,e}$ would be the consequence. Secondly, there is a nearly quadratic relation between α_c and the thickness h, which indicates a linear dependence on the Föppl-von Kármán number. So, we can conclude

$$|1 - \alpha_c| \sim h^2 \sim \gamma_{FvK}. \tag{10.3}$$

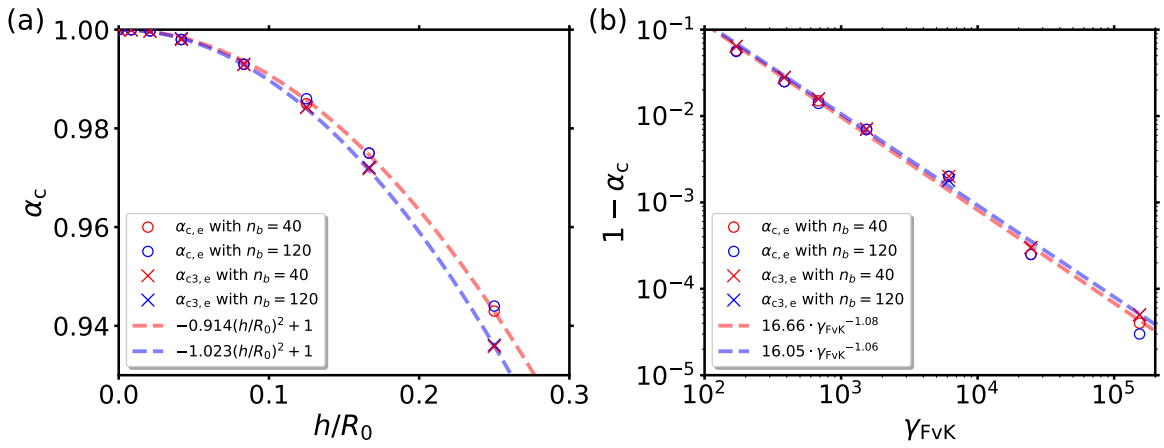

Figure 10.6.: (a): Critical swelling factors as a function of the disk's thickness h for two different discretizations. The swelling factors were each extracted from whole deformation cycles with a step size of $\Delta\alpha = 10^{-5}$ for $h/R_0 \leq 0.1$ and $\Delta\alpha = 10^{-4}$ for $h/R_0 > 0.1$. Otherwise the system is the same as before with $R_{in}/R_0 = 0.5$ and $k_{in}/k_{out} = 0.24$ and only pseudo-hysteresis effects. The dashed lines show fit curves of the numerical data. (b): Same data points as in (a), but plotted to show $1 - \alpha_c$ as a function of the dimensionless Föppl-von Kármán number γ_{FvK}, which was defined in eq. (9.8). The dashed lines show linear regressions on the logarithmic data.

That means, the disk's thickness h provides an excellent tool to change the dimensionless control parameter γ_{FvK} and with this parameter, the position of the transition can be controlled in a linear way. If the material is only able to swell slightly, for example when the swelling is driven by local heating, the thickness only has to be lowered sufficiently and the transition to the elliptic dome-like shape or the hyperbolic saddle shape can still occur. On the other hand, in order to prevent any bending, the thickness should be increased. But it should be kept in mind that if h is chosen too big, the assumption of a two-dimensional flat disk with $h \ll R_0$, the basic assumption of our model here, becomes really questionable. In a real, experimentally created system, if several disks of the same size are built of the same material but with different thickness, the relation between the critical α_c and the thickness changes to $|1 - \alpha_c| \sim h$, since the stretch energy then also scales with the thickness: $Y_{3D} = hY_{2D} \sim h$. But the message remains the same as the intuition tells: Thinner disks are easier to bend than thicker disks.

10.3. Additional energy barrier

In this section, we want to expand our disk in order to have a region of real hysteresis in the deformation cycle. In an experiment only a real hysteresis can be observed. Because of fluctuations, the size of a pseudo-hysteretic region should shrink to zero.[1] Therefore, a real hysteresis region can be created by introducing an additional energy barrier. This barrier has the effect that the disk is not able to switch directly from the flat conformation into the curved conformation even if that would lower the total energy. An additional energy to overcome the barrier is needed at first, which stabilizes the flat disk. In order to introduce an additional

[1] A quick estimate for a disk consisting of a typical hydrogel with $Y_{2D}/h \approx 10\,\mathrm{kN/m^2}$ and $\gamma_{FvK} = 1000$ yields that the thermal fluctuations at a temperature of 300 K are already stronger than the artificial noise in the previous section, when the disk is smaller than $R_0 \approx 100\,\mu\mathrm{m}$. In consequence, disks on a micro scale probably show no observable pseudo-hysteresis.

energy barrier and to investigate its effects, it is advised to define a slightly different relative coordinate system than before, which results in a translation of our coordinate system in the z-direction. The center of mass of the edge of the disk is defined as the origin of the system:

$$\frac{1}{n_\mathrm{B}} \sum_{i=1}^{n_\mathrm{B}} \boldsymbol{r}_{\mathbf{B},i} = \mathbf{0}. \tag{10.4}$$

In the flat state, this is the same coordinate system that we had before, the disk is located in the plane with $z = 0$. But in the elliptic dome-like conformation, the edge ring now defines the plane with $z = 0$ and all other vertices move out of that plane. During the transition into the curved shape, primarily the z-coordinate of the non-boundary vertices is changing. As soon as the critical swelling factor α_c is reached in the deformation cycle, the energy can be lowered by moving all vertices out of the plane in a way that an elliptic (or hyperbolic) shape is the result. The idea is now to punish a z-movement first. We have to ensure that moving the vertices out of the plane increases the energy a bit. That leads to the effect that the flat conformation stays stable until the swelling is that strong, that the additional energy is available in the system. The additional potential energy is now defined as the sum over potential energies of every vertex i that depend only on the vertices' z-coordinates:

$$E_z = \sum_i E_{z,i}(z). \tag{10.5}$$

We only want to stabilize the flat disk during the deformation cycle and do not want to change the curved shape with the additional potential. Therefore, the potential $E_{z,i}(z)$ for every vertex has to be very weak and, in addition, it has to be strongly localized around $z = 0$ in order to keep the influence on the elliptic dome or the hyperbolic saddle as small as possible. Several very different types of potentials are able to accomplish these tasks. In order not to use an abstract artificial potential, but a more natural effect, we choose a modified Lennard-Jones potential, which imitates a van der Waals force. The minimum of the potential is set to $z = 0$ by combining the attractive parts of two potentials:

$$E_{z,i}(z) = \begin{cases} 4\varepsilon \left[\left(\frac{z + \sqrt[6]{2}\sigma}{\sigma} \right)^{-12} - \left(\frac{z + \sqrt[6]{2}\sigma}{\sigma} \right)^{-6} \right], & z \geq 0 \\ 4\varepsilon \left[\left(\frac{-z + \sqrt[6]{2}\sigma}{\sigma} \right)^{-12} - \left(\frac{-z + \sqrt[6]{2}\sigma}{\sigma} \right)^{-6} \right], & z < 0. \end{cases} \tag{10.6}$$

This potential is visualized in fig. 10.7.

We have two free parameters to adjust the potential. The prefactor $\varepsilon > 0$ controls the strength of the potential, the height of the energy barrier. The higher ε is, the more difficult it is for the disk to reach a curved conformation. A higher ε can even completely suppress

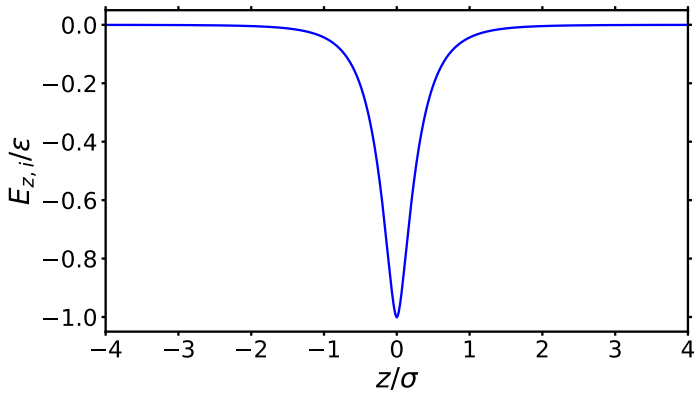

Figure 10.7.: Additional potential $E_{z,i}(z)$ of a single vertex i. In the state of a flat disk, all vertices are located at $z = 0$ in the minimum. In the curved conformation, nearly all vertices are either still in the minimum or at $z \gg \sigma$, where the influence of the potential is nearly non-existent.

the transition to a curved shape. Furthermore, the range of the potential can be adjusted via σ. In order to keep the influence on the curved shape as small as possible, we want σ to be very small, but always positive. On the other hand, when σ is chosen too small numerical problems occur due to high energy gradients in a very small region. Therefore, a compromise has to be found in the simulation. Promising parameters are $\varepsilon = 1.5 \cdot 10^{-10}\, k_{\text{out}} R_0^2$ for $n_{\text{B}} = 120$ boundary vertices and $\sigma = 0.01\, R_0$. Note that ε has to be adjusted in order to keep the total potential energy constant, if the number of vertices in the mesh is changed. The chosen value for σ has the effect, that in the curved conformation nearly all vertices are either still in the minimum of the potential or at $z \gg \sigma$, where the influence of the potential is effectively vanishing. Together with the very weak ϵ the influence of the energy barrier on the final curved conformation is nearly non-existent: The relative difference in the total energy between an elliptic dome with energy barrier and a dome without at the same α is less than $5 \cdot 10^{-9}$. It is very astonishing that this small energy barrier has a huge impact on the hysteresis region on the other hand. In the following, we investigate exactly the same disk as in the section before, that corresponds to the diagram 10.5, but with the additional potential E_z. The results are shown in a similar diagram, fig. 10.8. In the same manner as before in the section above, we start at $\alpha = 1$ in the force-free rest state, which is also the minimum of the additional potential energy. Again, when the stretching factor is decreased (increased), the disk remains flat with vanishing bending energy, while the spring energy increases. Similar to the case without the additional potential, we reach a critical point $\alpha_{\text{c,e}}$ ($\alpha_{\text{c,h}}$), where the system becomes unstable and the lowest eigenvalue of the Hessian matrix becomes negative. In fig. 10.8 that happens at about $\alpha \approx 0.97$ ($\alpha \approx 1.06$), where the red areas start. As before in fig. 10.5, the disk still remains flat until $\alpha_{\text{c2,e}}$ ($\alpha_{\text{c2,h}}$) is reached, where the transition into the dome-like (saddle-like) shape occurs. At this point after the transition, the energies of the systems with additional potential and without are nearly identical as mentioned above and there are no negative eigenvalues left. Increasing (decreasing) α again, we still see the same behavior as before: In the red area of pseudo-hysteresis, the system stays curved, where it was flat and unstable before. The real qualitative difference appears when we reach the point $\alpha_{\text{c,e}}$ ($\alpha_{\text{c,h}}$) again. Here, the shapes in fig. 10.5 became flat again, but with the additional energy barrier, the system still keeps its curved shape over the whole yellow region. In this region, the disk was flat *and* stable on the first way but is now curved on the way back. This is the region of a real hysteresis, that has no equivalent in fig. 10.5. Finally, when the system reaches $\alpha_{\text{c3,e}} > \alpha_{\text{c,e}}$ ($\alpha_{\text{c3,h}} < \alpha_{\text{c,h}}$), the disk becomes flat again.

After all, we now have a region of real hysteresis and directly next to it again a region of pseudo-hysteresis that is even expanded compared to the system without additional potential. For a demonstration and a proof of concept of the usability of a swelling disk as a microswimmer, it is irrelevant whether the propulsion comes from a real hysteresis or a pseudo-hysteresis. In the simulation, especially with the additional hydrodynamic interaction in chapter 11, there are always pseudo-hysteretic effects next to the region of real hysteresis. The effective total hysteresis, which is relevant for the swimming mechanism, is a combination of both effects. The size and the position of these effects depend on nearly every parameter in the system and the simulation (the disk's thickness h, the inner radius R_{in}, the fluctuations δ_{max}, the ratio of the spring constants $k_{\text{in}}/k_{\text{out}}$ as well as the energy barrier parameters ε and σ). Any chosen set of parameters would be quite arbitrary in the following. Therefore, we drop the additional energy barrier ($\varepsilon = 0$) due to simplicity. The main message and the qualitative results stay the same.

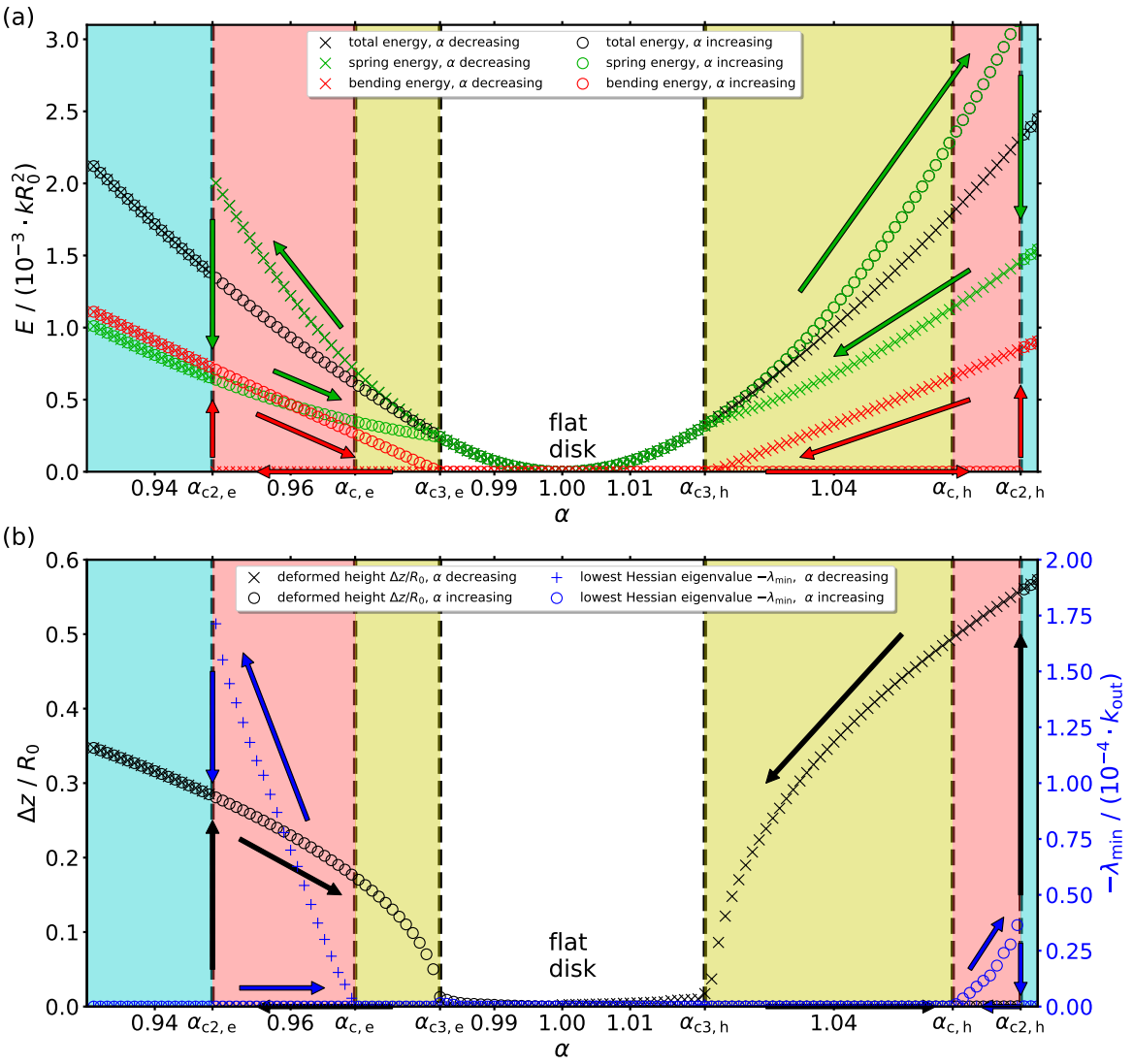

Figure 10.8.: Energies (a), shape's height Δz and negative of the lowest Hessian eigenvalue $-\lambda_{\text{min}}$ (b) in the spring mesh model as functions of the stretch factor α. Circles denote numerical values calculated with increasing α, while crosses are related to decreasing α. The region with a real hysteresis is marked in yellow, while pseudo-hysteretic effects are marked in red. The disk is always flat if it is located in the white area and always curved in the blue regions. Arrows illustrate the directions inside the hysteresis loops. The simulated system is the same system from fig. 10.5 but with an additional potential energy for each vertex given by eq. (10.6). The parameters of the potential were set to $\varepsilon = 1.5 \cdot 10^{-10}\, k_{\text{out}} R_0^2$ and $\sigma = 0.01\, R_0$. Note that the total energy and the spring energy are identical in the flat state.

10.4. Constant Gaussian curvature

In this section, our primary objective is to verify the possibility to control the shape of the deformed disk with the target metric, i.e. with the swelling function $\alpha(r_0)$. Therefore, we choose a special example: We want the deformed disk to have a positive constant Gaussian curvature. There is only a single possible immersion in the $\mathbb{R}^3$ with a positive constant K: the sphere. So, the question is: How do we have to choose the swelling function $\alpha(r_0)$ to deform the disk into a spherical shape? The question of a constant K in this context was also briefly discussed in refs. [48, 110], but it was presented very incompletely there. In the following, we

want to go into deeper details.

We start with the relation between K and the swelling function from section 8.15,

$$K(\rho) = \frac{-\frac{\partial^2}{\partial\rho^2}[r_0(\rho)\alpha(r_0(\rho))]}{r_0(\rho)\alpha(\rho)} = \frac{-\frac{\partial^2}{\partial\rho^2}h(\rho)}{h(\rho)}, \tag{10.7}$$

with the substitution $h(\rho) = r_0(\rho)\alpha(r_0(\rho))$. So the first step is to find $h(\rho)$ that leads to a constant K. We make an ansatz $h(\rho) = (1/a)\sin(a\rho)$, with a real constant a and get

$$K = a^2. \tag{10.8}$$

In a similar way the ansatz $h(\rho) = (1/a)\sinh(a\rho)$ would lead to a negative constant Gaussian curvature. Now we reverse the substitution:

$$r_0(\rho)\alpha(r_0(\rho)) = \frac{1}{a}\sin(a\rho). \tag{10.9}$$

At the end of the day, we are interested in $\alpha(r_0)$, but since r_0, ρ and α are all linked to each other, we first have to find $r_0(\rho)$. We use the definition of ρ, eq. (8.11), and express r_0 as the inverse function of ρ: $r_0 = \rho^{-1}$. With the help of the derivative of the inverse function, we find

$$r_0'(\rho) = \frac{1}{\rho'(r_0)} = \frac{1}{\alpha(r_0)}. \tag{10.10}$$

Consequently, we get a differential equation for $r_0(\rho)$,

$$\frac{r_0(\rho)}{r_0'(\rho)} = \frac{1}{a}\sin(a\rho), \tag{10.11}$$

which is solved by

$$r_0(\rho) = c\tan\left(\frac{a\rho}{2}\right) \tag{10.12}$$

with a real constant c that has the dimension of a length. Then, α follows from eq. (10.10),

$$\alpha(\rho) = \frac{2}{ac}\cos^2\left(\frac{a\rho}{2}\right). \tag{10.13}$$

Now we know $\alpha(\rho)$ but that is still not what we need because we need $\alpha(r_0)$ to be able to swell the right positions on the undeformed disk. So, we have to calculate $\rho(r_0)$ by inverting eq. (10.12):

$$\rho(r_0) = \frac{2}{a}\operatorname{artan}\left(\frac{r_0}{c}\right). \tag{10.14}$$

At this point, the meaning of the constant c becomes visible: It is a factor which scales the coordinate r_0 such that the same radial arc length ρ results. On the other hand, this constant gives us the ability to control the resulting arc length for a given r_0, especially since r_0 is limited to $r_{0,\max} = R_0$. Substituting ρ into α, we finally find the swelling function $\alpha(r_0)$ that leads to a constant positive Gaussian curvature K:

$$\alpha(r_0) = \frac{2}{\sqrt{K}}\frac{c}{r_0^2 + c^2} \tag{10.15}$$

with $c \in (0, \infty)$.

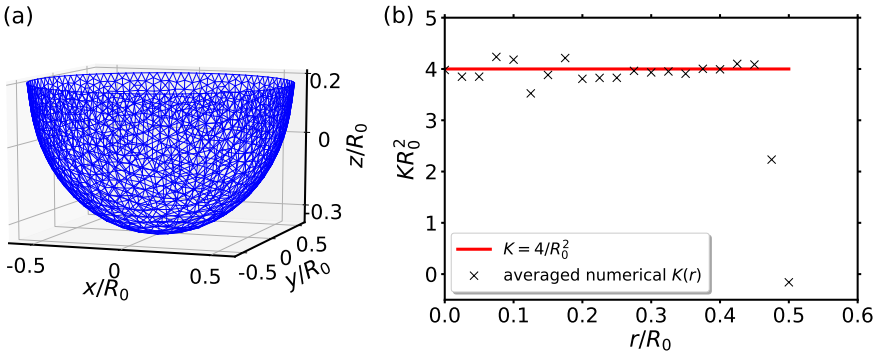

Figure 10.9.: Numerical results for a disk deformed into a half sphere with $R = 0.5\,R_0$. (a): Mesh of the deformed disk in the three-dimensional space. (b): Radial dependence of the Gaussian curvature as an average value over circular rings with a thickness of $\Delta r = 0.025 R_0$.

This swelling function is implemented now instead of the piecewise constant swelling function that is used in the other sections. In addition, we do not use the divided mesh with an additional inner ring, but a simple triangulation of the whole flat disk. For this calculation, the thickness of the disk was lowered, and the Föppl-von Kármán number was set to $\gamma_{\mathrm{FvK}} = 1.07 \cdot 10^5$. For a concrete example we choose a Gaussian curvature of $K = 4/R_0^2$ and set the constant c to $c = R_0$. The isometric immersion of a metric with a constant Gaussian curvature of $K = 4/R_0^2$ is a sphere with a radius of $R = 0.5\,R_0$. With the help of eq. (10.14) we find that the maximum radial arc length on the deformed shape is $\rho_{\max} = \pi/4 R_0$ which is the arc length from the pole to the equator on a sphere of radius $R = 0.5\,R_0$. So, we expect the disk to take the shape of a half sphere with the mentioned radius. The numerical results for a mesh with $n_{\mathrm{b}} = 100$ vertices on the boundary are shown in fig. 10.9. The resulting shape is obviously very similar to the desired half sphere of the radius $R = 0.5\,R_0$, actually the average radius is found to be $\overline{R} \approx 0.505\,R_0$. In addition, the graph (b) on the right of fig. 10.9 shows the Gaussian curvature, averaged over the polar angle φ, depending on the radial coordinate r of the deformed shape. Except for the boundary at $r \approx 0.5$, the Gaussian curvature fluctuates slightly below the value of $4/R_0^2$ and is nearly constant, which satisfies the expectations well.

Negative constant Gaussian curvature

The same procedure could be repeated in order to achieve a negative constant Gaussian curvature. An analogous derivation to the section above yields

$$\alpha(r_0) = \frac{2}{\sqrt{-K}} \frac{c}{c^2 - r_0^2}. \tag{10.16}$$

Despite the fact that the swelling function diverges at $r_0 = c$, there is a more fundamental problem with a negative Gaussian curvature: Hilbert's theorem of differential geometry states that no complete surface of constant negative Gaussian curvature can be immersed in $\mathbb{R}^3$ [66]. Indeed, the search for immersions of hyperbolic planes, surfaces with negative Gaussian curvature, is a highly non-trivial task. Several theorems in differential geometry state additional exclusion criteria for the existence of an immersion with negative curvature. The most important is probably Efimov's theorem which states that no complete surface can be immersed in the Euclidean $\mathbb{R}^3$ with a Gaussian curvature $K \leq \mathrm{const} < 0$, which means that an immersion is impossible not only for constant negative Gaussian curvatures, but for completely negative Gaussian curvatures in general [47, 103]. *If* an immersion exists, there must be at least one point on the surface where K converges to 0.

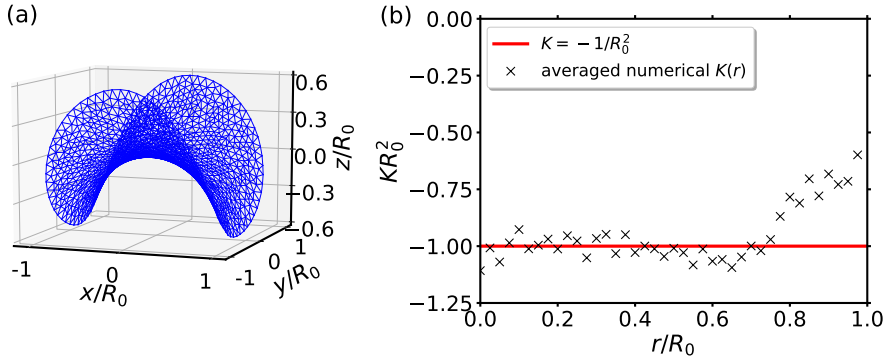

Figure 10.10.: Numerical results for a disk deformed in order to achieve a Gaussian curvature of $K = -1/R_0^2$. (a): Mesh of the deformed disk in the three-dimensional space. (b): Radial dependence of the Gaussian curvature as an average value over circular rings with a thickness of $\Delta r = 0.025\, R_0$.

As a consequence of these theorems, we do not find an immersion with completely negative or even constant negative Gaussian curvature as it was possible in the positive case with the sphere, even if (10.16) is used. Nevertheless, we can get a non-Euclidean shape, which is not totally free of stresses and does not completely satisfy the target metric, but whose curvature is quite close to the desired constant negative Gaussian curvature. Figure 10.10 shows the numerical results of an implementation of the swelling function (10.16) with $K = -1/R_0^2$ and $c = 2\, R_0$. A saddle like shape, very similar to the shapes that were discussed in the previous sections, is formed. This shape provides a roughly constant Gaussian curvature up to about 70 % of the maximum radial coordinate. In the outer regions, the absolute of the curvature quickly decreases, in a comparable manner as it was observed in the system with piecewise constant swelling in sec. 10.1.1.

11. Swimming in a fluid

With the deformation behavior of the elastic disk being understood, we can now go on to use these deformations as a propulsion in an external liquid. First, we start with a general introduction to the hydrodynamic interaction and the simplified Rotne-Prager model that is used in this thesis. This introduction follows closely the argumentations and notation by J.K.G. Dhont, see ref. [41]. Later, the general properties of a hydrodynamic simulation as well as the combination with the swelling disk are the topic of the subsequent section.

11.1. Hydrodynamic interaction

At first, definitions of some basic properties of the fluid that shall surround the elastic disk are needed. The local velocity of the fluid, $\boldsymbol{u}(\boldsymbol{r},t)$, is a function of the position in the fluid and a function of the time t since we regard dynamical processes. The local pressure is called $p(\boldsymbol{r},t)$ and $\rho_\mathrm{h}(\boldsymbol{r},t)$ describes the mass density of the fluid. These quantities have to be understood as mean values over small volume elements, because we operate on a small length scale, but not on a molecular scale, where each fluid particle would be described individually.

11.1.1. Navier-Stokes equation and Stokes equation

In the following, we assume the mass density of the fluid to be constant, $\rho_\mathrm{h}(\boldsymbol{r},t) = \rho_\mathrm{h} = \mathrm{const}$, so the fluid is incompressible. The continuity equation of the fluid, which is a result of the mass conservation, then simplifies drastically:

$$\begin{aligned} \frac{\partial \rho_\mathrm{h}(\boldsymbol{r},t)}{\partial t} + \nabla \cdot [\rho_\mathrm{h}(\boldsymbol{r},t) \cdot \boldsymbol{u}(\boldsymbol{r},t)] &= 0 \\ \Rightarrow \nabla \cdot \boldsymbol{u}(\boldsymbol{r},t) &= 0. \end{aligned} \tag{11.1}$$

To calculate the motion of the fluid, we need an equation of motion. The motion of the fluid is described by the Navier-Stokes equation for an incompressible fluid. We skip the derivation here and refer to ref. [41] for a complete presentation. The Navier-Stokes equation is a non-linear partial differential equation that we use in the form

$$\rho_\mathrm{h} \frac{\partial \boldsymbol{u}(\boldsymbol{r},t)}{\partial t} + \rho_\mathrm{h} \boldsymbol{u}(\boldsymbol{r},t) \cdot \nabla \boldsymbol{u}(\boldsymbol{r},t) = \eta \nabla^2 \boldsymbol{u}(\boldsymbol{r},t) - \nabla p(\boldsymbol{r},t) + \boldsymbol{f}_\mathbf{ext}(\boldsymbol{r},t). \tag{11.2}$$

The constant η is the sheer viscosity of the fluid and $\boldsymbol{f}_\mathbf{ext}(\boldsymbol{r},t)$ describes an external force density on the volume element that is located at $\boldsymbol{r}$. Together with the continuity equation (11.1) and specific boundary conditions, the behavior of the fluid is well defined. Solutions of the Navier-Stokes equation are very challenging but fortunately not necessary here, since microswimmers operate in a regime, where the Navier-Stokes equation can be simplified. In order to do so, we consider a spherical particle with the radius a and with a velocity $\boldsymbol{v}$ that moves in the fluid. With this length scale and together with the velocity, the viscosity and the density, we can rewrite the Navier-Stokes equation in a dimensionless form. Therefore, we use dimensionless quantities: Times rescale to $\tilde{t} = t\rho_\mathrm{h} a^2/\eta$, the fluid velocity to $\tilde{\boldsymbol{u}} = \boldsymbol{u}/|\boldsymbol{v}|$, coordinate derivatives via $\tilde{\nabla} = a\nabla$, the pressure with $\tilde{p} = p/(a|\boldsymbol{v}|\rho_\mathrm{h})$ and finally forces as

$\tilde{\boldsymbol{f}}_{\mathbf{ext}} = \boldsymbol{f}_{\mathbf{ext}} a/(\rho_\mathrm{h}|\boldsymbol{v}|^2)$. The dimensionless Navier-Stokes equation then becomes

$$\frac{\partial \tilde{\boldsymbol{u}}(\tilde{\boldsymbol{r}},\tilde{t})}{\partial \tilde{t}} + \tilde{\boldsymbol{u}}(\tilde{\boldsymbol{r}},\tilde{t}) \cdot \tilde{\nabla}\tilde{\boldsymbol{u}}(\tilde{\boldsymbol{r}},\tilde{t}) = \frac{1}{Re}\tilde{\nabla}^2\tilde{\boldsymbol{u}}(\tilde{\boldsymbol{r}},\tilde{t}) - \tilde{\nabla}\tilde{p}(\tilde{\boldsymbol{r}},\tilde{t}) + \tilde{\boldsymbol{f}}_{\mathbf{ext}}(\tilde{\boldsymbol{r}},\tilde{t}). \tag{11.3}$$

The dimensionless quantity

$$Re = \frac{\rho_\mathrm{h} a|\boldsymbol{v}|}{\eta} \tag{11.4}$$

is called *Reynolds number* and can be used for predictions about the general behavior of a fluid. At low Reynolds numbers, the flow of the fluid is usually laminar, while it becomes turbulent for higher Re. Microswimmers are very small objects, usually on a micro scale. From this small size, and also small velocities, very low Reynolds numbers $Re \ll 1$ follow [84, 117]. Bacteria as a prominent natural example, show Reynolds numbers of the order of 10^{-5} [82]. As a consequence, the term $\frac{1}{Re}\tilde{\nabla}^2\tilde{\boldsymbol{u}}(\tilde{\boldsymbol{r}},\tilde{t})$ dominates over the term $\tilde{\boldsymbol{u}}(\tilde{\boldsymbol{r}},\tilde{t}) \cdot \tilde{\nabla}\tilde{\boldsymbol{u}}(\tilde{\boldsymbol{r}},\tilde{t})$, so the latter can be neglected. If we restrict the observation of the fluid to longer time scales, that means time scales that are much longer than the hydrodynamic time scale τ_H, we can make further simplifications. The hydrodynamic time scale is given by the time that a shear wave needs to travel over the distance of the size a of a particle in the fluid. For time scales with $t \gg \tau_\mathrm{H}$ distortions in the fluid can be assumed to propagate instantly. The consequence is that perturbations of the fluid, that are caused by a slow moving microswimmer, are visible in the whole system at the same time. So, the system instantly reacts to any changes and the time derivative in the Navier-Stokes equation can be neglected. An estimation for the hydrodynamic time scale τ_H is given by

$$t \gg \tau_\mathrm{H} \approx a^2 \frac{\rho_\mathrm{h}}{\eta}. \tag{11.5}$$

Another interpretation of this time scale is that a Brownian particle does not show a ballistic trajectory anymore and can be described statistically. Therefore, it is also called the *Brownian timescale*. For further details and derivations, see ref. [41]. With the assumption of low Reynolds numbers and only considering long time scales, the Navier-Stokes equation simplifies to

$$\nabla p(\boldsymbol{r},t) - \eta\nabla^2\boldsymbol{u}(\boldsymbol{r},t) = \boldsymbol{f}_\mathrm{ext}(\boldsymbol{r},t). \tag{11.6}$$

This equation, the *creeping flow equation*, or also often called *Stokes equation*, describes sufficiently the motion of a microswimmer at low Reynolds numbers on long time scale. It is a linear equation with only external time dependencies. The motion is set in an overdamped limit where inertial effects are neglectable and the fluid velocity is directly proportional to external forces. Consequences are much simpler solution techniques and also the scallop theorem, which are presented in the following section.

11.1.2. Oseen and Rotne-Prager matrix

A self-propelling microswimmer exerts forces $\boldsymbol{f}_\mathrm{ext}(\boldsymbol{r},t)$ on the fluid with every part of its body. These forces cause a change of the fluid velocity field $\boldsymbol{u}(\boldsymbol{r},t)$, which causes forces back on other parts of the swimmer. So, we need to know the new velocity field that is the result of the force $\boldsymbol{f}_\mathrm{ext}(\boldsymbol{r},t)$. In order to get that, we start with the simplest case, a point force at the position $\boldsymbol{r}$,

$$\boldsymbol{f}_\mathrm{ext}(\boldsymbol{r},t) = \boldsymbol{f}_\mathbf{0}(t)\delta(\boldsymbol{r}) \tag{11.7}$$

with the total force $\boldsymbol{f_0}(t) = \int \boldsymbol{f}_{\text{ext}}(\boldsymbol{r'},t)\mathrm{d}\boldsymbol{r'}$. Since the Stokes equation is linear, $\boldsymbol{u}$ has to be linear in $\boldsymbol{f}_{\text{ext}}$ and may be the result of a superposition of several acting forces $\boldsymbol{f}_{\text{ext},i}$:

$$\boldsymbol{u}(\boldsymbol{r},t) = \int \sum_i \underline{\underline{\boldsymbol{T}}}(\boldsymbol{r}-\boldsymbol{r'})\boldsymbol{f}_{\text{ext},i}(\boldsymbol{r'},t)\mathrm{d}\boldsymbol{r'}. \tag{11.8}$$

The matrix $\underline{\underline{\boldsymbol{T}}}$ is the Oseen matrix [41] and represents a Green's function of the Stokes equation. It is given by

$$\underline{\underline{\boldsymbol{T}}}(\boldsymbol{r}) = \frac{1}{8\pi\eta}\frac{1}{|\boldsymbol{r}|}\left[\underline{\underline{\boldsymbol{I}}} + \frac{\boldsymbol{r}\otimes\boldsymbol{r}}{|\boldsymbol{r}|^2}\right], \tag{11.9}$$

where $\underline{\underline{\boldsymbol{I}}}$ is the identity matrix. Now we know in principle the effects of forces on the velocity field and can go one step ahead. We consider two particles of the same size that are placed in the fluid at the positions $\boldsymbol{r_i}$ and $\boldsymbol{r_j}$. If their distance is big compared to their radius, $|\boldsymbol{r_i}-\boldsymbol{r_j}| \gg a$, then we can regard these particles as being point-like. If the particles move with velocities v_i and v_j, then they exert forces $\boldsymbol{f_i}$ and $\boldsymbol{f_j}$ on the fluid and the fluid exerts the same forces with opposed sign back on the particles. But such a force on the fluid changes the velocity field of the fluid via eq. (11.8), so one particle changes the environment of the other particle. They interact with each other through the fluid. A longer derivation shows that the velocity of a point-like particle i is related to the force $\boldsymbol{f_i}$ that it exerts on the fluid and the forces $\boldsymbol{f_j}$, that are caused by the other particles, via

$$\boldsymbol{v_i} = \frac{1}{6\pi\eta a}\boldsymbol{f_i} + \sum_{j\neq i}\underline{\underline{\boldsymbol{T}}}(\boldsymbol{r_i}-\boldsymbol{r_j})\boldsymbol{f_j}. \tag{11.10}$$

The prefactor $1/(6\pi\eta a)$ is the well-known Stokes friction law. This is an approximation that is only valid for great distances between the particles. It is the leading order of hydrodynamic interaction that takes into account how perturbation waves of a particle influence another particle. In reality, a particle i that disturbs the fluid also sees a reflection of its own disturbance, because the induced velocity at the particle j influences i, too. Theoretically, the disturbance waves are infinitely often reflected, while the amplitude is reduced with every reflection. As a result, the real interaction between two particles is a serial expansion in the radius to distance ratio $a/|\boldsymbol{r_i}-\boldsymbol{r_j}|$, where the Oseen matrix in eq. 11.10 represents the first order of interaction with point-like particles.

In this thesis, we take one higher order into account, which represents the interaction between spherical particles that are not point-like, but still neglects reflections, since these would lead to a much more complicated model. This level of interaction is described by the Rotne-Prager matrix [41, 126]. The velocity of the spherical particle i is then related to the forces on the other particles via

$$\begin{aligned}\boldsymbol{v_i} = \frac{1}{6\pi\eta a}\boldsymbol{f_i} + \sum_{j\neq i}\frac{1}{6\pi\eta a}\Bigg(&\frac{3a}{4|\boldsymbol{r_i}-\boldsymbol{r_j}|}\left(\underline{\underline{\boldsymbol{I}}} + \frac{(\boldsymbol{r_i}-\boldsymbol{r_j})\otimes(\boldsymbol{r_i}-\boldsymbol{r_j})}{|\boldsymbol{r_i}-\boldsymbol{r_j}|^2}\right)\\ &+ \frac{a^3}{4|\boldsymbol{r_i}-\boldsymbol{r_j}|^3}\left(\underline{\underline{\boldsymbol{I}}} - 3\frac{(\boldsymbol{r_i}-\boldsymbol{r_j})\otimes(\boldsymbol{r_i}-\boldsymbol{r_j})}{|\boldsymbol{r_i}-\boldsymbol{r_j}|^2}\right)\Bigg)\boldsymbol{f_j}.\end{aligned} \tag{11.11}$$

It should also be noted that rotations and torques are completely neglected here. This relation (11.11) between forces and particle velocities is the core of our hydrodynamic model. When the elastic disk is deformed due to swelling, the resulting forces in every part of the disk are known. These forces are also exerted on the fluid and, therefore, can be translated into velocities and the overall movement of every part of the disk can be calculated. The

relation (11.11) between forces and velocities can be written down for every particle in the fluid, which results in a $3N$-dimensional linear equation system for N particles:

$$\boldsymbol{v} = \underline{\underline{\boldsymbol{M}}}\boldsymbol{f}. \tag{11.12}$$

The vectors $\boldsymbol{v}$ and $\boldsymbol{f}$ store all $3N$ velocity and force components. $\underline{\underline{\boldsymbol{M}}}$ is called the mobility matrix and is given by eq. (11.11). Note that $\underline{\underline{\boldsymbol{M}}}$ is a function of all particle positions. The disk deforms and pushes itself with the help of the fluid. If the disk shall swim longer distances, then the swelling must take place repeatedly. Therefore, the swelling also must be reversed, which we called the deformation cycle in sec. 10.2.

At this point, care should be taken to the linearity of the Stokes equation. This linearity in $\boldsymbol{u}$ results in the time invariance of the equation. So, if the disk swims with a total velocity $\boldsymbol{v}$ due to its swelling, then the motion reverses perfectly if the swelling is reverted. It is completely irrelevant how fast the swelling or deswelling occurs, the disk reaches its original position if the swelling reverses perfectly. This phenomenon, that a microswimmer at low Reynolds numbers in laminar flows cannot swim by a reversible motion is called the *scallop theorem* [117]. It states that a single degree of freedom is not sufficient for swimming at low Reynolds numbers due to time invariance.

The swelling elastic disk can overcome this problem and break the time invariance with its (pseudo-) hysteresis effects. Due to the hysteresis, the unswelling process is not an exact reversion of the swelling and a net swimming distance after a complete deformation cycle can result. So, the hysteresis is the inevitable engine of the swimming.

11.2. Hydrodynamic simulation

11.2.1. Hydrodynamic spring mesh model

In order to calculate swimming motions of the swelling disk, the spring mesh has to be combined with the hydrodynamic model, which was introduced in the previous section. The basic idea is to represent the continuous disk with a mesh of small spheres. These spheres interact with the fluid and are connected to each other via mechanical springs. So, the spheres are localized at the vertices of the spring mesh. The springs themselves do not interact with the fluid. A requirement to apply the Oseen or Rotne-Prager model of the hydrodynamic interaction is that the distances between the spheres, the length of the springs, must be much greater than their radius a. On the other hand, the consequence is, that the spheres only cover a small part of the disk's area and fluid can flow through the surface, which is impossible with a continuous impermeable material in reality. This is a drawback due to the simplicity of the model. But the hydrodynamic interaction between the spheres keeps this problem surprisingly small, if the discretization is fine enough, as it is discussed in sec. 13.2. So, the spheres' radius a has to be chosen as big as possible on the one hand, but on the other hand it must not violate the assumption $a \ll l_0$ of being small compared to the springs' unswollen rest lengths. A good compromise was found to be $a = 0.1 \cdot 2\pi R_0/n_\mathrm{B} \approx 0.1\, l_{0,\mathrm{B}}$ with $l_{0,\mathrm{B}}$ being the springs' unswollen rest length on the boundary of the disk. This value is used for most of the calculations. It is important to note, that we assume the springs to start and end in the center of the spheres and not on the surface. This simplifies the model and also the disk does not change its size if a is varied.

Figure 11.1 shows the spring mesh of the original disk with spheres of the mentioned standard radius for two different discretizations. Although the number of spheres increases with higher discretizations and shorter spring length, the area that is covered by the spheres stays the same, since the absolute radius of the spheres decreases in the same way to keep the relation between a and $l_{0,\mathrm{B}}$ valid.

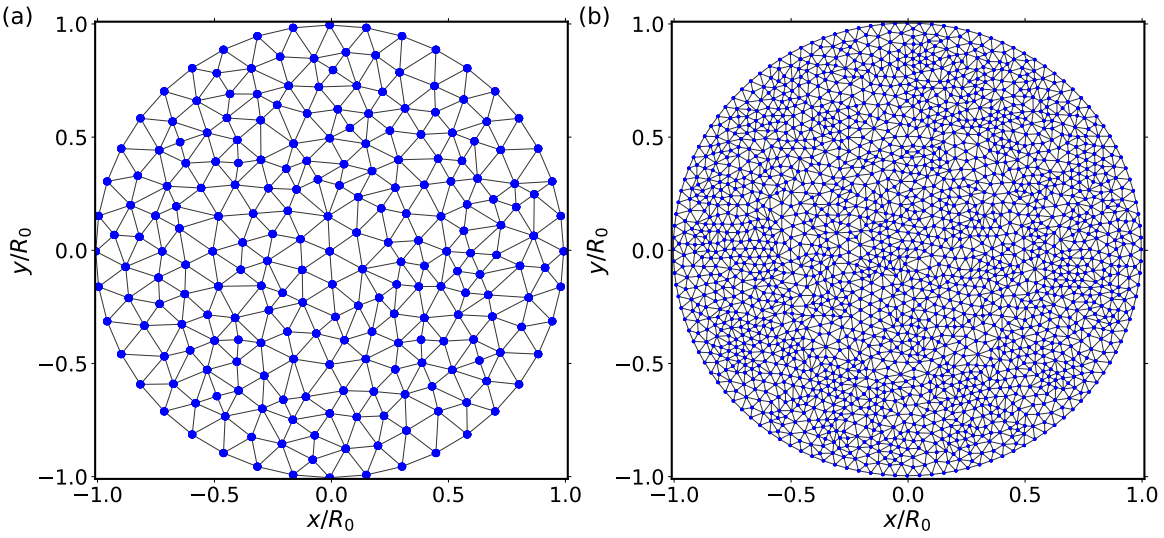

Figure 11.1.: Delauney triangulation of the flat disk for $R_{\mathrm{in}}/R_0 = 0.5$ with (a): $n_{\mathrm{B}} = 40$ and (b): $n_{\mathrm{B}} = 120$. The spheres that are assumed at the vertex positions have a radius $a = 0.1 \cdot 2\pi R_0/n_{\mathrm{B}}$ and are illustrated in blue. The black lines between these spheres represent the springs. The spring mesh is the same as already shown in fig. 9.1.

11.2.2. Time scales and procedure of the simulation

Combining the hydrodynamics with the swelling process, we have to pay special attention to the time scales of this problem. The time scale of the swelling process, that means the time that is needed by the disc to run through a whole deformation cycle, is given by the physical and chemical properties of the system and also depends on the method used to achieve the swelling. Since a basic condition of our setup is to be set at low Reynolds numbers, it is reasonable to assume that the swelling is much slower than the hydrodynamic interaction. If a vertex of the disk slightly moves due to swelling, then every other vertex will instantly react. In order to calculate the trajectories of every vertex in the swelling process, we discretize the deformation cycle at first. This is done in a comparable way as in sec. 10.2. The deformation cycle consists of n single swelling steps. The swelling factor α is changed by $\Delta\alpha$ in every single step. Each step takes the time T_{el}, so the whole deformation cycle takes nT_{el}. Effectively, we replace a slow continuous swelling by multiple small instantaneous steps, where higher forces can occur. This does not cause any problems with the hydrodynamics since higher forces directly result in higher velocities on the one hand, but on the other hand the linearity of the Stokes equation ensures that the swimming distance is independent of any velocities, only the trajectory of the deformation is relevant, as it was discussed in the previous section.

After each swelling step, the mesh shall relax to its new equilibrium shape. This relaxation process is the place where the hydrodynamic interaction comes into play. The spheres at the vertex positions move and thereby interact with each other. The finally reached rest state must be the same as in the dry case without a fluid: If every sphere has found its equilibrium of forces, no net force remains and, therefore, all velocities become zero as demanded by eq. 11.11. Without any movement, the fluid cannot exert any forces, so the mesh must take its intrinsic force equilibrium. That means that the resulting shapes could be calculated by an energy minimization as presented in the previous chapter, but in order to track the movement of the whole disk as a swimmer, i.e. the movement of its center of mass, the trajectories of every single sphere are needed. After the swelling, the forces on each sphere in the mesh, caused by the springs and the gradient of the bending energy, are known. Then, eq. (11.11) can be used to calculate the resulting velocities and these velocities can be integrated in order to get new

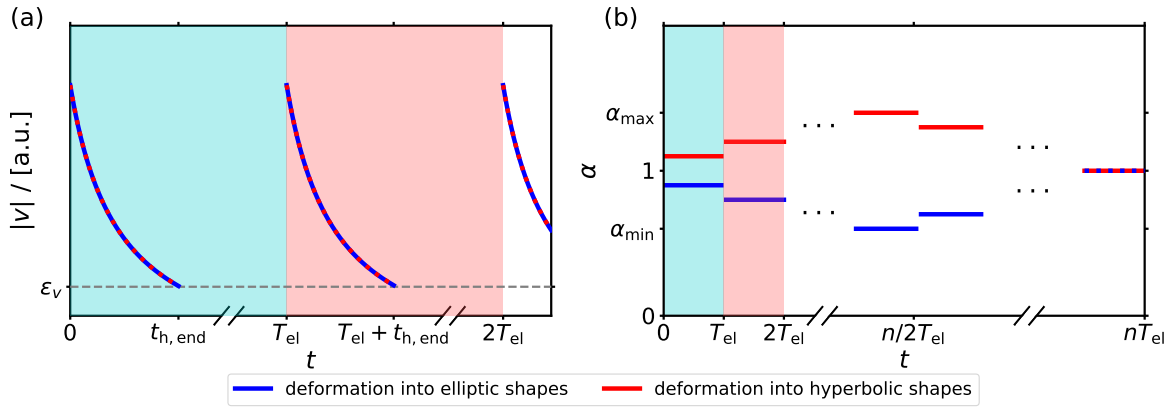

Figure 11.2.: Illustration of the two time scales in the hydrodynamic simulation. (a): Vertex velocities in arbitrary units as a function of time in the first two swelling steps. (b): Time representation of the deformation cycle in terms of the swelling factor α as a function of the time for elliptic and hyperbolic deformation cycles. The colored areas illustrate the same time intervals in (a) and (b). Note that the time axes are interrupted to represent $t_{\mathrm{h,end}} \ll T_{\mathrm{el}}$ and $n \gg 1$.

vertex positions until the new equilibrium is reached. That is the case, when the absolute of the forces in the mesh falls below a threshold ε_{f}, which is equivalent to the vanishing energy gradient from sec. 9.3. Since the forces are related linearly to the velocities, the definition of a velocity threshold ε_{v} would also be equivalent. The time $t_{\mathrm{h,end}}$ when the equilibrium during a single swelling step is reached is the second time scale of the combined problem. It is assumed to be much shorter than the deformation time scale, $t_{\mathrm{h,end}} \ll T_{\mathrm{el}}$, and is primarily defined by the viscosity of the fluid, see the dimensionless time below. Figure 11.2 illustrates the two time scales of the simulation. At $t = 0$, α is changed, which results in high forces and sphere velocities. The spheres move until the threshold is reached at $t_{\mathrm{h,end}}$ and then the time jumps to T_{el}. There, α is changed again. This procedure is repeated until the original state with $\alpha = 1$ is reached at $t = nT_{\mathrm{el}}$ again. The difference between the positions of the center of mass at $t = 0$ and $t = nT_{\mathrm{el}}$ is the effective swimming distance Δs_{CoM} of the disk for one deformation cycle. So, the average speed of the disk can be defined as $v_{\mathrm{disk}} = \Delta s_{\mathrm{CoM}}/(nT_{\mathrm{el}})$. The integration of the vertex velocities is implemented with a simple Euler step:

$$\boldsymbol{r}_{i,m+1} = \boldsymbol{r}_{i,m} + \Delta t \boldsymbol{v}_{i,m} \tag{11.13}$$

with a small time step Δt. In the beginning of that integration, the acting forces and resulting velocities are relatively high, so the vertices quickly move towards their equilibrium position. But after a short time, forces and velocities rapidly decrease to a kind of slow plateau and cause a high amount of integration steps to be necessary to reach the threshold. This slows down the simulation drastically especially for higher discretizations, since forces and energy gradients have to be calculated in every single step. A dynamical adaption of the step size Δt is recommended to counter this problem to a certain degree.

In the simulation, we also assume the deformation of the disk to be sufficiently slow during the shape transition, when the disk snaps into the curved conformation. This is possibly a critical point for the realization in a real experiment. If the deformation during the transition is too fast, then the assumption of low Reynolds numbers may be violated due to the higher velocities.

viscosities	time	velocities
$\tilde{\eta} = 1 \cdot \eta$	$\tilde{t} = tk_{\text{out}}/(R_0\eta)$	$\tilde{\boldsymbol{v}} = \boldsymbol{v}\eta/k_{\text{out}}$

Table 11.1.: Summery of dimensionless quantities related to the hydrodynamics.

11.2.3. Dimensionless quantities

Since the time came abroad as a new physical dimension with the hydrodynamics, the table of dimensionless quantities, which was begun in sec. 9.4, must be expanded now. As a new basic unit, we use the fluids viscosity η. Together with the already known basic units R_0 and k_{out} we get the relations shown in table 11.1. Note that we now use a different way to non-dimensionalize the time than we did in the context of the dimensionless Navier-Stokes equation (11.3). The dimensionless time below is a more suited version, because it is independent of the artificial sphere radius and it respects the elastic properties of the disk. Apart from numerical prefactors, $R_0\eta$ can be interpreted as the friction constant of the whole disk.

11.3. Swimming distance

During the simulation of several deformation cycles with hydrodynamic interactions, the position of the disk's center of mass gives information about the swimming capabilities. In the following, the swimming behavior is discussed with the help of the standard example disk, which was already used several times in this thesis, with $R_{\text{in}}/R_0 = 0.5$, $\gamma_{\text{FvK}} = 600$ and $k_{\text{in}}/k_{\text{out}} = 0.24$. For simplicity, we do not use an additional potential energy here. The swimming is provided only by the pseudo-hysteretic effects. Figure 11.3 shows the behavior of the disk's center of mass for two different cases. In the first one (blue), the disk deforms into an elliptic dome-like shape and α cycles in the interval $\alpha \in [\alpha_{\min} = 0.95, 1]$. Analogously, the hyperbolic saddle shape is represented in red with $\alpha \in [1, \alpha_{\max} = 1.05]$. The simulation started at $t = 0$ and ran until $t = 20\,T_{\text{el}}$ was reached, so 20 complete deformation cycles were simulated. Figure 11.3 (a) shows the z-coordinate of the disk's center of mass, z_{CoM}, as a function of the time.

In the elliptic case, sharp peaks into negative z-values are visible. These peaks recur periodically, one time in every deformation cycle. But in total, a net movement in positive z-direction is observable. That means, the disk moves in negative direction during the first part of the swelling cycle, but then moves slightly more in positive direction on the way back to the flat disk. As an example, the first deformation cycle is shown in detail in fig. 11.3 (c). Here we can see the effects of the elastic pseudo-hysteresis in detail. In the first part of the deformation cycle, the disk only deforms in plane and stays flat, no movement in z-direction perpendicular to the disk's plane is possible. As soon as the point of the shape transition is reached, the disk deforms into the dome-like shape, which results (on this swelling time scale) in an instantaneous movement in the direction of the dome's tip. When the direction of swelling turns again, the movement of the center of mass also turns. The system moves into the direction of the opening of the dome until the disk is flat again. This movement into the opening's direction is slightly stronger than the movement into the tip's direction during the transition. By fitting a linear function to the center of mass' z-coordinate at the end of each deformation cycle, see fig. 10.1 (b), we find an average velocity of about $v_{\text{disk,e}} = \Delta z_{\text{CoM}}/T_{\text{el}} = 6.7 \cdot 10^{-4}\, R_0/T_{\text{el}}$, so the center of mass moves effectively over a distance of $6.7 \cdot 10^{-4}\, R_0$ per deformation cycle. But it should be kept in mind, that this velocity depends on the size of the pseudo-hysteresis region and thus the fluctuation, which were set

to $\delta_{\max} = 5 \cdot 10^{-5}\, R_0$ in this case.

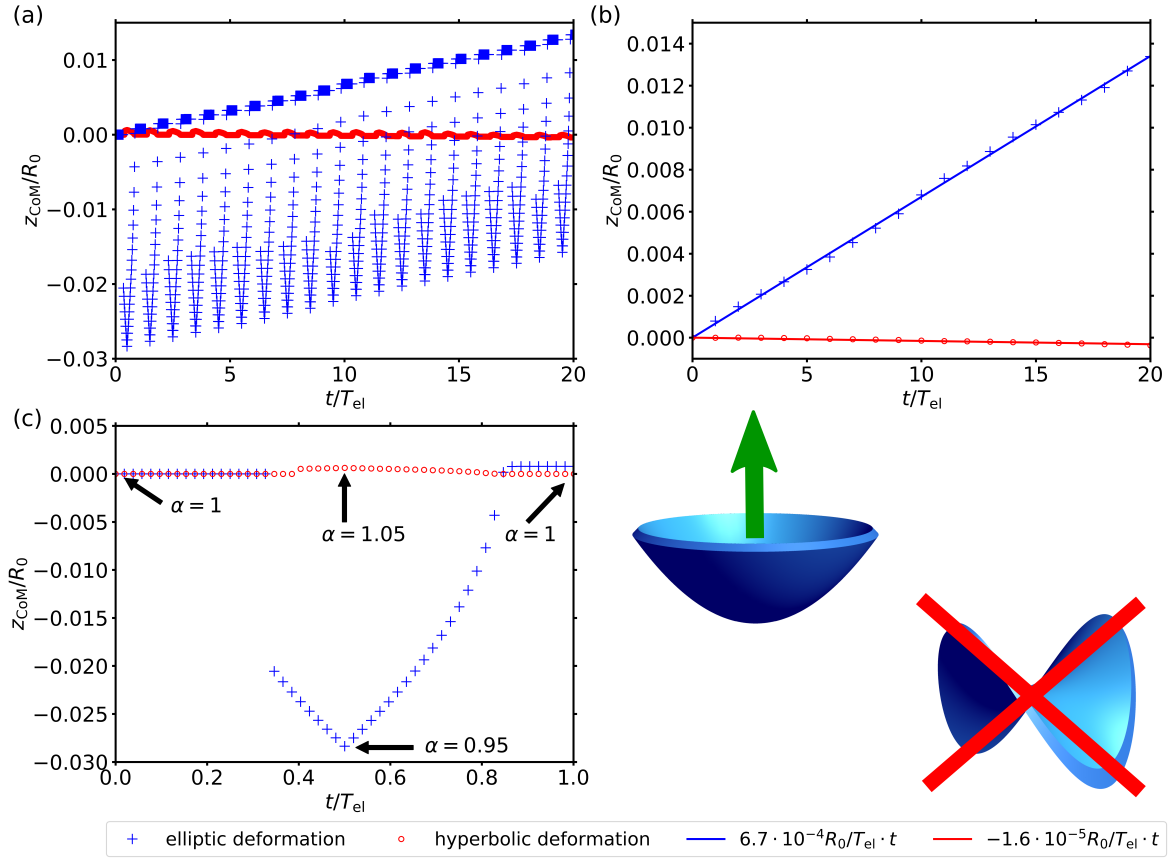

Figure 11.3.: z-coordinate of the disk's center of mass as a function of the time. Blue crosses are related to the elliptic shape with $\alpha_{\min} = 0.95$, while red circles correspond to the hyperbolic shape with $\alpha_{\max} = 1.05$. The swelling factor α was changed in steps of $\Delta\alpha = 2 \cdot 10^{-3}$ and a maximum shaking distance of $\delta_{\max} = 5 \cdot 10^{-5}\, R_0$. (a): Overview over 20 deformation cycles. (b): The center of mass' z-coordinate at the end of each deformation cycle together with fit functions to the numerical data. (c): Zoom to the first deformation cycle.

The behavior of the hyperbolic shape, contrasted in red, is quite different. In fig. 11.3 (a), a movement is only barely visible. The hyperbolic system shows a similar periodic peak structure as the elliptic system does, but with a much smaller swimming distance. Compared to the elliptic case, the movement within a single deformation cycle and also the total movement are smaller by a factor of more than 40. This results in a total movement speed of $v_{\mathrm{disk,h}} = -1.6 \cdot 10^{-5}\, R_0/T_{\mathrm{el}}$, in negative z-direction. After all, the elliptic shape is an extremely more efficient swimmer than the hyperbolic shape. The question which arises now is: Why does the hyperbolic swimmer move at all? Due to the symmetry of the saddle shape, see sec. 10.1, we would expect that it does not move in any way, because the hydrodynamic forces on every vertex should exactly cancel out each other. Since there is no preferential direction, no resulting movement could occur. This principle can be easily understood with the help of a simplified five-sphere model in chapter 12. So, the slight movement from figure 11.3 has its origin probably founded in inhomogeneities of the mesh together with the fluctuations. These inhomogeneities could result in different vertex velocities in different parts of the mesh during the deformation, which results in the small total movement. The swimming speed of the disk, i.e. the net movement within a single deformation cycle is strongly depending on the position and the size of the hysteresis region. The extent of the hysteresis effects,

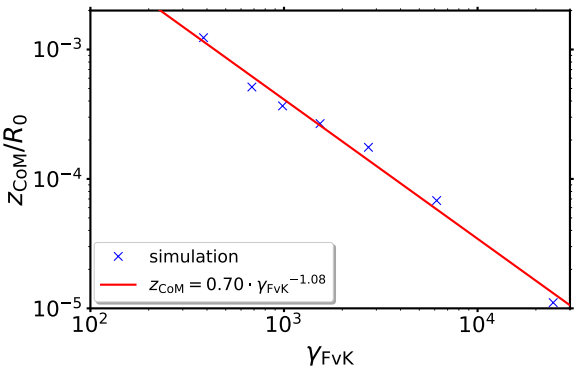

Figure 11.4.: Average value of the disk's center of mass after a complete deformation cycle as a function of γ_{FvK}. The corresponding system featured $n_{\mathrm{B}} = 60$, $R_{\mathrm{in}}/R_0 = 0.5$, $k_{\mathrm{in}}/k_{\mathrm{out}} = 0.24$,$a = 0.1 \cdot 2\pi R_0/n_{\mathrm{B}}$ and $\delta_{\max} = 5 \cdot 10^{-5}\, R_0$.

however, are primarily depending on the disk's thickness to radius ratio h/R_0 and, therefore, the Föppl-von Kármán number, as it was already discussed in sec. 10.2 (despite the fact that the size of the real hysteresis can also be controlled with an additional potential energy that was presented in sec. 10.3). Consequently, we should take a look at the swimming distance as a function of γ_{FvK}. Figure 11.4 shows the z-coordinate of the swimmer's center of mass after a full deformation cycle for different γ_{FvK}. The movement distance seems to diverge for thicker disks ($\gamma_{\mathrm{FvK}} \to 0$), because the disks become more difficult to bend, while the size of the pseudo-hysteresis region increases. On the other hand, there is nearly no swimming for very thin disks ($\gamma_{\mathrm{FvK}} \to \infty$), the disks immediately bend into the curved conformation in the swelling process, so there is only a very small transition and thus nearly no swimming distance. The functional dependency can be approximated by the power law $z_{\mathrm{CoM}} = 0.70 \cdot {\gamma_{\mathrm{FvK}}}^{-1.08}$. Special attention should be paid to the following source of errors here: In order to get comparable data for different values of γ_{FvK}, the fluctuations in the mesh during the swelling process must stay at the same size, so the vertex movement distance $\delta_{\max}$ must not be varied and was set to $\delta_{\max} = 5 \cdot 10^{-5}\, R_0$. Otherwise the numerical pseudo-hysteresis region would be manipulated artificially and, therefore, the different swimming distances would lack significance. But on the other hand, that means that for very thin disks, at very high γ_{FvK}, the height of the curved shape and the movement distance of the disk approach the size of the fluctuations, causing high relative errors.

11.4. Linear deformation

The objective of this section is to prove that the hysteresis in the deformation process is a necessary condition for a net swimming movement. Therefore, we deactivate the hysteresis by implementing a linear deformation bevavior. The basic idea is to move the vertices of the disk on trajectories which are obtained as a linear interpolation between the vertex positions in the flat disk and the vertex positions in the maximum deformed shape. First of all, all vertex positions in the flat state are saved. Then the maximum deformed shape, here with $\alpha = 0.95$ is calculated via energy minimization and again the vertex positions are saved. Since the vertex trajectories and the vertex velocities are prescribed now, the hydrodynamic simulation is not force driven anymore, but velocity driven, which is an often used technique to simulate microswimmers with special deformation cycles [105].

Since we use the same hydrodynamic model, the basic relation $\boldsymbol{v} = \underline{\underline{\boldsymbol{M}}}\boldsymbol{f}$ is still valid, but now we know the velocities instead of the forces. That means in detail, we know $N-1$ relative velocities and we are interested in the center of mass' velocity. The forces can no longer be calculated from the spring mesh. Since we force the vertices on artificial trajectories, hydrodynamic forces related to these velocities are the consequence. Rewriting the force-

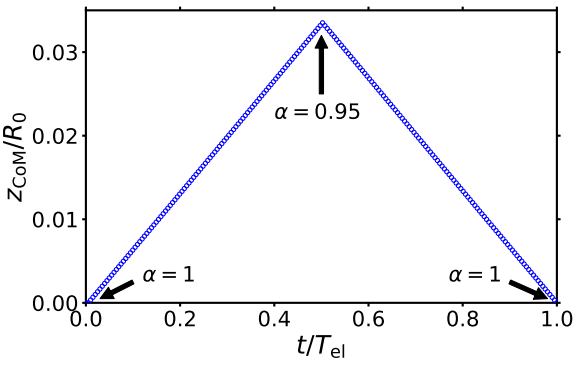

Figure 11.5.: z-coordinate of the center of mass in the artificial linear deformation cycle. The target shape corresponds to an elliptic shape with $\alpha = 0.95$, $R_{in}/R_0 = 0.5$, $\gamma_{FvK} = 600$, $k_{in}/k_{out} = 0.24$, $n_B = 100$ and was calculated via energy minimization.

velocity relation with relative velocities

$$\boldsymbol{v} - \boldsymbol{v}_{\mathbf{CoM}} = \underline{\underline{\boldsymbol{M}}}\boldsymbol{f} - \boldsymbol{v}_{\mathbf{CoM}} \tag{11.14}$$

and demanding that no total force shall act on the disk, $\sum \boldsymbol{f_i} = 0$, enables us to solve the resulting linear equation system and calculate the acting forces and the final missing velocity. Then, the center of mass' velocity and position are accessible.

The results for an elliptic shape with $\alpha = 0.95$ are shown in fig. 11.5. Since every vertex is moving on a linear trajectory, the center of mass does the same until it the system reaches the final configuration at $t = 0.5\,T_{el}$: The elliptic shape with $\alpha = 0.95$ that was calculated via energy minimization. After that, all velocities get a sign and the motion exactly reverses. So after the complete cycle, no net movement remains, as expected, which verifies the algorithm.

12. Five-sphere model

In this chapter, we develop a very simple model of a swimmer consisting of only five spheres. This is the most primitive model that shares similar deformation characteristics with the swelling disk. The main advantage can be found in the fact that many of the disk's properties can be easily understood with this simple model.

The first question that has to be answered is: Why do we need five spheres for the simplest possible model of the disk? Three spheres are actually needed to construct a microswimmer that is able to move [105, 124]. Two spheres only have a single degree of freedom (change of their distance), so the scallop theorem forbids swimming here. Three spheres allow different swimming motions, but these are insufficient, since three points always lay inside of a plane. Consequently, three spheres form at best a two-dimensional swimmer, but not a three-dimensional one. To construct a real three-dimensional swimmer, four spheres are needed at least. If three of these four spheres form an equilateral triangle and the fourth one is placed in its center off mass, with all spheres connected to each other, then the deformation of the disk to an elliptic shape could be simulated. This would result in the spheres forming a kind of pyramid. But no shape similar to a hyperbolic saddle would be possible. Therefore, we need at least five spheres.

These five spheres are placed in the shape of a square in the $(z = 0)$-plane with one sphere in the center of the square. So, the coordinates are set to

$$\boldsymbol{r_{1,0}} = -R_0\boldsymbol{e_x}, \quad \boldsymbol{r_{2,0}} = -R_0\boldsymbol{e_y}, \quad \boldsymbol{r_{3,0}} = R_0\boldsymbol{e_x}, \quad \boldsymbol{r_{4,0}} = R_0\boldsymbol{e_y}, \quad \boldsymbol{r_{5,0}} = \boldsymbol{0}. \tag{12.1}$$

The additional index 0 indicates the original undeformed state. In order to define forces on the spheres and the deformation behavior, several different ways are possible. One possibility, the most natural one, would be a small version of the spring mesh model we used before: The spheres 1 to 4 are each connected to the central sphere, 5, with a spring and four additional springs are defined on the edges: ($\boldsymbol{r_1}$,$\boldsymbol{r_2}$), ($\boldsymbol{r_2}$,$\boldsymbol{r_3}$), ($\boldsymbol{r_3}$,$\boldsymbol{r_4}$) and ($\boldsymbol{r_4}$,$\boldsymbol{r_1}$). In addition, a bending energy can be defined on the central sphere, as it was explained in sec. 9.2. So basically, this would be the same model as we had before, just with $n_\mathrm{B} = 4$. We resign from this idea, since for this swimmer model is artificial anyways and a more direct control over the deformation is possible in another way.

Instead, we define a deformation pattern with prescribed sphere trajectories and a priori unknown forces, which is conceptually similar to the approach in sec. 11.4. This deformation pattern consists of three phases which are inspired by the deformation of the elastic disk. The first phase represents the in-plane deformation during the swelling process before the disk bends. The second phase simulates the shape transition and the bending into the third dimension. Thus, it is primarily a deformation in z-direction. In the third phase the swimmer finally relaxes to its original state.

To quantify these deformation phases, we define the spheres' positions at the end of each phase. This deformation pattern is visualized in fig. 12.1. The basic principle of the deformation pattern is the observation that the vertices of the elastic disk move closer to the central axis during the transition into the elliptic dome-like curved shape. The dome shape has a smaller rotational inertia then the unswollen disk. This is taken into account by moving the spheres closer to the central sphere during the first phase:

$$\boldsymbol{r_{1,1}} = -\beta R_0\boldsymbol{e_x}, \quad \boldsymbol{r_{2,1}} = -\beta R_0\boldsymbol{e_y}, \quad \boldsymbol{r_{3,1}} = \beta R_0\boldsymbol{e_x}, \quad \boldsymbol{r_{4,1}} = \beta R_0\boldsymbol{e_y}, \quad \boldsymbol{r_{5,1}} = \boldsymbol{0}. \tag{12.2}$$

Note that these positions are given in coordinates relative to the central sphere. The quantity β is a kind of new dimensionless swelling factor for the in-plane deformation with $0 < \beta < 1$ in the realistic case. After that, in the second phase, the spheres are moved in z-direction. Now we have to differ two cases. First, all four outer spheres are moved by Δz in positive z-direction, see fig. 12.1 (2a). A pyramid structure results, which represents the elliptic dome-like shape. Or as the second possibility, two spheres (1 and 3) move in positive z-direction, while the other two (2 and 4) move for the same distance in negative direction, as shown in fig. 12.1 (2b). This is the equivalent to a hyperbolic saddle. Consequently, we have

$$\begin{aligned} \boldsymbol{r}_{\mathbf{1,2a}} &= \begin{pmatrix} -\beta R_0 \\ 0 \\ \Delta z \end{pmatrix}, \quad \boldsymbol{r}_{\mathbf{2,2a}} = \begin{pmatrix} 0 \\ -\beta R_0 \\ \Delta z \end{pmatrix}, \quad \boldsymbol{r}_{\mathbf{3,2a}} = \begin{pmatrix} \beta R_0 \\ 0 \\ \Delta z \end{pmatrix} \\ \boldsymbol{r}_{\mathbf{4,2a}} &= \begin{pmatrix} 0 \\ \beta R_0 \\ \Delta z \end{pmatrix}, \quad \boldsymbol{r}_{\mathbf{5,2a}} = \mathbf{0} \end{aligned} \tag{12.3}$$

or

$$\begin{aligned} \boldsymbol{r}_{\mathbf{1,2b}} &= \begin{pmatrix} -\beta R_0 \\ 0 \\ \Delta z \end{pmatrix}, \quad \boldsymbol{r}_{\mathbf{2,2b}} = \begin{pmatrix} 0 \\ -\beta R_0 \\ -\Delta z \end{pmatrix}, \quad \boldsymbol{r}_{\mathbf{3,2b}} = \begin{pmatrix} \beta R_0 \\ 0 \\ \Delta z \end{pmatrix} \\ \boldsymbol{r}_{\mathbf{4,2b}} &= \begin{pmatrix} 0 \\ \beta R_0 \\ -\Delta z \end{pmatrix}, \quad \boldsymbol{r}_{\mathbf{5,2b}} = \mathbf{0}. \end{aligned} \tag{12.4}$$

In the last phase, finally all spheres move directly back to their original positions $\boldsymbol{r}_{\boldsymbol{i},\mathbf{0}}$. The spheres move on linear trajectories between the given states, so also the velocities are known. The acting forces and the velocity of the center of mass in the lab frame can be calculated in the same way as it was done for the linear deformation of the elastic disk in sec. 11.4.

The movement of the swimmer's center of mass is shown in fig. 12.2 (a). There are several curves showing the z-coordinate of the center of mass during a single deformation cycle in the case of the elliptic shape for different values of the spheres' radius a. The orange dotted line represents the hyperbolic case and stays constantly at zero, so the hyperbolic swimmer does not move at all. This is easy to explain in this model. We consider the forces acting on the central sphere, which are caused by the other spheres. Since the spheres 1 to 4 always move symmetrically in the x- and y-direction, forces in these directions directly add up to zero. The same happens with the z-component: In the phase (2b), the spheres 1 and 3 move in positive z-direction, so they cause a force f_z in the same direction on the central sphere. But the spheres 2 and 4 move into the opposite direction over the same distance, so they always keep the same distance to the central sphere as the other two. As a result, the force caused by 2 and 4 is $-f_z$ and, thus, in the end, the central sphere is free of forces and does not move. The same principle is the reason why the elastic disk cannot be propelled by deformations into a hyperbolic shape. The small movement, that was observed in sec. 11.3, was caused by slight deviations from this perfect symmetry.

In the elliptic case, things are different. While there is also no motion in z-direction in the first phase, since the movement is set in the $(z = 0)$-plane there, the swimmer moves in negative z-direction in the second phase. This can be explained descriptively by the following consideration. While the four outer spheres move in positive direction, the central sphere moves four times the distance in the negative direction (in the center of mass frame). Since the outer spheres have larger distances to each other than to the central sphere, the hydrodynamic interaction with the central sphere is stronger. The negative movement dominates and a small total movement in negative direction is the result. In the final phase, the spheres' velocities

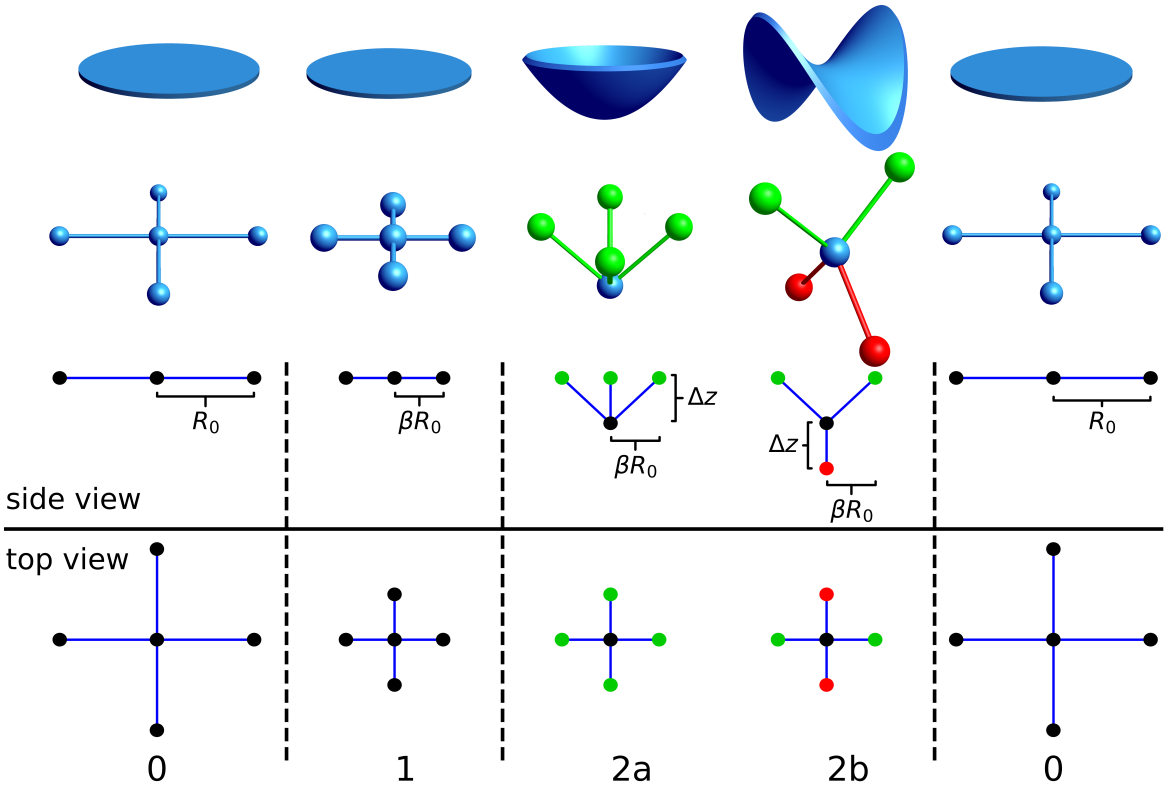

Figure 12.1.: Visualization of the deformation cycle of the 5-sphere swimmer. The numbers indicate the state at the end of the respective phase and zero is associated to the undeformed original state. The first row shows three-dimensional illustrations of the corresponding elastic disk, while the second row presents illustrations of the five-sphere model in the same deformation phases. The third row shows a view from the side (looking in positive y-direction), while the lower row gives a view from the top in negative z-direction. Spheres with $z = 0$ are colored in black, $z = \Delta z$ in green and $z = -\Delta z$ in red. The connecting lines indicate structural connections between the spheres without a direct physical meaning. They help to recognize the structure of the swimmer.

are higher, since they have to move over a longer distance in the same time due to the additional movement in the x- and y-direction. Although the z-components of the relative velocities stay the same, the additional movement of the outer spheres in radial direction creates a kind of additional pull on the central sphere. Mathematically, this is caused by the dyadic product terms in the velocity-force relation (11.11), which couples the different force components to each other. As a consequence, the swimmer's center of mass moves faster in positive z-direction in the third phase than it moved in $-z$-direction in the second phase. The total velocity decreases during the third phase, the position-time curve becomes flatter in the end. The cause of this effect is quickly found in the rapidly increasing distance between the spheres and thus the weaker hydrodynamic interaction. But in total, a net movement in the positive z-direction remains for $a < 0.2\,R_0$.

Figure 12.2 (b) shows the net movement of the center of mass after one complete deformation cycle as a function of the spheres' radius a. This function can be roughly separated in two parts. First, there is a linear increase. This is easily explained, as the hydrodynamic interaction between the spheres increases with their radius and at $a = 0$ there is no total movement of the swimmer, because the spheres cannot move without any interaction with the fluid. But for higher values of a, the slope decreases and becomes negative so that the

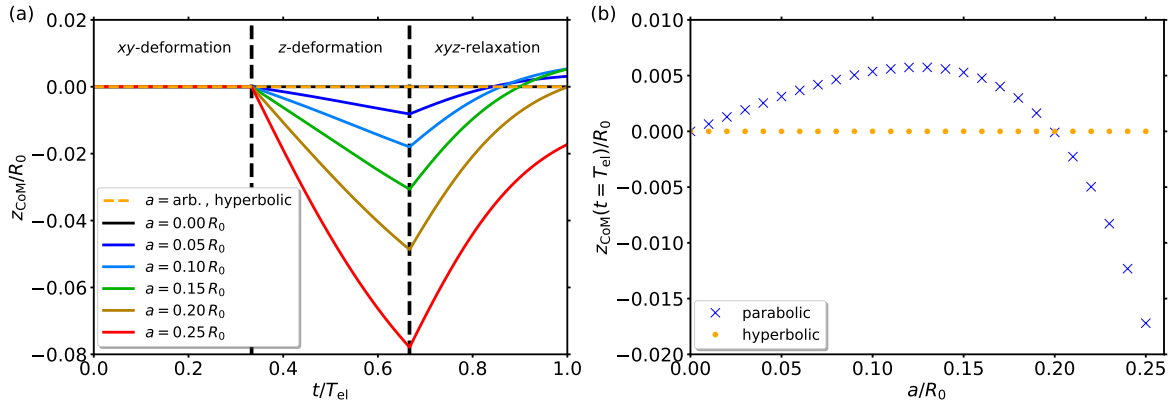

Figure 12.2.: (a): z-coordinate of the center of mass of the five-sphere swimmer as a function of the time over one complete deformation cycle for different sphere sizes. The black dashed lines indicate the start and end times of the different deformation phases. The swelling factor was set to $\beta = 0.5$ and the z-displacement to $\Delta z = 0.5\,R_0$. All curves corresponding to the hyperbolic deformation pattern collapse to $z_{\mathrm{CoM}}(t) = 0$.
(b): z-coordinate of the center of mass after one deformation cycle, $z_{\mathrm{CoM}}(t = T_{\mathrm{el}})$, as a function of the spheres' radius a for a swimmer with the same deformation parameters.

swimmer even starts to move in the opposite direction for $a > 0.2\,R_0$. This behavior is not to be expected at first, since bigger spheres should simply increase the interaction and, therefore, increase the swimming distance even further. So, the question arises, which effect is the cause of this behavior. To answer that question a brief look to the basic requirements of the hydrodynamic interaction model is advised, because it should be noted again, that the condition $a \ll R_0$ must not be violated while using the Oseen- or Rotne-Prager model. But with $a = 0.2\,R_0$, or even $a = 0.25\,R_0$, this is definitely the case. With $a = 0.25\,R_0$, the spheres are even in self contact in the second phase, because $\beta = 0.5$ was used here. Therefore, the change of the swimming direction is an artefact of the violation of the conditions of the hydrodynamic model. The spheres' radius a should always stay in the linear region of 12.2 (b) in order to keep the model at least partly valid with physically reasonable results.

To finalize this chapter about the five-sphere swimmer, the influence of the swelling factor β shall be investigated. Figure 12.3 shows the swimmer distance after one deformation cycle as a function of β for the same swimmer as before with $a = 0.1\,R_0$. It is convincing that there is no effective swimming at $\beta = 1$, because that means there is no deformation in the x- and y-direction. So only a one-dimensional z-deformation remains without any total movement due to the scallop theorem. With $\beta < 1$, a swimming movement in positive z-direction can be observed. Further reduction of β leads to a nearly linear increase of the swimming distance. This can be explained by the increased hydrodynamic interaction. Smaller values of β have a comparable effect on the hydrodynamic interaction as higher values of a. While the 5-sphere swimmer is comparable to the swelling elastic disk in principle for $\beta < 1$, there is no such analogy for $\beta > 1$. Nevertheless, the behavior of the 5-sphere swimmer can also be examined in that case. Increasing β has the opposite effect on the swimmer and causes a swimming movement into the negative z-direction. The reason for that behavior is found in the hydrodynamic interaction in the second phase now dominating over the interaction in the third phase. While there is a lower limit for small values of β, because of the condition that the spheres' distance is much greater than their radius must not be violated, there is no such limit for high values of β. Increasing β even further, see fig. 12.3 (b), we find a minimum at about $\beta = 3.5$. Going on, for very high values of β, the swimming distance converges to zero. In that case, the spheres are so far away from each other for most of the time in the

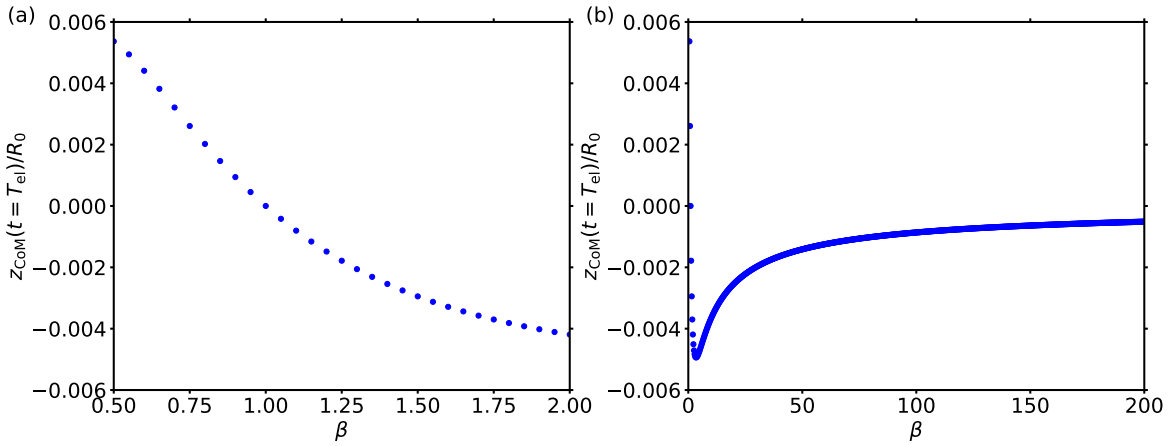

Figure 12.3.: z-coordinate of the center of mass of the five-sphere swimmer as a function of the swelling factor β. (a) shows a zoom-in of the whole curve shown in (b). The curves correspond to a swimmer with $a = 0.1\,R_0$ and $\Delta z = 0.5\,R_0$.

deformation cycle, that there is effectively no hydrodynamic interaction left.

13. Velocity field of the fluid

The objective of the following chapter is to investigate the interaction between the swimmer and the fluid. Therefore, the velocity fields $\boldsymbol{u}(\boldsymbol{r})$, which are caused by the disk's and the five-sphere swimmer's deformation, are calculated during the different phases of the deformation cycle in a first section. The swimmers are then characterized with a comparison of the structure of their velocity field. In the second section, the fluid stream through the surface of the deformed disk is used in order to estimate the errors of the swimmer model, especially the method of modelling a continuous surface with sparse spheres.

13.1. Characterization of the velocity field

In the literature about microswimmers, it is quite common to compare different swimmers by the fluid velocity field $\boldsymbol{u}(\boldsymbol{r})$, which they create with their motion [30, 46, 84, 92, 151]. The flow fields are characterized in comparison to the flow field of a spherical swimmer, i.e., a swimmer that propels itself by generating a tangential fluid flow on its surface. Spherical swimmers are a widely used model of microswimmers and were originally described by Lighthill in 1952 [95]. Later, Blake corrected and improved the model [17]. The swimmer itself consists of a spherical body with is able to disturb its surface. This surface can perform different deformation patterns to create radial and tangential fluid flow. As a result, different velocity fields and, therefore, different types of swimming can be induced. The velocity field of a nearly spherical swimmer of radius R with rotational symmetry can be described in spherical coordinates (the z-axis is parallel to the swimming direction) in the swimmer frame by a series expansion with the Legendre polynomials P_n [17]:

$$\begin{aligned} u_r(r,\theta) = &-|\boldsymbol{v}_{\mathbf{CoM}}|\cos\theta + A_0\frac{R^2}{r^2}P_0 + \frac{2}{3}(A_1+B_1)\frac{R^3}{r^3}P_1(\cos\theta) \\ &+ \sum_{n=2}^{\infty}\left[\left(\frac{1}{2}n\frac{R^n}{r^n} - \left(\frac{1}{2}n-1\right)\frac{R^{n+2}}{r^{n+2}}\right)A_nP_n(\cos\theta) + \left(\frac{R^{n+2}}{r^{n+2}} - \frac{R^n}{r^n}\right)B_nP_n(\cos\theta)\right], \end{aligned} \tag{13.1}$$

$$\begin{aligned} u_\theta(r,\theta) = &|\boldsymbol{v}_{\mathbf{CoM}}|\sin\theta + \frac{1}{3}(A_1+B_1)\frac{R^3}{r^3}V_1(\cos\theta) \\ &+ \sum_{n=2}^{\infty}\left[\frac{1}{2}n\left(\frac{1}{2}n-1\right)\left(\frac{R^n}{r^n} - \frac{R^{n+2}}{r^{n+2}}\right)A_nV_n(\cos\theta)\right. \\ &\left. + \left(\frac{1}{2}n\frac{R^{n+2}}{r^{n+2}} - \left(\frac{1}{2}n-1\right)\frac{R^n}{r^n}\right)B_nV_n(\cos\theta)\right], \end{aligned} \tag{13.2}$$

$$u_\varphi(r,\theta) = 0. \tag{13.3}$$

The polar angle is given by θ. u_r describes the radial component of the field and u_θ the tangential component in polar direction respectively. The azimuthal component u_φ vanishes due to the rotational symmetry. The functions $P_n(\cos\theta)$ are the n-th Legendre polynomials and V_n describes their derivatives via

$$V_n(\cos\theta) = \frac{-2}{n(n+1)}\frac{\partial}{\partial\theta}P_n(\cos\theta). \tag{13.4}$$

The constants A_n and B_n are real coefficients carrying information about the characteristics of the field $\boldsymbol{u}$. The coefficients A_n are related to the radial deformation of the surface and the B_n to the tangential deformation. This becomes easily visible on the surface at $r = R$:

$$u_r(r = R,\theta) = \sum_{n=0}^{\infty} A_n P_n(\cos\theta), \tag{13.5}$$

$$u_\theta(r = R,\theta) = \sum_{n=0}^{\infty} B_n V_n(\cos\theta). \tag{13.6}$$

A swimmer which only swims by self-deformation is free of external forces. Then the coefficient A_1 always vanishes, because a finite A_1 would cause the swimmers center of mass to move in empty space without external forces. The center of mass' velocity is given by

$$|\boldsymbol{v}_{\mathbf{CoM}}| = \frac{1}{3}(2B_1 + A_1) = \frac{2}{3}B_1, \tag{13.7}$$

so it is only related to B_1 in our case. The higher modes quickly decrease in higher distance to the swimmer with $r \gg R$, so the far field is dominated by the lower modes. We now use this behavior to characterize the swimmer by its velocity field. All orders with $n > 2$ in the series expansion (13.1) are neglected. Now the highest order ($n = 2$) describes a dipole moment. Therefore, we interpret the radial component of the far field of the swimmer as the field of a force dipole aligned in swimming direction. The radial component of the velocity field created by a simple force dipole at $r = 0$ is given by [84]

$$u_r(r,\theta) = \frac{p}{4\pi\eta r^2} P_2(\cos\theta). \tag{13.8}$$

The dipole moment p can be positive or negative depending on the orientation of the dipole. Comparing the dipole field with the second order of (13.1) (and using $R^2/r^2 \gg R^4/r^4$), we get

$$(A_2 - B_2)R^2 = \frac{p}{4\pi\eta}. \tag{13.9}$$

That means that the sign of $(A_2 - B_2)$ decides over the sign of the dipole moment p and this sign characterizes general types of swimmers. A swimmer whose far field shows the characteristics of a dipole field with $p > 0$ is called a *pusher*. Fluid comes from the side to the swimmer and is pushed away at the front and at the back. The swimmer seems to push itself through the fluid. Usually pushers create their thrust at their rear side. Typical examples for pushers are many bacteria like E. coli and also sperm cells [84, 128]. On the other hand, $p < 0$ represents a *puller*. Fluid streams towards the swimmer from the front and from the back and is pushed away at the swimmer's sides. These swimmers often have their moving mechanism at the front, pulling themselves through the fluid. The typical prototype of a puller is the alga of the type Chlamydomonas [84, 128]. In order to be able to compare the field types of different swimmers not only in a qualitative but also in a quantitative way, we define the swimmer characterization ratio

$$\gamma = \frac{A_2 - B_2}{|B_1|}. \tag{13.10}$$

This ratio or similar defined ratios are often[1] used to characterize velocity fields of microswimmers. Now we can also define further types of swimmers: $\gamma = 0$ is called a neutral swimmer.

[1] In the literature in the case of a squirmer (only tangential deformation with $A_n = 0$), this ratio is sometimes inaccurately defined as $\gamma = B_2/B_1$, which is insufficient without a further definition of the sign of B_1.

The far field only consists of the modes up to the first order. The limiting cases $\gamma \to \infty$ and $\gamma \to -\infty$ correspond to a swimmer that is actually not moving because of $B_1 = 0$. This is called a *shaker* as the swimmer moves the fluid but does not propel itself.
Assuming that a swimmer shares the velocity field of a such a spherical swimmer, it can be characterized by calculating the coefficients B_1 and $(A_2 - B_2)$ from its velocity field. This provides also the possibility to compare the swelling elastic disk with the five-sphere model. In order to do so, the velocity field $\boldsymbol{u}(r,\theta)$ is needed in the simulation.
The velocity field of the fluid can be calculated at the position $\boldsymbol{r}$ by placing a test sphere there and calculating its velocity. This test sphere only moves due to the hydrodynamic forces of all the other spheres. So, the Rotne-Prager relation (11.11) can be used to calculate $\boldsymbol{u}$ when the direct force term $\boldsymbol{f_i}$ is abandoned:

$$\begin{aligned}\boldsymbol{u}(\boldsymbol{r}) = \sum_j \frac{1}{6\pi\eta a}\Bigg(&\frac{3a}{4|\boldsymbol{r}-\boldsymbol{r_j}|}\left(\underline{\underline{\boldsymbol{I}}} + \frac{(\boldsymbol{r}-\boldsymbol{r_j})\otimes(\boldsymbol{r}-\boldsymbol{r_j})}{|\boldsymbol{r}-\boldsymbol{r_j}|^2}\right)\\ &+ \frac{a^3}{4|\boldsymbol{r}-\boldsymbol{r_j}|^3}\left(\underline{\underline{\boldsymbol{I}}} - 3\frac{(\boldsymbol{r}-\boldsymbol{r_j})\otimes(\boldsymbol{r}-\boldsymbol{r_j})}{|\boldsymbol{r}-\boldsymbol{r_j}|^2}\right)\Bigg)\boldsymbol{f_j}.\end{aligned} \tag{13.11}$$

The sum is running over all spheres j of the swimmer.
The five-sphere model consists of three different deformation phases with completely different motions of the swimmer, so the ratio γ has to be calculated in each phase. In detail, γ is calculated at the beginning of each phase. These three phases can also be defined for the swelling disk. The first phase and, therefore, the first evaluation of the velocity field is set right at the beginning of the swelling cycle, when there is only motion in the $(z = 0)$-plane. The second evaluation point, corresponding to the second phase, is set when the transition to the elliptic shape occurs and when the mesh shows the greatest changes in the simulation. Finally, the third evaluation point is located at the beginning of the way back in the deformation cycle. These evaluation points are chosen to give the highest possible fluid velocities and are preferred over a time average over the whole phases. The velocity fields $\boldsymbol{u}(\boldsymbol{r})$ at the specified evaluation points of all three phases are shown in fig. 13.1. Different colors indicate the absolute of the fluid velocity, the arrows indicate the direction. All six plots show the $(y = 0)$-plane. The thick black line represents a cut through the swelling disk, while the black circles indicate the spheres of the five-sphere swimmer. The red arrows show the direction of motion of the specific part of the swimmer during the deformation process. There is a surprisingly good qualitative agreement between the disk swimmer and the five-sphere swimmer. That means that the deformation pattern of the five-sphere swimmer models the swelling process of the elastic disk quite well. Only one abnormality can be observed in the velocity field of the disk in the first phase. There is an asymmetry in the field between the left side (negative x-values) and the right side (positive x-values), which should not occur due to the rotational symmetry of the disk. This is probably caused by an inhomogeneous deformation behavior during the simulation due to the discretization of the mesh.
Knowing the complete velocity field $\boldsymbol{u}(\boldsymbol{r})$, the coefficients B_1 and $(A_2 - B_2)$ can now be calculated in order to characterize the swimming motion. The first coefficient B_1 is trivial, only the velocity of the swimmer's center of mass is needed. On the other hand, the calculation of $(A_2 - B_2)$ is more sophisticated. In order to get $(A_2 - B_2)$, we need to know the second order in the series expansions (13.1) or (13.2). While several different methods are possible, the most precise one seems to be to use the fact that the Legendre polynomials P_n form an complete orthogonal system on the interval $[-1, 1]$,

$$\int_{-1}^{1} P_n(x)P_m(x)\mathrm{d}x = \frac{2}{2n+1}\delta_{nm} \tag{13.12}$$

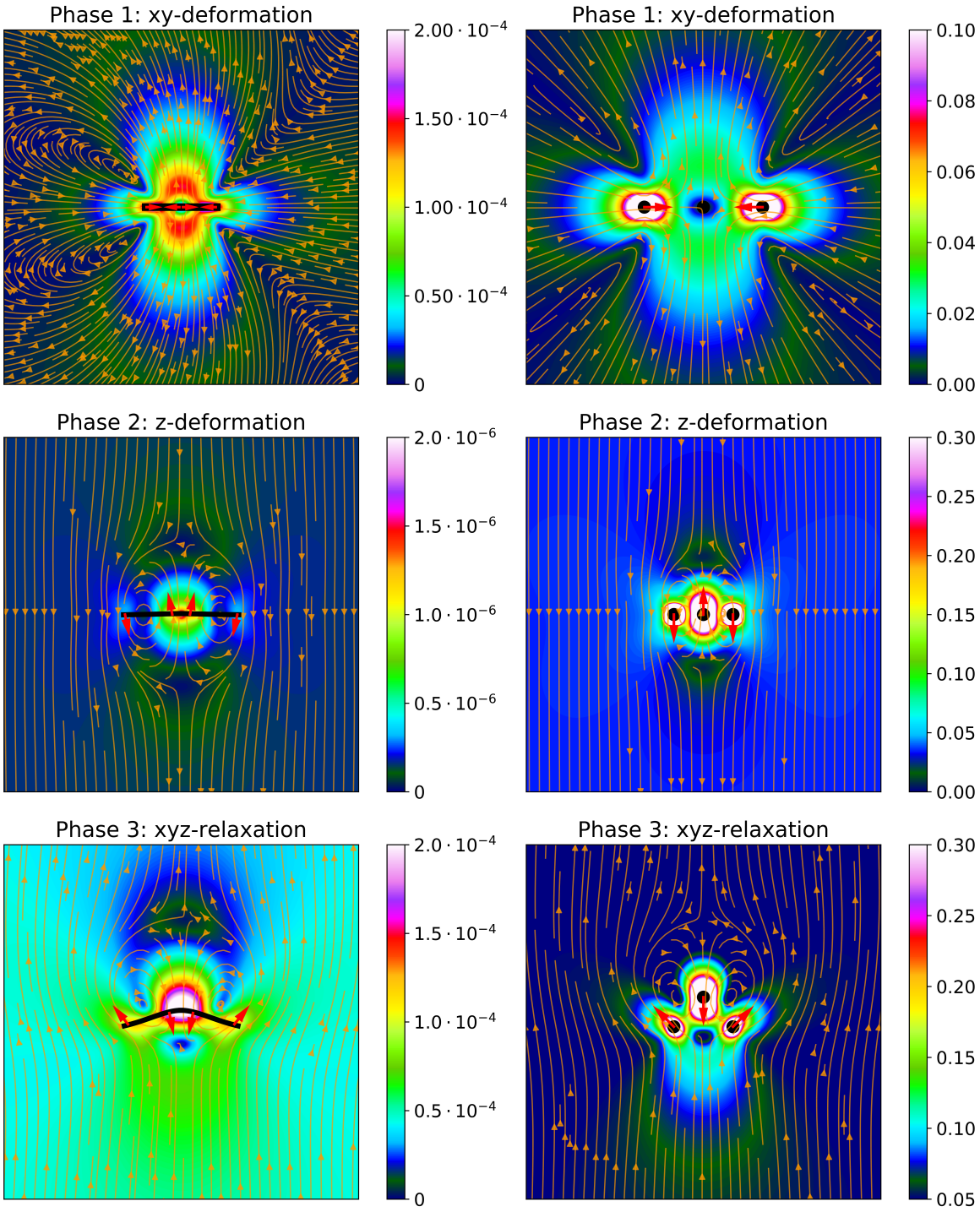

Figure 13.1.: Velocity field $\boldsymbol{u}(\boldsymbol{r})$ in the $(y = 0)$-plane for each deformation phase. The left side shows a disk with $n_\mathrm{B} = 50$, $R_\mathrm{in}/R_0 = 0.5$, $\gamma_\mathrm{FvK} = 600$, $k_\mathrm{in}/k_\mathrm{out} = 0.24$, and $a = 0.1 \cdot 2\pi R_0/n_\mathrm{B}$. The right side shows a five-sphere swimmer with $\beta = 0.5$, $\Delta z = 0.5\,R_0$ and $a = 0.1\,R_0$. Colors indicate the absolute $|\boldsymbol{u}|$ in units of k_out/η for the disk swimmer and in units of R_0/T_{el} for the five-sphere swimmer. The arrows show the direction of the fluid velocity vectors.

with the Kronecker delta, δ_{nm}. With that knowledge, $(A_2 - B_2)$ can be determined via

$$\frac{2}{5}(A_2 - B_2)\left(\frac{R}{r}\right)^2 = \int_{-1}^{1} P_2(\cos\theta) u_r(r,\theta) \mathrm{d}\cos\theta$$

$$\Leftrightarrow A_2 - B_2 = \frac{5}{2}\left(\frac{r}{R}\right)^2 \int_{-1}^{1} P_2(\cos\theta) u_r(r,\theta) \mathrm{d}\cos\theta. \tag{13.13}$$

This integral is evaluated numerically in the far field at $r = 10\,R_0$. The constant R still describes the radius of the assumed spherical swimmer. Neither the deformed disk, nor the five-sphere swimmer are spherical, so an assumption for R has to be done. In the undeformed state, the spring mesh of the disk has a radius of R_0 in the $(z = 0)$-plane and a vanishing height in the z-direction. So, we use $R = 0.5\,R_0$ as a rough approximation of the demanded spherical shape.
The results for the coefficients of the same simulations that generated the velocity fields in fig. 13.1 are shown in table 13.1. Again, we see a good qualitative agreement between the swelling disk and the five-sphere model. In the first deformation phase the swimmers (nearly) do not move, which results in $\gamma \approx \infty$, both the disk and the five-sphere swimmer form a shaker. In the second phase, when the disk deforms out of the plane at the shape transition, the velocity field is the field of a pusher. And also in the third phase, when the disk and the five-sphere swimmer relax back to the original state, both agree in being a puller.
When the coefficients B_1 and $(A_2 - B_2)$ are known, the velocity field can be calculated up to the second order. In order to judge the quality of the assumption of the velocity field being like a spherical swimmer field, the field from the series expansion (13.1) and (13.2) shall be compared to the velocity fields from the simulations. These comparisons are shown in fig. 13.2

phase 1	disk	five-sphere	swimmer type
B_1	$2.02 \cdot 10^{-8}$	0	
$A_2 - B_2$	$1.75 \cdot 10^{-3}$	$3.16 \cdot 10^{-1}$	
$\gamma = (A_2 - B_2)/\lvert B_1\rvert$	$8.69 \cdot 10^{5}$	∞	shaker
phase 2	**disk**	**five-sphere**	**swimmer type**
B_1	$2.38 \cdot 10^{-7}$	$5.23 \cdot 10^{-2}$	
$A_2 - B_2$	$1.36 \cdot 10^{-9}$	$1.31 \cdot 10^{-2}$	
γ	$5.70 \cdot 10^{-3}$	$2.50 \cdot 10^{-1}$	pusher
phase 3	**disk**	**five-sphere**	**swimmer type**
B_1	$-6.54 \cdot 10^{-5}$	$-7.32 \cdot 10^{-2}$	
$A_2 - B_2$	$-7.70 \cdot 10^{-4}$	$-4.50 \cdot 10^{-1}$	
γ	-11.77	-6.14	puller

Table 13.1.: Coefficients of the series expansions (13.1) and (13.2) for the swelling disk and the five-sphere swimmer that correspond to figures 13.1 and 13.2.

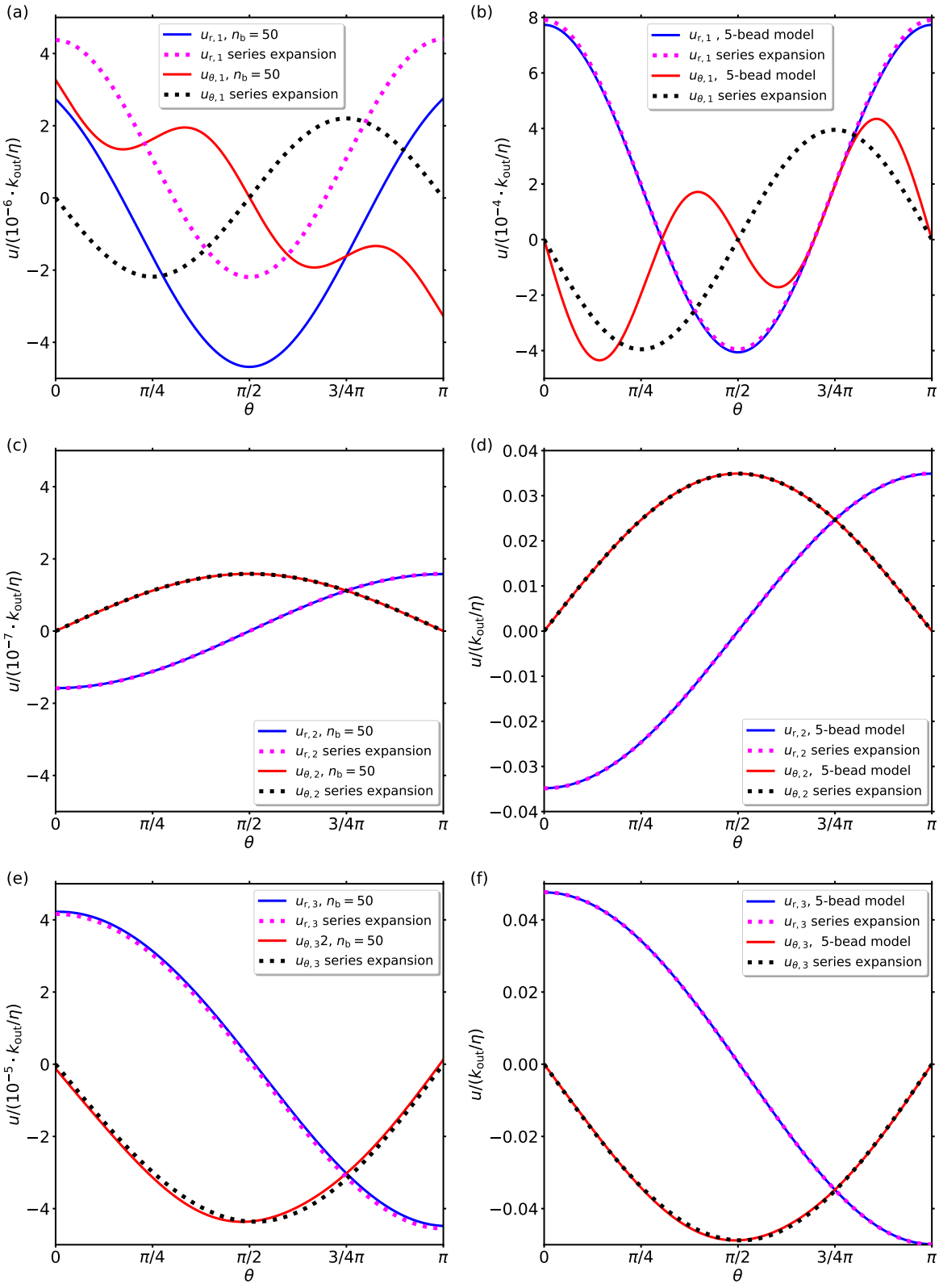

Figure 13.2.: Comparison of the radial and polar component of the spherical swimmer velocity field with the field from the numerical simulations as functions of the polar angle θ at $r = 10\,R_0$. The dashed lines show the series expansion (13.1) and (13.2), while the solid lines correspond to the simulations. (a) and (b) show the first phase of deformation, (c) and (d) the second phase and (e) and (f) the third one. The graphs on the left side correspond to the swelling disk, the right side to the five-sphere model. These diagrams are exactly related to the flow fields shown in fig. 13.1.

for the same simulations that already featured the velocity fields from fig. 13.1. In the first phase of the deformation, high deviations show up for the disk, see fig. 13.2 (a) and also in the polar components of the five-sphere swimmer in fig. 13.2 (b). These deviations can be explained by two effects: First, the swimmers are planar in the first phase, violating the spherical model in the most possible way. Secondly, the disk does not deform in a symmetrical way, as already mentioned before. But then in the second phase, (c)+(d), and in the third phase, (e)+(f), there is a really good agreement between the series expansion and the simulation for both the radial and the polar component.

13.2. Fluid stream through the surface

A major drawback of the spring-mesh model with hydrodynamic interaction by spheres at the vertices is that the spheres only cover a small part of the disk. In consequence, the fluid is able to stream through the swimmer's surface in this model, which is not possible for a real swimmer with a continuous surface. In this section, the error of the model by this effect shall be quantified. Therefore, the fluid stream through the swimmer surface needs to be calculated.
In theory, the fluid velocity field relative to the surface $\boldsymbol{u}(\boldsymbol{r}) - \boldsymbol{v_S}(\boldsymbol{r})$ is needed in the surface between the spheres and has to be integrated over the whole surface S. The vector $\boldsymbol{v_S}(\boldsymbol{r})$ describes the local velocity of the swimmer surface. The integral becomes a sum over all triangles of the Delauney triangulation. Then, the stream j_S through the surface, i.e. the normal component of the velocity multiplied with the surface area, can be expressed via

$$j_S = \int_S (\boldsymbol{u}(\boldsymbol{r}) - \boldsymbol{v_S}(\boldsymbol{r})) \cdot \boldsymbol{n} \mathrm{d}A = \sum_i \int_{A_i} (\boldsymbol{u}(\boldsymbol{r}) - \boldsymbol{v_i}) \cdot \boldsymbol{n_i} \mathrm{d}A. \tag{13.14}$$

The surface normal vector is given by $\boldsymbol{n}$. The sum on the right side runs over all triangles i with the area A_i of the triangulation. To calculate the integral about a single triangle, the velocity field $\boldsymbol{u}$ needs to be evaluated within this triangle. Therefore, we calculate $\boldsymbol{u}$ via eq. (13.11) at four defined points $\boldsymbol{t_1}$ to $\boldsymbol{t_4}$, which are illustrated in fig. 13.3. The points $\boldsymbol{t_1}$ to $\boldsymbol{t_3}$ are placed on the mid points of the triangle's edges and $\boldsymbol{t_4}$ is placed in the triangle's center of mass. The velocity field at the vertices (to be more precise on the surface of the vertex spheres) is assumed to be identical to the vertex velocities, representing the no-slip boundary conditions. After all, we know $\boldsymbol{u}$ at seven points within the triangle. These points form six sub triangles. Inside of each sub-triangle, $\boldsymbol{u}$ is interpolated linearly, so the integral for the fluid stream can be calculated analytically. The surface velocity $\boldsymbol{v_S}(\boldsymbol{r})$ is also a simple interpolation between the vertex velocities. The total integral finally needs to be corrected by the area that is covered by the vertex spheres, where no fluid can stream through.

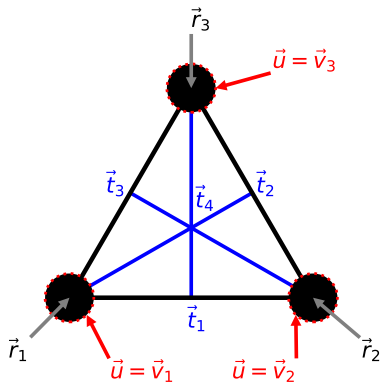

Figure 13.3.: Illustrative sketch for the readout points inside of a single triangle. The black circles represent the spheres at the vertices of the mesh. The red dots on the spheres' surfaces indicate the no-slip boundary condition of the fluid.

Being able to calculate the fluid stream through the swimmer's surface, j_S, we also need to define a reference value for the interpretation of j_S. Therefore, we define the fluid stream j_P through a theoretically perfectly permeable surface that moves with a velocity $\boldsymbol{v_S}$ through the fluid. The ratio $|j_S/j_\mathrm{P}|$ gives information about the quality of the sphere-mesh model in terms of modelling a continuous impermeable surface. $|j_S/j_\mathrm{P}| = 0$ represents the perfect case when no fluid may pass through the surface. On the other hand, $|j_S/j_\mathrm{P}| = 1$ represents a completely permeable surface moving through a fluid at rest. The ratio $|j_S/j_\mathrm{P}|$ for different discretizations as a function of the spheres' radius a is shown in fig. 13.4, at the beginning of the third deformation phase at $\alpha = 0.95$. In principle, all discretizations show the same behavior: There is a high fluid stream through the surface for small radii a, which is not surprising, because $a = 0$ represents a permeable surface. Then, with increasing a, $|j_S/j_\mathrm{P}|$ quickly decreases and reaches a minimum, before it starts to increase again slightly. This increase can be interpreted in a similar way as the decrease of the swimming speed of the five-sphere swimmer for higher a, which was discussed in the previous chapter. The spheres' radius is not very small anymore compared to the spheres' distance and, therefore, violates a basic condition of the hydrodynamic model. The minimum position varies slightly with the discretization but it turns out that the value $a = 0.1 \cdot 2\pi R_0/n_\mathrm{B}$, which was used for most of the simulations in this thesis, is a very good choice for most of the discretizations.

After all, especially for the higher discretizations, the fluid stream through the surface is surprisingly small, regarding that only the smallest part of the surface is covered by spheres. A brief estimation states that with $a = 0.1 \cdot 2\pi R_0/n_\mathrm{B}$ only about 3.6 % of the surface area are covered by the spheres. But on the other hand, the total number of spheres and therefore the number of point forces in the first order of the hydrodynamic interaction, which are independent of a, see eq. (11.11), increases with ${n_\mathrm{B}}^2$. That is the reason, why higher forces act on the fluid between the spheres for finer discretizations leading to a smaller permeability. Nevertheless, these results should not be over-interpreted. The hydrodynamic interaction of the Rotne-Prager model is not meant to model a continuous surface and higher orders of the interaction, especially self-interaction via reflections of waves in the fluid, should play an important role in a more realistic model.

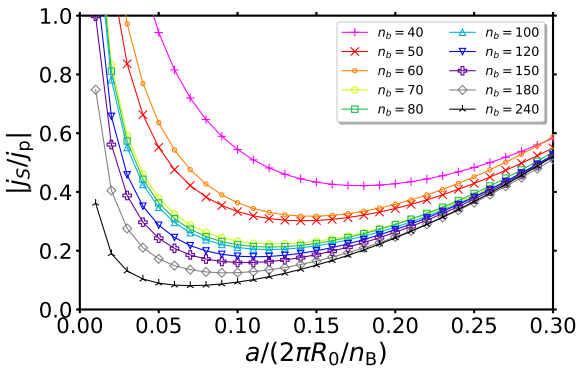

Figure 13.4.: Relative fluid stream through the swimmer's surface as a function of the spheres' radius a for different discretizations. The diagram corresponds to a swimmer with $R_\mathrm{in} = 0.5\,R_0$, $\gamma_\mathrm{FvK} = 600$, $k_\mathrm{in}/k_\mathrm{out} = 0.24$ and was captured in the deformation cycle at $\alpha = 0.95$ at the beginning of the third deformation phase.

14. Conclusion and outlook

The basic idea of this second part of the thesis was to use a possible hysteretic behavior of a shape transition in the swelling process of a flat elastic disk as the propulsion for a microswimmer. The problem consisted of two parts, the pure elastic problem of describing the deformation of the disk due to swelling and secondly the interaction with the surrounding fluid. In order to give only a proof of concept and a description of the basic behavior, the simplest viable models were used. Therefore, the quantitative results should not be over-interpreted.

Applying methods from differential geometry, we found that a flat circular elastic disk with rotational symmetry should be deformed into an elliptic curved surface, when the inner regions of the disk swell stronger than the outer regions. In the opposite case, a hyperbolic shape with negative Gaussian curvature can be expected. To simulate the deformation behavior of the elastic disk, a two-dimensional spring mesh was used to discretize its area. While the adjustment of the spring constants allows to realize any two-dimensional Young modulus Y_{2D}, the Poisson ratio ν is fixed to $\nu = 1/3$ as a major drawback. A bending energy was also added and implemented via area gradients. Inspired by an experiment by Pezulla et. al. [110], we multiplied a piecewise constant swelling function to the springs rest length. A swelling factor α was applied to the springs in the outer region, while the factor $1/\alpha$ was used in the inner region. It was also shown that this swelling pattern is equivalent to swelling with the factors α^2 and 1 after a global rescaling. This should be the simplest system to realize experimentally in the future. Calculating the preferred state of the disk via energy minimization, the disk takes an elliptic dome-like conformation for sufficiently strong swelling with $\alpha < 1$ and a hyperbolic saddle-like shape for $\alpha > 1$. Changing the swelling factor α in small steps, the interplay between the stretch energy of the springs and the bending energy was found to cause a shape transition that exhibits a numerical pseudo-hysteresis. At a critical value of the swelling factor, depending on fluctuations, the disk suddenly jumps to a non-flat conformation with a finite bending energy. This transition does not show a real hysteretic behavior, because there is no energy barrier that has to be overcome in order to switch from the flat disk into the curved shape. Moving the swelling factor α back to 1, the shape becomes flat again in a smooth and continuous way.

To validate the results of the spring model, the Gaussian curvature of the curved disk provided a valid tool for a comparison with numerical and experimental results from ref. [110]. Despite some deviation in the outer regions of the disk, there was a good agreement in the central region. At the end of the chapter about the dry deformation, a small excursion to other swelling functions followed. It was shown that shapes with a positive constant Gaussian curvature are accurately accessible and negative constant Gaussian curvatures are only nearly possible, which verified the predictions from differential geometry.

The hydrodynamic interaction was added for long time scales and low Reynolds numbers, which is the appropriate limit for microswimmers. The continuous surface of the disk was modelled by a mesh of spheres, each vertex of the spring mesh was assumed to be a sphere with a finite size. These spheres carried the hydrodynamic interaction, while the springs were invisible for the fluid. The hydrodynamic interaction itself was modelled by a simple Rotne-Prager interaction, which requires high distances between the spheres, compared to their radii, so the sphere mesh was only sparse and left the biggest parts of the surface area uncovered. Simulating whole swelling cycles of the disk with hydrodynamic interaction, we found a net

movement of the disk which was deformed into the elliptic dome shape. The direction of the movement is parallel to the symmetry axis in the direction of the opening of the dome. The hyperbolic saddle shape showed only little movement, probably due to discretization effects, because symmetry arguments forbid a movement of this object.

After that, a five-sphere model was introduced as a minimal model for the swimming mechanism of the swelling disk. Therefore, the deformation of the disk was categorized in three different phases, a first phase of in plane deformation, a second phase with the transition into a three-dimensional conformation and a third phase with the relaxation back to the original state. The five-sphere model helped to understand the swimming process within each single phase and was also able to show the limits of the validity of the hydrodynamic interaction model.

Finally, the fluid velocity fields were investigated. The swelling disk and the five-sphere swimmer showed a very good qualitative agreement, which underlines the ability of the five-sphere swimmer to model the behavior of the disk. Comparisons to the velocity field of a spherical swimmer allowed us to characterize the swimming type of our swimmers. The first phase corresponds to an immobile shaker, the second phase represents a pusher and the third one a puller. Also, the fluid stream through the disk's surface indicated, that using small spheres to model a continuous surface, leads to smaller errors than it could be assumed in the first place, at least for higher discretizations.

After all, it was proven that a flat elastic disk could be used as a microswimmer, if it is deformed into an elliptic shape by a swelling process that shows any kind of hysteresis effects. Nevertheless, as for all self-deforming swimmers, the swimming distance per deformation cycle is very small and depends on the extend of the numerical pseudo-hysteresis. In an experimental realization, there is possibly no pseudo-hysteresis at all, because a real system may always find a deformation mode that directly leads to the curved shape as soon as the critical swelling factor is reached. Then, an additional potential is needed in order to create an energy barrier which results in a real hysteretic behavior. Possible realizations could be a van der Waals force (which can be imitated by a Lennard-Jones potential, as it was used in sec. 10.3) or additional magnetic particles in the disk, whose energetic ground state is the flat conformation. The size of the hysteresis region and thus the swimming distance per deformation cycle then depend on the properties of the additional potential. But the qualitative effects and swimming results in the simulation are the same. There, it is not relevant whether the scallop theorem is bypassed by a real- or a pseudo-hysteresis.

In an experimental realization, a high frequency for swelling and the deformation process is needed to ensure reasonable swimming speeds. A possible idea for a set-up is a thin elastic disk consisting of a highly stretchable thermoresponsive hydrogel [13, 42]. The inner region could be coated with a material that features higher light absorption abilities. Then, a laser could heat the inner regions, inducing thermal swelling. If the swimmer is small enough, this process should be applicable with a sufficient high frequency, but on the other hand thermal interactions between the disk and the fluid should also be taken into account. On the theoretical side of the problem, a quantitatively more reliable investigation is advised. Therefore, better models are needed. On the one hand, finite elements could be used to discretize the disk and solve differential equations of more advanced elastic models in order to have a more realistic elasticity. That way, the whole space of elastic parameters should be accessible. On the other hand, also the fluid should be discretized to model the continuous surface as a boundary condition correctly. Also, self-interactions of different parts of the disk via reflections of waves in the fluid could be modelled that way, which is completely missing in the Rotne-Prager model. However, the downside of this idea is a massive increase of the necessary computation time. But if this disadvantage is accepted, also the full Navier-Stokes equation can be solved, giving the possibility to operate also in the regime of higher Reynolds

numbers, where inertial effects become important. In that regime, a different swimming behavior can be expected. There, the quick deformation into the dome-like conformation can be interpreted as a movement that is similar to the movement of a scallop. As a consequence, the dome-like disk should propel itself into the opposite direction, the direction of the tip of the dome. In addition, that means that a Reynolds number must exist, where both swimming effects cancel each other and the disk does not move.

Literature

[1] Afkhami, S., Tyler, A. J., Renardy, Y., St. Pierre, T. G., Woodward, R. C., and Riffle, J. S. Deformation of a hydrophobic ferrofluid droplet suspended in a viscous medium under uniform magnetic fields. *J. Fluid Mech. 663* (2010), 358.

[2] Anthony, C. R., Kamat, P. M., Thete, S. S., Munro, J. P., Lister, J. R., Harris, M. T., and Basaran, O. A. Scaling laws and dynamics of bubble coalescence. *Phys. Rev. Fluids 2* (2017), 083601.

[3] Arkhipenko, V., Barkov, I. D., and Bashtovoi, V. G. Shape of a drop of magnetized fluid in a homogeneous magnetic field. *Magnetohydrodynamics 14*, 3 (1979), 373.

[4] Arnold, D. N., and Wendland, W. L. On the asymptotic convergence of collocation methods. *Math. Comput. 41*, 164 (1983), 349.

[5] Arnold, D. N., and Wendland, W. L. The convergence of spline collocation for strongly elliptic equations on curves. *Numer. Math 47*, 3 (1985), 317.

[6] Aumaitre, E., Knoche, S., Cicuta, P., and Vella, D. Wrinkling in the deflation of elastic bubbles. *Eur. Phys. J. E 36*, 3 (2013), 22.

[7] Aïssa, B., Daniel, T., Haddad, E., and Jamroz, W. Self-healing materials systems: Overview of major approaches and recent developed technologies. *Adv. Mater. Sci. Eng. 2012* (2012).

[8] Bacri, J., and Salin, D. Instability of ferroluid magnetic drops under magnetic field. *J. Phys. Lett. 43*, 17 (1982), 649.

[9] Barthès-Biesel, D. Modeling the motion of capsules in flow. *Curr. Opin. Colloid Interface Sci. 16*, 1 (2011), 3–12.

[10] Basaran, O. A., and Wohlhuter, F. K. Effect of nonlinear polarization on shapes and stability of pendant and sessile drops in an electric (magnetic) field. *J. Fluid Mech. 244* (1992), 1.

[11] Bashtovoi, V., Pogirnitskaya, S., and Reks, A. Determination of the shape of a free drop of magnetic fluid in a uniform magnetic field. *Magnetohydrodynamics 23*, 3 (1988), 248–251.

[12] Baudet, V., Beuve, M., Jaillet, F., Shariat, B., and Zara, F. Lattice models in micromechanics. *Proceedings of the 17th International Conference in Central Europe on Computer Graphics, Visualization and Computer Vision (WSCG 2009)* (2009), 145–152.

[13] Belal, K., Stoffelbach, F., Lyskawa, J., Fumagalli, M., Hourdet, D., Marcellan, A., De Smet, L., de la Rosa, V. R., Cooke, G., Hoogenboom, R., and Woisel, P. Recognition-mediated hydrogel swelling controlled by interaction with a negative thermoresponsive lcst polymer. *Angew. Chem. 55*, 45 (2016), 13974–13978.

[14] Ben Amar, M., and Pomeau, Y. Crumpled paper. *Proc. Royal Soc. A 453*, 1959 (1997), 729–755.

[15] Ben Messaoud, G., Sánchez-González, L., Probst, L., and Desobry, S. Influence of internal composition on physicochemical properties of alginate aqueous-core capsules. *J. Colloid Interface Sci. 469* (2016), 120–128.

[16] Bickel, T., Majee, A., and Würger, A. Flow pattern in the vicinity of self-propelling hot janus particles. *Phys. Rev. E 88* (2013), 012301.

[17] Blake, J. A spherical envelope approach to ciliary propulsion. *J. Fluid Mech. 46* (1971), 199–208.

[18] Bohlius, S., Harald, P., and Brand, H. R. Pattern formation in ferrogels: analysis of the rosensweig instability using the energy method. *J. Phys. Condens. Matter 18*, 38 (2006), S2671–S2684.

[19] Boltz, H.-H., and Kierfeld, J. Shapes of sedimenting soft elastic capsules in a viscous fluid. *Phys. Rev. E 92* (2015), 033003.

[20] Boudouvis, A. G., Puchalla, J. L., and Scriven, L. E. Magnetohydrostatic equilibria of ferrofluid drops in external magnetic fields. *Chem. Eng. Commun. 67*, 1 (1988), 129.

[21] Boudouvis, A. G., Puchalla, J. L., Scriven, L. E., and Rosensweig, R. E. Normal field instability and patterns in pools of ferrofluid. *J. Magn. Magn. Mater. 65*, 2-3 (1987), 307.

[22] Brakke, K. A. The surface evolver. *Experimental Mathematics 1*, 2 (1992), 141–165.

[23] Brown, R. A., and Scriven, L. E. The shape and stability of rotating liquid drops. *Proc. Royal Soc. London Ser. A 371*, 1746 (1980), 331.

[24] Brown, W. F. Thermal fluctuations of a single-domain particle. *Phys. Rev. 130* (1963), 1677–1686.

[25] Buenemann, M., and Lenz, P. Mechanical limits of viral capsids. *Proc. Natl. Acad. Sci. U.S.A. 104*, 24 (2007), 9925–9930.

[26] Carin, M., Barthès-Biesel, D., Edwards-Lévy, F., Postel, C., and Andrei, D. C. Compression of biocompatible liquid-filled HSA-alginate capsules: Determination of the membrane mechanical properties. *Biotechnol. Bioeng. 82*, 2 (2003), 207–212.

[27] Centers for Disease Control and Prevention / Hayes, P. S., and White, M. S. Escherichia coli TEM image, 1995. This image was released in the public domain and was taken from https://phil.cdc.gov/details.aspx?pid=9995.

[28] Cerda, E., and Mahadevan, L. Conical Surfaces and Crescent Singularities in Crumpled Sheets. *Phys. Rev. Lett. 80*, 11 (1998), 2358–2361.

[29] Chen, G.-Q., Grinfeld, M., and Knops, R. *Differential Geometry and Continuum Mechanics*. Springer International Publishing, 2015.

[30] Chisholm, N. G., Legendre, D., Lauga, E., and Khair, A. S. A squirmer across reynolds numbers. *J. Fluid Mech. 796* (2016), 233–256.

[31] Christodoulou, K. N., and Scriven, L. E. Discretization of free surface flows and other moving boundary problems. *J. Comput. Phys 99*, 1 (1992), 39.

[32] Ciarlet, P. G. An introduction to differential geometry with applications to elasticity. *J. Elast. 78*, 1 (2005), 1–215.

[33] Collins, R. T., Jones, J. J., Harris, M. T., and Basaran, O. A. Electrohydrodynamic tip streaming and emission of charged drops from liquid cones. *Nat. Phys. 4* (2008), 149.

[34] Collins, R. T., Sambath, K., Harris, M. T., and Basaran, O. A. Universal scaling laws for the disintegration of electrified drops. *Proc. Natl. Acad. Sci. USA 110*, 13 (2013), 4905.

[35] Costabel, M. *Symmetric Methods for the Coupling of Finite Elements and Boundary Elements (Invited contribution).* Springer, Berlin, 1987, pp. 411–420.

[36] Cowley, M. D., and Rosensweig, R. E. The interfacial stability of a ferromagnetic fluid. *J. Fluid Mech. 30*, 4 (1967), 671.

[37] Datta, S. S., Kim, S.-H., Paulose, J., Abbaspourrad, A., Nelson, D. R., and Weitz, D. A. Delayed buckling and guided folding of inhomogeneous capsules. *Phys. Rev. Lett. 109*, 13 (2012), 134302.

[38] Degen, P., Peschel, S., and Rehage, H. Stimulated aggregation, rotation, and deformation of magnetite-filled microcapsules in external magnetic fields. *Colloid Polym. Sci. 286*, 8 (2008), 865.

[39] Degen, P., Zwar, E., Schulz, I., and Rehage, H. Magneto-responsive alginate capsules. *J. Phys.: Condens. Matter 27*, 19 (2015), 194105.

[40] Desbrun, M., Meyer, M., Schröder, P., and Barr, A. H. Implicit fairing of irregular meshes using diffusion and curvature flow. In *Proceedings of the 26th Annual Conference on Computer Graphics and Interactive Techniques* (New York, NY, USA, 1999), SIGGRAPH '99, ACM Press/Addison-Wesley Publishing Co., pp. 317–324.

[41] Dhont, J. *An Introduction to Dynamics of Colloids.* Studies in Interface Science. Elsevier Science, 1996.

[42] Dinarvand, R., and D'Emanuele, A. The use of thermoresponsive hydrogels for on-off release of molecules. *J. Control. Release 36*, 3 (1995), 221 – 227.

[43] Discher, D. E., Boal, D. H., and Boey, S. K. Simulations of the erythrocyte cytoskeleton at large deformation. ii. micropipette aspiration. *Biophys. J. 75*, 3 (1998), 1584 – 1597.

[44] Djellouli, A., Marmottant, P., Djeridi, H., Quilliet, C., and Coupier, G. Buckling instability causes inertial thrust for spherical swimmers at all scales. *Phys. Rev. Lett. 119* (2017), 224501.

[45] do Carmo, M. *Differential Geometry of Curves and Surfaces.* Prentice-Hall, 1976.

[46] Downton, M., and Stark, H. Simulation of a model microswimmer. *J. Phys. Condens. Matter 21* (2009), 204101.

[47] Efimov, N. The impossibility in euclidean 3-space of a complete regular surface with a negative upper bound of the gaussian curvature,. *Dokl. Akad. Nauk SSSR 150* (1963), 1206–1209.

[48] Efrati, E., Sharon, E., and Kupferman, R. Buckling transition and boundary layer in non-euclidean plates. *Phys. Rev. E 80* (2009), 016602.

[49] Eschenburg, J., and Jost, J. *Differentialgeometrie und Minimalflächen.* Masterclass. Springer Berlin Heidelberg, 2013.

[50] Espona-Noguera, A., Ciriza, J., Cañibano-Hernández, A., Fernandez, L., Ochoa, I., Saenz del Burgo, L., and Pedraz, J. L. Tunable injectable alginate-based hydrogel for cell therapy in Type 1 Diabetes Mellitus. *Int. J. Biol. Macromol. 107*, PartA (2018), 1261–1269.

[51] Fery, A., and Weinkamer, R. Mechanical properties of micro- and nanocapsules: Single-capsule measurements. *Polymer 48*, 25 (2007), 7221–7235.

[52] Fetzer, J., Kurz, S., and Haas, M. *Numerische Berechnung elektromagnetischer Felder.* Expert-Verlag, Renningen-Malmsheim, 2002.

[53] Freund, R., and Hoppe, R. *Stoer/Bulirsch: Numerische Mathematik 1*, 10th ed. Springer, Berlin, Heidelberg, 2007.

[54] Gailītis, A. Formation of the hexagonal pattern on the surface of a ferromagnetic fluid in an applied magnetic field. *Journal of Fluid Mechanics 82*, 3 (1977), 401–413.

[55] Galassi, M. *GNU Scientific Library Reference Manual (3rd Ed.).* 2018. http://www.gnu.org/software/gsl/.

[56] Gao, C., Donath, E., Moya, S., Dudnik, V., and Möhwald, H. Elasticity of hollow polyelectrolyte capsules prepared by the layer-by-layer technique. *Eur. Phys. J. E 5*, 1 (2001), 21.

[57] Gibbs, B. F., Kermasha, S., Alli, I. ., and Mulligan, C. N. Encapsulation in the food industry: a review. *Int. J. Food Sci. Nutr. 50*, 3 (1999), 213–224.

[58] Gittleman, J. I., Abeles, B., and Bozowski, S. Superparamagnetism and relaxation effects in granular $Ni - SiO_2$ and $Ni - Al_2O_3$ films. *Phys. Rev. B 9* (1974), 3891–3897.

[59] Golestanian, R. Synthetic mechanochemical molecular swimmer. *Phys. Rev. Lett. 105* (2010), 018103.

[60] Golestanian, R., and Ajdari, A. Analytic results for the three-sphere swimmer at low reynolds number. *Phys. Rev. E 77* (2008), 036308.

[61] Grinfeld, P. *Introduction to Tensor Analysis and the Calculus of Moving Surfaces.* Springer New York, 2013.

[62] Harris, M. T., and Basaran, O. A. Capillary electrohydrostatics of conducting drops hanging from a nozzle in an electric field. *J. Colloid Interface Sci. 161*, 2 (1993), 389 – 413.

[63] Hegemann, J. *Deformation behavior of elastic shells and biological cells.* PhD thesis, Technische Universität Dortmund, 2018.

[64] Hegemann, J., Knoche, S., Egger, S., Kott, M., Demand, S., Unverfehrt, A., Rehage, H., and Kierfeld, J. Pendant capsule elastometry. *J. Colloid Interface Sci. 513* (2018), 549–565.

[65] Herminghaus, S., Maass, C. C., Krüger, C., Thutupalli, S., Goehring, L., and Bahr, C. Interfacial mechanisms in active emulsions. *Soft Matter 10* (2014), 7008–7022.

[66] Hilbert, D. Ueber Flaechen von konstanter Gaussscher Kruemmung. *Trans. Am. Math. Soc. 2* (1901), 87–99.

[67] Holligan, D. L., Gillies, G. T., and Dailey, J. T. Magnetic guidance of ferrofluidic nanoparticles in an in vitro model of intraocular retinal repair. *Nanotechnology 14*, 6 (2003), 661.

[68] Jackson, J. *Klassische Elektrodynamik*, 4th ed. de Gruyter, Berlin, 2006.

[69] Jurvetson, S. Image of a ferrofluid in a magnetic field, 2006. This image was taken from https://www.flickr.com/photos/jurvetson/136481113/. It has been released under the Creative Commons BY 2.0 license: https://creativecommons.org/licenses/by/2.0/.

[70] Karyappa, R. B., Deshmukh, S. D., and Thaokar, R. M. Deformation of an elastic capsule in a uniform electric field. *Phys. Fluids 26*, 12 (2014), 122108.

[71] Kittel, C. Physical theory of ferromagnetic domains. *Rev. Mod. Phys. 21* (1949), 541–583.

[72] Klein, R. *Algorithmische Geometrie*. Springer, Berlin, Heidelberg, 2005.

[73] Klein, Y., Efrati, E., and Sharon, E. Shaping of elastic sheets by prescription of non-euclidean metrics. *Science 315*, 5815 (2007), 1116–1120.

[74] Knoche, S. *Instabilities and shape analyses of elastic shells*. PhD thesis, Technische Universität Dortmund, 2014.

[75] Knoche, S., and Kierfeld, J. Buckling of spherical capsules. *Phys. Rev. E 84*, 4 (2011), 046608.

[76] Knoche, S., and Kierfeld, J. The secondary buckling transition: Wrinkling of buckled spherical shells. *Eur. Phys. J. E 37*, 7 (2014), 62.

[77] Knoche, S., and Kierfeld, J. Secondary polygonal instability of buckled spherical shells. *EPL 106*, 2 (2014), 24004.

[78] Knoche, S., Vella, D., Aumaitre, E., Degen, P., Rehage, H., Cicuta, P., and Kierfeld, J. Elastometry of deflated capsules: Elastic moduli from shape and wrinkle analysis. *Langmuir 29*, 40 (2013), 12463–12471.

[79] Kornberger, B. Fade2D Delauney Trianglulation library, 2016. http://www.geom.at/products/fade2d/.

[80] Kost, A. *Numerische Methoden in der Berechnung elektromagnetischer Felder*. Springer, Berlin, Heidelberg, 1994.

[81] Küchler, N., Löwen, H., and Menzel, A. M. Getting drowned in a swirl: Deformable bead-spring model microswimmers in external flow fields. *Phys. Rev. E 93* (2016), 022610.

[82] Kumar, M. S., and Philominathan, P. The physics of flagellar motion of e. coli during chemotaxis. *Biophys. Rev. 2*, 1 (2010), 13–20.

[83] Landau, L. D., and Lifshitz, E. M. *Theory of Elasticity.* Pergamon, Oxford, 1970.

[84] Lauga, E., and Powers, T. The hydrodynamics of swimming microorganisms. *Rep. Prog. Phys. 72* (2008).

[85] Lavrova, O. *Numerical methods for axisymmetric equilibrium magnetic-fluid shapes.* PhD thesis, Otto-von-Guericke University Magdeburg, 2006.

[86] Lavrova, O., Matthies, G., Mitkova, T., Polevikov, V., and Tobiska, L. Numerical treatment of free surface problems in ferrohydrodynamics. *J. Phys. Condens. Matter 18*, 38 (2006), S2657.

[87] Lavrova, O., Matthies, G., Polevikov, V., and Tobiska, L. Numerical modeling of the equilibrium shapes of a ferrofluid drop in an external magnetic field. *Proc. Appl. Math. Mech. 4*, 1 (2004), 704.

[88] Lavrova, O., Polevikov, V., and Tobiska, L. Equilibrium shapes of a ferrofluid drop. *Proc. Appl. Math. Mech. 5*, 1 (2005), 837.

[89] Leick, S., Degen, P., and Rehage, H. Rheologische Eigenschaften von Kapselmembranen. *Chemie Ingenieur Technik 83*, 8 (2011), 1300–1304.

[90] Leick, S., Henning, S., Degen, P., Suter, D., and Rehage, H. Deformation of liquid-filled calcium alginate capsules in a spinning drop apparatus. *Phys. Chem. Chem. Phys. 12*, 12 (2010), 2950–2958.

[91] Li, F., Josephson, D. P., and Stein, A. Cheminform abstract: Colloidal assembly: The road from particles to colloidal molecules and crystals. *Angew. Chem. Int. Ed. Engl. 50* (2011), 360–88.

[92] Li, G.-J., and Ardekani, A. M. Hydrodynamic interaction of microswimmers near a wall. *Phys. Rev. E 90* (2014), 013010.

[93] Li, H., Halsey, T. C., and Lobkovsky, A. Singular shape of a fluid drop in an electric or magnetic field. *EPL 27* (1994), 575.

[94] Libai, A., and Simmonds, J. G. *The Nonlinear Theory of Elastic Shells.* Cambridge University Press, Cambridge, 1998.

[95] Lighthill, M. On the squirming motion of nearly spherical deformable bodies through liquids at very small reynolds numbers. *Commun. Pure Appl. Math. 5*, 2 (1952), 109–118.

[96] Liszka, T., and Orkisz, J. The finite difference method at arbitrary irregular grids and its application in applied mechanics. *Comput. Struct. 11*, 1 (1980), 83 – 95.

[97] Liu, X., Kaminski, M. D., Riffle, J. S., Chen, H., Torno, M., Finck, M. R., Taylor, L., and Rosengart, A. J. Preparation and characterization of biodegradable magnetic carriers by single emulsion-solvent evaporation. *J. Magn. Magn. Mater. 311*, 1 (2007), 84.

[98] Liu, X., Kent, N., Ceballos, A., Streubel, R., Jiang, Y., Chai, Y., Kim, P. Y., Forth, J., Hellman, F., Shi, S., Wang, D., Helms, B. A., Ashby, P. D., Fischer, P., and Russell, T. P. Reconfigurable ferromagnetic liquid droplets. *Science 365*, 6450 (2019), 264–267.

[99] Maki, Y., Ito, K., Hosoya, N., Yoneyama, C., Furusawa, K., Yamamoto, T., Dobashi, T., Sugimoto, Y., and Wakabayashi, K. Anisotropic structure of calcium-induced alginate gels by optical and small-angle X-ray scattering measurements. *Biomacromolecules 12*, 6 (2011), 2145–2152.

[100] Menzel, A. M., Saha, A., Hoell, C., and Löwen, H. Dynamical density functional theory for microswimmers. *J. Chem. Phys. 144*, 2 (2016), 024115.

[101] Meyer, M., Desbrun, M., Schröder, P., and Barr, A. H. Discrete differential-geometry operators for triangulated 2-manifolds. In *Visualization and Mathematics III* (Berlin, Heidelberg, 2003), H.-C. Hege and K. Polthier, Eds., Springer Berlin Heidelberg, pp. 35–57.

[102] Michel, J. P., Ivanovska, I. L., Gibbons, M. M., Klug, W. S., Knobler, C. M., Wuite, G. J. L., and Schmidt, C. F. Nanoindentation studies of full and empty viral capsids and the effects of capsid protein mutations on elasticity and strength. *Proc. Natl. Acad. Sci. U.S.A. 103*, 16 (2006), 6184–6189.

[103] Milnor, T. Efimov's theorem about complete immersed surfaces of negative curvature. *Adv. Math. 8* (1972), 474–543.

[104] Mondal, S., Phukan, M., and Ghatak, A. Estimation of solid–liquid interfacial tension using curved surface of a soft solid. *Proc. Natl. Acad. Sci. 112*, 41 (2015), 12563–12568.

[105] Najafi, A., and Golestanian, R. Simple swimmer at low reynolds number: Three linked spheres. *Phys. Rev. E 69* (2004), 062901.

[106] Nocedal, J., and Wright, S. *Numerical Optimization*. Springer Series in Operations Research and Financial Engineering. Springer-Verlag New York, 2006.

[107] Odenbach, S. *Magnetically Controllable Fluids and Their Applications*. Springer, Berlin Heidelberg, 2002.

[108] Ostoja-Starzewski, M. Lattice models in micromechanics. *Appl. Mech. Rev. 55* (2002), 35–60.

[109] Palagi, S., Mark, A. G., Reigh, S., Melde, K., Qiu, T., Zeng, H., Parmeggiani, C., Martella, D., Sanchez-Castillo, A., Kapernaum, N., Giesselmann, F., Wiersma, D., Lauga, E., and Fischer, P. Structured light enables biomimetic swimming and versatile locomotion of photoresponsive soft microrobots. *Nat. Mater. 15* (2016), 647–653.

[110] Pezzulla, M., Shillig, S. A., Nardinocchi, P., and Holmes, D. P. Morphing of geometric composites via residual swelling. *Soft Matter 11* (2015), 5812–5820.

[111] Pieper, G., Rehage, H., and Barthès-Biesel, D. Deformation of a capsule in a spinning drop apparatus. *J. Colloid Interface Sci. 202*, 2 (1998), 293–300.

[112] Poznyak, E., and Shikin, E. Analytical apparatus of the theory of imeddings of negative curvature two-dimensional manifolds. *Sov. Math. 30* (1986), 56–60.

[113] Pozrikidis, C. *Modeling and Simulation of Capsules and Biological Cells.* Chapman and Hall/CRC, Boca Raton, 2003.

[114] Press, W., Teukolsky, S., Vetterling, W., and Flannery, B. *Numerical recipes: the art of scientific computing*, 3rd ed. Cambridge University Press, Cambridge, 2007.

[115] Princen, H. M., Zia, I. Y. Z., and Mason, S. G. Measurement of interfacial tension from the shape of a rotating drop. *J. Colloid Interface Sci. 23*, 1 (1967), 99–107.

[116] Puljiz, M., Huang, S., Auernhammer, G. K., and Menzel, A. M. Forces on rigid inclusions in elastic media and resulting matrix-mediated interactions. *Phys. Rev. Lett. 117* (2016), 238003.

[117] Purcell, E. Life at low reynolds number. *Am. J. Phys. 45* (1977), 3–11.

[118] Quilliet, C., Zoldesi, C., Riera, C., van Blaaderen, A., and Imhof, A. Anisotropic colloids through non-trivial buckling. *The European Physical Journal E 27*, 1 (2008), 13–20.

[119] Ramanujan, S. Modular equations and approximations to π. *Q. J. Math. 45* (1914), 350.

[120] Ramos, A., and Castellanos, A. Conical points in liquid-liquid interfaces subjected to electric fields. *Phys. Lett. A 184*, 3 (1994), 268–272.

[121] Rehage, H., Husmann, M., and Walter, A. From two-dimensional model networks to microcapsules. *Rheol. Acta 41*, 4 (2002), 292–306.

[122] Reissner, E. Stresses and Small Displacements of Shallow Spherical Shells. I. *J. Math. Phys. 25*, 1-4 (1946), 80.

[123] Reissner, E. Stresses and Small Displacements of Shallow Spherical Shells. II. *J. Math. Phys. 25*, 1-4 (1946), 279–300.

[124] Rizvi, M. S., Farutin, A., and Misbah, C. Three-bead steering microswimmers. *Phys. Rev. E 97* (2018), 023102.

[125] Rosenweig, R. E. *Ferrohydrodynamics.* Cambridge University Press, Cambridge, 1985.

[126] Rotne, J., and Prager, S. Variational treatment of hydrodynamic interaction in polymers. *J. Chem. Phys. 50*, 11 (1969), 4831–4837.

[127] Sacanna, S., Irvine, W. T. M., Rossi, L., and Pine, D. J. Lock and key colloids through polymerization-induced buckling of monodisperse silicon oil droplets. *Soft Matter 7* (2011), 1631.

[128] Saintillan, D., and Shelley, M. *Theory of Active Suspensions.* Springer-Verlag New York, 2015, pp. 319–358.

[129] Salsac, A.-V., Zhang, L., and Gherbezza, J. Measurement of mechanical properties of alginate beads using ultrasound. *19Ème Congrès Français De Mécanique* (2009), 1–6.

[130] San-Vicente, G., Aguinaga, I., and Celigueta, J. Cubical mass-spring model design based on a tensile deformation test and nonlinear material model. *IEEE Trans. Vis. Comput. Graph. 18*, 2 (2012), 228–241.

[131] Seung, H. S., and Nelson, D. R. Defects in flexible membranes with crystalline order. *Phys. Rev. A 38* (1988), 1005–1018.

[132] Smith, E., Howard, L., and Dymek, E. Chlamydomonas reinhardtii SEM image, 1996. This image was released in the public domain and was taken from http://remf.dartmouth.edu/images/algaeSEM/source/4.html.

[133] Spagnolie, S. E., and Lauga, E. Hydrodynamics of self-propulsion near a boundary: predictions and accuracy of far-field approximations. *J. Fluid Mech. 700* (2012), 105–147.

[134] Sternberg, S. *Curvature in Mathematics and Physics*. Dover books on mathematics. Dover Publications, Incorporated, 2012.

[135] Stone, H. A., Lister, J. R., and Brenner, M. P. Drops with conical ends in electric and magnetic fields. *Proc. Royal Soc. A 455*, 1981 (1999), 329.

[136] Stratton, J. A. *Electromagnetic Theory*. McGraw-Hill, New York, 1941.

[137] Sun, J.-Y., Zhao, X., Illeperuma, W. R. K., Chaudhuri, O., Oh, K. H., Mooney, D. J., Vlassak, J. J., and Suo, Z. Highly stretchable and tough hydrogels. *Nature (London) 489* (2012), 133.

[138] Sun, S., Zeng, H., Robinson, D. B., Raoux, S., Rice, P. M., Wang, S. X., and Li, G. Monodisperse MFe_2O_4 (M = Fe, Co, Mn) Nanoparticles. *J. Am. Chem. Soc. 126*, 1 (2004), 273–279.

[139] Suryo, R., and Basaran, O. A. Local dynamics during pinch-off of liquid threads of power law fluids: Scaling analysis and self-similarity. *J. Non-Newton. Fluid Mech. 138*, 2 (2006), 134.

[140] Vella, D., Ajdari, A., Vaziri, A., and Boudaoud, A. Wrinkling of Pressurized Elastic Shells. *Phys. Rev. Lett. 107*, 17 (2011), 174301.

[141] Vella, D., Ajdari, A., Vaziri, A., and Boudaoud, A. The indentation of pressurized elastic shells: from polymeric capsules to yeast cells. *J. R. Soc. Interface 9*, 68 (2012), 448–55.

[142] Voltairas, P., Fotiadis, D., and Massalas, C. Elastic stability of silicone ferrofluid internal tamponade (sfit) in retinal detachment surgery. *J. Magn. Magn. Mater. 225*, 1 (2001), 248.

[143] Vonnegut, B. Rotating Bubble Method for the Determination of Surface and Interfacial Tensions. *Rev. Sci. Instrum. 13*, 1 (1942), 6–9.

[144] Wendland, W. L. *On Asymptotic Error Estimates for Combined BEM and FEM*. Springer, Vienna, 1988, pp. 273–333.

[145] Wilson, C. T. R., and Taylor, G. I. The bursting of soap-bubbles in a uniform electric field. *Math. Proc. Cambridge Philos. Soc. 22*, 5 (1925), 728.

[146] Wischnewski, C. *Numerische Berechnung der Deformation elastischer Kapseln durch Ferrofluide*. Master's thesis, Technische Universität Dortmund, 2015.

[147] Wischnewski, C., and Kierfeld, J. Spheroidal and conical shapes of ferrofluid-filled capsules in magnetic fields. *Phys. Rev. Fluids 3* (2018), 043603.

[148] Wischnewski, C., Zwar, E., Rehage, H., and Kierfeld, J. Strong deformation of ferrofluid-filled elastic alginate capsules in inhomogenous magnetic fields. *Langmuir 34* (2018), 13534–13543.

[149] Witten, T. A. Stress focusing in elastic sheets. *Rev. Mod. Phys. 79*, 2 (2007), 643–675.

[150] Wohlhuter, F. K., and Basaran, O. A. Shapes and stability of pendant and sessile dielectric drops in an electric field. *J. Fluid Mech. 235* (1992), 481.

[151] Yang, M., Wysocki, A., and Ripoll, M. Hydrodynamic simulations of self-phoretic microswimmers. *Soft Matter 10* (2014), 6208–6218.

[152] Zeleny, J. Instability of electrified liquid surfaces. *Phys. Rev. 10*, 1 (1917), 1.

[153] Zhang, Y., Chan, H. F., and Leong, K. W. Advanced materials and processing for drug delivery: The past and the future. *Adv. Drug Deliv. Rev. 65*, 1 (2013), 104 – 120.

[154] Zhu, G.-P., Nguyen, N.-T., Ramanujan, R. V., and Huang, X.-Y. Nonlinear deformation of a ferrofluid droplet in a uniform magnetic field. *Langmuir 27*, 24 (2011), 14834.

[155] Zwar, E. *Verkapselung magnetischer Nanopartikel als stabile Ferrofluide sowie Charakterisierung ihrer Anordnung an Grenzflächen.* PhD thesis, Technische Universität Dortmund, 2018.

[156] Zwar, E., Kemna, A., Richter, L., Degen, P., and Rehage, H. Production, deformation and mechanical investigation of magnetic alginate capsules. *J. Phys. Condens. Matter 30*, 8 (2018), 085101.

Acknowledgement

An dieser Stelle möchte ich all jenen danken, die zur Entstehung dieser Arbeit beigetragen haben. An erster Stelle ist dies Professor Dr. Jan Kierfeld, der diese Arbeit über fast vier Jahre betreute und mir immer mit Ratschlägen und Anmerkungen zur Seite stand.

Ebenso gilt mein Dank Professor Dr. Heinz Rehage. Zum einen für die Übernahme des Zweitgutachtens, zum anderen aber auch für die sehr erfolgreiche Kooperation mit seiner Arbeitsgruppe. In diesem Kontext möchte ich mich insbesondere bei Dr. Elena Zwar für die sehr angenehme und lehrreiche Zusammenarbeit bei der Planung, Umsetzung und Analyse des Kapselexperiments bedanken.

Meinen Bürokollegen Hendrik Ender und Matthias Schmidt danke ich für die vielen anregenden Diskussionen, Ideen, Tipps und technischen Hilfestellungen. Bedanken möchte ich mich auch bei Natalie Jäschke für ihre Korrekturanmerkungen und die gegenseitigen Aufmunterungen. Mein finaler Dank gilt meiner Verlobten, Anika Henke, die für mich immer mein Fels in der Brandung war, mich jederzeit auf jede nur erdenkliche Weise unterstützte und damit einen nicht unwesentlichen Anteil daran hatte, dass diese Arbeit in dieser Form entstehen konnte.